UWB Pulse Radar for Human Imaging and Doppler Detection Applications

A Dissertation Presented for the
Doctor of Philosophy
Degree
The University of Tennessee, Knoxville

Yazhou Wang
May 2012

Copyright © 2012 by Yazhou Wang
All rights reserved.

Dedication

To my parents, Shusheng Wang and Fengyun Zou, and my wife, Chen Li,

whose encouragement and support have made this possible.

To my beloved daughter, Enora Anpei Wang.

Acknowledgements

I wish to acknowledge the many people who have helped to make this work possible, especially my advisor Dr. Aly Fathy who has brought me into this interesting and exciting area of ultra-wideband. He has always helped to make my research focused on when I get sidetracked on impractical research interest. He has taught me how to "Work Smart, Not Hard" in doing research. He has been a great mentor, encouraging and helping me both within and outside my research.

I would like to thank Dr. Mohamed Mahfouz for his supervision and unique insights on applying ultra-wideband technology for early breast cancer detection. I would also like to thank my committee members: Dr. Marshall O. Pace, Dr. Syed K. Islam, and Dr. Gong Gu, for reviewing my dissertation and providing helpful advices.

I would like to thank Dr. Moeness G. Amin, Villanova University, and Dr. Mohamed Mahfouz for providing financial support to make this research possible. I would also like to thank Rogers Corporation and Taconic Corporate for providing free samples of microwave frequency substrate.

I would like to express my appreciation to both past and current members at the antenna and microwave group: Songnan Yang, Cemin Zhang, Song Lin, Chunna Zhang, Sungwoo Lee, Mohamed Awida, Esam Elkhouly, Michael Kuhn, Depeng Yang, Yun Koo, Ki Shin, Reza Ghahremani, Jonathan Turnmire, Nathan Rowe, Jeho Lee, for all your advices and support. Especially, I would like to thank Quanhua Liu for the help in implementing the data acquisition module and performing experiments with me; and Yunqiang Yang for helping me get familiar with the previous radar prototype ASAP and answering many technical questions.

Last but not the least, thanks to Emily Pritchard and Jon Huber for their help in developing and modeling the breast phantom. Thanks to Rimon Tadross for showing me how to use ultrasound machine for breast phantom imaging.

Abstract

We were motivated to develop new technologies capable of identifying human life through walls. Our goal is to pinpoint multiple people at a time, which could pay dividends during military operations, disaster rescue efforts, or assisted-living. Such system requires the combination of two features in one platform: seeing-through wall localization and vital signs Doppler detection.

Ultra-wideband (UWB) radar technology has been used due to its distinct advantages, such as ultra-low power, fine imaging resolution, good penetrating through wall characteristics, and high performance in noisy environment. Not only being widely used in imaging systems and ground penetrating detection, UWB radar also targets Doppler sensing, precise positioning and tracking, communications and measurement, and etc.

A robust UWB pulse radar prototype has been developed and is presented here. The UWB pulse radar prototype integrates seeing-through imaging and Doppler detection features in one platform. Many challenges existing in implementing such a radar have been addressed extensively in this dissertation. Two Vivaldi antenna arrays have been designed and fabricated to cover 1.5-4.5 GHz and 1.5-10 GHz, respectively. A carrier-based pulse radar transceiver has been implemented to achieve a high dynamic range of 65dB. A 100 GSPS data acquisition module is prototyped using the off-the-shelf field-programmable gate array (FPGA) and analog-to-digital converter (ADC) based on a low cost solution: equivalent time sampling scheme. Ptolemy and transient simulation tools are used to accurately emulate the linear and nonlinear components in the comprehensive simulation platform, incorporated with electromagnetic theory to account for through wall effect and radar scattering.

Imaging and Doppler detection examples have been given to demonstrate that such a “Biometrics-at-a-glance” would have a great impact on the security, rescuing, and biomedical applications in the future.

Table of Contents

Chapter 1 Introduction 1

1.1 State-of-the-art 2

1.1.1 Current Status of Human Imaging 2

1.1.2 Current Status of Doppler Detection 6

1.2 UWB Pulse Radar for Human Imaging and Doppler Detection 8

1.3 Challenges in Designing Such a UWB Pulse Radar 11

1.4 Contributions 12

1.5 Organization of the Dissertation 13

Chapter 2 System Development of UWB Pulse Radar 15

2.1 Operation Frequency Selection 16

2.2 8-10 GHz UWB Pulse Radar System 19

2.3 1.5-4.5 GHz UWB Pulse Radar System 20

2.3.1 Transceiver RF Front-end 20

2.3.2 1.5-4.5 GHz Vivaldi Antenna and Array Design 25

2.4 Reconfigurable UWB Pulse Radar System 31

2.4.1 Transceiver RF Front-end 31

2.4.2 1.5-10 GHz Vivaldi Antenna and Array Design 32

2.5 Low Cost, High Speed Data Acquisition Module 38

2.5.1 Equivalent-time Sampling Scheme 39

2.5.2 1st Generation Hardware 40

2.5.3 2nd Generation Hardware 42

2.5.4 3rd Generation Hardware 43
2.6 Conclusion 46
Chapter 3 System Level Simulation of UWB Pulse Radar 48
3.1 Simulation Platform Architecture 49
3.1.1 Initialization 50
3.1.2 Radar Transmitter Operation 50
3.1.3 Through Wall Propagation 52
3.1.4 Electromagnetic Scattering by 3-D Radar Objects 57
3.1.5 UWB Radar Receiver Modeling 59
3.1.6 Wideband Microwave Beamformer 61
3.2 Experimental Validation 63
3.3 System Performance Prediction 68
3.3.1 Pulse Waveform Optimization 68
3.3.2 System Performance Prediction 74
3.4 Conclusion 75
Chapter 4 UWB Pulse Radar for Imaging Applications 77
4.1 Real-time Through Wall Human Tracking 77
4.1.1 Microwave Beamforming Algorithm 78
4.1.2 Through-Wall Effects 81
4.1.3 Imaging Resolution 84
4.1.4 Through Wall Imaging of Multiple Static Targets 90
4.1.5 Real-time Tracking of a Walking Person 92

4.1.6 Real-time Through Wall Tracking of Two Walking Persons 93
4.2 3-D Human Imaging 97
4.2.1 3-D Microwave Beamformer 98
4.2.2 3-D Imaging of a Human Mock-up 102
4.3 Early Breast Cancer Detection 105
4.3.1 Breast Imaging System 106
4.3.2 Breast Imaging Antenna Design 107
4.3.3 Novel Calibration Approach for Clutter Removal 114
4.3.4 Numerical Simulation and Experimental Results 118
4.4 Conclusion 123
Chapter 5 UWB Pulse Radar for Doppler Detection Applications 124
5.1 Micro-Doppler Signature Extraction 125
5.1.1 Basic Theory 125
5.1.2 Radar Signal Processing 127
5.2 Doppler Ambiguity 129
5.3 Human Gait Analysis 130
5.3.1 Human Walking Without Arm Swing 131
5.3.2 Human Walking With One-Arm Swing 133
5.3.3 Human Walking With Two-Arm Swing 135
5.4 Doppler Tracking of Two Persons 137
5.5 Through Wall Respiration Detection of Stationary People 144
5.5.1 Single Person Experiment 147

5.5.2 Two Persons at Different Distances 150
5.5.3 Two Persons at Same Distance, But Different Angles 153
5.6 Alternative Technology: CW Doppler Radar 156
5.6.1 CW Doppler Radar Prototype 156
5.6.2 Doppler Detection Experiment 159
5.6.3 Comparison with UWB Pulse Radar 165
5.6.4 Summary of Two Radar Technologies 169
5.7 Conclusion 170
Chapter 6 Conclusions and Future Work 172
6.1 Accomplishments and Contributions 172
6.2 Publications 174
6.3 Conclusion 176
6.4 Direction of Future Work 178
List of References 180
Appendix 188
Appendix A Matlab Code 189
A.1 Reflection and Transmission Through a Multiple Layer Wall 189
A.2 2-D Backprojection Beamformer for Microwave Imaging 193
A.3 3-D Backprojection Beamformer for Microwave Imaging 196
A.4 3-D Electromagnetic Scattering Using MoM 199
A.5 UWB Pulse Radar Micro-Doppler Spectrogram Extraction 209
A.6 UWB Pulse Radar Micro-Doppler Wigner-Ville spectrum Extraction 211

Appendix B MoM Method for Solving Electromagnetic Scattering Problem 213

Appendix C FPGA Source Code Used to Implement the DDC in CW Radar 215

Vitae 220

List of Tables

Table 1.1 Comparison of Various Imaging Technologies 2

Table 1.2 State-of-the-art of Human Imaging Radar 6

Table 1.3 State-of-the-art of Doppler Detection Radar 8

Table 1.4 Comparisons of Various Radar Technologies for Imaging & Doppler Detection 10

Table 2.1 Characteristics of Various Building Materials 18

Table 2.2 Isolation requirement between radar transmitter and receiver 24

Table 2.3 Dynamic range analysis of the radar transceiver 24

Table 2.4 Comparison of the three arrays in detailed performance 38

Table 2.5 Comparison of three generations data acquisition and transfer module 45

Table 4.1 Computational Efficiency Comparison of Various Imaging Algorithms 78

Table 5.1 Comparison of Developed CW and UWB PD Radar Prototypes 170

List of Figures

Figure 1.1 A vehicle borne UWB impulse imaging radar developed by U.S. Army Research Laboratory for imaging of building interior [14]. 4

Figure 1.2 A FMCW imaging radar working at 500 MHz to 2 GHz for through wall surveillance, developed by Allan R. Hunt [15]. 4

Figure 1.3 A real-time UWB imaging radar system operating at 8-10 GHz for seeing through low-loss wall materials by Yunqiang Yang [16], [17]. 5

Figure 2.1 Simulated one-way through wall reflection and transmission through various building materials, with a thickness of 20cm. 18

Figure 2.2 Detailed diagram of the previously developed 8-10 GHz radar imaging system. 20

Figure 2.3 Detailed block diagram of the developed UWB impulse radar. 21

Figure 2.4 Photograph of the developed UWB PD radar RF front-end module. 22

Figure 2.5 Link budget analysis of the radar transceiver. 23

Figure 2.6 HFSS model and prototype of the compact wideband Vivaldi antenna, with a size of 12cm × 9cm and a thickness of 31-mil. 26

Figure 2.7 Simulation and experimental VSWR result of the fabricated Vivaldi antenna. 27

Figure 2.8 Dimension and photograph of the fabricated Vivaldi sub-array. 28

Figure 2.9 Measured return loss of the Vivaldi sub-array, showing good match at 1 to 5.5 GHz. 29

Figure 2.10 Measured radiation pattern of the Vivaldi sub-array, showing good directional characteristics over the operation frequency. 30

Figure 2.11 Photograph of the 1×8 Vivaldi antenna array. 31

Figure 2.12 Detailed block diagram of the reconfigurable imaging radar system. 32

Figure 2.13 HFSS model and prototype of the fabricated 1.5-10 GHz Vivaldi antenna. . 33

Figure 2.14 Simulated and measured return loss of the Vivaldi antenna. 34

Figure 2.15 Measured radiation pattern at 4 GHz and 10 GHz respectively, showing good directional radiation characteristics. 34

Figure 2.16 Dimension and photograph of the fabricated 1.5-10 GHz Vivaldi Array. 35

Figure 2.17 Measured return loss of the 8-element Vivaldi array. 36

Figure 2.18 Measured gain of the compact array from 2-10 GHz. 36

Figure 2.19 Co-pol and Cross-pol E-plane radiation pattern at 4 GHz. 37

Figure 2.20 Co-pol and Cross-pol E-plane radiation pattern at 10 GHz. 37

Figure 2.21 Equivalent-time sampling scheme. 39

Figure 2.22 Photograph of the 1st generation data sampling, storage and transfer module, utilizing a Xilinx Virtex-4 FPGA evaluation board and two Maxim-IC MAX104 ADC evaluation boards. 41

Figure 2.23 Detailed diagram of 1st generation data acquisition, storage and transfer module. 41

Figure 2.24 Photograph of the 2nd generation data sampling, storage and transfer module, utilizing a Xilinx Virtex-4 FPGA evaluation board and two Texas Instruments ADS54RF63 ADC evaluation boards. 42

Figure 2.25 Photograph of the 3rd generation compact, 100GS/s data acquisition module, integrating FPGA, dual channel ADC, programmable time delay and USB microcontroller in a 4-layer PCB circuit board. 44

Figure 2.26 Block diagram of the 3rd generation data acquisition and transfer module. .. 44

Figure 3.1 Generic system simulation model including six blocks. 50

Figure 3.2 Simulation model of UWB radar transmitter in ADS. 51

Figure 3.3 Simulation and measurement of the transmitted signals emitted by the UWB transmitter. The transmitted signal is periodic with T_0 = 100ns. 52

Figure 3.4 Measured permittivity of drywall and brick-wall from 1 to11 GHz. 55

Figure 3.5 Reflected and transmitted signal through different wall materials..... 56

Figure 3.6 Bistatic RCS of a losslessy dielectric sphere with a radius of 5cm at f = 3 GHz (ε_r = 4, μ_r = 1, σ = 0). 58

Figure 3.7 Bistatic RCS of a lossy dielectric sphere with a radius of 5cm at f = 3 GHz (ε_r = 4, μ_r = 1, σ = 0.2 S/m). 59

Figure 3.8 Agilent ADS Ptolemy simulation incorporating Matlab source and sinks, Matlab through-wall and target scattering models, UWB radar receiver, and 8-bit MAX104 ADCs. 60

Figure 3.9 ADS model of I/Q radar receiver front-end. 60

Figure 3.10 Comparison of recovered pulse signals from simulation and experiment. 61

Figure 3.11 3-D wideband microwave beamformer model. 63

Figure 3.12 3-D imaging of a wooden block, with a size of 45cm x 35cm x 1cm. 64

Figure 3.13 Recovered image results of a wooden block: (a) Simulation results, and (b) Experimental results. The target is put at a down range of 2.2 m. 65

Figure 3.14 Simulation geometry of two metallic cylinders within the wall. 66

Figure 3.15 Simulation imaging results of two cylindrical targets within a drywall. The two cylinders are put at a down range of 0.7m. Dotted white lines indicate the true target location and shape. 67

Figure 3.16 A human phantom target used in the simulation. 70

Figure 3.17 Simulation results of a human phantom target using a 300ps Gaussian pulse signal source. Solid white lines indicate the true target shape while dotted white lines indicate the true target position. 71

Figure 3.18 Simulation results of a human phantom target using a 300ps monocycle pulse signal source (1st derivative of Gaussian pulse). Solid white lines indicate the true target shape while dotted white lines indicate the true target position. 72

Figure 3.19 Simulation results of a human phantom target using a 1ns incident Gaussian pulse signal. Solid white lines indicate the true target shape while dotted white lines indicate the true target position. 73

Figure 3.20 Simulated SNR of received pulse signal versus target distance when seeing through a 6-inch drywall and a 6-inch brick-wall respectively. 74

Figure 4.1 Simplified synthetic beam-forming algorithm. 80

Figure 4.2 Near-field Backprojection microwave beamformer. 81

Figure 4.3 Through-wall model. 82

Figure 4.4 Obtained radar images before and after compensation for wall effects. White rectangular marker shows the true target position. 83

Figure 4.5 Experimental setup of the down range resolution measurement using dihedral as radar object 85

Figure 4.6 Acquired images of the dihedral target when placed at different distances to the radar system, also indicating the images of metal door and metal railing. 86

Figure 4.7 Experimental setup of the cross range resolution measurement using two dihedral objects 88

Figure 4.8 Recovered radar images when the two dihedrals are separated at different distances *d*. 89

Figure 4.9 Experiment setup of through wall imaging of multiple static objects using the developed radar. 90

Figure 4.10 Experimental imaging results of detecting multiple static targets through a cement wall. 91

Figure 4.11 Real-time location tracking of single walking person in a LOS scenario 93

Figure 4.12 Real-time tracking of two walking persons through a cement block, two objects walking toward opposite directions. 94

Figure 4.13 Real-time tracking of two walking persons through a cement block, two objects walking toward the same direction. 96

Figure 4.14 3-D microwave beamformer model. 101

Figure 4.15 3-D beamformer flow chart 101

Figure 4.16 Old coordinate (x, y, z) translates to a new one (x', y', z') 102

Figure 4.17 A human mock-up object used in 3-D imaging experiment. 103

Figure 4.18 Recovered image results of a human mock-up object: (a) Simulation result of human mock-up model, and (b) Experimental result. 104

Figure 4.19 Detailed block diagram of the developed UWB microwave imaging system prototype at UT. 106

Figure 4.20 Geometry of the proposed wideband tapered slot antenna after optimization. $W1$ = 19mm, $W2$ = 1.6mm, $W3$ = 3.4mm, $W4$ = 2.3mm, $L1$ = 19mm, $L2$ = 5.2mm, $L3$ = 9.5mm, R = 2.0. 108

Figure 4.21 Simulation model of the proposed antenna in HFSS. The interaction between antenna and breast tissue is taken into account in the design. 109

Figure 4.22 Parametric studies of the proposed wideband slot antenna. 111

Figure 4.23 Prototype of the proposed wideband slot antenna. 112

Figure 4.24 Return loss measurement of the designed tapered microstrip slot antenna. 113

Figure 4.25 Semispherical antenna array for clinical examination using the designed wideband microstrip slot antenna. 114

Figure 4.26 Geometry of a cylindrical microwave imaging system. The two filled square icons indicate the Tx/Rx antenna pair at position Pi while the two non-filled square icons show the antenna pair at the next position Pi+1 after the rotation. 117

Figure 4.27 Measured signal returns when Tx/Rx antennas are at positions P_i and P_{i+1}. 117

Figure 4.28 Corrected signal after the calibration. The signal due to tumor reflection/scattering is highlighted. 118

Figure 4.29 Geometry of the experimental setup. 119

Figure 4.30 Detection of a 5mm diameter tumor from a cylindrical breast phantom based on experimental data. 120

Figure 4.31 Detection of two breast tumors from a cylindrical breast phantom based on experimental data. 121

Figure 4.32 Detection of a 5mm diameter tumor from an ellipse cylindrical breast phantom based on FDTD simulation data using CST. 122

Figure 5.1 Acquired results when the person walking without arm swing. 132

Figure 5.2 Acquired results when the person walking with one-arm swing. 134

Figure 5.3 Acquired results when the person walking with two-arm swing. 136

Figure 5.4 Experiment of tracking two persons walking toward same direction, one walking faster while the other slower. 138

Figure 5.5 Experiment of tracking two persons walking toward opposite directions. 140

Figure 5.6 Experiment of tracking two persons walking toward the same direction but at different distances, one is closer to the radar while the other further from the radar. 142

Figure 5.7 Experiment of tracking two persons walking toward different directions and at different distances too. 145

Figure 5.8 Localization and respiration detection of single person through a cement wall, showing a respiratory rate of 27 breaths per minute and a Doppler frequency of 0.48 Hz. 148

Figure 5.9 Localization and respiration detection of two persons through a cement wall. The two persons stand at different distances to the radar, one is closer while the other is further. 151

Figure 5.10 Localization and respiration detection of two persons through a cement wall. The two persons stand at the same distance to the radar, but at different cross ranges. The 1st person breathes faster while the 2nd one breathes slower. 154

Figure 5.11 Detailed block diagram of the CW Doppler radar prototype. 159

Figure 5.12 Detailed block of the quadrature DDS implemented in FPGA. 159

Figure 5.13 Experimental setup of sensing a person riding exercise bike. 160

Figure 5.14 Acquired spectrogram when sensing a person riding exercise bike using the developed CW Doppler radar. 161

Figure 5.15 Experimental setup of sensing a person walking/jogging on the treadmill. 163

Figure 5.16 Acquired spectrogram of sensing a person walking/jogging on the treadmill using the developed CW Doppler radar. 164

Figure 5.17 Acquired spectrogram of sensing a person riding exercise bike using the developed UWB PD radar. 166

Figure 5.18 Acquired spectrogram of sensing a person walking/jogging on the treadmill using the developed UWB PD radar. 168

List of Abbreviations

ADC	Analog-to-digital Converter
CW	Continuous Wave
DAS	Delay and Sum
DDC	Digital Down Converter
FFT	Fast Fourier Transform
FMCW	Frequency Modulated Continuous Wave
FPGA	Field-programmable gate array
GPR	Ground Penetrating Radar
IF	Intermediate Frequency
LNA	Low Noise Amplifier
LO	Local Oscillator
LOS	Line-of-sight
LUT	Lookup Table
m-D	micro-Doppler
MoM	Method of Moments
PD	Pulse Doppler
PRF	Pulse Repetition Frequency
PRT	Pulse Repetition Time
RCS	Radar Cross Section
SAR	Synthetic Aperture Radar
SNR	Signal-to-noise Ratio
STFT	Short Time Fourier Transform
TOT	Time on Target
TWI	Through-wall Imaging
UWB	Ultra-wideband
VCO	Voltage Controlled Oscillator
VNA	Vector Network Analyzer

Chapter 1

Introduction

Ultra-wideband (UWB) devices operate by employing very narrow or short duration pulses that result in very large or wideband transmission bandwidth. UWB technology holds great promise for a lot of new applications that will significantly benefit government, public safety, businesses, and consumers. The recent FCC ruling for UWB increased the interest for investigating this technology for imaging systems (e.g., through-wall imaging (TWI), ground penetrating radars (GPRs), surveillance systems, and medical imaging devices), vehicular radar systems, and communications and measurement systems [1].

Human localization and motion detection, in particular, have attracted a lot of attention nowadays by many researchers using this new enabling technology because of its big impact on multitude of applications. Typically, human locations estimation can be achieved by radar imaging while their motions can be extracted through radar Doppler detection.

Human imaging can predict the location (i.e., distance and angle) of the objects by acquiring brighter pixels for objects in the recovered images and has been widely used in many applications. For example, it has been used in security surveillance to detect and track terrorists' locations through a building wall or any other blockage. Another example is for rescuing applications, where it is an effective tool to search for trapped persons during fire or earthquake. Additionally, in biomedical applications, it is an alternative method for early breast cancer detection by successfully imaging the cancerous breast tissue. Similar technology can also be applied for mines detection through ground penetration or remote sensing—and the list goes on.

Meanwhile, Doppler detection, is helpful for better understanding the activities of human objects and can enhance the detection capability. For example, in security surveillance, besides detecting the locations of the terrorists, the gait analysis through Doppler detection can be used to judge if they carry any weapons or not. In rescuing

applications, Doppler feature can help search earthquake survivors through their vital signs. In addition, Doppler device can be used to monitor the respiration of patients in hospitals and investigate the daily activity of elderly people at home.

In the following, we will firstly review the state-of-the-art of human imaging and Doppler detection technologies respectively, and then introduce the UWB pulse radar which is an attractive radar technique that can achieve both features simultaneously.

1.1 State-of-the-art

1.1.1 Current Status of Human Imaging

Various technologies have been proposed for human imaging, including narrow band microwave radar [2], UWB microwave radar [3]-[8], acoustics [9], infrared [10], and etc. The comparison of various imaging technologies is listed in Table 1.1, in terms of resolution, day/night operation, wall penetration and motion tracking capability. Researchers have concentrated on developing UWB microwave radar for its numerous advantages, such as high detection target range accuracy, good penetrating wall characteristics, operation unaffected by day/night or weather conditions, improved immunity to external radiation and noise, and etc.

Table 1.1 Comparison of Various Imaging Technologies

	Narrowband Radar	**Ultrasound**	**Infrared**	**X-ray**	**UWB Radar**
Resolution	Poor	Good	Good	Good	Good
Day/Night Operation	Yes	Yes	No	No	Yes
Wall Penetration	Good	Marginal	Good	Good	Good
Motion Tracking	Yes	Yes	No	No	Yes

Relevant literature has introduced the development of UWB microwave imaging radars in both frequency and time domains. Many UWB imaging radar prototypes have been implemented with frequency domain techniques based on using vector network analyzer (VNA). For example, a radar prototype has been presented in [11] for imaging of two targets in close proximity of each other behind a wall. In [12], a ground penetrating radar was built up to detect the signatures of complex buried objects. Recently, this method has been extended for early breast cancer detection working at 3-10 GHz [13]. But, the design of UWB systems using frequency domain techniques is still limited by the complexity of its signal processing and the expensive cost of the VNA. In addition, it is very difficult to make the radar portable and compact because of the utilization of heavy and bulky VNA.

Meanwhile, the recent and continuous advancements of commercial UWB components have attracted many attentions and efforts to develop and implement UWB imaging radar using time-domain tools. For example, UWB synchronous impulse reconstruction radar has been developed and presented to image the interior of a building structure by U.S. Army Research Laboratory in [14], as shown in Figure 1.1. UWB frequency modulated continuous wave (FMCW) imaging radar system was also developed for through wall detection and surveillance in [15], as shown in Figure 1.2.

In parallel with these efforts, my group has also developed a real-time UWB see through wall imaging radar system based on field-programmable gate array (FPGA) by Yunqiang Yang [16], [17], as shown in Figure 1.3. The system operates at 8-10 GHz in order to acquire a relatively high imaging resolution when seeing through low-loss building materials, such as drywall, wooden wall and glass.



Figure 1.1 A vehicle borne UWB impulse imaging radar developed by U.S. Army Research Laboratory for imaging of building interior [14].



Figure 1.2 A FMCW imaging radar working at 500 MHz to 2 GHz for through wall surveillance, developed by Allan R. Hunt [15].

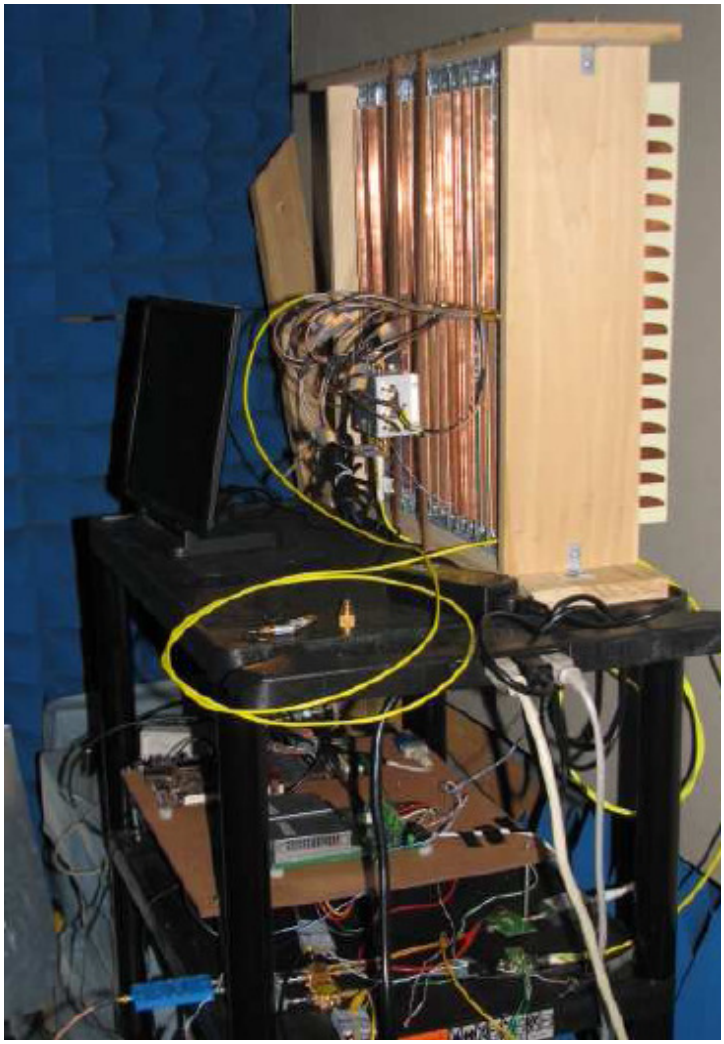


Figure 1.3 A real-time UWB imaging radar system operating at 8-10 GHz for seeing through low-loss wall materials by Yunqiang Yang [16], [17].

There are also few commercially available UWB through wall imaging systems that are based on time-domain techniques, such as the PULSON® 400 radar sensor module from Time Domain® [18], prism 200 through-wall radar from Cambridge Consultants [19], and XaverTM 800 vision system from Camero-tech [20]. The state-of-the-art of the UWB pulse imaging radar is list in Table 1.2.

Table 1.2 State-of-the-art of Human Imaging Radar

Group/Company	Operation Frequency	Range	Display Mode	Resolution	Radar Technique
Dehmollaian et al. [11]	1-3 GHz	Not Available	2D	Not Available	Frequency Domain, UWB
Panzner et al. [12]	5k - 20GHz	Not Available	2D	1-2 cm	Frequency Domain, UWB
Klemm et al. [13]	3-10 GHz	Not Available	3D	4-6 mm	Frequency Domain, UWB
US Army Research Lab [14]	300M - 3GHz	25 m	2D	Not Available	UWB Pulse
AKELA. Inc [15]	500M - 2 GHz	40 m	2D	10 cm	UWB FMCW
Yang [16],[17]	8-10 GHz	15 m	2D	10 cm	UWB Pulse
Time Domain® [18]	3.1-6.3 GHz	20 m	2D	Not Available	UWB Pulse
Cambridge Consultants [19]	1.7-2.2 GHz	20 m	2D/3D	30 cm	Not Available
Camero-Tech Ltd. [20]	3-10 GHz	20 m	2D/3D	20 cm	Not Available

1.1.2 Current Status of Doppler Detection

Nowadays, most of the researchers and groups concentrate on using continuous wave (CW) radar for Doppler detections due to its simpler system design and implementation, and lower development cost. For example, CW microwave Doppler radar operating at 2.4 GHz was developed for sensing of multi-mover in [21]. CW microwave Doppler radar was also widely used for vital sign detection and life detection [22]-[25]. In [26], CW Doppler radar was extended to extracting the Doppler signatures

for biometric characterization. Signal processing and Doppler extraction method for CW Doppler radar were also discussed in [27]-[33]. Although it is simpler and cheaper to design and implement CW Doppler radar, CW radar does not give any range information or cannot track the location of the target at all. Those have significantly limited the utilization of CW radar in many applications, such as detecting the terrorists through the wall, monitoring the activities of elderly people at home, where both location and Doppler signatures of the radar targets are needed.

In order to achieve both Doppler detection and imaging features in one radar platform, a wideband FMCW Doppler radar was developed to operate at 500 MHz to 2 GHz for through wall imaging and motion detection [34]. In addition, UWB pulse compression radar was also designed and implemented for searching and detecting trapped people by detecting their breathing information [35], [36], and an impulse radio UWB radar system was introduced for vital signs monitoring [37]. Table 1.3 introduces the state-of-the-art of the microwave Doppler radar systems.

Table 1.3 State-of-the-art of Doppler Detection Radar

Research Group	Technology	Operation Frequency	Range	Application
Lin et al. [21]	CW	2.4 GHz	10 m	Moving target sensing
Li et al. [22]	CW	5.8 GHz	Non-contact	Vital sign detection
Zhou et al. [23]	CW	2.4 GHz	Non-contact	Heartbeat monitoring
Chen et al. [24], [25]	CW	10 GHz	30 m	Life detection
Silvious et al. [26]	CW	400 MHz/17 GHz	Not Available	Biometric characterization
Hunt [34]	FMCW	500M - 2GHz	40 m	Motion detection
Zaikov et al. [35] and Sachs et al. [36]	Pulse compression	1M - 4.5 GHz	Not Available	Trapped people detection
Lazaro et al. [37]	UWB Pulse	3.1 – 10.6 GHz	Not Available	Vital sign monitoring

1.2 UWB Pulse Radar for Human Imaging and Doppler Detection

To summarize the state-of-the-art of imaging radars, the frequency domain technique based on VNA is not recommended due to its high cost and portability limitation. FMCW imaging system shows good imaging performance, however, it is very expensive and needs complicated signal processing to design wideband FMCW radar. On the contrary, UWB pulse radar has progressed substantially in recent years to be widely used by many researchers and laboratories and is considered as a very attractive candidate for human imaging applications. UWB pulse radar shows the capability of sensing human objects in a harsh environment, even in through wall scenario.

Meanwhile for Doppler detection radars, CW radar has been widely used for a long time for Doppler applications due to its simpler system architecture and lower prototyping cost. However, simple CW radar does not render target range information, which is of great importance in human detection and sensing applications. Both FMCW and pulse compression radar have the potential to achieve both high range resolution and Doppler detection capability. However, their system complexity, signal processing difficulty, and development cost of the wideband FMCW and pulse compression radar are much higher. In contrast, UWB pulse Doppler (PD) radar tends to achieve a better compromise between system performance and prototyping cost when acquiring both high resolution range profile and Doppler detection capability simultaneously. Table 1.4 lists the comparison of various radar technologies for imaging and Doppler detection applications.

Therefore, UWB pulse radar technique has been used for both human imaging and Doppler detection applications in this dissertation.

Table 1.4 Comparisons of Various Radar Technologies for Imaging & Doppler Detection

Characteristics	**CW Radar**	**FMCW Radar**	**Pulse Compression Radar**	**UWB Pulse Radar**
Range Resolution	No range information	Good (if use wideband)	Good	Good
Doppler Resolution	Time on target (TOT)	TOT	Pulse Repetition Time (PRT) × M	PRT × M (# of slow-time samples)
Detection Range (with same peak power)	Long	Long	Marginal	Marginal
Doppler Ambiguity	No	PRT	PRT	PRT
Easy to Separate T/R Coupling	No	No	Yes	Yes
Separate Multipath Propagations	Poor	Poor	Good	Good
Data Acquisition	Simpler	Marginal	Marginal	Hard
System Complexity	Simpler	High (if use wideband)	High	Marginal
Signal Processing Complexity	Low	High	High	Low
Cost	Low	High (if use wideband)	High	Marginal

1.3 Challenges in Designing Such a UWB Pulse Radar

Although UWB pulse radar has gained a lot of attention and efforts by researchers, the available UWB pulse radars today still have their own limitations, when used for human imaging and Doppler detection applications. Most of the available UWB pulse radar systems provide imaging capability, but do not include Doppler detection feature in the same platform [14], [16]-[18]. In addition, UWB pulse radars operating at higher UWB band [16]-[18], [37] work well for line-of-sight (LOS) or through low-loss materials detection, such as drywall, wood, and glass, but will suffer from the high through attenuation when seeing through high-loss materials, such as typical brick and concrete building walls, breast tissue, and other high water-content materials.

It is a very challenging job to design a good UWB pulse radar prototype for human imaging and Doppler detection applications. A list of these challenges includes:

a) Develop and implement imaging function and Doppler detection capability in one radar platform. The imaging feature prefers a wide system bandwidth in order to achieve a high range resolution. However, a wideband signal means a large amount of data to be recorded and stored per cycle which could significantly slow down the system refresh rate. Meanwhile, in order to extract the Doppler signatures from target motions, especially from object's fast movements like running, the digitized data of the collected signal must be stored at a very high system refresh rate in order to avoid the Doppler ambiguities. This would mandate a very fast signal digitization and system update rate when processing the UWB pulse signal.

b) Develop a robust radar prototype with a high dynamic range in order to operate well in a highly cluttered environment, such as detection through brick and concrete building walls. The radar transceiver needs to detect the small scattered signals from radar targets, as well as tolerate the strong reflections from the building wall.

c) Design of wideband antennas, dividers and antenna arrays, especially at lower UWB band as it requires a larger relative bandwidth.

d) Accurate modeling and simulation of a complicated radar system. No commercial software or developed tools have been available to analyze and simulate a complete UWB pulse radar yet.

To overcome these challenges, a high speed data acquisition module was implemented to digitize the narrow UWB pulse signal. USB2.0 data communication link was used to upload the data to a PC in order to achieve a fast system refresh rate. A robust radar transceiver was developed, with a high dynamic range of 65dB. Wideband Vivaldi antennas and arrays were designed and fabricated, covering the entire UWB imaging band of 1.99 to 10.6 GHz. A system level simulation platform was developed to accurately simulate and predict the performance of UWB pulse radar systems. The main contributions of this dissertation will be introduced in the following section, followed by detailed description of each chapter.

1.4 Contributions

My major contributions include:

- Developed and implemented a robust UWB pulse radar prototype operating at 1.5-4.5 GHz for human imaging and Doppler detection applications, achieving real-time imaging and Doppler detection features in one platform;
- Developed a reconfigurable UWB pulse radar architecture which achieves a good compromise between imaging resolution and through barrier attenuation.
- Developed a system level simulation platform to optimize and predict the performance of UWB pulse radar systems, by integrating linear and nonlinear analysis, circuit and electromagnetic simulation in one model.
- Designed and implemented two wideband Vivaldi antennas and arrays for the radar systems, operating at 1.5-4.5 GHz and 1.5-10 GHz respectively, with good directional radiation patterns over the operating range.

- Implemented high speed data acquisition and transfer module based on equivalent-time sampling strategy and USB2.0 data link, achieving a sampling rate of 100 GS/s and data transfer rate of 25 MB/s.
- Extended UWB pulse radar for real-time imaging of more than one object at a time, and 3-D image recovery of radar target.
- Extended UWB pulse radar for early breast cancer detection, demonstrating the capability of detecting 5mm diameter tumor in phantom experiment.
- Extended UWB pulse radar for monitoring the physical activities of moving persons and detecting the respiration of stationary human targets in through wall/barrier scenarios.
- Implemented a CW radar prototype as an alternative to UWB pulse radar for Doppler detection applications, giving pros and cons of each radar technology.

1.5 Organization of the Dissertation

The rest of the dissertation is organized as follows:

Chapter 2 discusses the system development of UWB pulse radar. After presenting two system building blocks: one operating at higher UWB band (8-10 GHz) while the other at lower UWB band (1.5-4.5 GHz), we also introduced a reconfigurable system diagram which can reconfigure the frequency band between two. The hardware prototyping of radar transceiver RF front-end and high speed data acquisition module will be introduced in details. Design methods of two wideband antennas and arrays will be introduced, one working for lower UWB band while the other covering the entire UWB band. The strategy to select the system operation frequency will also be explained in this chapter.

Chapter 3 introduces a system level simulation platform that can be used to analyze and predict the performance of 3-D UWB imaging radar systems. The simulator includes six blocks and the detailed information and function of each block will be discussed. Simulation results will be compared with experimental ones to validate the

platform. We will also demonstrate how to use the developed simulation platform to predict the system performance of UWB pulse radar.

Chapter 4 presents how UWB pulse radar can be used for imaging applications. Three examples will be given in details, including real-time through wall human imaging, radar target 3-D imaging and early breast cancer detection. 2-D/3-D Backprojection microwave beamforming algorithm is utilized for image recovery and will be introduced. Imaging resolution, i.e., range resolution and azimuth resolution, of the developed UWB pulse radar is acquired through both theoretical analysis and measurement. Early breast cancer example shows the capability of detecting 5 mm tumor target by using UWB pulse radar technology.

Chapter 5 shows the capability of UWB pulse radar for Doppler detection applications. Theory and equations will be given on extracting Doppler frequency shifts from UWB pulse radar. Three examples will be presented in this chapter, including human gait analysis, Doppler detection of more than one moving human target, and respiration detection of stationary people in through wall environment. After that, we will introduce an alternative method based on CW Doppler radar. Both developed UWB and CW radar prototypes will be used to acquire the Doppler results with the same experimental setups. Pros and cons of the two radar technologies will be discussed too.

Chapter 6 summarizes the dissertation, highlights the contributions of this work, and puts forward several directions of future work.

Chapter 2

System Development of UWB Pulse Radar

Even though researchers have paid a lot of attention to designing UWB radar systems and have introduced significant improvement in hardware development, there are many basic issues need to be addressed related to the practical implementation of the UWB system, for example, selection of optimal frequency, design of a robust UWB radar transceiver, implementation of a fast speed data acquisition module with low cost solutions, achieving fast system refresh rate for Doppler detection, design of wideband antennas and arrays, and etc. But definitely, in the last few years, there has been significant progress in developing various basic blocks of UWB transceivers [38]-[41].

In this chapter, we will discuss our strategy to select an optimal operation frequency for UWB pulse radar, and the details of the radar block diagram design. In selecting the operating frequency, there are two factors needed to be considered here, through-barrier (e.g., wall, debris) attenuation and radar azimuth resolution, and we need to make a good compromise between both. Meanwhile, to describe the various radar block diagrams, we will introduce two UWB pulse radar platforms that we have developed through the course of this effort: one working at 8-10 GHz [16] for good azimuth resolution when seeing through low-loss materials, while the other operating at 1.5-4.5 GHz [42] for low through-attenuation when seeing through high-loss materials. After that, we needed to combine such two capabilities and have developed a reconfigurable UWB pulse radar architecture [43] which can switch the operation frequency between higher and lower UWB bands and will be presented here as well. The methods of designing wideband Vivaldi antennas and arrays [44] for the radar platform will be discussed. The hardware development of high speed data acquisition module will also be introduced in details [45]. In our implementation, equivalent time sampling scheme has been utilized to achieve a low cost solution for high speed sampling [46]. USB2.0 data communication link has been developed to upload the digitized data to PC, achieving a fast system refresh rate [45].

2.1 Operation Frequency Selection

The operation frequency is determined based on the optimal design and implementation of the UWB pulse radar system. In most time, the radar needs to detect and investigate the human objects in a harsh environment, such as through the barrier, debris or blockage. In another application like in early breast cancer detection, the microwave signal has to penetrate through the normal breast tissue before seeing the cancerous tissue, which is very lossy as well. Therefore, the through barrier attenuation has to be accounted for during the development of the UWB pulse radar.

Here, we primarily focus on two items: through barrier attenuation and azimuth image resolution. It is well-known that through barrier attenuation increases with frequency. Hence, a lower frequency band usage is recommended to minimize the seeing through loss for better signal to noise ratio or even receive an adequate detectable signal after going through a round trip propagation through the wall. However, better azimuth image resolution is acquired when operating at higher frequencies, with the same radar aperture. Therefore, a compromise is required between an acceptable through barrier attenuation and adequate imaging resolution.

To better understand the through barrier attenuation of a UWB pulse signal, transmission characteristics are analyzed for various building materials, including drywall, wood, glass, brick, and concrete. The typical complex permittivity of these materials [47], [48] is listed in Table 2.1. It is approximately assumed that the materials are homogeneous and both the real and imaginary parts are constant over our analysis frequency from DC to 12 GHz. A 6-inch thickness was utilized for all materials in the analysis.

The propagation characteristics through the drywall, wooden wall, glass, brick wall, and concrete wall over the DC-12 GHz frequency range are presented in Figure 2.1. Details of the analysis will be given below. It should be noted that this is only due to a one-way propagation. These loss calculations were carried out using the plane wave reflection and transmission theory in [49].

A single layer, homogeneous wall structure was assumed in the analysis, with a complex permittivity of ε^* and a thickness of d. θ_0 is the angle of incidence while θ_1 is the angle of refraction in the wall media, we have $k_0 sin\theta_0 = k_1 sin\theta_1$ according to Snell's law. Then the reflection coefficient $\Gamma_\perp$ and transmission coefficient $T_\perp$ are given by

$$\Gamma_\perp = \frac{\Gamma_{0w}\left(1 - e^{-j2k_1 \cos\theta_1 d}\right)}{1 - \Gamma_{0w}^2 e^{-j2k_1 \cos\theta_1 d}} \tag{2-1}$$

$$T_\perp = \frac{\left(1 - \Gamma_{0w}^2\right)e^{-jk_1 \cos\theta_1 d}}{1 - \Gamma_{0w}^2 e^{-j2k_1 \cos\theta_1 d}} \tag{2-2}$$

where

$$k_1 = w\sqrt{\mu\varepsilon^*} \tag{2-3}$$

$$\Gamma_{0w} = \frac{\sqrt{\varepsilon_0}\cos\theta_0 - \sqrt{\varepsilon^*}\cos\theta_1}{\sqrt{\varepsilon_0}\cos\theta_0 + \sqrt{\varepsilon^*}\cos\theta_1} \tag{2-4}$$

The Matlab code that was used to acquire the through wall reflection coefficient and transmission coefficient can be found in Appendix A.1. In radar operation, the signal travels a round trip and is attenuated twice by the wall. Therefore, it is suggested that the operation frequency does not go beyond 6 GHz for seeing through brick-wall or 4 GHz for seeing through concrete-wall.

Table 2.1 Characteristics of Various Building Materials

Material	**ε'**	**ε''**	**Loss Tangent***
Drywall	2.0	0.01	0.005
Wood	2.5	0.05	0.02
Glass	6.4	0.032	0.005
Brick	4.0	0.2	0.05
Concrete	6.8	0.9	0.13

* Loss tangent values were approximately assumed constant in the microwave range.

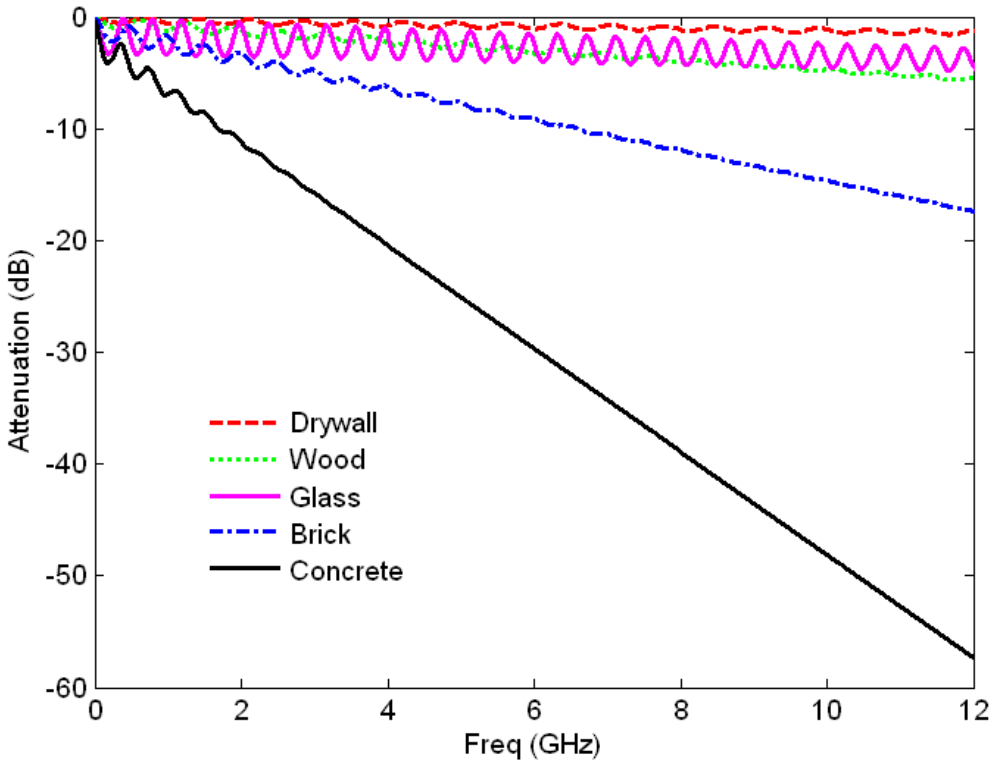


Figure 2.1 Simulated one-way through wall reflection and transmission through various building materials, with a thickness of 20cm.

As expected, the signal decays faster at higher frequencies when penetrating through various building materials. The attenuation is acceptable when penetrating through drywall, wood and glass over the analysis frequency range DC-12 GHz. However, the attenuation increases significantly with frequency for brick wall and concrete wall, as shown in Figure 2.1. For example, the attenuation is over 10 dB and 30 dB at 6 GHz for brick wall, and concrete wall respectively.

2.2 8-10 GHz UWB Pulse Radar System

A 8-10 GHz UWB pulse radar was developed by Yunqiang Yang [16], [17] for seeing through low-loss materials, and its system diagram is depicted in Figure 2.2. A 1ns pulse was utilized in the system and up-converted to 9 GHz in the transmitter side. A carrier frequency of 9 GHz was chosen in order to acquire a high azimuth resolution when penetrating through low loss material scenarios. The modulated signal passed through two stages of amplification before being sent out by a wideband antipodal Vivaldi subarray [50]. Sixteen subarrays, placed in a line, were employed in the receiver side to collect the reflected signal. After the received signal is amplified and demodulated, I and Q signals were obtained and forwarded to the analog-to-digital converter (ADC) for sampling, using the equivalent time sampling scheme [46]. Next, all the sampling data were sent to a FPGA circuitry for real-time imaging process. A monitor, driven by the FPGA, displayed the recovered real-time 2-D images. For more information about this system, refer to [17].

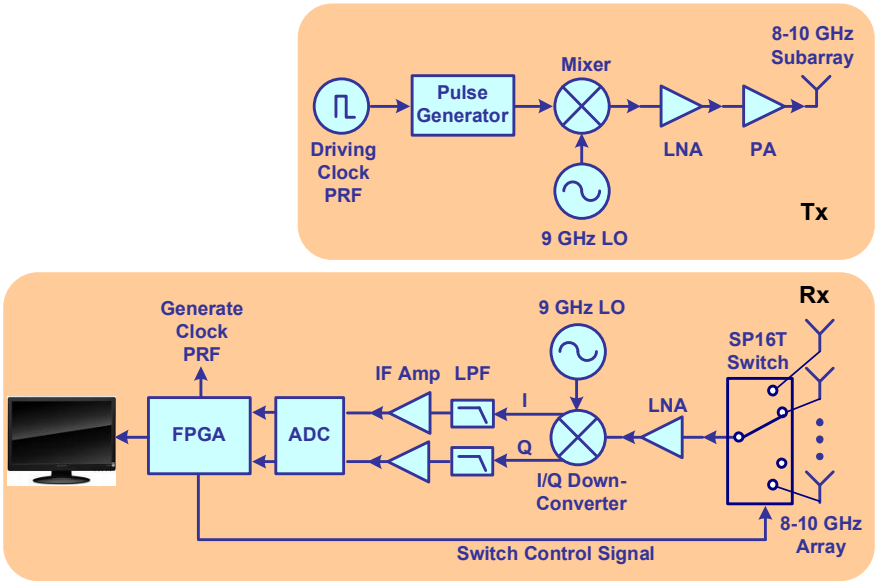


Figure 2.2 Detailed diagram of the previously developed 8-10 GHz radar imaging system.

2.3 1.5-4.5 GHz UWB Pulse Radar System

Based on the simulation results of through wall attenuation, it has been suggested that the operation frequency should not go beyond 4 GHz to be capable of seeing through brick wall and concrete-wall as well. Based on our previous discussion about image resolution and signal attenuation, we have considered fabricating a system operating over 1-4 GHz as the optimal operation frequency band for seeing through various high-loss wall materials. However, due to the availability limitations of wideband commercial components, an operation frequency of 1.5 GHz to 4.5 GHz was selected and applied in our developed UWB pulse radar system, with a carrier frequency of 3 GHz.

2.3.1 Transceiver RF Front-end

The detailed block diagram of the developed UWB Doppler radar is shown in Figure 2.3. At the transmitting link, a 10 MHz driving clock generated by FPGA circuitry is used to drive a 700ps Gaussian pulse generator. The Gaussian pulse is modulated by a

3 GHz carrier signal through a Hittite HMC213 mixer before passing through a driving RF amplifier Hittite HMC753 and a high gain power amplifier Mini-Circuits ZHL-42. The amplified signal is then sent out via a wideband Vivaldi antenna. At the receiver side, the collected radar returned signal is amplified by a Hittite HMC753 low noise amplifier (LNA) before being down-converted into baseband. The down conversion is implemented by mixing the modulated signal with the same 3 GHz carrier signal through Hittite HMC213 mixer. Therefore, the developed radar is a coherent system, i.e., transmitter and receiver use the same carrier signal from a Mini-Circuits ZX95-3360 voltage controlled oscillator (VCO). Next, the baseband I and Q signals are low-pass filtered and amplified before being sent to data sampling and acquisition module.

The photograph of the in-house designed transceiver RF front-end prototype is shown in Figure 2.4.

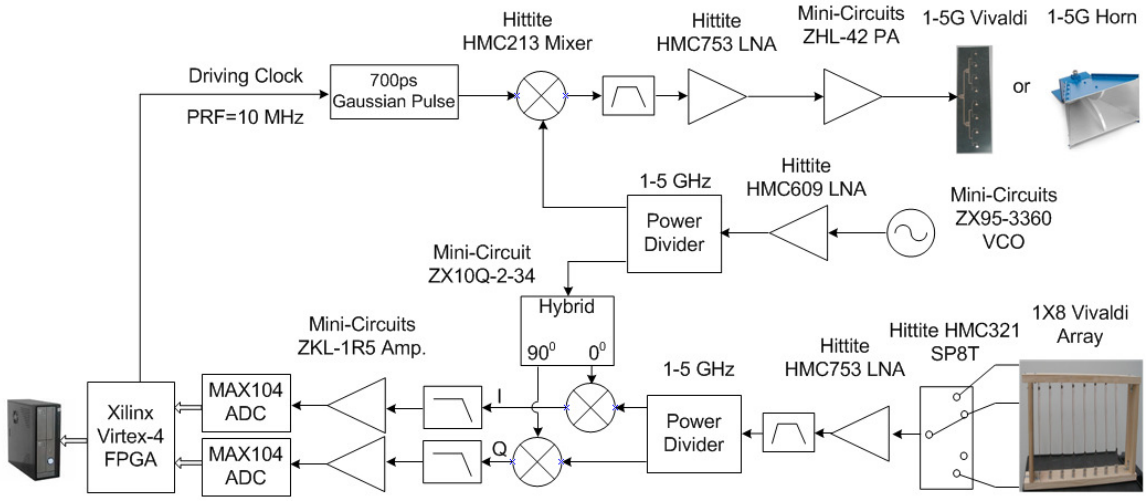


Figure 2.3 Detailed block diagram of the developed UWB impulse radar.

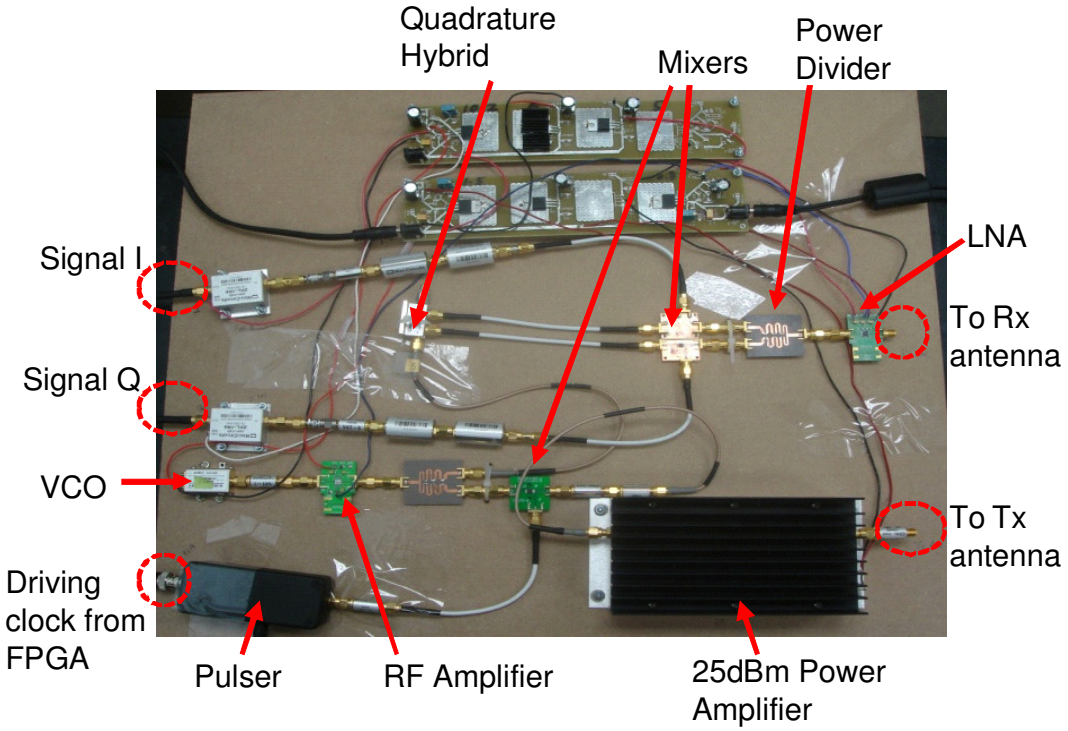


Figure 2.4 Photograph of the developed UWB PD radar RF front-end module.

Figure 2.5 introduces the link budge analysis of the radar transceiver. The radar transmitting power level is mainly decided by the last stage power amplifier. The selected commercial component ZHL-42PA from Mini-Circuits provides a 1dB output power compression point of 28dBm. However, we have left slight margin when driving the power amplifier to avoid the obvious nonlinearity and signal distribution observed at the spectrum analyzer. A 25dBm output power is finally generated and sent to transmitting antenna. At the receiver side, the commercial LNA HMC753 has a 1dB input compression point of 1dBm. Meanwhile, it is found that the commercial mixer HMC213 claims a 1dB input gain compression point of 9dBm and that is the limiting factor for maximum receiver input power level. Based on that, we have figured out the maximum input power level injected into radar receiver to be 0dBm. Therefore, the minimum isolation requirement between the radar transmitter and receiver is 25 dB, which can be easily achieved by separating the transmitting and receiving antennas apart, or putting the

transmitting antenna slight forward to reduce the coupling between them. Table 2.2 shows the analysis of the isolation requirement between radar transmitter and receiver.

The dynamic range of the radar receiver is also calculated step by step, as shown in Table 2.3. The thermal noise floor of the receiver is -174 dBm/Hz, or -114 dBm/MHz. The radar receiver has a bandwidth of about 3 GHz and therefore, the noise floor of the radar receiver is -79 dBm. The receiver has a noise figure of approximately 8dB, which is mainly due to the cable loss, SP8T switch loss, and the noise figure of the HMC753 LNA. Meanwhile, the minimum signal-to-noise ratio (SNR) required in order to reconstruct an acceptable imaging quality is 6dB [51]. Subsequently, we can acquire the radar receiver sensitivity to be -65 dBm. Since the receiver 1dB input compression point is 0dBm, the receiver has a dynamic range of as large as 65 dB.

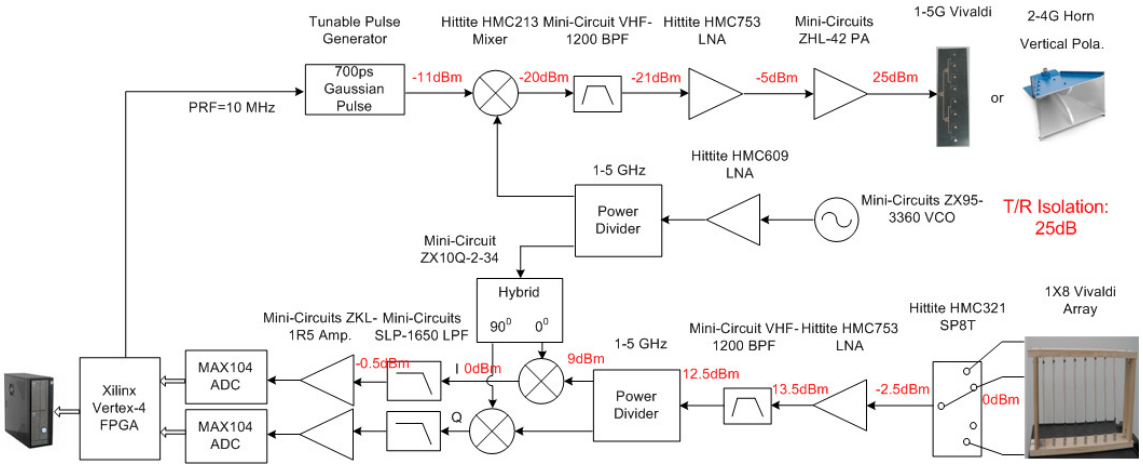


Figure 2.5 Link budget analysis of the radar transceiver.

Table 2.2 Isolation requirement between radar transmitter and receiver

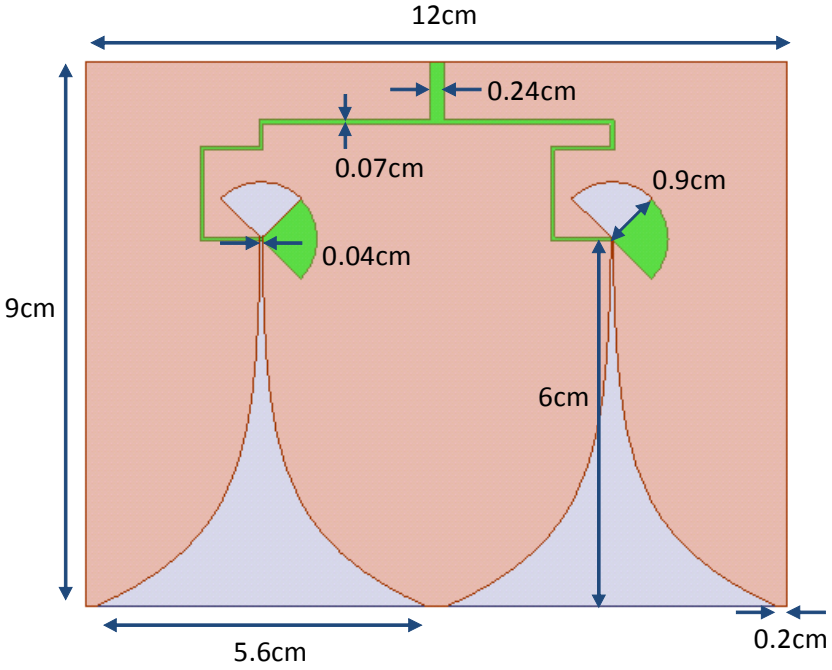
Parameters	**Values**
Transmitter Total Power (dBm)	25
Rx 1dB Compression Point (dBm)	0
Required Tx-Rx Isolation (dB)	25
Tx/Rx Isolation easily achieved by putting Tx and Rx antennas apart	

Table 2.3 Dynamic range analysis of the radar transceiver

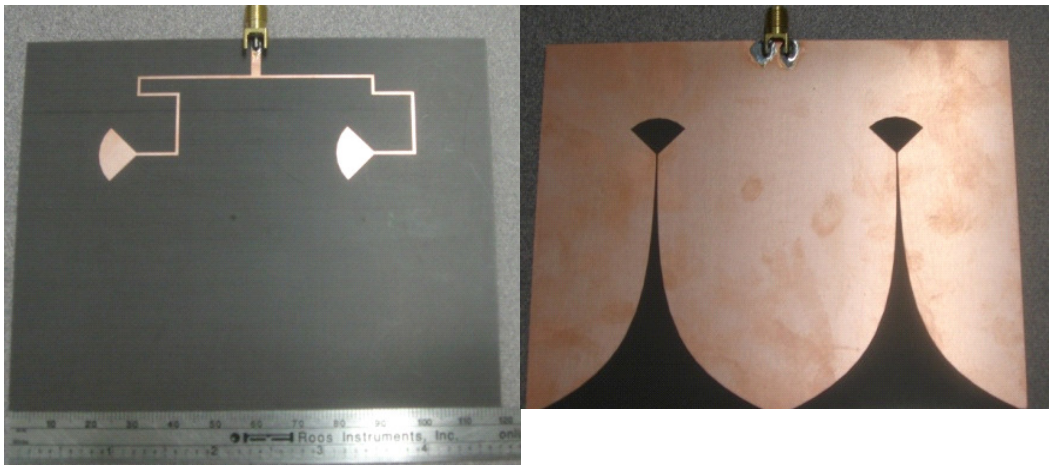
Parameters	**Values**
Rx Thermal Noise Floor (dBm/Hz)	-174
Rx Thermal Noise Floor (dBm/MHz)	-114
Receiver Bandwidth (GHz)	3
Receiver Thermal Noise Floor (dBm)	-79
Receiver Noise Figure (dB)	8
Receiver Noise Floor (dBm)	-71
Required SNR (dB)	6 (for acceptable image quality)
Receiver Sensitivity (dBm)	-65
Rx 1dB Compression Point (dBm)	0
Receiver Dynamic Range (dB)	65

2.3.2 1.5-4.5 GHz Vivaldi Antenna and Array Design

A good antenna candidate for portable UWB radar systems should have feature wideband, directional radiation pattern, and low phase distortion operation while being small size and low cost. There are different options to design such antenna including stacked patch [52], microstrip slot [52], antipodal/tapered slot Vivaldi [53], coupled sectorial loops [54], elliptical-shaped dipole/monopole [55], and etc. Here, we use an exponential taper slot Vivaldi antenna that has been developed for our UWB radar prototype due to its many advantages. The HFSS simulation model and photograph of the fabricated Vivaldi antenna is shown in Figure 2.6, with a size of 12cm by 9cm. It is fabricated on a 31-mil thick Rogers RT5880 substrate, which has a dielectric constant of 2.2 and loss tangent of 0.0009. A wideband microstrip line to slotline transition [56] is utilized to feed the exponential tapered slot and has significantly enhanced the impedance bandwidth. Measured VSWR performance agrees very well with the simulation one, showing a good match at 1 to 5.5 GHz, as introduced in Figure 2.7.



(a) HFSS model



(b) Photograph of the prototype

Figure 2.6 HFSS model and prototype of the compact wideband Vivaldi antenna, with a size of 12cm × 9cm and a thickness of 31-mil.

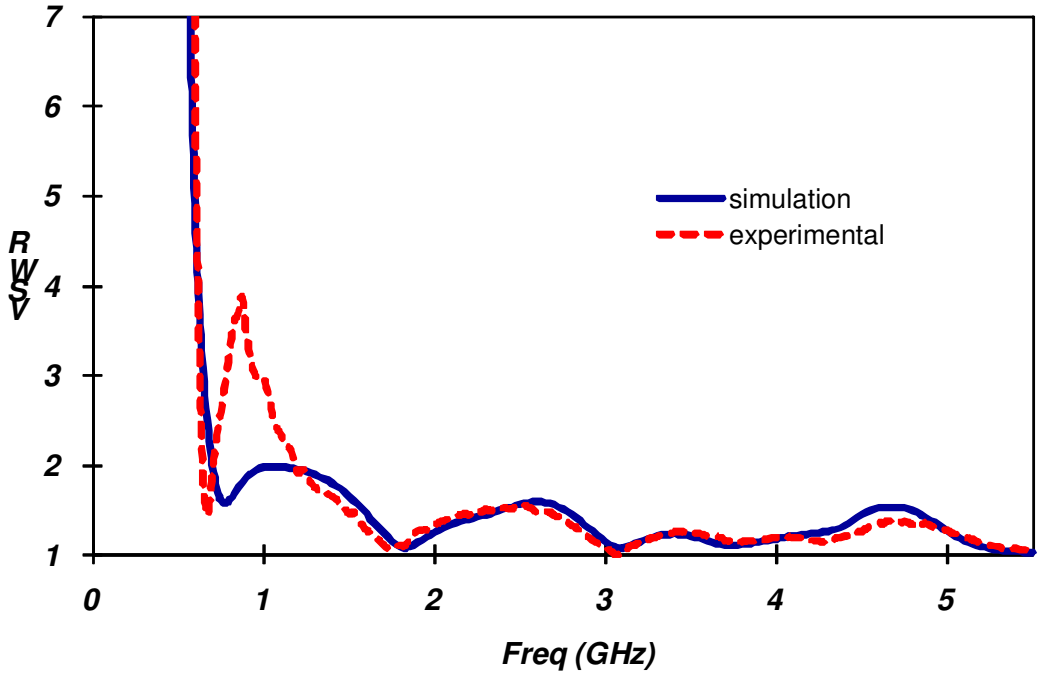
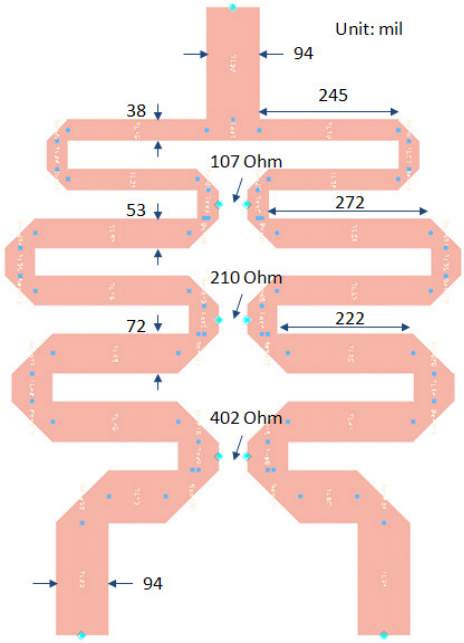
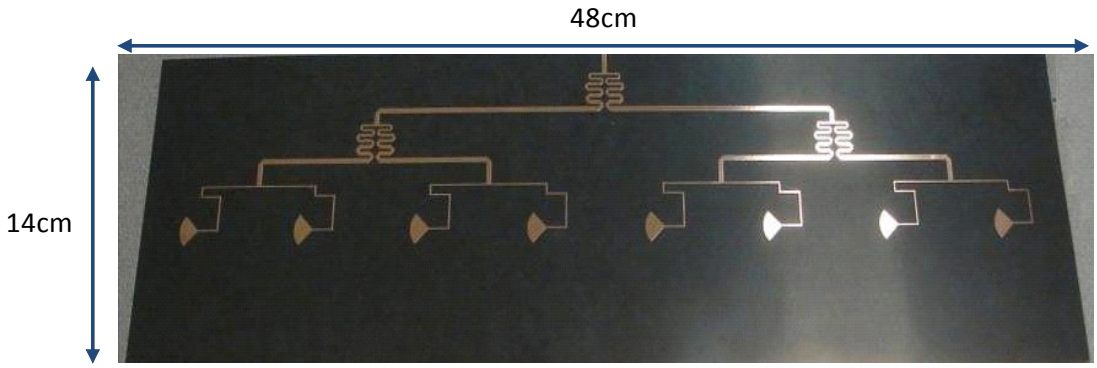


Figure 2.7 Simulation and experimental VSWR result of the fabricated Vivaldi antenna.

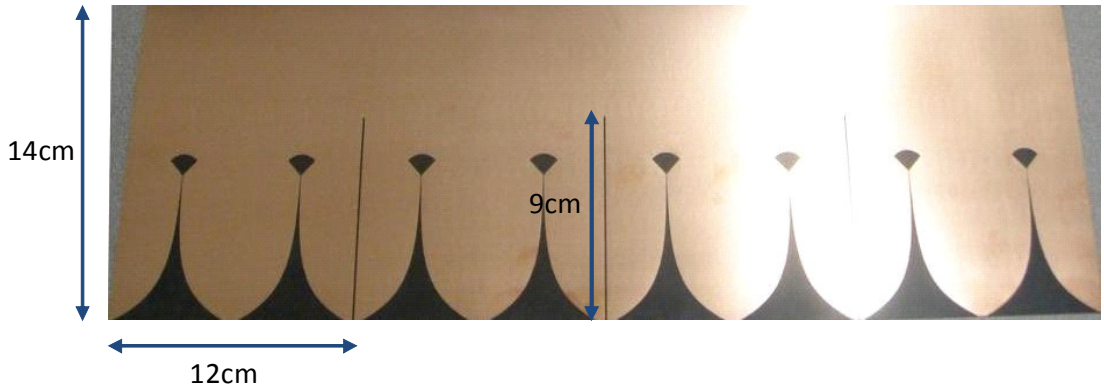
The designed Vivaldi antenna was utilized as the basic building block to design a sub-array in order to increase the overall gain and narrow down the beamwidth, as shown in Figure 2.8. Three-section wideband power divider [57] was utilized to form the feeding network. Measured return loss indicates a good matching performance of the antenna from 1 to 5.5 GHz, as shown in Figure 2.9.



(a) Dimension of the three-section wideband divider used in the prototype



(b) Top view of the prototype



(c) Bottom view of the prototype

Figure 2.8 Dimension and photograph of the fabricated Vivaldi sub-array.

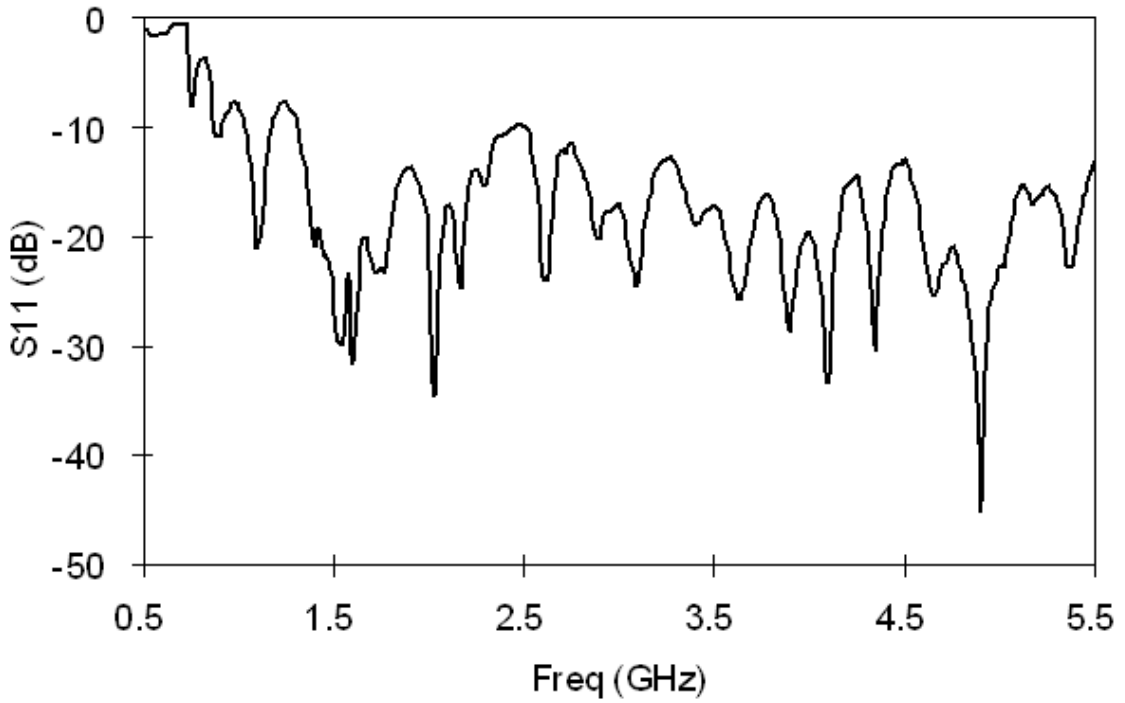
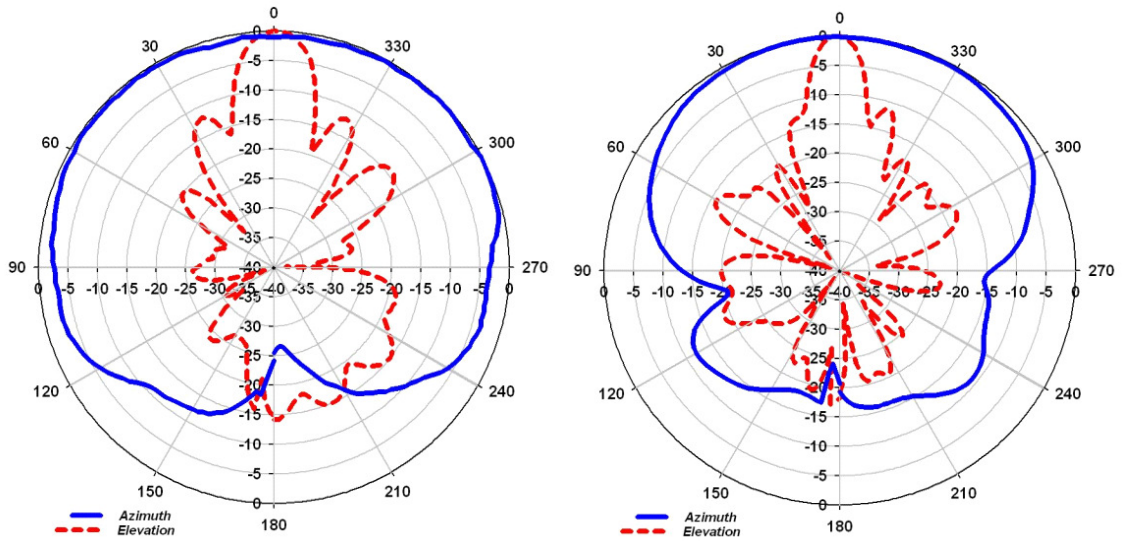
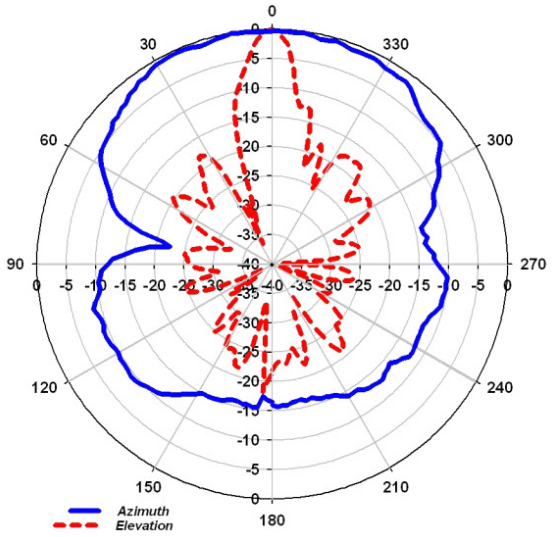


Figure 2.9 Measured return loss of the Vivaldi sub-array, showing good match at 1 to 5.5 GHz.

The Vivaldi sub-array achieves good directional radiation patterns over the operation frequency based on measurement, as introduced in Figure 2.10. A 3dB beamwidth of 12 degrees at E-plane and 120 degrees at H-plane have been achieved at 3 GHz. Figure 2.11 shows a photograph of a 1×8 Vivaldi antenna array, which is composed of eight Vivaldi sub-arrays assembled uniformly along a horizontal platform. The eight elements are connected to a Hittite HMC321 SP8T RF switch to select the signal channel sequentially to achieve a synthetic aperture radar (SAR) operation.



(a) 2 GHz (b) 3 GHz



(c) 4 GHz

Figure 2.10 Measured radiation pattern of the Vivaldi sub-array, showing good directional characteristics over the operation frequency.

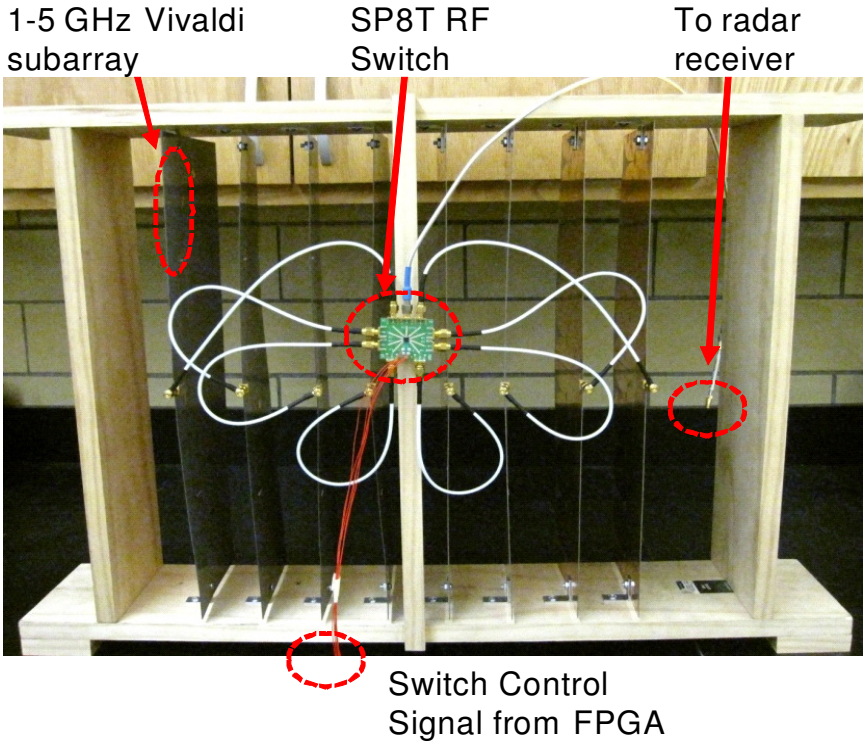


Figure 2.11 Photograph of the 1×8 Vivaldi antenna array.

2.4 Reconfigurable UWB Pulse Radar System

To provide lower frequencies for high loss walls and higher frequencies for a higher azimuth resolution, we have developed a reconfigurable UWB pulse radar system augmenting the above features of both previously developed antennas. The introduced reconfigurable radar system with a switchable operating frequency extending over the 1.5-10 GHz frequency range will provide operational flexibility. The operation frequency of the system can be adjusted by using the SPDT switches in the system.

2.4.1 Transceiver RF Front-end

The detailed block diagram of the UWB SAR is outlined in Figure 2.12. The radar transceiver can be easily reconfigured to work at either 1.5-4.5 GHz or 8-10 GHz by

changing the system carrier signal and the BPF at the receiver front-end. A clock with 10 MHz pulse repetition frequency (PRF) from the FPGA is amplified by a buffer amplifier before driving a 300ps-1ns Gaussian pulse generator. The pulse signal is then modulated by a carrier signal. The modulated signal passes through two stages of amplification and is then transmitted via a wideband Vivaldi antenna. At the Rx link, the acquired signals are amplified by a wideband LNA. The signals are band-pass filtered and then down-converted into I and Q channels by mixing the same carrier with the received signals. Then, the recovered I and Q data are low-pass filtered and amplified before being sent to the ADCs for sampling using the equivalent-time sampling scheme [46]. Next, all the sampling data are sent to a FPGA circuitry for storage. Last, the collected data is transferred to the computer and a microwave beam-forming algorithm implemented by a Matlab program is applied to recover the radar image [58], which is given in Appendix A.2.

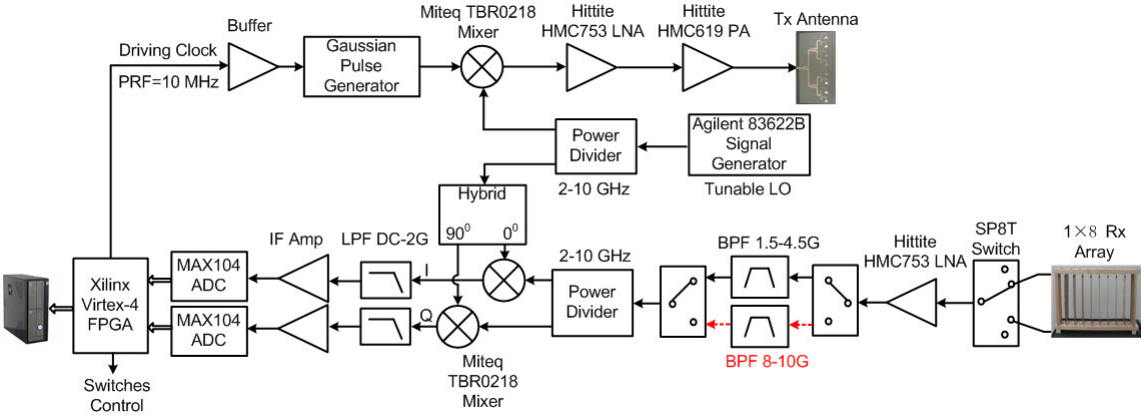


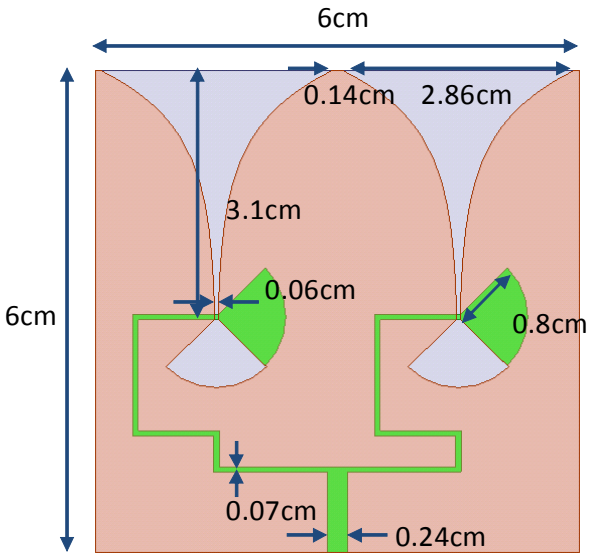
Figure 2.12 Detailed block diagram of the reconfigurable imaging radar system.

2.4.2 1.5-10 GHz Vivaldi Antenna and Array Design

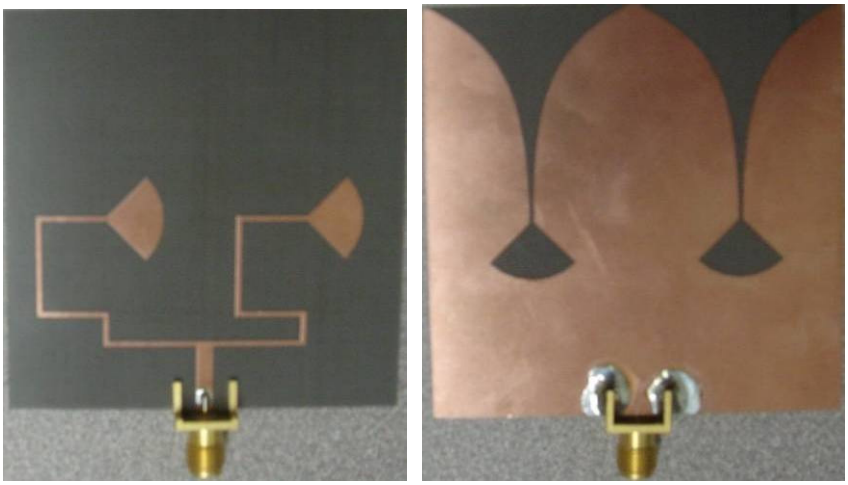
For the reconfigurable UWB antenna, a UWB Vivaldi array is designed to cover the entire 1.5-10 GHz UWB frequency range. The configuration of the two-element Vivaldi array is depicted in Figure 2.13. A Rogers RT5880 substrate was used, with a relative permittivity of 2.2 and a thickness of 31 mils. A wideband transition, from the slot line to a 100Ω microstrip line, was successfully designed. This has greatly simplified the design and offered a bandwidth of up to one decade [56]. Next, two 100Ω microstrip

lines are shunted to achieve a 50Ω impedance. The width of the single tapered slot, *W*, is 30 mm, which is one wavelength at the highest operating frequency (10 GHz) to avoid any grating lobes in the E-plane of the Vivaldi array.

The measured return loss of the two-element Vivaldi array matches the simulated one, as shown in Figure 2.14. Both results indicate an acceptable match over the 1.5-10 GHz frequency range. Figure 2.15 demonstrates satisfactory measured radiation patterns of the two-element Vivaldi array over the operating frequency range.



(a) HFSS model



(b) Photograph of the prototype

Figure 2.13 HFSS model and prototype of the fabricated 1.5-10 GHz Vivaldi antenna.

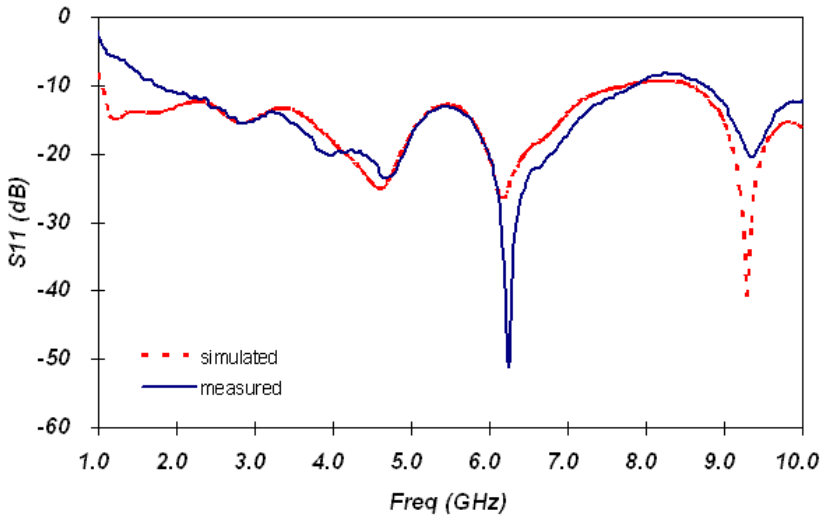
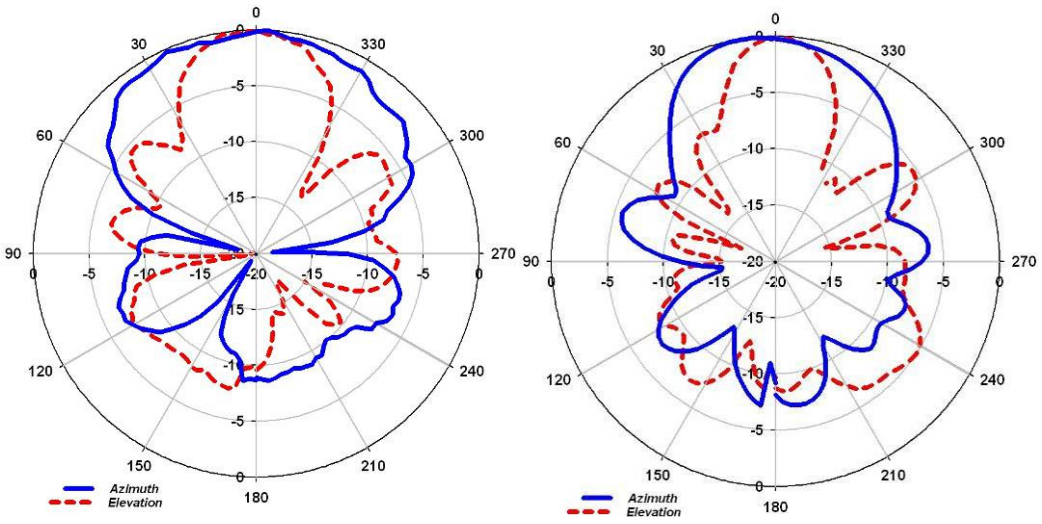


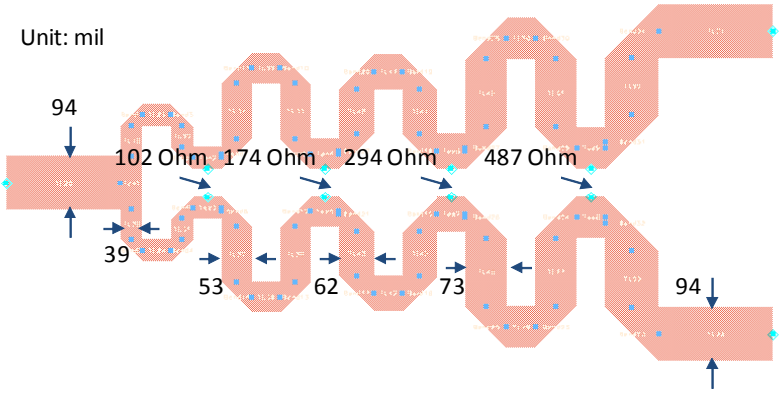
Figure 2.14 Simulated and measured return loss of the Vivaldi antenna.



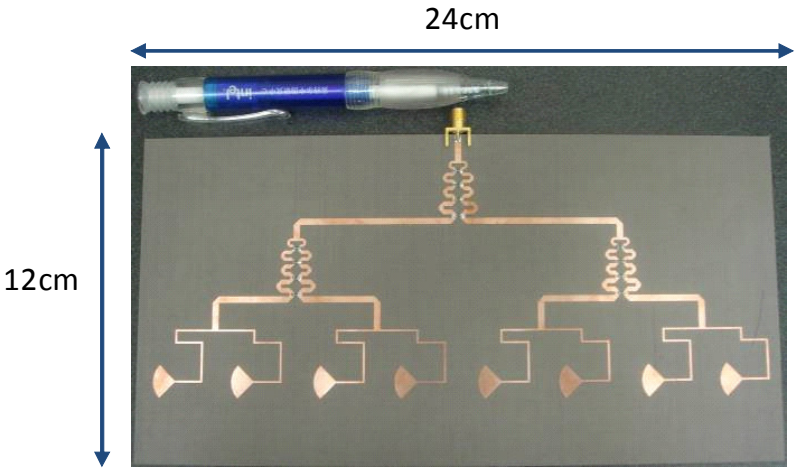
(a) 4 GHz (b) 10 GHz

Figure 2.15 Measured radiation pattern at 4 GHz and 10 GHz respectively, showing good directional radiation characteristics.

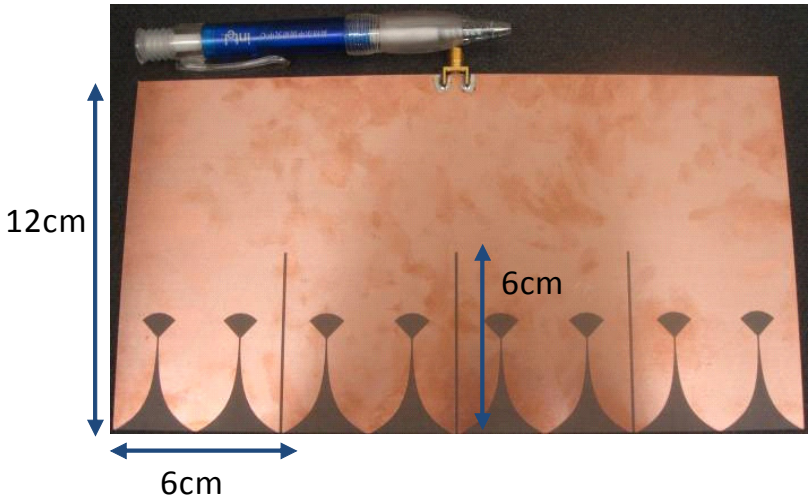
The developed two-element Vivaldi array is extended to an 8-element E-plane array design, by using the 4-section wideband Wilkinson divider [57], as presented in Figure 2.16.



(a) Dimension of the four-section wideband divider used in the prototype



(b) Top view of the prototype



(c) Bottom view of the prototype

Figure 2.16 Dimension and photograph of the fabricated 1.5-10 GHz Vivaldi Array.

Figure 2.17 shows the measured return loss of the eight-element compact Vivaldi array. Better than -10 dB matching was achieved between 1.5-10 GHz, the operation frequency band for our reconfigurable system. The measured gain of the compact eight-element Vivaldi array is indicated in Figure 2.18. Approximately 5-8 dB gain is acquired at 2-4 GHz and 12-13 dB gain at 8-10 GHz.

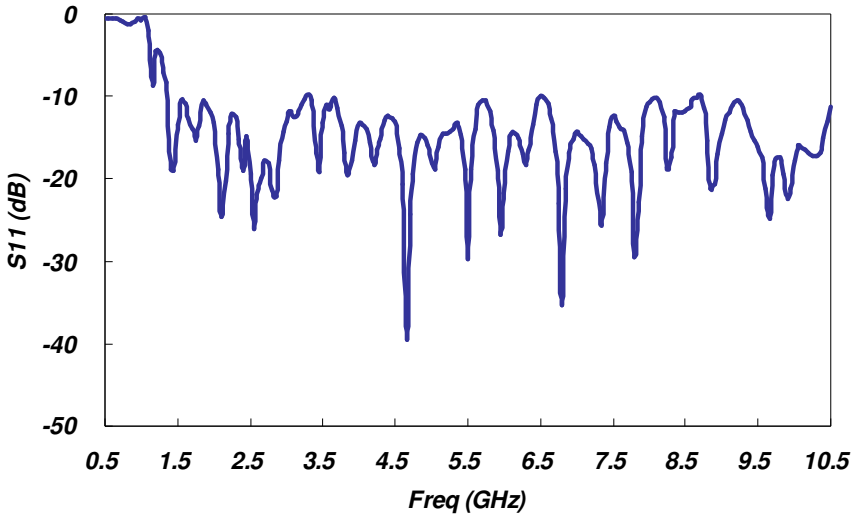


Figure 2.17 Measured return loss of the 8-element Vivaldi array.

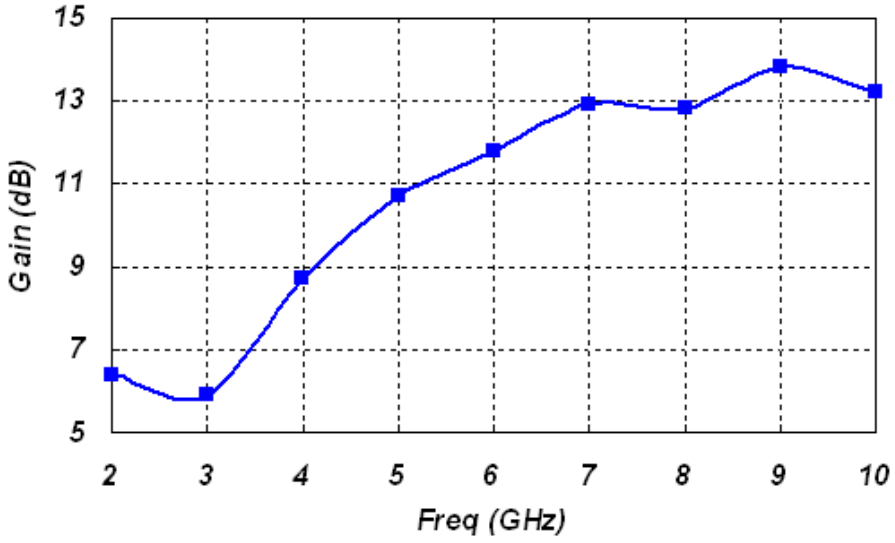


Figure 2.18 Measured gain of the compact array from 2-10 GHz.

Figures 2.19 and 2.20 present the E-plane radiation pattern, as well as the cross polarization radiation at 4 GHz and 10 GHz respectively. The array has a low side lobe level, about -13dB side lobe level at 4 GHz and -12 dB at 10 GHz. Good polarization performance is also achieved by the proposed compact array. The cross polarization is less than -30 dB at 4 GHz, and less than -20 dB at 10 GHz, both at broadside. The E-plane 3dB beamwidth is 12 degrees at 4 GHz and 5 degrees at 10 GHz.

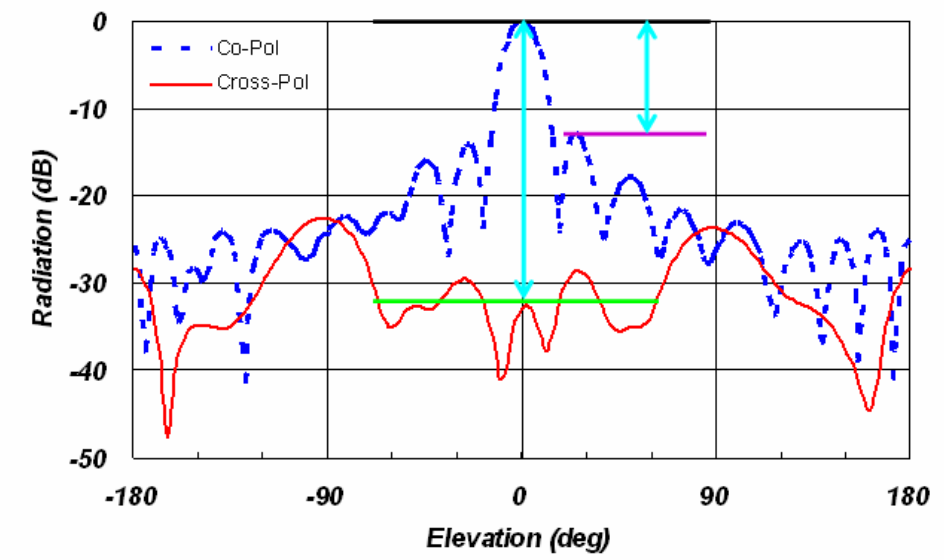


Figure 2.19 Co-pol and Cross-pol E-plane radiation pattern at 4 GHz.

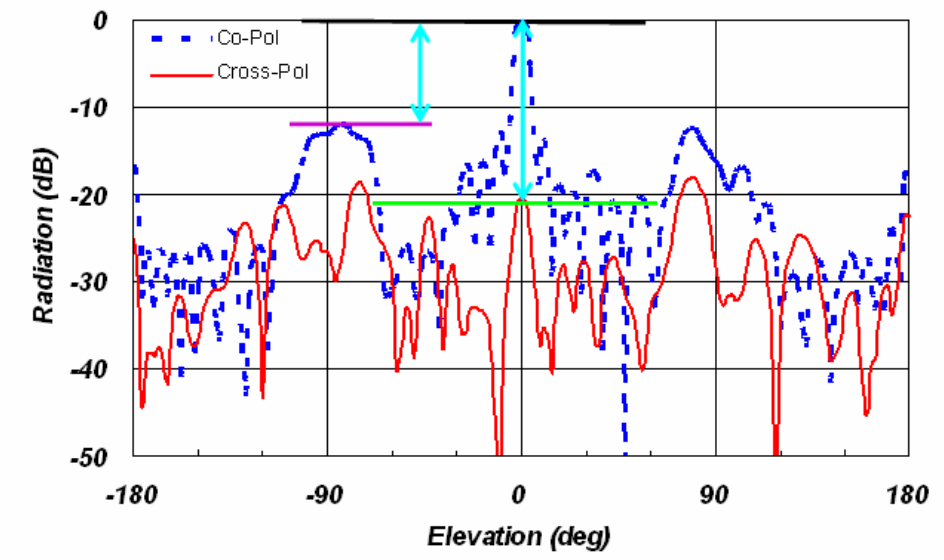
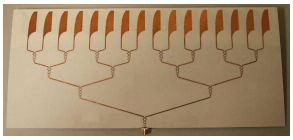
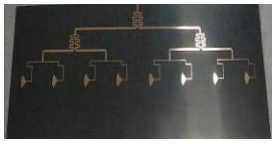
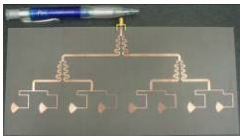


Figure 2.20 Co-pol and Cross-pol E-plane radiation pattern at 10 GHz.

The three arrays are compared in details in Table 2.4, in terms of bandwidth, gain, cross polarization performance and E-plane beamwidth.

Table 2.4 Comparison of the three arrays in detailed performance

	Previous 8-10.6 GHz Antipodal Array 	1.5-4.5 GHz Tapered Slot Vivaldi Array 	1.5-10 GHz Tapered Slot Vivaldi Array 
Bandwidth	8-12 GHz (8-10.6 GHz used by system)	1.5-4.5 GHz	1.5-10 GHz
Antenna Size (Single Element Size×Number)	4.3cm×2.4cm×16 =165 cm^2	9×6cm×8 =432 cm^2	6cm×3cm×8 =144 cm^2
Gain	13-14 dB @ 8-10 GHz	10-13 dB @ 2-4 GHz	12-13 dB @ 8-10 GHz 5-8 dB @ 2-4 GHz
Cross-Polarization	<-15 dB @ 8-10 GHz	<-15 dB @ 2-4 GHz	<-15 dB @ 8-10 GHz <-18 dB @ 2-4 GHz
3dB Beamwidth (E-plane)	4^o @ 10 GHz	10^o @ 4 GHz	5^o @ 10 GHz 12^o @ 4 GHz

2.5 Low Cost, High Speed Data Acquisition Module

According to Nyquist sampling theorem, UWB system requires an extremely high sampling rate in order to digitize a wideband signal without any distortion. In our implementation for example, a 700ps Gaussian pulse occupies a bandwidth of approximately 2 GHz, which requires at least 4 GS/s sampling rate. An even higher sampling rate (e.g., >10 Gs/s) is desired in order to acquire the pulse shape information.

However, such high speed ADC chips are still not available from most of the vendors, such as Texas Instruments, Maxim, National Semiconductor, and etc. Recently, Fujitsu has developed a super-high-speed 56 GS/s ADC chip with 8-bit resolution using CMOS process technology, but it is very expensive [59]. Therefore, an equivalent-time sampling method is applied based on the off-the-shelf ADC and it is really a low-cost solution.

2.5.1 Equivalent-time Sampling Scheme

In the equivalent time sampling scheme, a train of pulses with a period of 100ns is utilized, as shown in Figure 2.21. Instead of digitizing and recovering the pulse signal in one signal cycle, the sampling trigger clock is set to have a period of (100ns+Δt) . The equivalent time sampling rate is decided by Δt and a fine resolution of few pico-second can be achieved by using commercial delay line chips. In our implementation, we have gone through three design generations and will be detailed in the following.

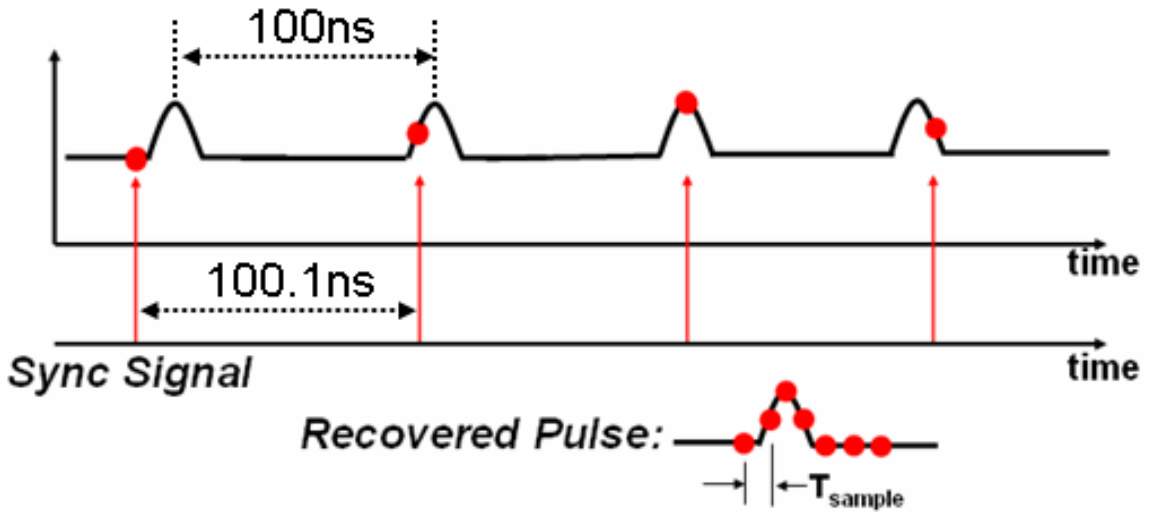


Figure 2.21 Equivalent-time sampling scheme.

2.5.2 1st Generation Hardware

Figure 2.22 shows a photograph of the 1st generation high speed data sampling, storage, and transfer module while Figure 2.23 introduces its detailed diagram that has been developed and detailed in reference [42]. The baseband I/Q signals are sent to two Maxim MAX104 ADCs for parallel data sampling. The MAX104 ADC has a maximum conversion rate of 1 GS/s and a full-power analog input bandwidth of 2.2 GHz. An equivalent-time sampling scheme is performed, in order to achieve a very high sampling rate. An off-the-shelf Xilinx Virtex-4 FPGA evaluation board is utilized with a Texas Instrument CDC5801 low-jitter clock multiplier/divider integrated on it. The signal is sampled using a 100 MHz clock and 10 samples are acquired in the first pulse period. After that, a 13.02ps time delay generated by the delay line chip CDC5801 is applied to the sampling clock before starting to digitize the next pulse period. The equivalent data conversion rate is determined by the time delay resolution and a high sampling speed of 76.8 GS/s has been achieved [60]. After 768 pulse periods, a complete pulse is acquired and all the digitized data are sent to a Xilinx Virtex-4 FPGA circuitry for storage and data transfer. The collected data is transferred to the computer in real-time through a USB2.0 communication cable, which provides a stable measured data uploading rate of 25 MB/s. After the data uploading is finished, the ADC will start to digitize the pulse signal again.

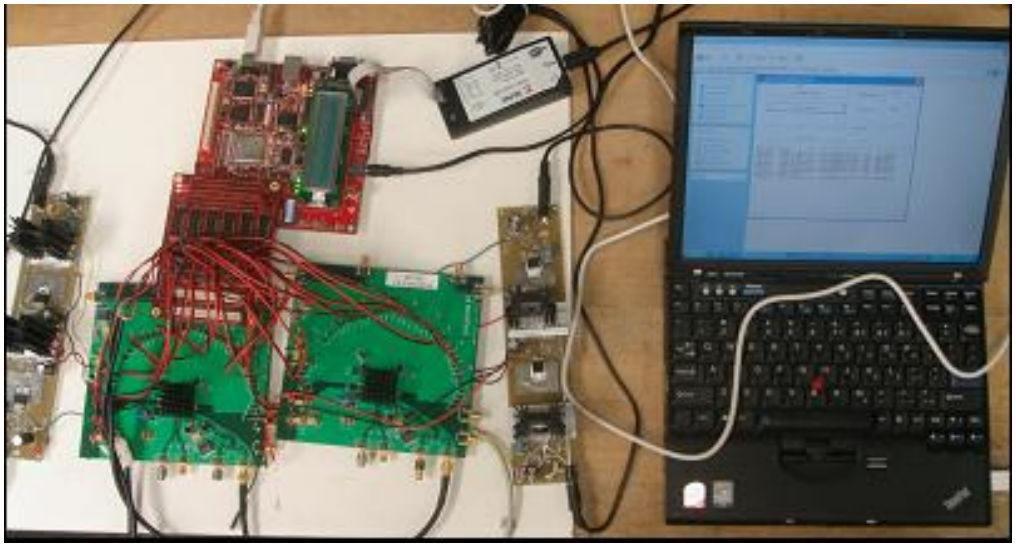


Figure 2.22 Photograph of the 1st generation data sampling, storage and transfer module, utilizing a Xilinx Virtex-4 FPGA evaluation board and two Maxim-IC MAX104 ADC evaluation boards.

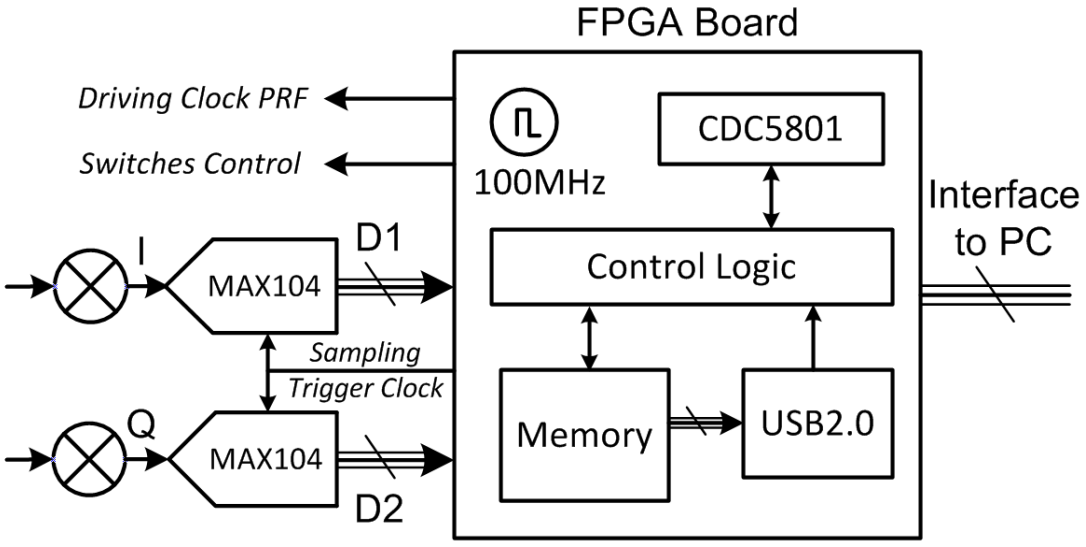


Figure 2.23 Detailed diagram of 1st generation data acquisition, storage and transfer module.

2.5.3 2nd Generation Hardware

MAX 104 has a resolution of 8-bit and an input signal range from -0.25V to +0.25V. MAX 104 lower resolution and smaller input signal range have limited the dynamic range of the data acquisition module, and also affected that of the radar receiver. In order to improve the dynamic range performance, we have designed the 2nd generation of the data acquisition module by replacing the MAX104 with ADS54RF63 from Texas Instruments, which has a resolution of 12-bit and an input signal range of 2.2 V_{pp}. The photograph of the 2nd generation is shown in Figure 2.24. After significantly increasing the input signal range as well as dynamic range of the data acquisition module, the radar detection range has been improved from about 5m to 12m.

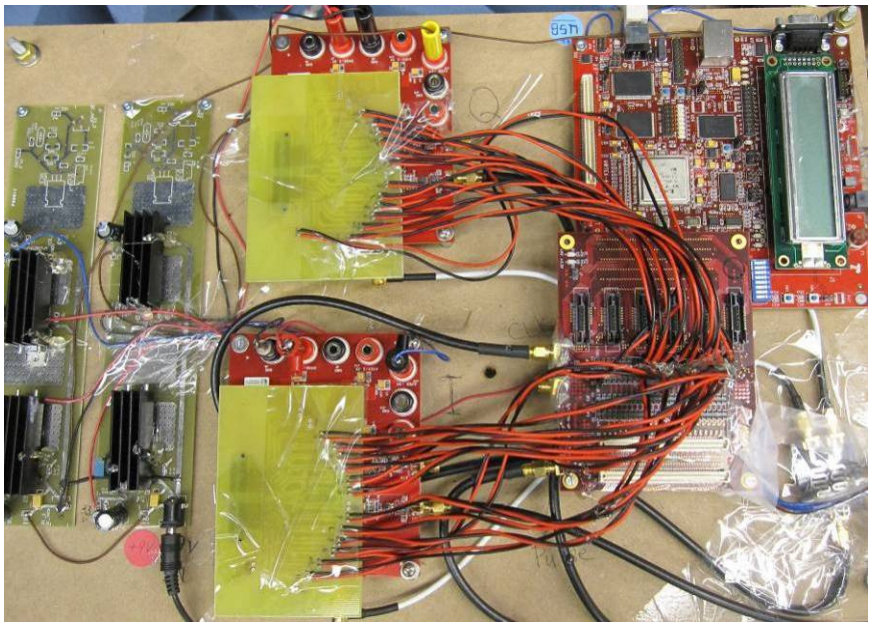


Figure 2.24 Photograph of the 2nd generation data sampling, storage and transfer module, utilizing a Xilinx Virtex-4 FPGA evaluation board and two Texas Instruments ADS54RF63 ADC evaluation boards.

2.5.4 3rd Generation Hardware

The first two generations still use separate evaluation boards for FPGA and ADC. The connection between FPGA and ADC is usually limited by the interface incompatibility and the need for extra connection boards and twisted wire pairs, as shown in Figures 2.22 and 2.24. These jumping wires may lead to robustness issues and increase cross talk. In order to make a robust and reliable module, the 3rd generation is designed by successfully putting all components together on a 4-layer printed PCB circuit board [45], as shown in Figure 2.25. The compact, highly integrated module achieves a maximum 100 GS/s data conversion rate using equivalent-time sampling strategy. The 3rd generation module utilizes a dual channel 16-bit ADC ADC16DV160 from National Semiconductor, a Micrel delay line chip SY100EP196, a Xilinx Virtex5 FPGA, a Cypress USB microcontroller CY7C68013, and etc.

The detailed block diagram of the 3rd generation high speed data acquisition module is shown in Figure 2.26. The data acquisition board has the flexibility to choose internal 150 MHz crystal or external clock source by using a 2x2 cross-point switch from ON Semiconductor. One switch output provides FPGA reference clock while the other generates a phase shifting clock for the delay line chip SY100EP196, which provides a programmable delay from 2ns to 12ns with 10ps fine increments. Using a dual channel ADC, ADC16DV160, allows a single chip to process I/Q signals simultaneously and significantly simplifies the board architecture and routing complexity. The I/Q signals are digitized by using a 150 MHz sampling clock while a 10ps delay is added to the sampling clock after every PRT. The 10ps clock shift resolution renders an equivalent sampling rate of 100GS/s. After digitizing a complete pulse, the module uploads the data to a computer via USB 2.0 communication link, which is controlled by a USB microcontroller CY7C68013 and provides a data rate of 25MB/s based on our measurements. To achieve an even faster data rate, a gigabit Ethernet transceiver such as 88E1111 from Marvell Semiconductor can be integrated into the current module.

The three generations of the data acquisition module are compared in details in Table 2.5.

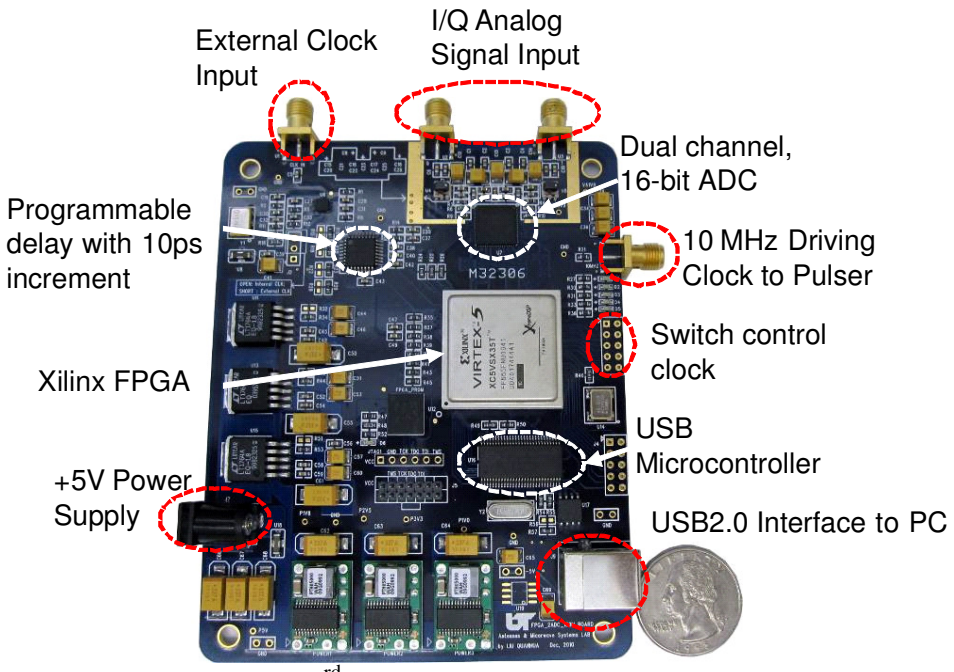


Figure 2.25 Photograph of the 3rd generation compact, 100GS/s data acquisition module, integrating FPGA, dual channel ADC, programmable time delay and USB microcontroller in a 4-layer PCB circuit board.

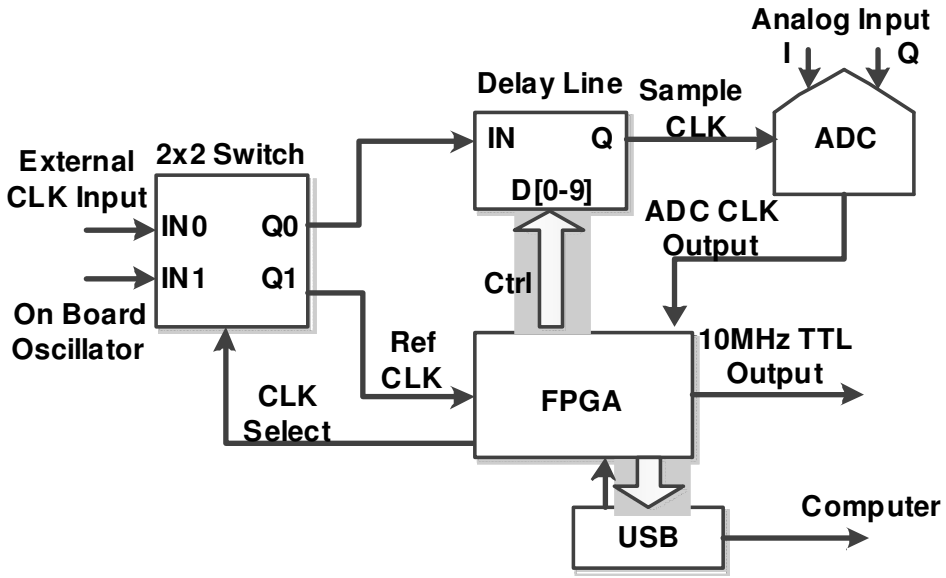


Figure 2.26 Block diagram of the 3rd generation data acquisition and transfer module.

Table 2.5 Comparison of three generations data acquisition and transfer module

Features	**1st Generation**	**2nd Generation**	**3rd Generation**
FPGA Model	Virtex-4	Virtex-4	Virtex-5
On-board Clock	100 MHz	100 MHz	150 MHz
ADC Model	Maxim MAX 104	Texas Instruments ADS54RF63	National Semiconductor ADC16DV160
Channel # per ADC	Single	Single	Dual
Analog Input Bandwidth	2.2 GHz	2.3 GHz	1.4 GHz
ADC Resolution	8-bit	12-bit	16-bit
Input Signal Range	±0.25V	2.2 V_{pp}	2.4 V_{pp}
Delay Line Chip	CDC5801	CDC5801	SY100EP196
Finest Sampling Interval	13.02 ps	13.02 ps	10 ps
Equivalent Conversion Rate	76.8 GS/s	76.8 GS/s	100 GS/s
Data Transfer Link	USB2.0	USB2.0	USB2.0
Transfer Rate	25 MB/s	25 MB/s	25 MB/s
Required Sampling Time (8 Rx Channel)	0.61 ms	0.61 ms	0.53 ms
Required Transfer Time (8 Rx Channel)	4.92 ms	9.83 ms	12.8 ms
System Refresh Rate (8 Rx Channel)	180 Hz	95 Hz	75 Hz
System Refresh Rate (Single Rx Channel)	1.44 kHz	760 Hz	600 Hz
Ambiguous Velocity (Single Rx Channel)	36 m/s	19 m/s	15 m/s

2.6 Conclusion

In this chapter, we have presented the system development and prototyping of UWB pulse radar in details. We were motivated to design such a radar system for, but not limited to, human imaging and Doppler detection applications in a harsh environment, such as through wall and debris. However, the developed UWB pulse radar can be easily extended for other applications, such as precise indoor localization, sensitive material monitoring, and asset tracking.

Optimal operation frequency is an important factor in designing UWB pulse radar, considering the fact that different applications require different performance concentration. For example, 8-10 GHz UWB band is recommended for seeing through low-loss materials in order to achieve good azimuth resolution while 1.5-4.5 GHz is suggested for seeing through high-loss materials in order to minimize the through attenuation. In order to achieve the function flexibility and make one platform adapted for many applications, we have introduced a reconfigurable radar imaging system. The reconfigurable system covers the entire UWB band from 1.5-10 GHz and can be reconfigured to switch the operation frequency between 1.5-4.5 GHz and 8-10 GHz.

The detailed design of various system components were also discussed here, including a reliable, high dynamic range transceiver, a low cost, high speed data acquisition module, and design of compact, wideband Vivaldi antennas and arrays. These components are the common blocks in UWB systems and can be easily applied for other systems as well. For better understanding and fast prototyping of new UWB radar systems, we have simulated the developed UWB pulse radar accurately in the system level and will present it in the next Chapter.

Conclusions:

1) The first step in design TWI radar is selecting the operation frequency. High frequency leads to high azimuth resolution, while relatively low frequency allows penetrating through walls. 1-4 GHz is regarded as the optimal

frequency band for seeing through high-loss materials, such as brick-wall and concrete-wall.

2) UWB radars are excellent candidate to address both imaging and human motion tracking. UWB Doppler radars are able to discriminate the motion Doppler effects of more than one object in the scene based on different locations in the scene.
3) Using a wideband antenna and a reconfigurable platform gives the flexibility of radar transceiver to operate at either 9 GHz or 3 GHz, combining two features in one platform.
4) Plane wave propagation formulas are adequate to calculate reflection and transmission characteristics for through wall propagation.
5) Vivaldi antennas/arrays are good candidate for UWB radar system because of their wideband performance and directional radiation characteristic. But the phase center variation with frequency may bring few mm errors in target localization.
6) FPGA can be used to carry out the array switch control, the data storage and handling, and real-time image recovery.
7) A tunable Gaussian pulse generator is applied in the radar prototype, providing a pulse width from 300ps to 1ns; typically, 700ps pulse is used in the system.
8) The radar is coherent, as the same carrier LO is used for transmitting and receiving chains.

Chapter 3

System Level Simulation of UWB Pulse Radar

Although the hardware development of UWB pulse radar has attracted a lot of attention, there is still a need to simulate the entire UWB pulse system accurately. Such an integrated simulation tool can significantly help in understanding and analyzing the overall system performance, logically illustrates the correlation between simulation and experimental results, and defines performance limits/constraints. The tool should go from component level, sub-system, to a full system level including time and frequency domains. These capabilities should clearly fulfill the need of a comprehensive simulation platform for a rapid design prototyping and optimization of radar systems including the complex UWB ones.

Many challenges exist in accurately simulating these complex UWB pulse systems including both circuits modeling (e.g., RF, analog and digital devices of the system) and electromagnetic modeling (e.g., through wall propagation and 3-D radar targets scattering). Additional complexity is added to developing a simulation tool by the need for antenna modeling [61] and imaging recovery algorithm as well. Preliminary analysis of some UWB systems has been previously addressed [62], [63], but still represents only partial modeling of the whole system.

Subsequently, we recognized the need for a complete UWB system simulator in one integrated platform using time-domain approach for both localization and imaging applications. Kuhn et al. [64], [65] has developed a comprehensive simulation framework for indoor UWB positioning system that has been validated using the experimental prototype in [66] and [67]. Along this line, we will present an extension of this effort in this chapter, to develop an analogous simulation model for through wall imaging applications as well. The new tool has some common blocks with Kuhn's simulation tool [64], [65] but has its own special blocks as well—details will follow.

3.1 Simulation Platform Architecture

Figure 3.1 shows a diagram of the proposed generic simulation framework to simulate our UWB system, which includes 6 blocks; but it can be easily extended to simulate other UWB pulse radar systems by using appropriate simulation blocks. The program is divided into different parts to follow the signal propagation path. First, the simulation platform requires some initial parameters (input parameters) at the beginning describing the operation of the system including all physical parameters. Then, Agilent ADS circuit simulation tools are used to simulate the UWB radar transmitter including all active or passive circuit components. The transmitted signal impinges on the wall and propagates through it to hit the target. So, a block is used to account for multiple through-wall-reflections and transmissions and the utilized method is defined in [49] and implemented here using Matlab. As expected, part of the signal is reflected from the wall and received by the UWB receiver while the rest penetrates through the wall and encounters the radar object. In our numerical simulation of the radar object scattering, the object reaction is calculated based on the Method of Moments (MoM) and is implemented using Matlab code as well. Next, the scattered signal penetrates through the wall again and is then collected by the UWB receiver in which the signal is amplified, demodulated, low-pass filtered and digitized. Finally, the digitized data is saved and a 3-D wideband microwave beamformer [68] (given in Appendix A.3) is applied to recover the 3-D images of the radar targets.

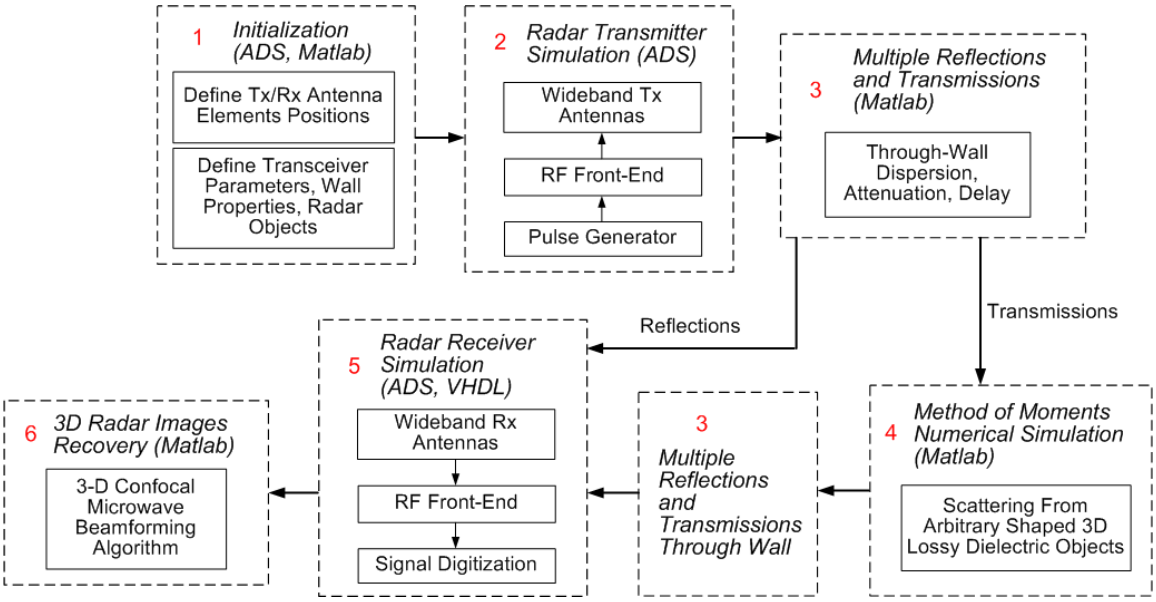


Figure 3.1 Generic system simulation model including six blocks.

3.1.1 Initialization

Some system parameters need to be initialized prior to the simulation based on wall type and experiment purpose. For example, usually, pulse shape, pulse width, carrier frequency are set according to the wall type. Meanwhile, for SAR operation, an electronic scanning is utilized, while both Tx antenna and Rx antenna array are moved mechanically to operate as a 25×25 planar Tx/Rx antenna array. For the time being, the properties of the wall, including thickness, permittivity and loss tangent are assumed, but eventually methods should be developed to provide a good estimation of wall parameters in specific cases like in a hostile environment for example.

3.1.2 Radar Transmitter Operation

Agilent ADS Ptolemy simulation incorporated with transient simulation tool is used to model the UWB radar transmitter, as shown in Figure 3.2. By using ADS transient simulation package, we have accurately modeled the pulse generator hardware in the simulation platform. Both the simulation and experimental results of transmitted

signals are shown in Figure 3.3 and good agreement has been observed. The transmitted signal is captured before the transmitting antenna in both simulation and measurement. The UWB transmitted pulse signal measured by using a high speed digital oscilloscope (Tektronix DPO 70804) includes a small carrier leakage which is also captured in the simulation. Both transmitting and receiving antennas are directional with a wide beamwidth and their gains are accounted for in the simulation platform as well.

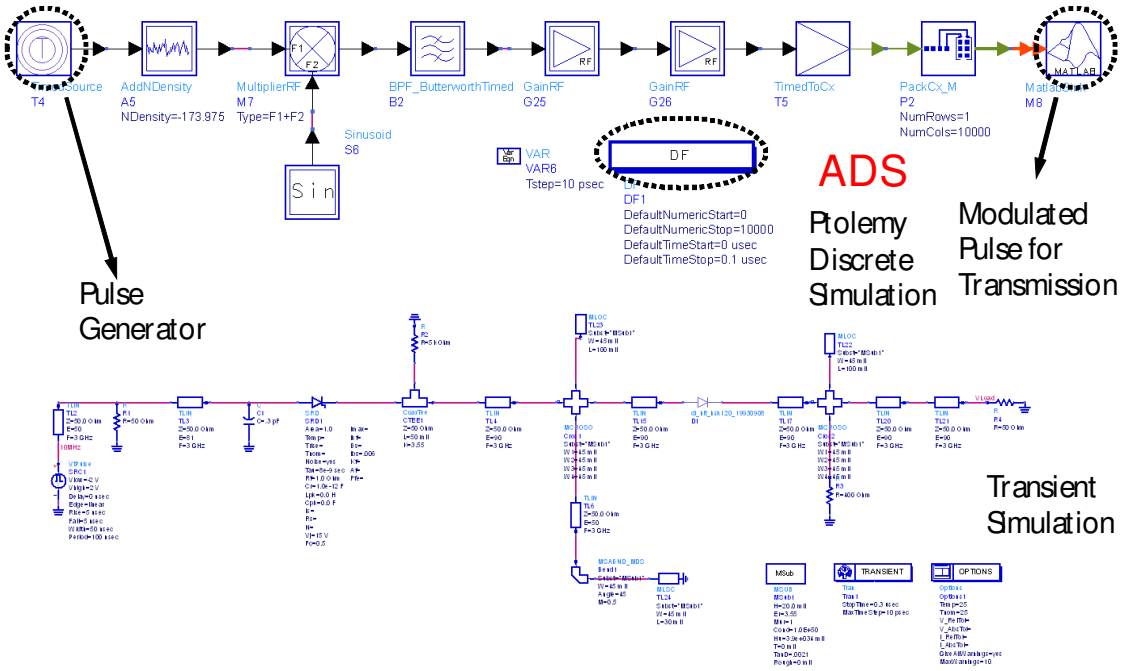


Figure 3.2 Simulation model of UWB radar transmitter in ADS.

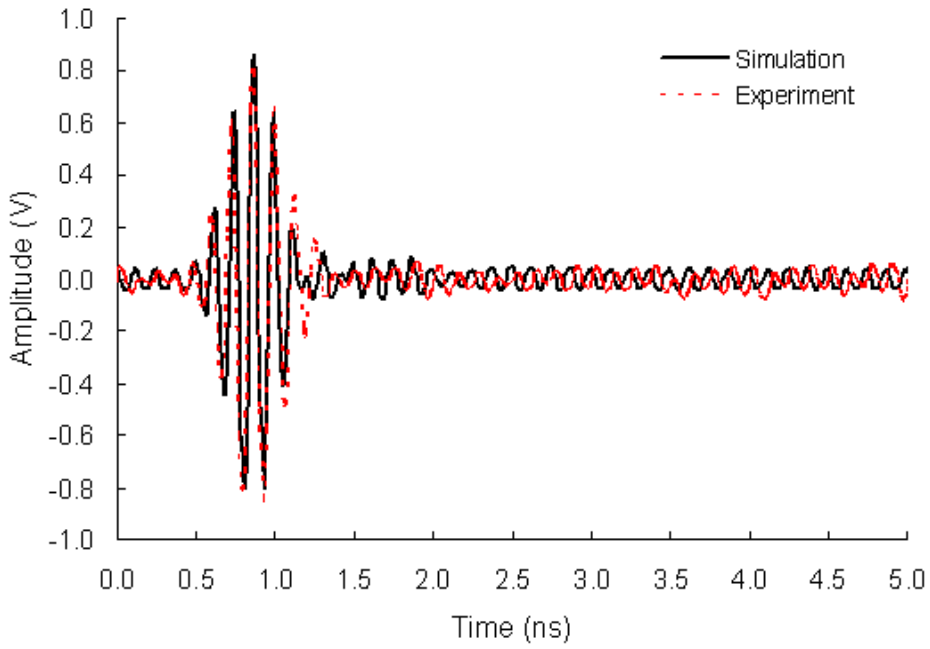


Figure 3.3 Simulation and measurement of the transmitted signals emitted by the UWB transmitter. The transmitted signal is periodic with T_0 = 100ns.

3.1.3 Through Wall Propagation

In our simulation platform, we assumed that the wall is homogeneous with known properties. But the fact that walls could be inhomogeneous, and not even flat surfaces or without known geometrical and electrical characteristics, all of these unknowns may obscure the electromagnetic signatures of the targets behind the wall and create ghost targets. The approach in [58] can be used to accurately estimate the parameters (i.e., dielectric constant, thickness) of a homogeneous, single layer wall during image recovery. However, it would be very difficult to accurately model an inhomogeneous or non-flat wall structure.

For a stratified multi-layer wall structure, the developed platform has been used to simulate the through-wall dispersion, attenuation and delay. A perpendicularly polarized plane wave at an incident angle of θ_0 is used in the simulation to mimic the experimental

setup. Assuming μ_i, σ_i, ε_i are the permeability, conductivity and permittivity of layer i, and θ_i is the wave propagation angle at layer I, an iterative method based on (3-1) to (3-7) is used to calculate the reflection coefficient $\Gamma_\perp$ and transmission coefficient $T_\perp$ for the perpendicular polarization case through N layers wall interfaces [49]. The Matlab code to implement these equations is listed in Appendix A.1.

$$A_i = \frac{e^{\psi_i}}{2}\left[A_{i+1}\left(1+Y_{i+1}\right)+B_{i+1}\left(1-Y_{i+1}\right)\right] \tag{3-1}$$

$$B_i = \frac{e^{-\psi_i}}{2}\left[A_{i+1}\left(1-Y_{i+1}\right)+B_{i+1}\left(1+Y_{i+1}\right)\right] \tag{3-2}$$

$$A_{N+1} = 1, \quad B_{N+1} = 0 \tag{3-3}$$

$$\Gamma_\perp = \frac{B_0}{A_0}, \quad T_\perp = \frac{1}{A_0} \tag{3-4}$$

where

$$Y_{i+1} = \frac{\cos\theta_{i+1}}{\cos\theta_i}\sqrt{\frac{\varepsilon_{i+1} - j\sigma_{i+1}/w}{\varepsilon_i - j\sigma_i/w}} \tag{3-5}$$

$$\Psi_i = d_i\gamma_i\cos\theta_i \tag{3-6}$$

$$\gamma_i = \pm\sqrt{jw\mu_i\left(\sigma_i + jw\varepsilon_i\right)} \tag{3-7}$$

For a single layer wall structure this model can be simplified as given by (3-8) to (3-11). Assuming ε^* and d are the complex permittivity and thickness of the wall, θ_0 is the angle of incidence while θ_1 is the angle of refraction in the wall media, we have $k_0 sin\theta_0 = k_1 sin\theta_1$ according to Snell's law. Then the reflection coefficient $\Gamma_\perp$ and transmission coefficient $T_\perp$ are given by

$$\Gamma_{\perp} = \frac{\Gamma_{0w}\left(1 - e^{-j2k_1 \cos\theta_1 d}\right)}{1 - \Gamma_{0w}^2 e^{-j2k_1 \cos\theta_1 d}} \tag{3-8}$$

$$T_{\perp} = \frac{\left(1 - \Gamma_{0w}^2\right) e^{-jk_1 \cos\theta_1 d}}{1 - \Gamma_{0w}^2 e^{-j2k_1 \cos\theta_1 d}} \tag{3-9}$$

where

$$k_1 = w\sqrt{\mu\varepsilon^*} \tag{3-10}$$

$$\Gamma_{0w} = \frac{\sqrt{\varepsilon_0}\cos\theta_0 - \sqrt{\varepsilon^*}\cos\theta_1}{\sqrt{\varepsilon_0}\cos\theta_0 + \sqrt{\varepsilon^*}\cos\theta_1} \tag{3-11}$$

The transmission coefficient $T_{\perp}$ given by (3-9) is a frequency dependent complex number. Its magnitude demonstrates the through wall attenuation while its phase indicates the through wall time delay.

Currently, the complex permittivity of various building materials are measured and brought to the simulation model in order to account for the wall dispersion. The fact that the dielectric properties are function of frequency will lead to signal distortion. An example of the measured complex permittivity of drywall and brick-wall at 1 to 11 GHz is shown in Figure 3.4, but it should be understood that these values will be very sensitive to humidity. In the simulation platform, different complex permittivity values are applied at different frequencies, in order to emulate the wall dispersion effect that happens in practice.

When investigating the through wall attenuation and time delay, the signal is sent out by the transmitting antenna at 0.5s, with amplitude from -1V to 1V. Figures 3.5(a) and (b) show the simulated and measured reflections and transmissions through a 6-inch drywall respectively at normal wave incidence, at the frequency band of 6-10 GHz. Both

transmitted signals from simulation and measurement show a similar amplitude of 0.2V and a time delay of approximately 0.7ns, validating the through wall simulation model. Subsequently, we applied the simulation model to a 6-inch brick-wall at 2-6 GHz in order to reduce the through wall losses, as shown in Figure 3.5(c). Comparing Figure 3.5(a) and (c), the transmitted signal through the brick-wall presents a longer time delay (about 1ns) than that through the same thickness drywall (i.e., about 0.8ns) due to the lower wave propagation velocity inside it. The wall frequency dispersion is manifested through noticeable broadening of the transmitted signals from both simulation and experiment. The pulse signal sent out from the UWB transmitter has a width of approximately 500ps while the signal width increases to about 650ps after penetrating through the wall.

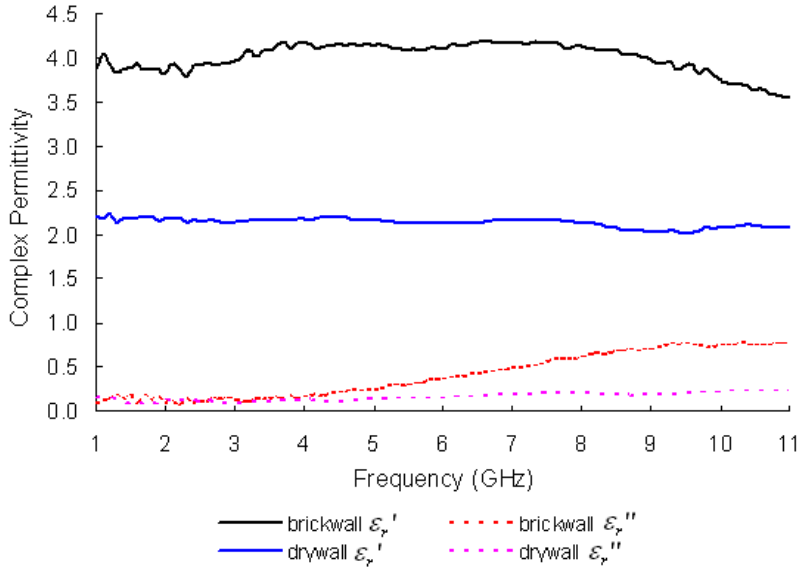
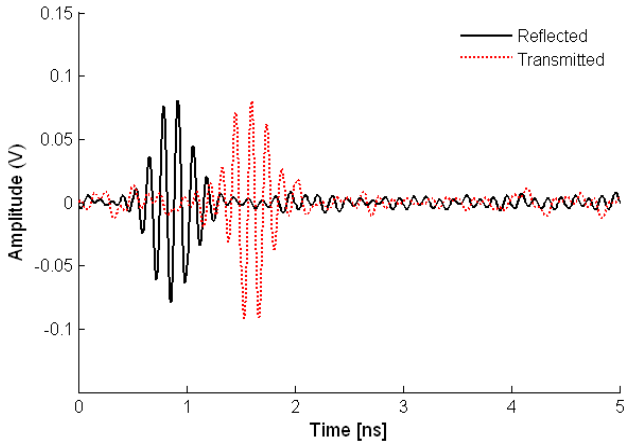
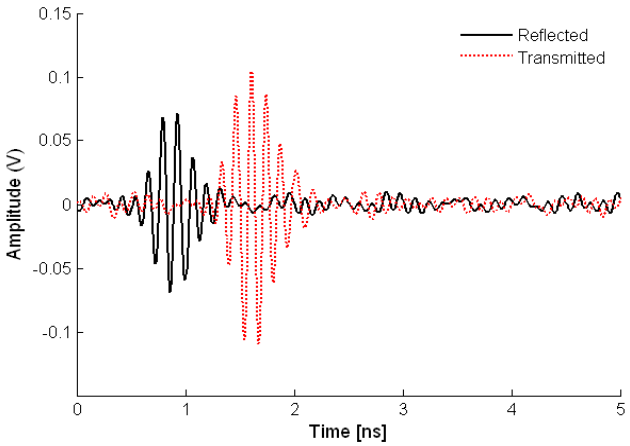


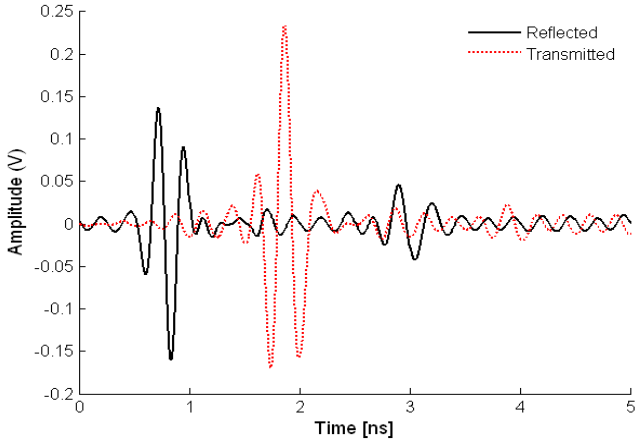
Figure 3.4 Measured permittivity of drywall and brick-wall from 1 to11 GHz.



(a) Simulation of a 6-inch drywall (at 6-10 GHz band)



(b) Measurement of a 6-inch drywall (at 6-10 GHz band)



(c) Simulation of a 6-inch brick-wall (at 2-6 GHz band)

Figure 3.5 Reflected and transmitted signal through different wall materials.

3.1.4 Electromagnetic Scattering by 3-D Radar Objects

Literature shows a continued interest in MoM technique for solving electromagnetic scattering problems. For example, an adaptive multiscale MoM was introduced in [69] for analyzing the scattering from 3D perfectly conducting structures and MoM was employed in [70] to solve the scattering from mixed conducting and dielectric objects. In addition, the scattering from homogeneous dielectric bodies was analyzed in [71] and tensor integral equation was used in [72] to determine the electromagnetic field inside heterogeneous biological bodies with arbitrary shape.

In our simulation platform, we have extended the MoM method in [72] for solving the electromagnetic scattering problem from heterogeneous, arbitrarily shaped human bodies, with the equations shown in Appendix B. To lower the computational cost, we have considered a homogeneous lossy dielectric target with complex permittivity ε^* and permeability μ_0. In our analysis, a plane wave is assumed as the incidence and considered to be a good approximation if the radar object locates at the far field of the radar transmitting and receiving antennas. The internal current density and scattered field are calculated sequentially using the equations in Appendix B, which are implemented using Matlab code as described in Appendix A.4.

To validate the MoM code, we have investigated the bistatic radar cross section (RCS) of a lossless and a lossy dielectric object respectively, where different antennas are used for transmitting and receiving. All the RCS results are observed at different angles θ, with a perpendicular polarization plane wave incidence at an angle of $\theta = 0^o$ and $\varphi = 90^o$. For ease of comparison, we have compared MoM results with exact solutions from Mie theory [73]. A free MiePlot program [74] has been utilized to acquire the exact solutions from Mie theory. Spherical object is used to validate the MoM code since Mie theory can only analyze the RCS of sphere.

In the first example, we considered a lossless homogeneous dielectric sphere with a radius of $0.5\lambda_0$ at 3 GHz. The sphere target has a relative permittivity of $\varepsilon_r = 4.0$ and a relative permeability of $\mu_r = 1.0$. The volume of the sphere is discretized into 4224 cubic cells with a side length of $0.05\lambda_0$. The calculated bistatic RCS using MoM numerical

method is shown in Figure 3.6. Good agreement is observed between the numerical results with the analytic solutions from Mie series, validating the present method.

For further validation, a lossy homogeneous dielectric sphere is considered with a radius of $0.5\lambda_0$ at 3 GHz. We use the same relative permittivity and relative permeability as that in the 1st example (i.e., $\varepsilon_r = 4.0$, $\mu_r = 1.0$). Meanwhile, the target is defined with a conductivity of 0.2 S/m. The volume of the lossy sphere is still divided into 4224 unknowns. Both Mie series solutions and MoM results are presented in Figure 3.7 and good agreement has been achieved.

Subsequently, we assume the MoM code can also be used to calculate the RCS of any arbitrary shape radar object.

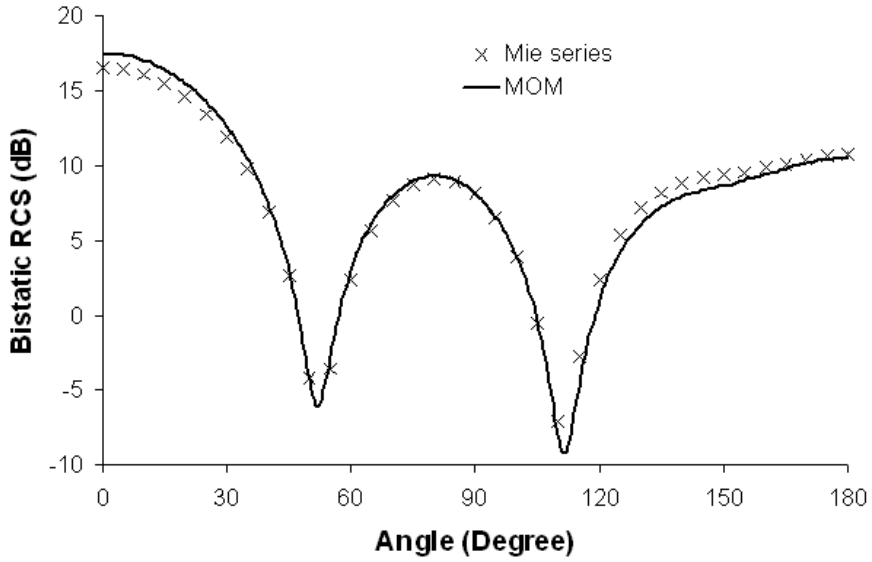


Figure 3.6 Bistatic RCS of a losslessy dielectric sphere with a radius of 5cm at f = 3 GHz ($\varepsilon_r = 4$, $\mu_r = 1$, $\sigma = 0$).

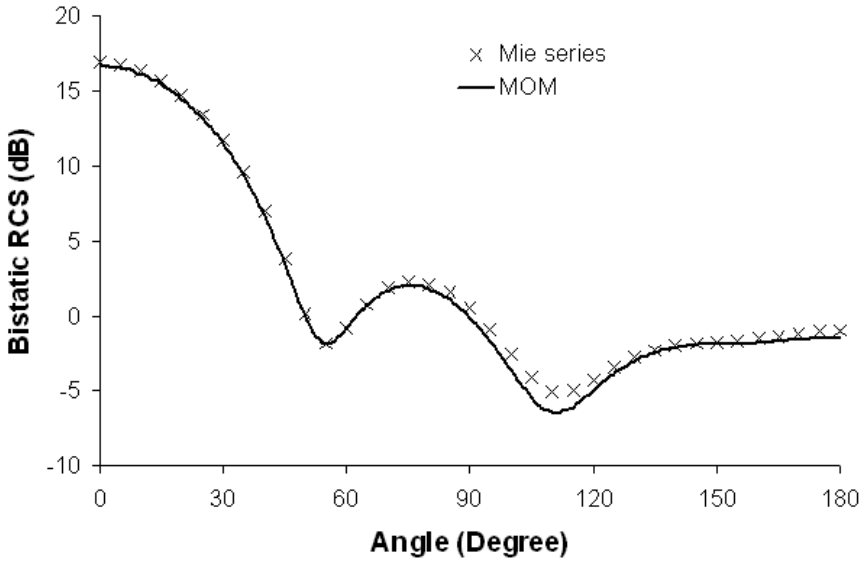


Figure 3.7 Bistatic RCS of a lossy dielectric sphere with a radius of 5cm at f = 3 GHz (ε_r = 4, μ_r = 1, σ = 0.2 S/m).

3.1.5 UWB Radar Receiver Modeling

Agilent ADS Ptolemy simulation incorporated with ADC module is used to model the UWB radar receiver including all active and passive components, as shown in Figure 3.8. The ADS model of I/Q radar receiver is shown in Figure 3.9. We have preformed an experiment to investigate the recovered baseband pulse signal from a metallic plate target, which was placed at a standoff distance of 1.5m behind a drywall. Meanwhile, we also used our simulation platform to analyze the same scenario and recover the baseband pulse signal. Figure 3.10 shows the recovered pulse signals from both simulation and experiment. Good agreement is achieved between the simulated and measured signals in terms of pulse shape, pulse width, and SNR.

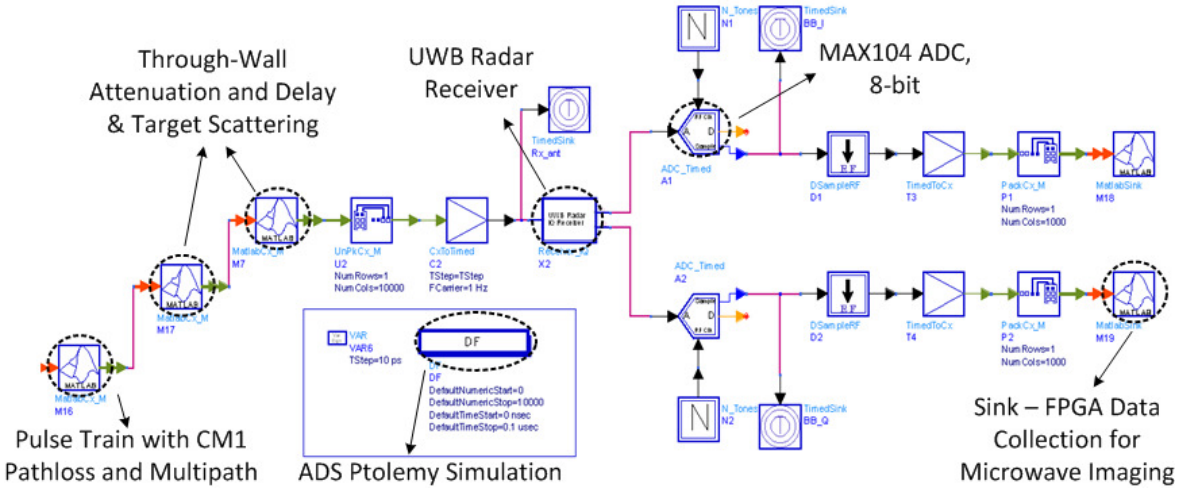


Figure 3.8 Agilent ADS Ptolemy simulation incorporating Matlab source and sinks, Matlab through-wall and target scattering models, UWB radar receiver, and 8-bit MAX104 ADCs.

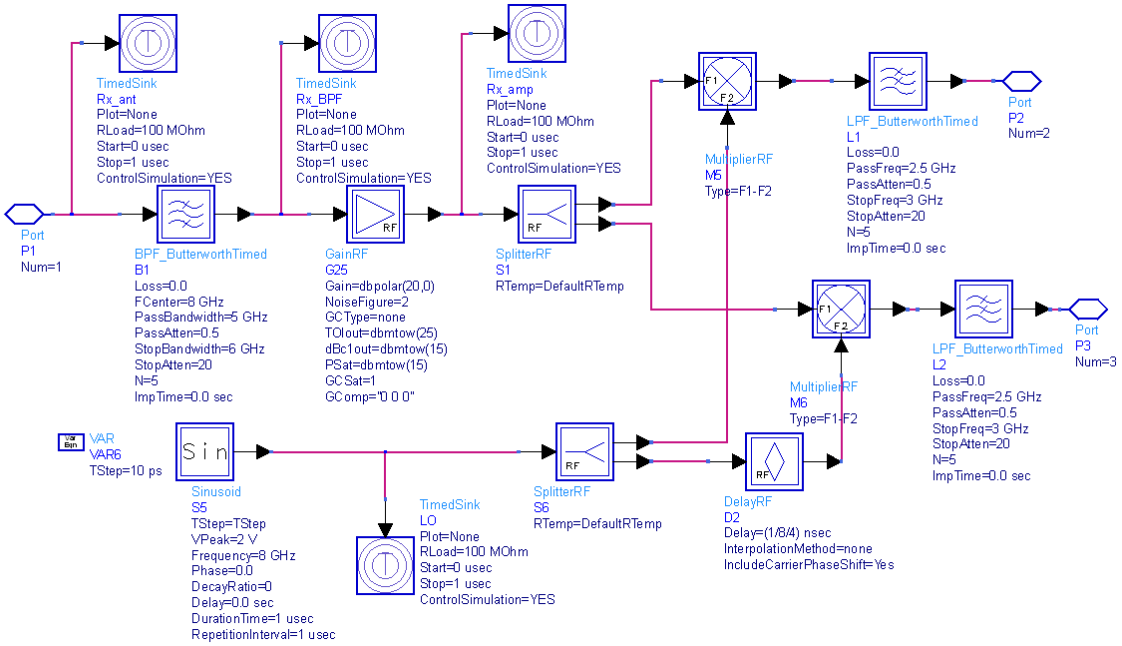


Figure 3.9 ADS model of I/Q radar receiver front-end.

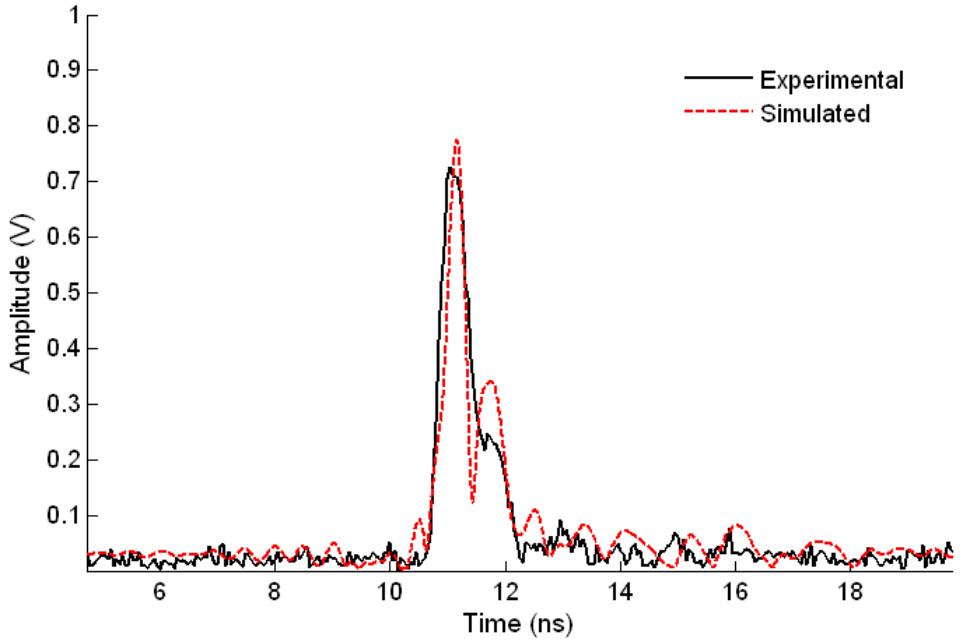


Figure 3.10 Comparison of recovered pulse signals from simulation and experiment.

3.1.6 Wideband Microwave Beamformer

After acquiring the baseband pulse signals, we have implemented a microwave beamformer in the simulation platform to reconstruct the image of radar objects. In our simulation platform, a 3-D wideband Backprojection algorithm [68] is used to achieve high computation efficiency. Consider a P-element planar transmitting array, located at $\{x_{tp}, y_{tp}, z_{tp}\}_{p=1}^{P}$, and a Q-element planar receiving array, located at $\{x_{rq}, y_{rq}, z_{rq}\}_{q=1}^{Q}$. Let $s_{p,q}(t)$ be the complex received baseband pulse signal. Since s is sampled in time, the sampled version of s is

$$s_{p,q}(n) = a_{p,q}(n) + jb_{p,q}(n) \tag{3-12}$$

where a and b are the in-phase and quadrature components of the received signal; p and q indicate that the signal is sent out by the pth transmitting antenna and acquired by the qth receiving antenna. A matched filter $h(n)$ is applied first to eliminate the out-of-band noise of the received baseband pulse, and the new signal is given by

$$z_{p,q}(n) = s_{p,q}(n) \otimes h(n) \tag{3-13}$$

where " $\otimes$ " denotes convolution operator; and $h(n)$ is the impulse response of the matched filter and its frequency response is given by

$$H(f) = \begin{cases} 1, & f \le f_{BW} \\ 0, & f > f_{BW} \end{cases} \tag{3-14}$$

where f_{BW} is the bandwidth of the received baseband pulse.

To recover the 3-D image, the surveillance space is divided into cubic voxels in cross range, down range and height, represented by the x, y and z coordinates respectively, as shown in Figure 3.11. For any selected voxel $V_m = \{x_m, y_m, z_m\}$, the confocal microwave imaging algorithm is applied to calculate its absolute image value $I(V_m)$ via

$$I(V_m) = \left| \sum_{p=1}^{P} \sum_{q=1}^{Q} w_{p,q}(V_m) z_{p,q}(n_{p,q}) e^{j\varphi_{p,q}(V_m)} \right| \tag{3-15}$$

where the index $n_{p,q}$ of $z_{p,q}$ locates the signal at correct time delay; $\varphi_{p,q}(V_m)$ shows the phase compensation for different traveling paths; and $w_{p,q}(V_m)$ introduces the amplitude compensation for different scattering loss, through wall attenuation, and propagation loss, respectively. The value of index $n_{p,q}$ is given by

$$n_{p,q} = \frac{l_{pm} + l_{mq}}{c \cdot \Delta t} \tag{3-16}$$

where l_{pm} indicates the equivalent traveling path from the pth transmitting antenna to the voxel V_m; l_{mq} indicates the equivalent traveling path from the voxel V_m to the qth receiving antenna; c is the speed of light in the air; and Δt is the pulse sampling interval. The wall effect should be taken into account when calculating the equivalent traveling path, for example, $l_{mq} = l_{mq1} + \sqrt{\varepsilon_r} l_{mq2} + l_{mq3}$ is the equivalent traveling path in Figure 3.10, where ε_r is the relative permittivity of the wall. The phase correction term is determined by the following equation,

$$\varphi_{p,q}(V_m) = \frac{2\pi f_c}{c}(l_{pm} + l_{mq}) \tag{3-17}$$

where f_c indicates the carrier frequency in the radar transceiver. The amplitude compensation is given by

$$w_{p,q}[dB] = L_{scatter}[dB] + L_{wall}[dB] + L_{propag.}[dB] \tag{3-18}$$

where $L_{scatter}$ is the scattering loss, L_{propag} introduces the propagation loss, and L_{wall} presents the through wall attenuation. The scattering loss and propagation loss are assumed constant, considering the fact that radar object usually locates in the far field of the radar system. The through wall attenuation L_{wall} is analyzed using equation (3-9) at the carrier frequency. After recovering the imaging information for voxel V_m, the same process is repeated and applied to the next voxel to obtain the related imaging value until all the voxels are solved. Lastly, a complete 3-D image is displayed. Appendix A.3 lists the Matlab program we implemented based on 3-D Bakcprojection beamforming method.

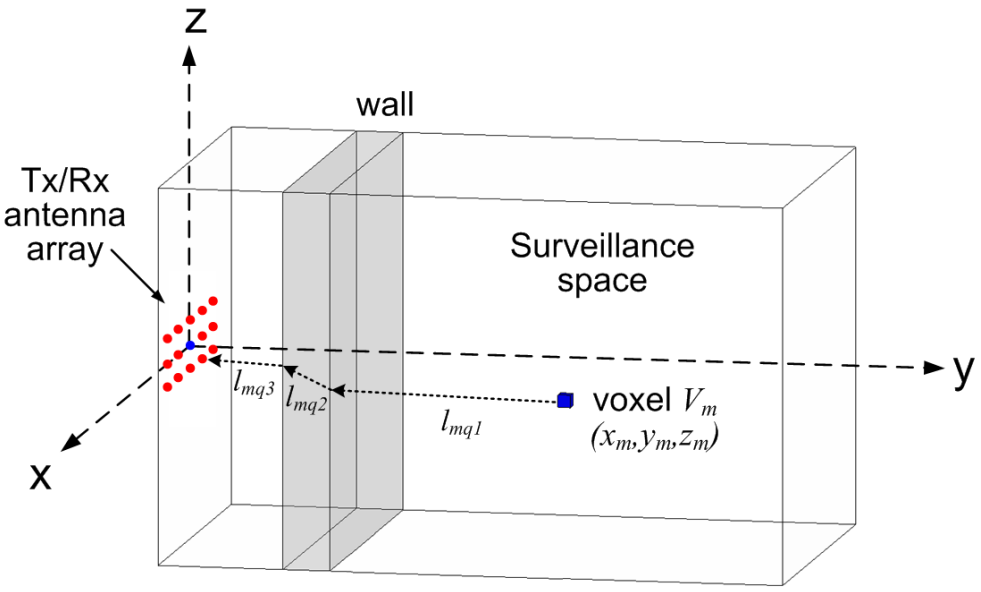


Figure 3.11 3-D wideband microwave beamformer model.

3.2 Experimental Validation

To validate the accuracy and demonstrate the capability of our advanced simulation platform, a simulation run was performed to recover the 3-D image of a wooden block, and then compared with the associated experimental result.

The imaged object has a size of 45cm x 35cm x 1cm, as shown in Figure 3.12. To increase the signal reflections, the block has been soaked in the water for few hours. The complex permittivity of the soaking block was then measured using an Agilent coaxial RF probe and brought into the simulation platform. An almost constant ε' of 13 was acquired between 2 and 10 GHz, while ε'' increases linearly from 0.2 (at 2 GHz) to 2.3 (at 10 GHz).

In the experimental setup, we have collected the signals at two scenarios: the first from background only before putting any target, and the second after placing the target. By subtracting the two signals with and without the target, the newly acquired signals are used in the image recovery process to remove the clutters. Similar clutters removal process was also applied in the simulation by subtracting the simulated signals with and without the target. The simulation result in Figure 3.13(a) accurately predicts the outline of the wooden block target, as well as its location. The recovered image from experiment agrees fairly well with that from simulation, as shown in Figure 3.13(b). It is worthy noted that the clutter removal process needs the measurement of the scene without target, which may not be available in many cases in practical life.

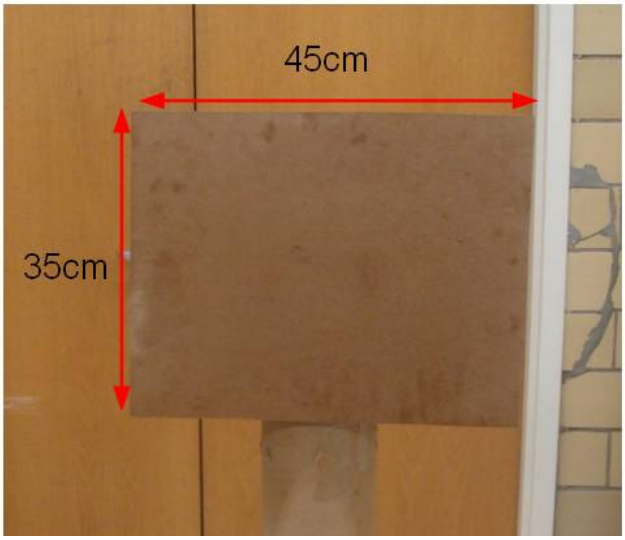
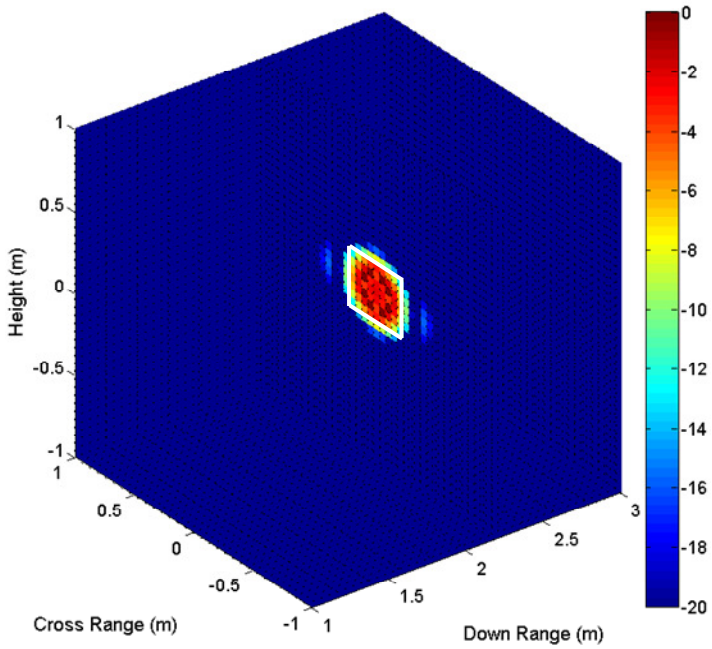
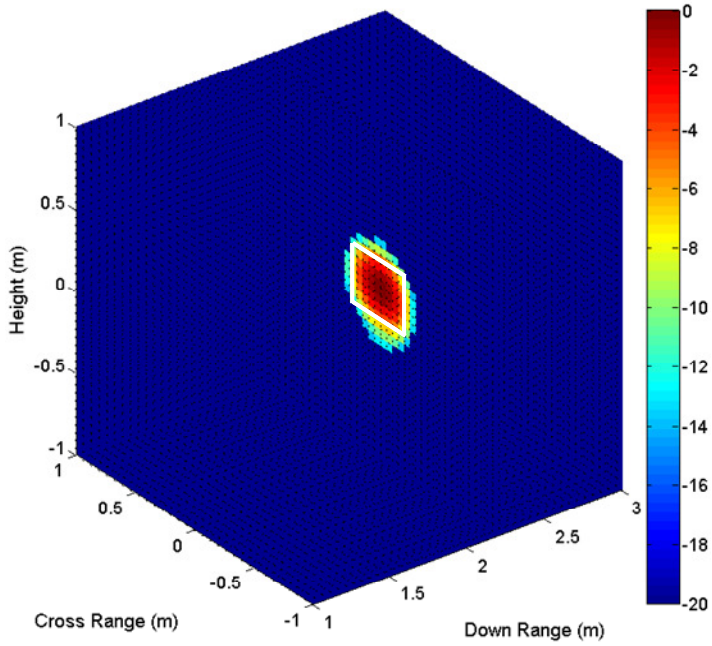


Figure 3.12 3-D imaging of a wooden block, with a size of 45cm x 35cm x 1cm.



(a) Simulation result



(b) Experimental result

Figure 3.13 Recovered image results of a wooden block: (a) Simulation results, and (b) Experimental results. The target is put at a down range of 2.2 m.

For further model validation and capability demonstration, the developed simulation platform has been applied to localize and image two metallic cylinders within a drywall. The simulation geometry of two copper cylinders within a very thick drywall is used in the simulation as shown in Figure 3.14. The radius of each cylinder is 8cm with a height of 4cm. Both targets are placed at a Down Range of 0.7m, with an edge to edge spacing of *d* in Cross Range. The radar transmitting and receiving antennas are put in the Cross Range/Height plane at a Down Range of 0m, facing the two cylinders.

The images of the two cylindrical targets are obtained with two spacing values. Figure 3.15(a) shows the imaging results in the plane of Down Range = 0.7m with a relatively large spacing *d* of 48cm. Then, the two cylinders were moved closer to an 8cm-apart, with the imaging results presented in Figure 3.15(b). The acquired images by the simulation platform have accurately indicated the true target location and shape in both cases. The results in Figure 3.15(b) also indicated that the proposed simulation platform has a better than 8cm cross range resolution, which is adequate for most of the through wall imaging applications. The distance *d* between the two cylindrical targets has been progressively reduced until we could not distinctly separate the two targets. It is found that the radar achieves a cross range resolution of approximately 6cm.

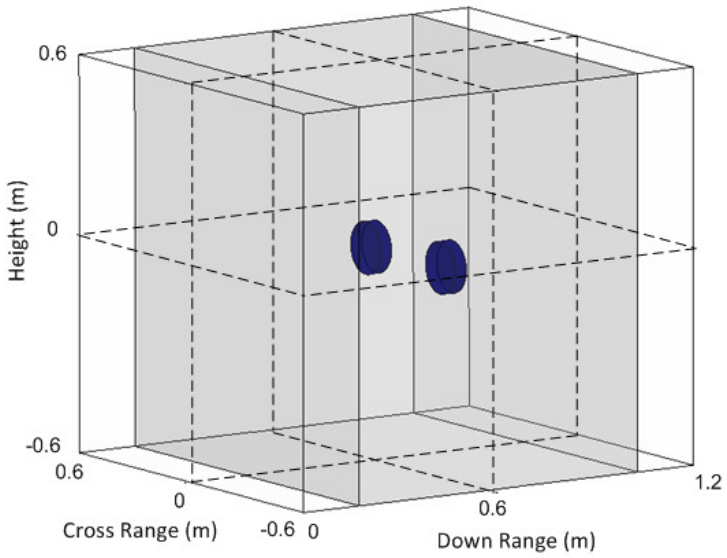
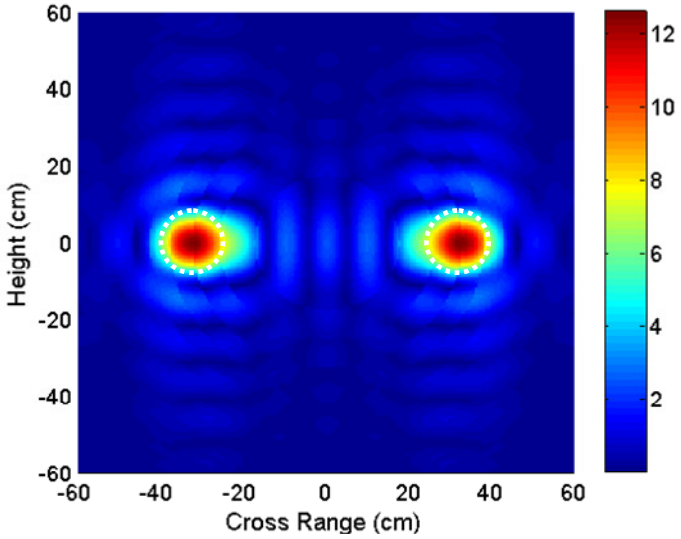
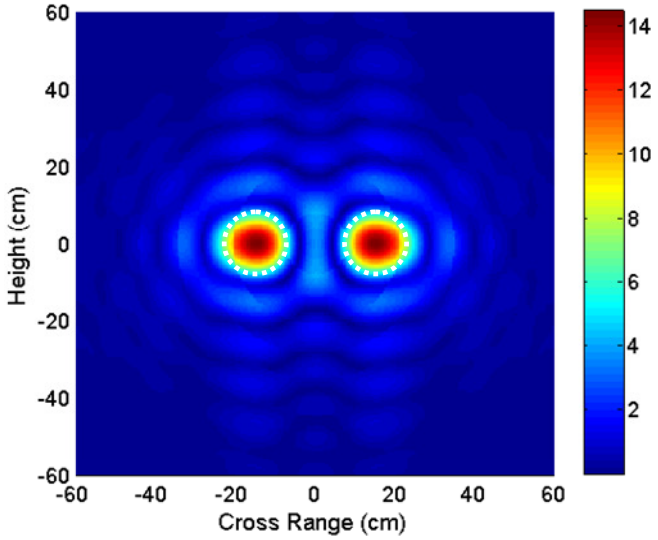


Figure 3.14 Simulation geometry of two metallic cylinders within the wall.



(a) d = 48cm, Down Range = 0.7m



(b) d = 8cm, Down Range = 0.7m

Figure 3.15 Simulation imaging results of two cylindrical targets within a drywall. The two cylinders are put at a down range of 0.7m. Dotted white lines indicate the true target location and shape.

3.3 System Performance Prediction

After validating the simulator, the developed simulation platform has been used to optimize the pulse waveform and predict the system performance and limitations of the UWB radar hardware. In Section 3.3.1, the simulation platform has been applied to optimize the pulse waveform to acquire the best image quality, when detecting a human phantom target through a brick-wall. Section 3.3.2 introduces how the simulation platform can predict the system detection range through received SNR, when seeing through a 6-inch drywall and a 6-inch brick-wall respectively.

3.3.1 Pulse Waveform Optimization

Waveform design and optimization has been recently investigated in many radar applications, considering the fact that in target detection and identification, an appropriate choice of radar waveform has a great effect on the amount of information obtained from the target, especially for extended targets [75]. Therefore, the design and optimization of the waveform is important for improving the performance of imaging radar system [76]. In the analysis, a single-layer, homogeneous wall model was assumed. When investigating different pulse waveforms, the same wall model was used to compensate for its effects.

We have applied the simulation platform to investigate the effects of different pulse shapes and pulse durations on a human phantom target behind a 6-inch brick wall. The human phantom target has a relative permittivity of 50 and a conductivity of 4 S/m to emulate the real body tissue [77]. It has a height of 1.4m, a width of 1.2m, a thickness of 0.2m and is placed at a Down Range of 2.2m, as shown in Figure 3.16.

Firstly, a Gaussian pulse and a monocycle pulse (i.e., 1st derivative of Gaussian pulse), both having the same duration of 300ps, are used as the input signals respectively in the simulation. To make a fair comparison, identical setups are assigned for all other blocks in the simulation platform.

Figure 3.17 shows the simulation results with the 300ps Gaussian pulse input. The Height – Cross Range cut of the recovered image, as shown in Figure 3.17(a), has predicted a reasonable outline of the human phantom target. The Height – Down Range cut in Figure 3.17(b) has accurately localized the target at a Down Range of 2.2m, with a resolution of approximately 5cm. Figure 3.18 introduces the simulation results using a 300ps monocycle pulse. It is evident that a clearer arm shape is gained in Figure 3.18(a) through a monocycle pulse waveform, compared to Figure 3.17(a). A similar Down Range resolution of 5cm has been achieved from the 300ps monocycle pulse signal, as shown in Figure 3.18(b). It is concluded that using a 300ps monocycle pulse renders similar Down Range resolution as using a 300ps Gaussian pulse, but tends to give slightly better image quality, when imaging a human phantom. It is worthy noted that the optimal shape of waveform totally depends on the frequency response of the radar object when illuminated by a wideband signal.

In addition to pulse shape, we have also applied the simulation platform to investigate the effects of different pulse durations. A wider Gaussian pulse signal (i.e., 1ns pulse) has been used as the system input in the simulation platform, which has the same setups for all other blocks as mentioned above.

It is observed that the 1ns Gaussian pulse generates the cleanest shape of the phantom target, with the least ghost targets around the true one, as shown in Figure 3.19(a). The main reason is that the average transmitted power is significantly increased if a constant peak power is maintained, by using a wider pulse signal. Therefore, a much higher SNR is expected in the received pulse signals. However, using a wider pulse signal also decreases the system bandwidth and therefore degrades the down range resolution significantly, as shown in Figure 3.19(b), which introduces a localization resolution of approximately 15cm. Therefore, a compromise needs to be made between the target shape recognition and the localization resolution. For some precise imaging and positioning applications, such as early breast cancer detection and surgery tools tracking, the localization accuracy is a must.

The simulation platform can also be used to investigate any other signal waveforms (e.g., chirp signal, coded pulse) and design the optimal signal waveform for a

radar object in through wall imaging applications. It is worth mentioning that in the current simulation platform, the wall parameters, such as permittivity and thickness, are assumed known. In most practical cases, the wall parameters are unknown and the method in [58] can be helpful to estimate the wall parameters during the image recovery.

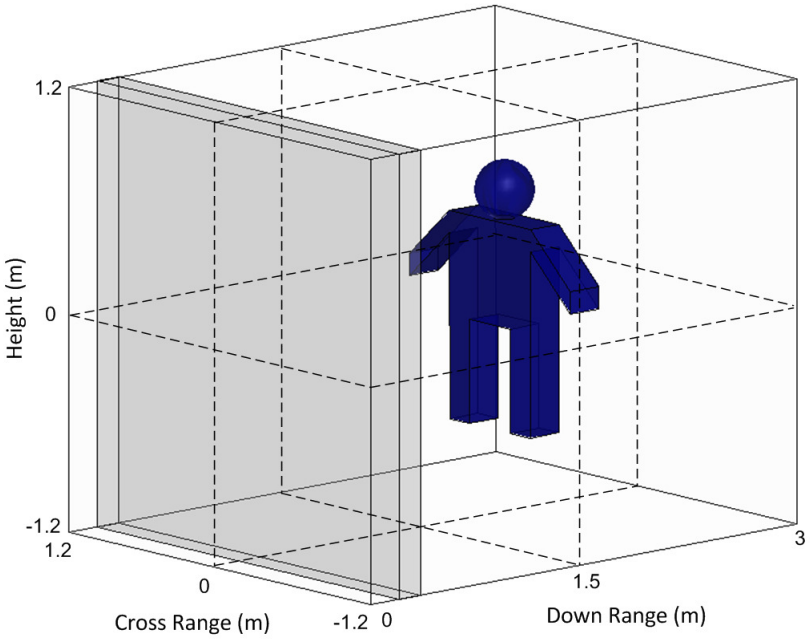
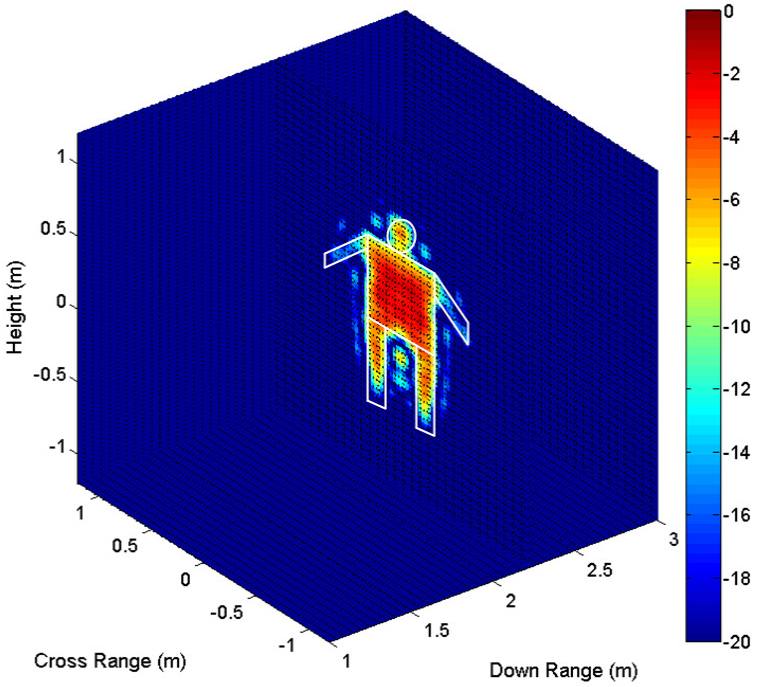
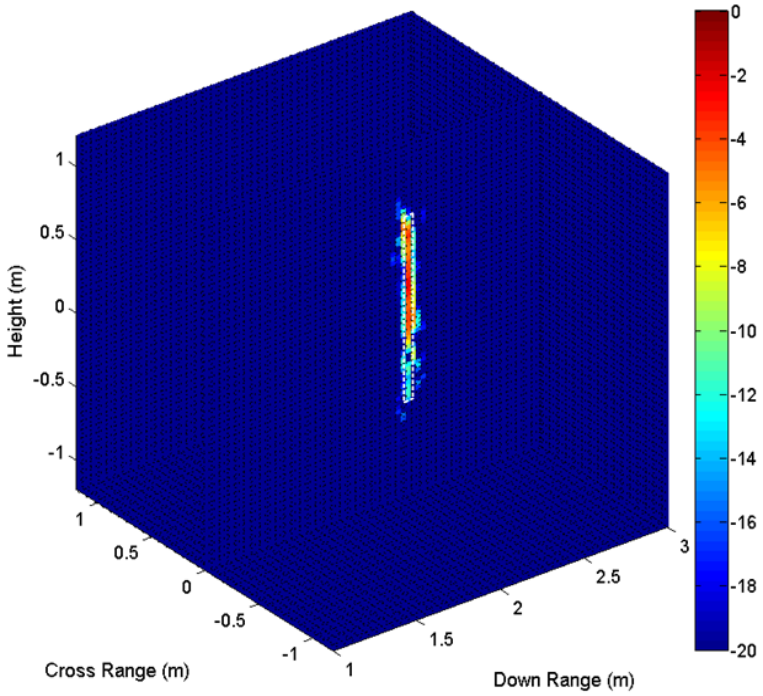


Figure 3.16 A human phantom target used in the simulation.

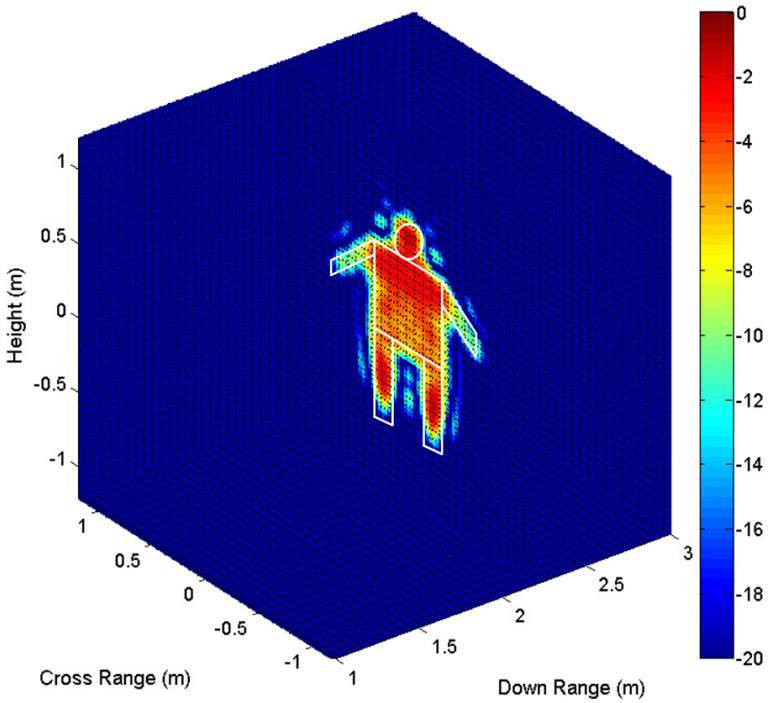


(a) Target shape recognition

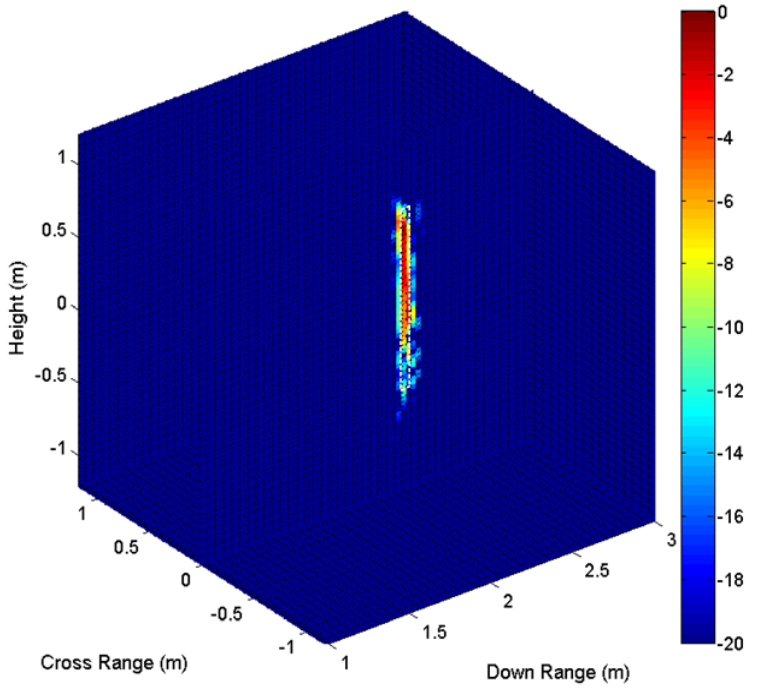


(b) Target Down range localization

Figure 3.17 Simulation results of a human phantom target using a 300ps Gaussian pulse signal source. Solid white lines indicate the true target shape while dotted white lines indicate the true target position.

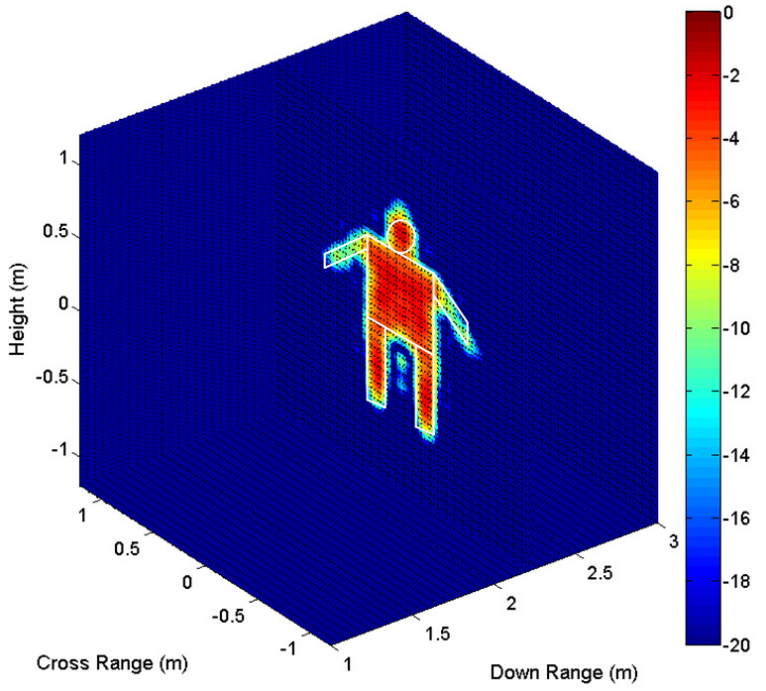


(a) Target shape recognition

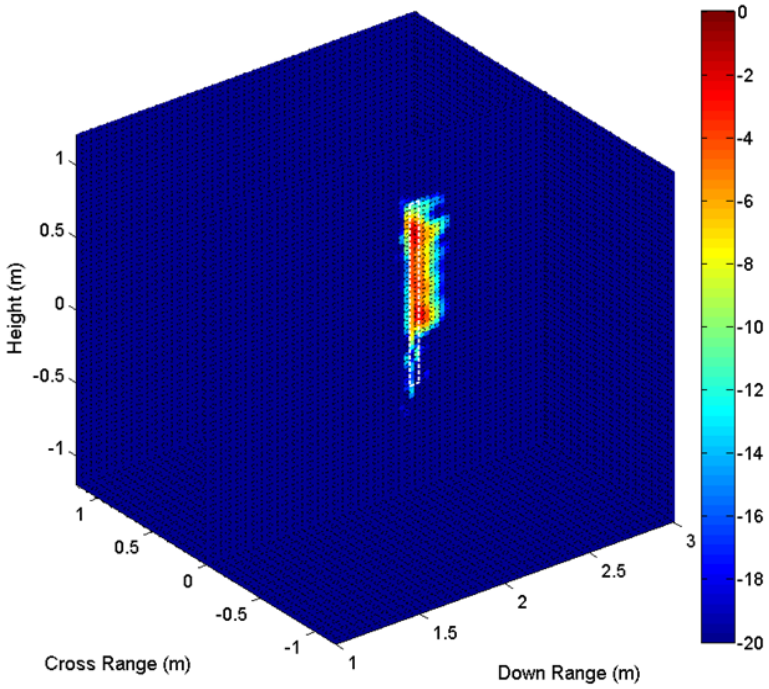


(b) Target Down range localization

Figure 3.18 Simulation results of a human phantom target using a 300ps monocycle pulse signal source (1st derivative of Gaussian pulse). Solid white lines indicate the true target shape while dotted white lines indicate the true target position.



(a) Target shape recognition



(b) Target Down range localization

Figure 3.19 Simulation results of a human phantom target using a 1ns incident Gaussian pulse signal. Solid white lines indicate the true target shape while dotted white lines indicate the true target position.

3.3.2 System Performance Prediction

The simulation platform is also a powerful tool to predict the SNR at the receiver side and system detection range when seeing through various wall materials. The radar system is set to operate at 2-6 GHz, with a carrier frequency of 4 GHz. The human phantom target, as shown in Figure 3.16, is used as the radar object, which has a RCS of approximately 1 m^2.

Figure 3.20 shows the simulated SNR of the received pulse signal versus the target distance for a 6-inch dry-wall and a 6- inch brick-wall respectively. Comparing the two plots, it is shown that the signal through the brick-wall has a 4 dB lower SNR than that through the dry-wall. It has been proven in [51] that a 6dB SNR renders a 5cm imaging resolution. The simulated results predict a system detection range of approximately 14m through a 6-inch dry-wall while 10m through a brick-wall, with a received signal SNR above 6dB, which are consistent with our experimental results.

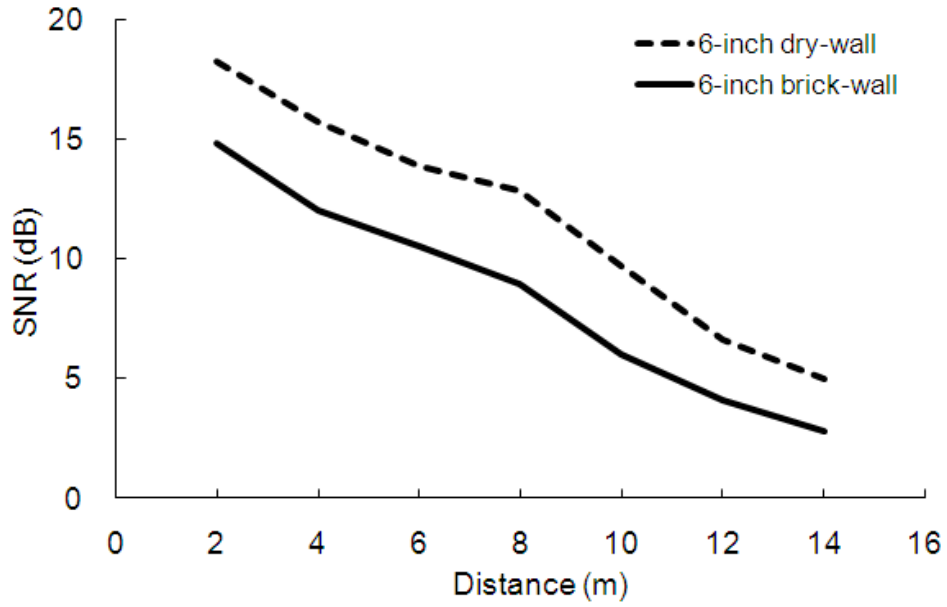


Figure 3.20 Simulated SNR of received pulse signal versus target distance when seeing through a 6-inch drywall and a 6-inch brick-wall respectively.

3.4 Conclusion

A comprehensive system level simulation platform has been developed using time-domain approach which can be used to optimize the design and predict the performance of the UWB pulse radars. Where, Agilent ADS Ptolemy simulation tools have been used to simulate the various RF, analog and digital devices, and through-wall effects and 3-D radar objects scattering have been modeled based on electromagnetic simulations. We are still missing the channel modeling as at this time as there are no available indoor/outdoor UWB channel models. Our simulator, however, can be easily extended upon the availability of such statistical channel model for the indoor/outdoor environment in through wall scenarios. A Backprojection microwave imaging algorithm has been applied for 3-D image recovery of radar objects. By integrating these functions in one platform, we have accounted for all the interface problems among different models and made it simpler to use. The simulation platform has been experimentally validated for dielectric objects using the developed UWB radar prototype. It is advantageous that system level simulation is included in the early stages of new UWB radar systems design for rapid prototyping and performance optimization. The developed simulation platform is also a powerful tool to predict the SNR at receiver side and system detection range when seeing through various wall materials.

Conclusions:

1) UWB pulse radar simulation requires a time domain solver to account for pulse dispersion, delay, and attenuation. The time domain solver includes combined Ptolemy and transient simulation for active/passive devices and frequency domain analysis combined with Fourier transform.
2) The antenna is placed in the far field to avoid solving complex near field problems. In the far field, electromagnetic propagation is assumed to be plane waves. This assumption is crucial in our subsequent analysis.
3) Walls are assumed to be infinite to simplify transmission and reflection calculations using a stratified media. TE or TM modes are assumed and no

coupling between the modes was assumed. Additionally, the walls are homogeneous with known parameters and physical dimensions. In real scenarios, most likely the wall characteristics are not known.

4) Accurate statistic channel models are still not available for UWB through wall applications and are eagerly desired to include indoor/outdoor mixed environment and wall interference in the system level simulation platform.
5) MoM is used to calculate the scattering from radar targets. No multiple reflections were assumed for calculating such scattering.
6) The tool can be used to search for the best transmitted signal shape that should be utilized for a certain radar target. In our case we found out that a 300ps monocycle pulse tends to give slightly better image quality than using a 300ps Gaussian pulse, when imaging a human phantom object.
7) The tool can also be used to predict the performance of UWB pulse radar, such as image resolution, detection range, received signal SNR, and etc.

Chapter 4

UWB Pulse Radar for Imaging Applications

UWB pulse radar sends out a series of short RF pulses and then listens to the echoes. By measuring how long it takes to receive the echo returns, system operators can estimate the range to the target/scatter. The angle of the incoming signal returns can be acquired by using a receiving antenna with a very narrow beamwidth, or utilizing a synthetic aperture array, to sweep the surveillance area, thus to predict the cross range of the radar object. Based on range and cross range information a full image can be recovered.

In this chapter, we will introduce three different imaging examples based on UWB pulse radar technology that spans a wide range of requirements: a) real-time through wall human tracking, b) 3-D human imaging, and c) early breast cancer detection. In the 1st application example, we will use the developed UWB pulse radar prototype to track more than one human object through the wall in *real-time*. In the 2nd example, we will introduce how to recover the 3-D image of a human mock-up object, providing both location and shape of the radar object. In the 3rd example, we will demonstrate how UWB pulse radar can be used for detecting very small cancerous breast tissues at early stage.

4.1 Real-time Through Wall Human Tracking

Real-time through wall human tracking has diverse applications, such as security surveillance, survivor rescuing, law enforcement, and etc. Real-time human tracking is achieved by successively recovering and displaying the image of radar targets at a high refresh rate. A calculation efficient microwave beamforming algorithm, Backprojection, was utilized in our system for real-time human tracking. The wall effect, i.e., wall attenuation and slower traveling speed inside the wall, was also accounted for in the imaging reconstruction. Experiments have been performed to demonstrate the capability

of UWB pulse radar for through wall imaging of multiple stationary and dynamic targets and two examples will be discussed in detail in the following sections.

4.1.1 Microwave Beamforming Algorithm

When recovering radar images, each image is composed of many pixels, or picture elements. Each pixel (picture element) in the radar image represents the radar backscatter for that area on the ground: darker areas in the image represent low backscatter, brighter areas represent high backscatter. Bright features mean that a large fraction of the radar energy was reflected back to the radar, while dark features imply that very little energy was reflected.

In the literature, there are a number of publications related to microwave imaging algorithms, such as Backprojection, Direct Frequency Domain Image Formation, The ω–κ Algorithm, Capon Beamformer, and Adaptive Capon Beamformer, etc. Table 4.1 compares the computational efficiency between algorithms by solving one specific example to simplify comparison [78]. The detailed information of how to calculate the total number of operations can be found in [78], which shows that Backprojection algorithm is the most efficient one for through wall radar imaging.

Table 4.1 Computational Efficiency Comparison of Various Imaging Algorithms

Algorithms	**Total number of floating-point operations**
Backprojection	2.2 M FLOP
Direct Frequency Domain Image Formation	14.2 M FLOP
The ω–κ Algorithm	5.9 M FLOP
Capon Beamformer	14 G FLOP
Adaptive Capon Beamformer (B-HDI Algorithm)	2.6 M FLOP

The simplified synthetic beam-forming structure is shown in Figure 4.1. The reflected signal from the target is assumed to be a plane wave to simplify the calculation and implementation. The following illustrated method makes it simpler and faster to recover the image of radar objects.

Let $z_i(n)$ be the complex received signal from antenna i, given by

$$z_i(n) = a_i(n) + b_i(n) \tag{4-1}$$

where a_i and b_i are the in-phase and quadrature components of the received signal. The output $y(n)$ represents the intensity (brightness) of the picture pixel at the n^{th} range cell and direction θ and is given by the following relation

$$y_i(n) = \sum_{n=1}^{N} w_i z_i(n) e^{j\varphi_i} \tag{4-2}$$

where N is the total number of receiving antennas, w_i is the correction for different wall attenuations and propagation loss and was assumed constant because of the same signal incidence angle.

$$w_1 = w_2 = \cdots = w_N = 1 \tag{4-3}$$

The phase component φ_i is applied to compensate for the phase difference due to distinct traveling paths. If we assume $\varphi_i = 0$ and the antenna spacing is d, the phase shift for signals from other receiving antennas is gathered as follows to cancel the phase delay, or advance, due to the different traveling lengths

$$\varphi_n = -(n-1) \cdot \beta_0 d \sin\theta \quad (1 \le n \le N) \tag{4-4}$$

Focusing the beam in the direction θ implies that the summation of all received signals should produce a maximum value for that particular direction.

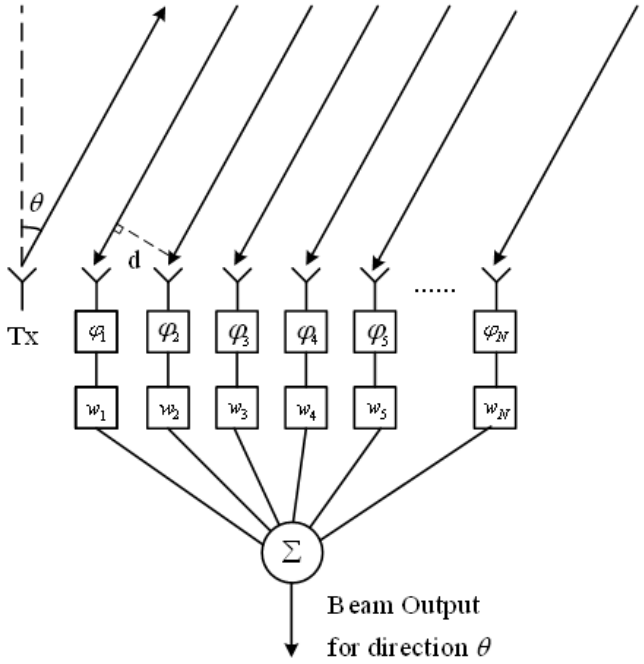


Figure 4.1 Simplified synthetic beam-forming algorithm.

The simplified synthetic beamformer is accurate when the target is far from the detection point, i.e., the target is at the far field. However, the assumption of the reflected plane wave is not completely accurate if the target exists at the near field. A near-field Backprojection microwave beamformer [79] is introduced in Figure 4.2. Instead of plane waves, the reflected signals from the scatterer are presumed to propagate from the scatter to the Rx antennas directly. With the near-filed beamformer, equation (4-2) will also be applied to produce the beam output. However, the magnitude correction coefficient w_i and the phase coefficient φ_i alter due to unequal propagation loss and travel lengths. The magnitude correction coefficient w_i due to different wall attenuation is given by

$$w_i = \frac{1-\Gamma_{0w}^2 e^{-j2k_w \cos\theta_2 t}}{\left(1-\Gamma_{0w}^2\right)e^{-jk_w \cos\theta_2 t}} \tag{4-5}$$

$$\Gamma_{0w} = \frac{\sqrt{\varepsilon_0}\cos\theta_1 - \sqrt{\varepsilon_w^*}\cos\theta_2}{\sqrt{\varepsilon_0}\cos\theta_1 + \sqrt{\varepsilon_w^*}\cos\theta_2} \tag{4-6}$$

where ε_w^* and t are the permittivity and thickness of wall, $k_w = 2\pi f\sqrt{\mu_0\varepsilon_w^*}$, θ_1 and θ_2 are the incidence angle and refraction angle, respectively. For phase compensation coefficient, if we still assume $\varphi_1 = 0$, then φ_n is achieved as follows

$$R_n = \sqrt{R_0^{\,2} + (n\cdot d)^2 - 2R_0(n\cdot d)\sin\theta} \quad (1 \le n \le N) \tag{4-7}$$

$$\varphi_n = \beta_0(R_n - R_1) \quad (1 \le n \le N) \tag{4-8}$$

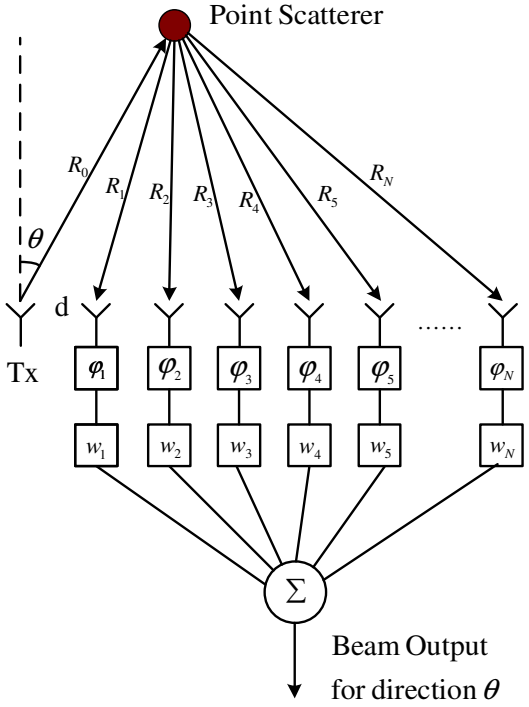


Figure 4.2 Near-field Backprojection microwave beamformer.

4.1.2 Through-Wall Effects

In a practical situation, the through-wall effects have to be accounted for in order to generate accurate images of the targets. The propagation wave slows down, encounters refraction, and is attenuated as it passes through the wall. If the wall effects are not

estimated accordingly, errors may occur in combining the post-data coherently. The through-wall model is presented in Figure 4.3. The surveillance space is divided into multiple pixels using range R and angle θ. The equivalent electrical length between the selected pixel and observation point is $L = L_1 + \sqrt{\varepsilon_r} L_2 + L_3$. The wall is assumed to be homogeneous and lossless, with a thickness t and a relative permittivity of ε_r. The detection radar has a standoff distance of d from the wall. Then, we can achieve incidence angle θ_1 and refraction angle θ_2 as follows

$$\sin\theta_1 = \sqrt{\varepsilon_r}\sin\theta_2 \tag{4-9}$$

$$(R\cos\theta - t - d)\tan\theta_1 + t\tan\theta_2 + d\tan\theta_1 = R\sin\theta \tag{4-10}$$

Next, the equivalent electrical length L is acquired by

$$\begin{aligned} L &= L_1 + \sqrt{\varepsilon_r} L_2 + L_3 \\ &= \frac{R\cos\theta - t - d}{\cos\theta_1} + \sqrt{\varepsilon_r}\frac{t}{\cos\theta_2} + \frac{d}{\cos\theta_1} \end{aligned} \tag{4-11}$$

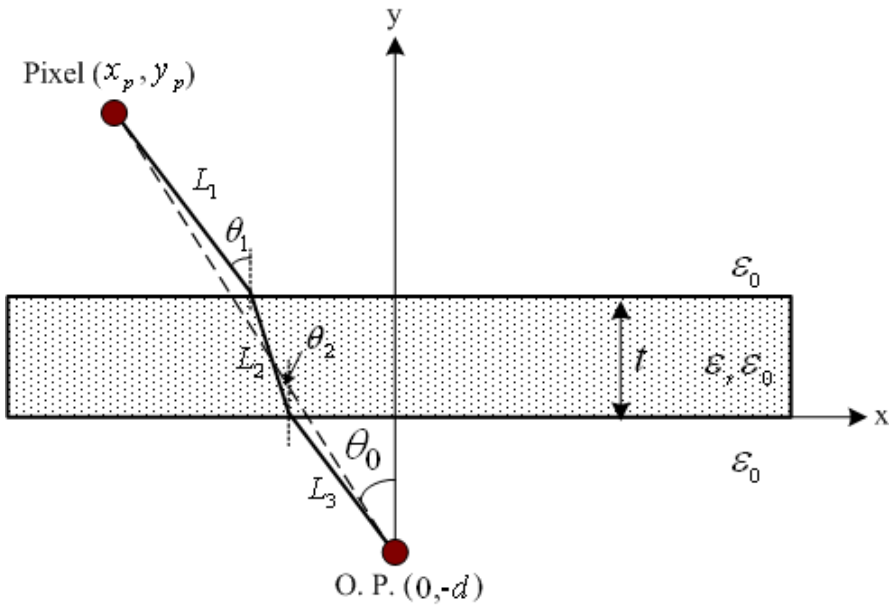
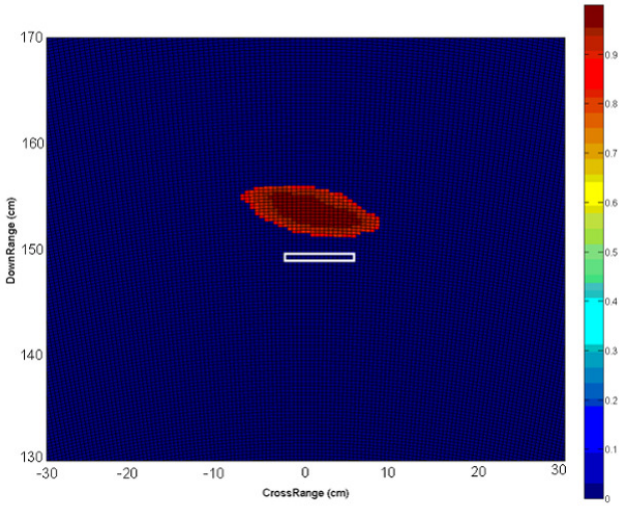
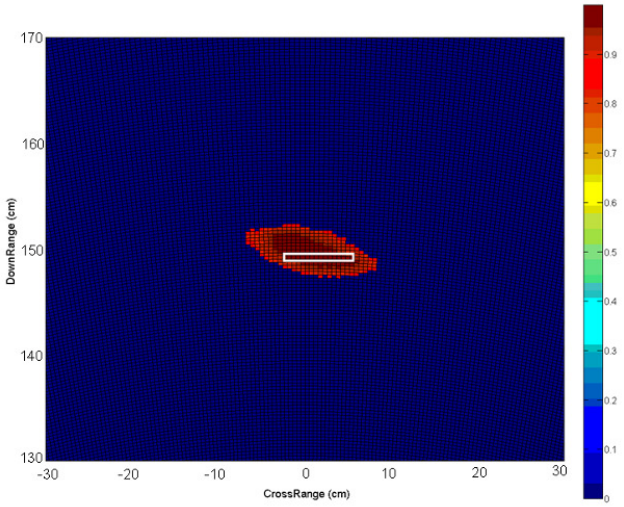


Figure 4.3 Through-wall model.

Figure 4.4(a) and (b) shows the recovered images of the target for two cases: before and after compensating for the wall effects. The drywall utilized in the experiment has a thickness of 4cm and a relative permittivity of 3.0. The real target position is defined in the pictures using a rectangular mark. Comparing Figure 4.4(a) and (b), the obtained target location is 4cm further from the detection point than its real position if the wall effect is not accounted for.



(a) Before compensation for wall effects



(b) After compensation for wall effects

Figure 4.4 Obtained radar images before and after compensation for wall effects. White rectangular marker shows the true target position.

4.1.3 Imaging Resolution

Two imaging resolutions will be considered here: range resolution (down range resolution) and azimuth resolution (cross range resolution).

For the radar to be able to distinguish two closely spaced elements in down range, their echoes must necessarily be received at different times. If using a narrower pulse signal, the radar system tends to achieve a better chance to separate two close objects in down range. For pulse imaging radar, the range resolution ΔR is given by [80]

$$\Delta R = \frac{c}{2B} = \frac{c\Delta t}{2} \tag{4-12}$$

where c is the speed of light, B is the bandwidth of the pulse signal, and Δt presents the width of the narrow pulse signal. The down range resolution can be calculated as 10.5 cm for the developed UWB pulse radar prototype, using the following parameters: $c = 3\times10^8$ m/s and $\Delta t = 700$ ps (700ps Gaussian pulse utilized in the system as shown in Figure 2.3). The down range resolution can be further improved by using a narrower pulse signal.

Experiments have been carried out to measure the down range resolution of the developed radar prototype, and then compare it with the theoretical results. The 1st experiment was performed by using a dihedral target, as the floor plan of the experimental setup presented in Figure 4.5. The radar prototype was placed in the corridor of the Engineering building, with the transmitting horn and receiving Vivaldi array facing the same direction. The spacing between the transmitting antenna and the closest receiving antenna is 50 cm. The dihedral was put at different standoff distances to the radar system to acquire the radar images.

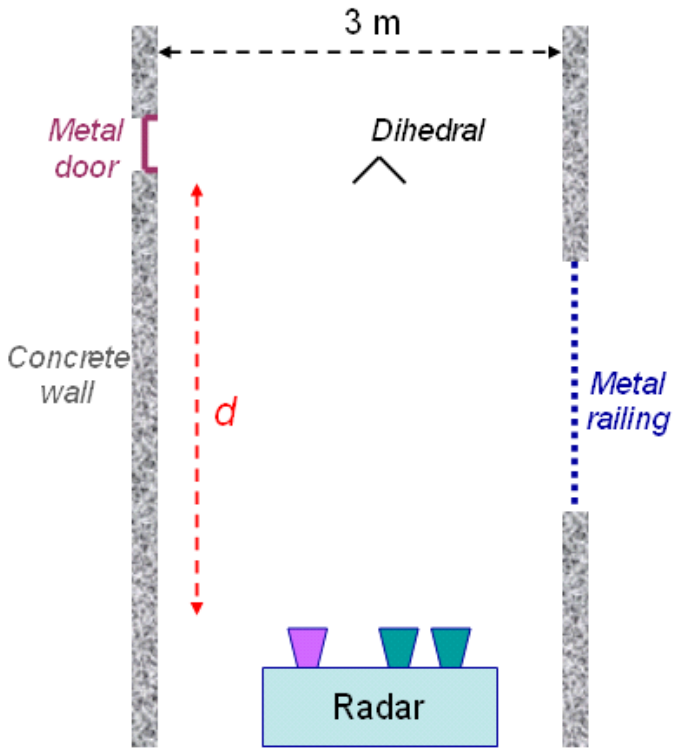
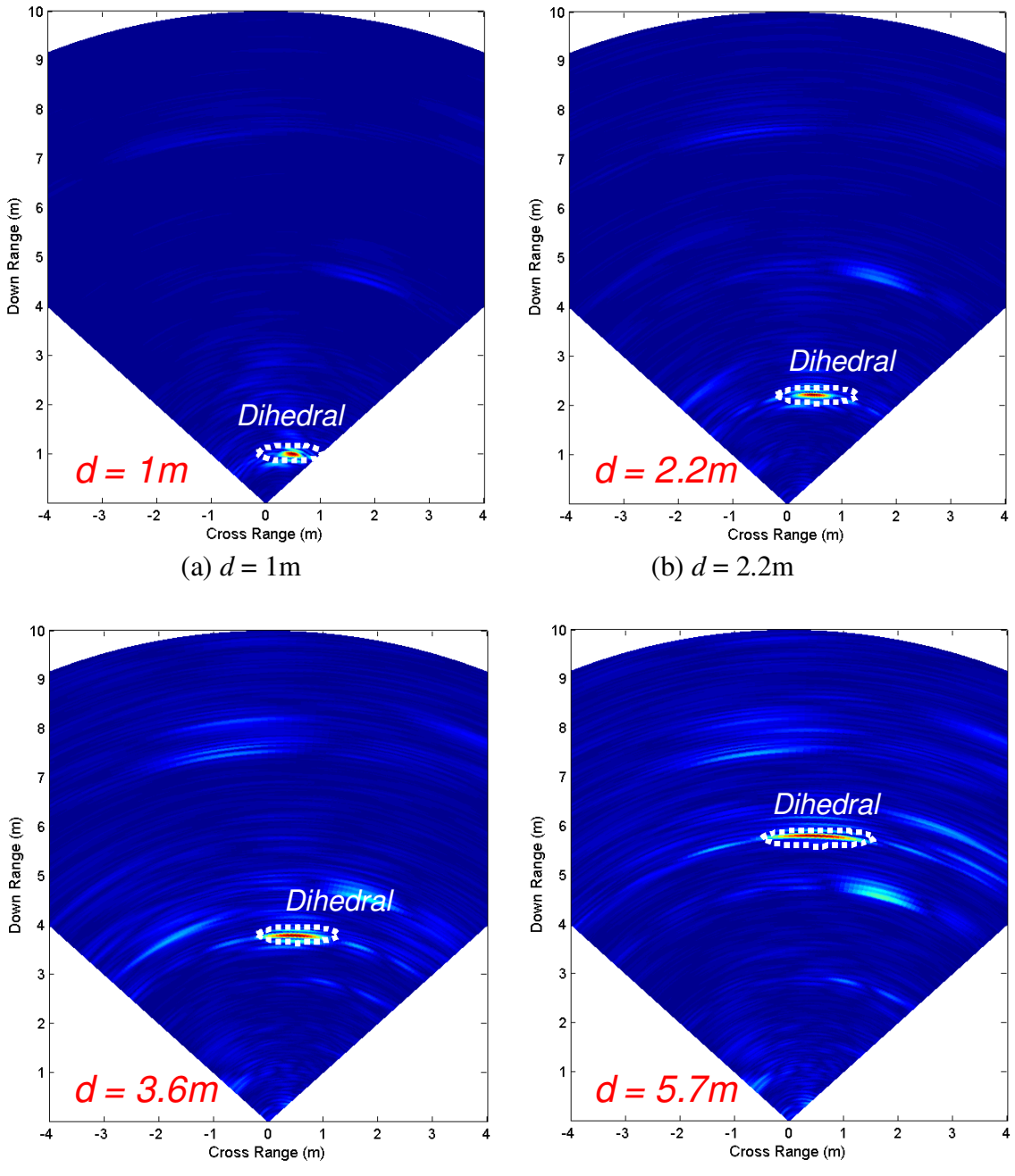


Figure 4.5 Experimental setup of the down range resolution measurement using dihedral as radar object.

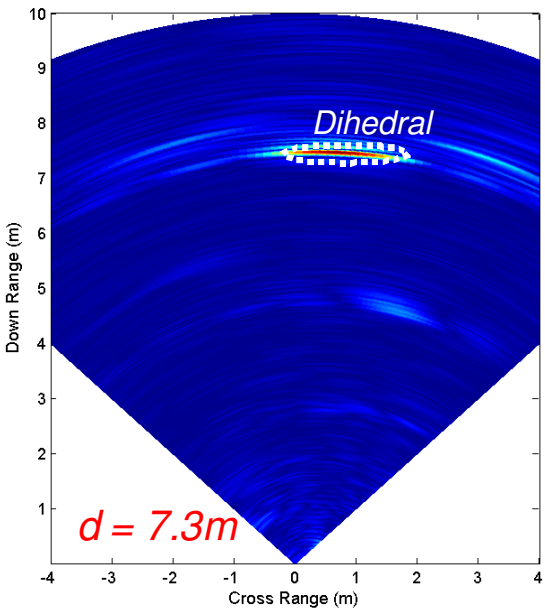
Figure 4.6 introduces the recovered images of the dihedral when it was placed at a distance of 1m, 2.2m, 3.6m, 5.7m, 7.3m, and 9.8m respectively. The acquired radar images indicate a down range resolution of approximately 10cm, validating the theoretical analysis result. It is worth mentioning that the recovered image also predicts the locations of the metal railing and metal door, in addition to the dihedral target.



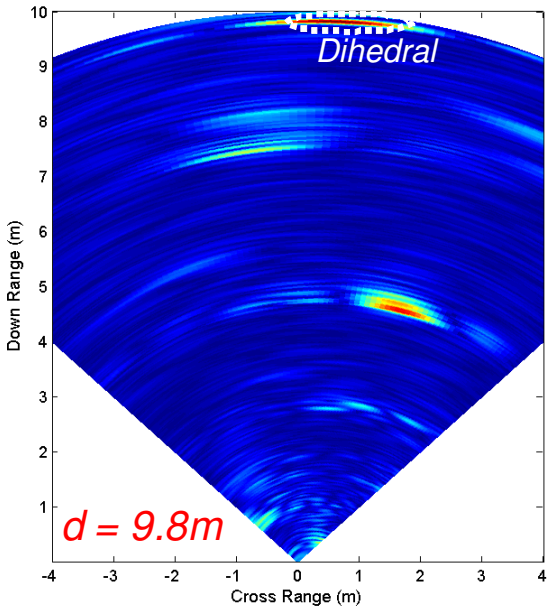
(a) d = 1m (b) d = 2.2m

(c) d = 3.6m (d) d = 5.7m

Figure 4.6 Acquired images of the dihedral target when placed at different distances to the radar system, also indicating the images of metal door and metal railing.



(e) d = 7.3m



(f) d = 9.8m

Figure 4.6 Continued.

Azimuth resolution, also called cross range resolution, describes the ability of an imaging radar to separate two closely spaced scatterers in the direction parallel to the motion vector of the sensor. Generally, several factors determine the cross range resolution of the imaging radar, including effective radar aperture, radar operation frequency, and the down range of the target. For the same down range, a better cross range resolution can be achieved if using a larger effective radar aperture or operating the radar at higher frequency range. For a real aperture radar, two targets in the azimuth or along-track resolution can be separated only if the distance between them is larger than the radar beamwidth. For the developed UWB pulse radar using SAR technique, the cross range resolution is a function of the effective aperture L and the wavelength λ, as shown below [80]

$$\Delta A_r = \frac{\lambda R}{L} \tag{4-13}$$

where ΔA_r is the cross range resolution, and R introduces the down range of the radar object.

An experiment was performed to test the cross range resolution of the developed radar prototype in the corridor, as the floor plan of the experimental setup shown in Figure 4.7. Two dihedral objects were used in the experiment, placed at the same distance to the radar, but at different cross range positions. A small metal can was put in front of the two dihedrals as a reference target. The two dihedrals were separated at a distance of *d*. During the experiment, we have kept increasing *d* until the two dihedrals can be distinguished in the recovered radar image. Figure 4.8 presents the recovered radar images when the two dihedrals were separated at different distances. As shown in Figure 4.8(a), the reflections of the two dihedrals overlap with each other in the recovered image, when they are put at a distance of 25cm. The image of the can was also observed in the recovered image. In addition, the recovered image also presents the locations of the metal door, metal railing, and the wall-railing junction. Next, we have moved the two dihedrals apart at a distance of 30cm, with the newly recovered image indicated in Figure 4.8(b), which has successfully separated the two dihedrals. The two dihedrals were further separated to a distance of 35cm, with the recovered image in Figure 4.8(c), which has presented the two images from the two dihedral objects.

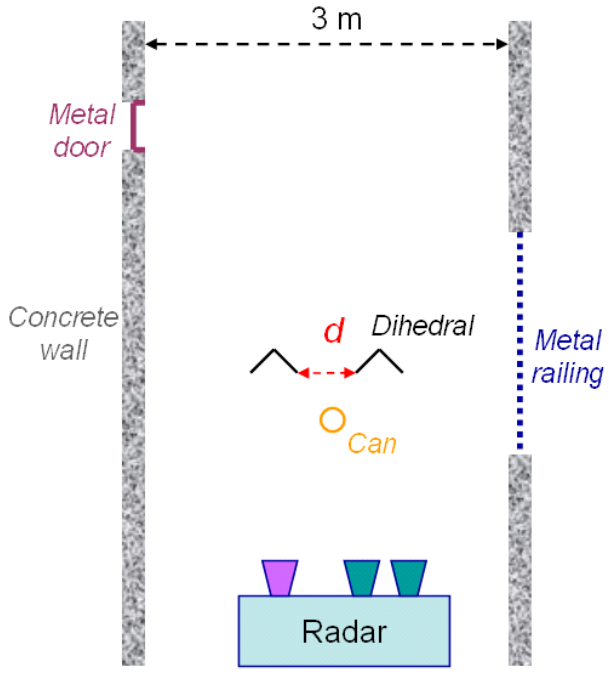
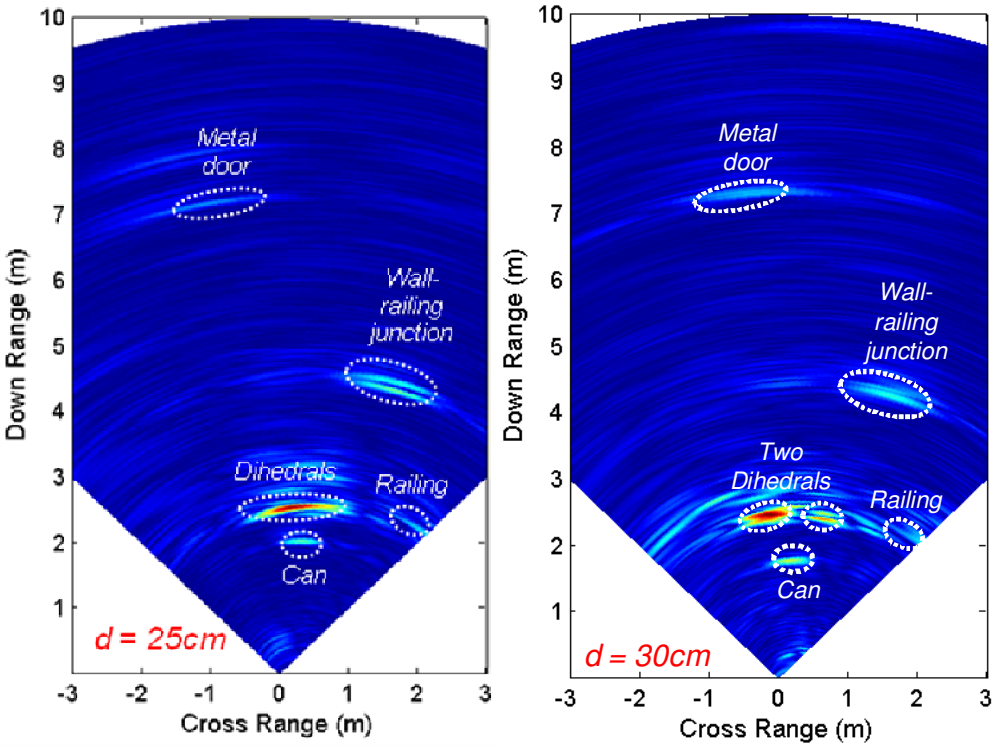
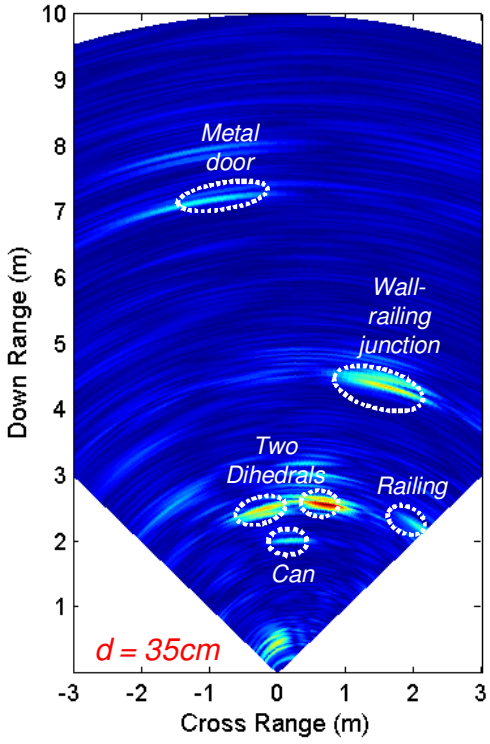


Figure 4.7 Experimental setup of the cross range resolution measurement using two dihedral objects.



(a) d = 25cm (b) d = 30cm



(c) d = 35cm

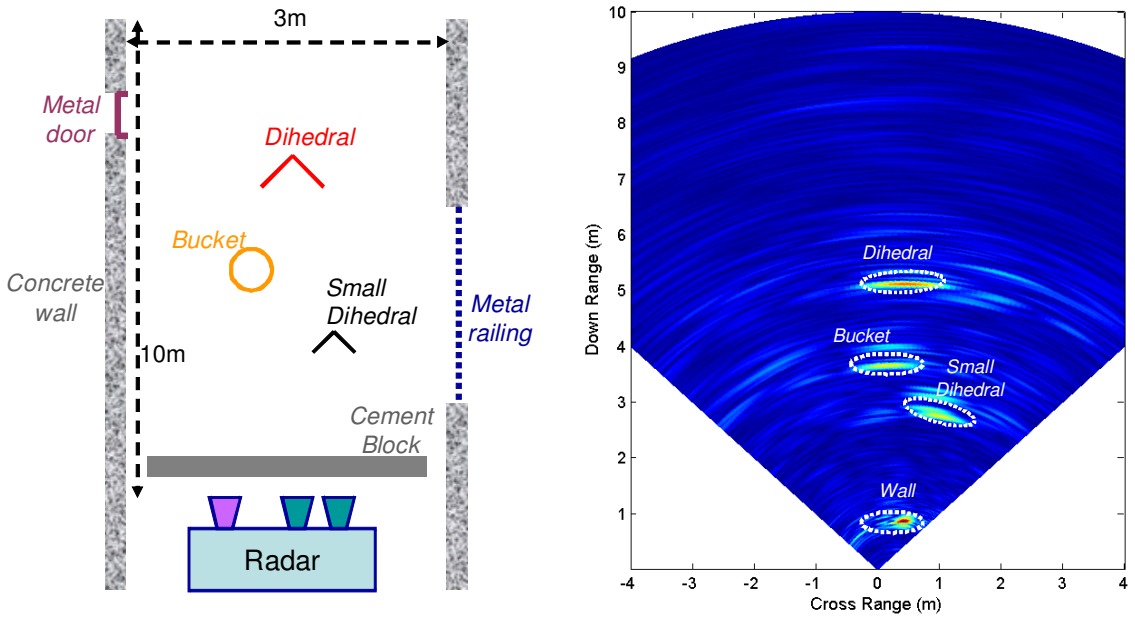
Figure 4.8 Recovered radar images when the two dihedrals are separated at different distances d.

4.1.4 Through Wall Imaging of Multiple Static Targets

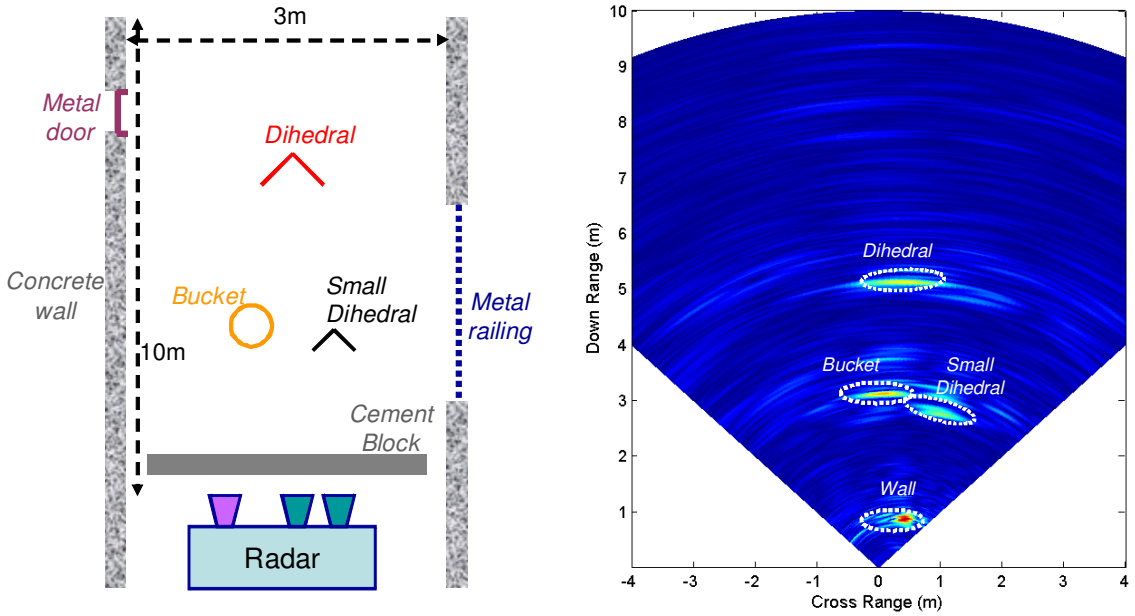
Experiments were performed to test the capability and performance of the developed UWB PD radar by investigating the radar image of multiple static objects. The experiment was setup at the corridor of engineering building to image multiple static targets through a cement block, as shown in Figure 4.9, where dihedral, bucket and small dihedral were used as the detection targets. The experimental result has accurately indicated the locations of the three targets, as well as the wall, as shown in Figure 4.10(a). To ensure that the images are from the exact targets as we expect, we have changed the scenario twice and then reconstructed the images again: the first time is to move the bucket closer to the radar, with the new recovered image shown in Figure 4.10(b); while the second time is to move the small dihedral closer to the radar, with the new acquired image introduced in Figure 4.10(c). The change of image has exactly reflected the change of target locations, validating the results.



Figure 4.9 Experiment setup of through wall imaging of multiple static objects using the developed radar.

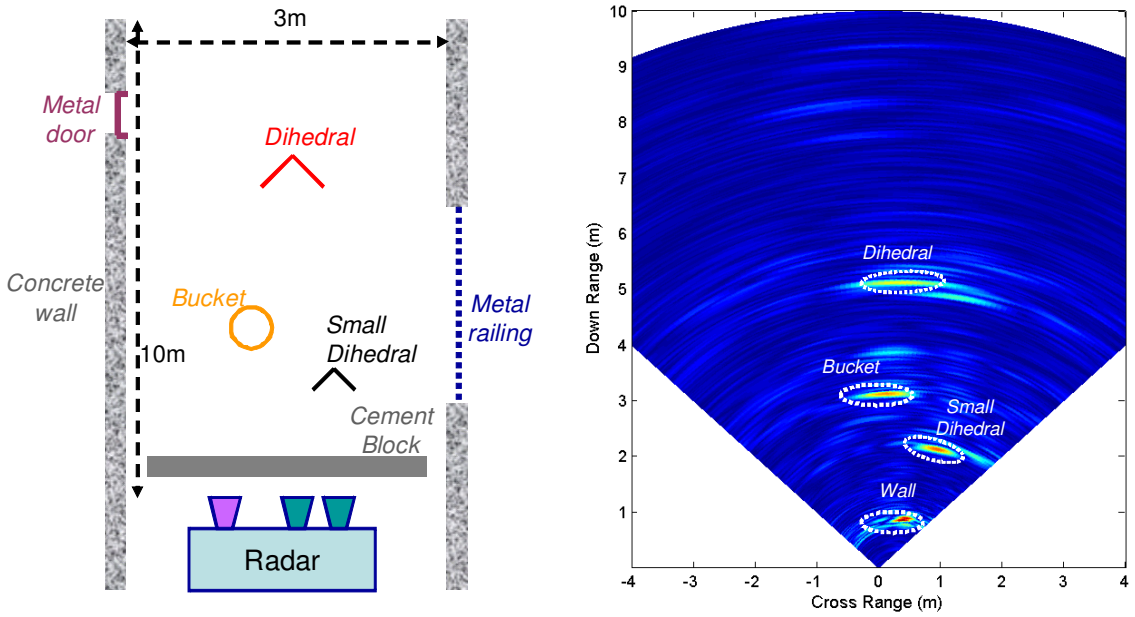


(a) Experimental setup and imaging result for initial scenario



(b) Move the bucket closer to the radar, keeping two dihedral targets at same position

Figure 4.10 Experimental imaging results of detecting multiple static targets through a cement wall.



(c) Move the small dihedral closer to the radar, keeping the other two fixed

Figure 4.10 Continued.

4.1.5 Real-time Tracking of a Walking Person

As discussed in Chapter 2, the developed radar prototype has a system refresh rate of 360 Hz if utilizing a sampling interval of 50 ps in the signal digitization. This fast refresh rate feature allows the real-time tracking of the moving target. An experiment was performed in the living room of an apartment to track and monitor a person walking counter clockwise in a LOS scenario. The living room has a size of 4m by 4m, with the radar sensor setup at the edge of the room in order to monitor the entire region. The walking trajectory of the person detected by the radar sensor has accurately predicted the true real-time target position, as shown in Figure 4.11, with the radar tracking result marked at every second.

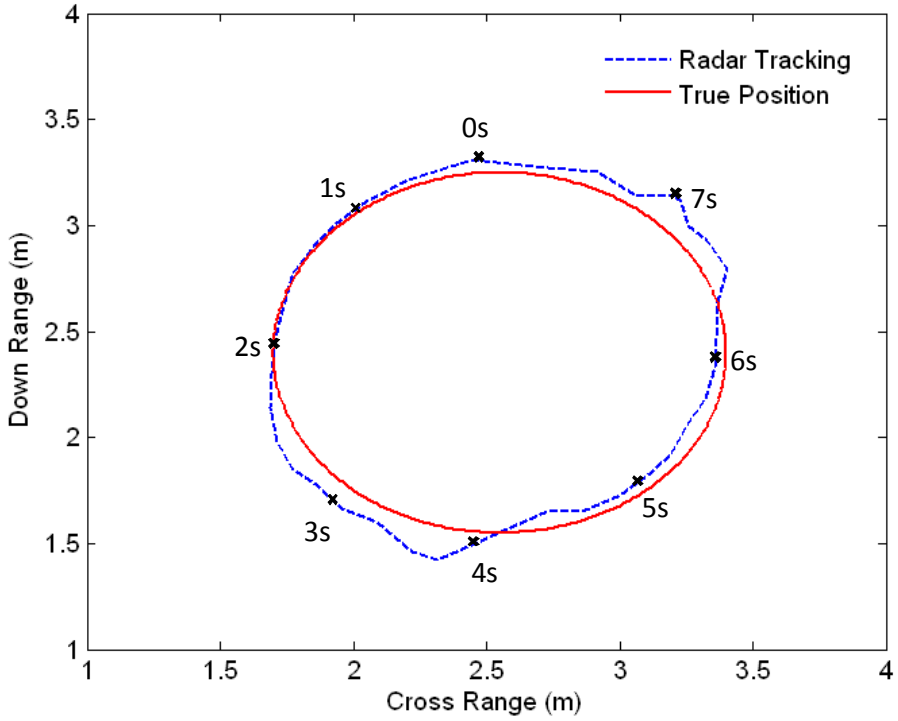


Figure 4.11 Real-time location tracking of single walking person in a LOS scenario.

4.1.6 Real-time Through Wall Tracking of Two Walking Persons

Two experiments were performed in the corridor of College of Engineering building to track two walking persons through a cement block, which has a thickness of 1cm. In the 1st experiment, the two persons walked in opposite directions, one approaching the radar while the other leaving the radar sensor. Figure 4.12 shows the real-time locations of the two moving persons at different time steps. As we introduced in Table 2.5, the developed radar prototype achieves a system refresh rate of 75 Hz. Therefore, 75 photo shots of the radar objects can be captured at every second. In Figure 4.12, the red mark shows the image of the 1st person while the pink mark indicated the image of the 2nd person. At 4.1sec, the 1st person was at a down range of 8m while the 2nd person at 4m. Next, the 1st person started to get closer to the radar while the 2nd person got further, as shown at 5s and 6s. The two persons met at 7.1s, with a down range of 6m. Next, the 1st person continued to walk toward the radar while the 2nd person walked further from the sensor, as presented at 8.1s, 9.1s, 9.8s, and 11.1s.

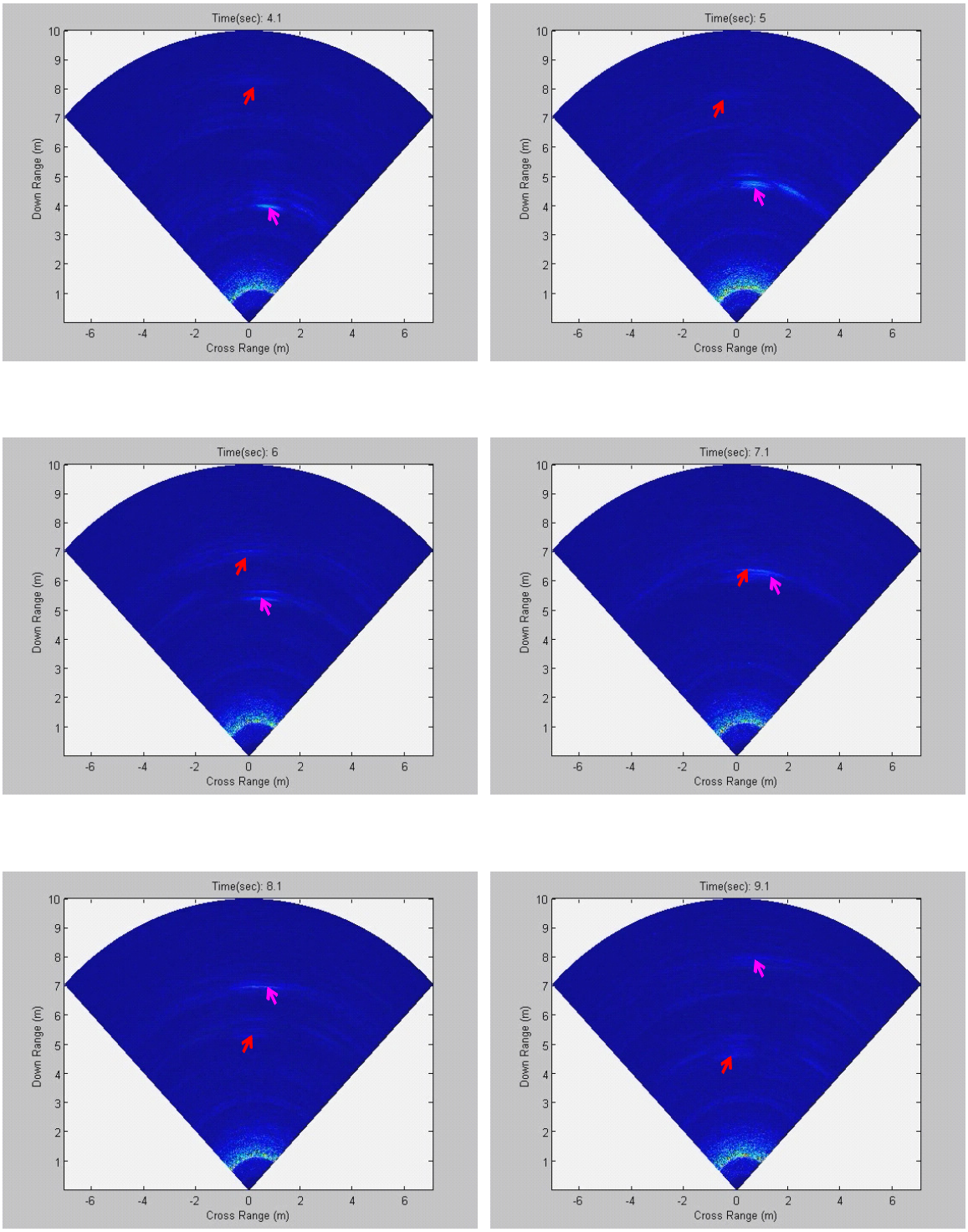


Figure 4.12 Real-time tracking of two walking persons through a cement block, two objects walking toward opposite directions.

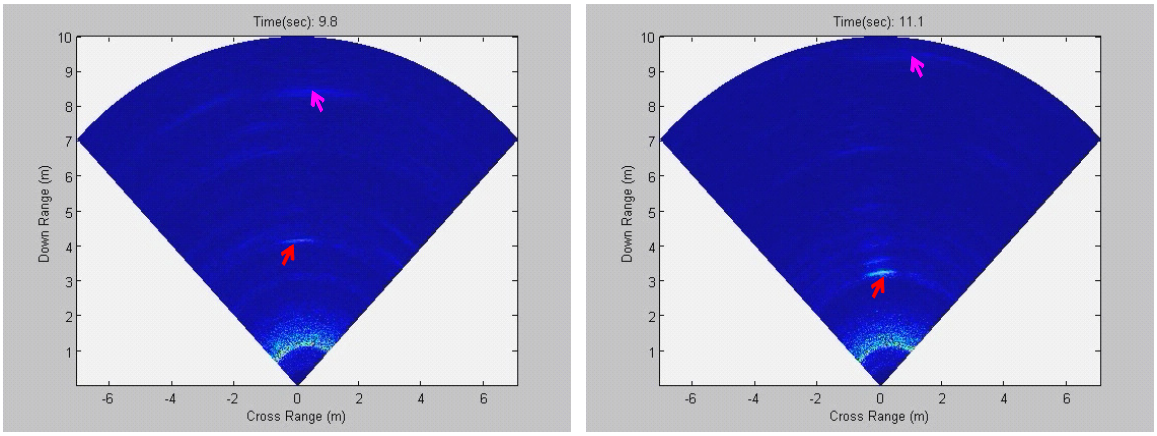


Figure 4.12 Continued.

The 2nd experiment was carried out to track two persons walking toward the same direction, but one walking faster while the other slower. The acquired locations of the two persons at different time steps are shown in Figure 4.13, where the red mark shows the image of the 1st person while the pink mark indicated the image of the 2nd person. The two persons started at the same distance of 10m at 0s. It can be seen from Figure 4.13 that the 2nd person walks much faster than the 1st person. At 4.2s, the 2nd person arrived at a down range of 6.5m while the 1st person was still 8.5m from the sensor. By 6.2s, the 2nd person already got to down range of 4.5m while the 1st person reached the down range of 7.5m. At 8.9s, the 2nd person walked close to the wall and started to walk back while the 1st person was still 5m from the sensor. By 12s, the two persons met at the down range 3.5m. For both experiments, the radar sensor has accurately tracked the real-time locations of the two walking persons, demonstrating the capability and performance of the developed UWB pulse radar prototype for real-time human tracking applications.

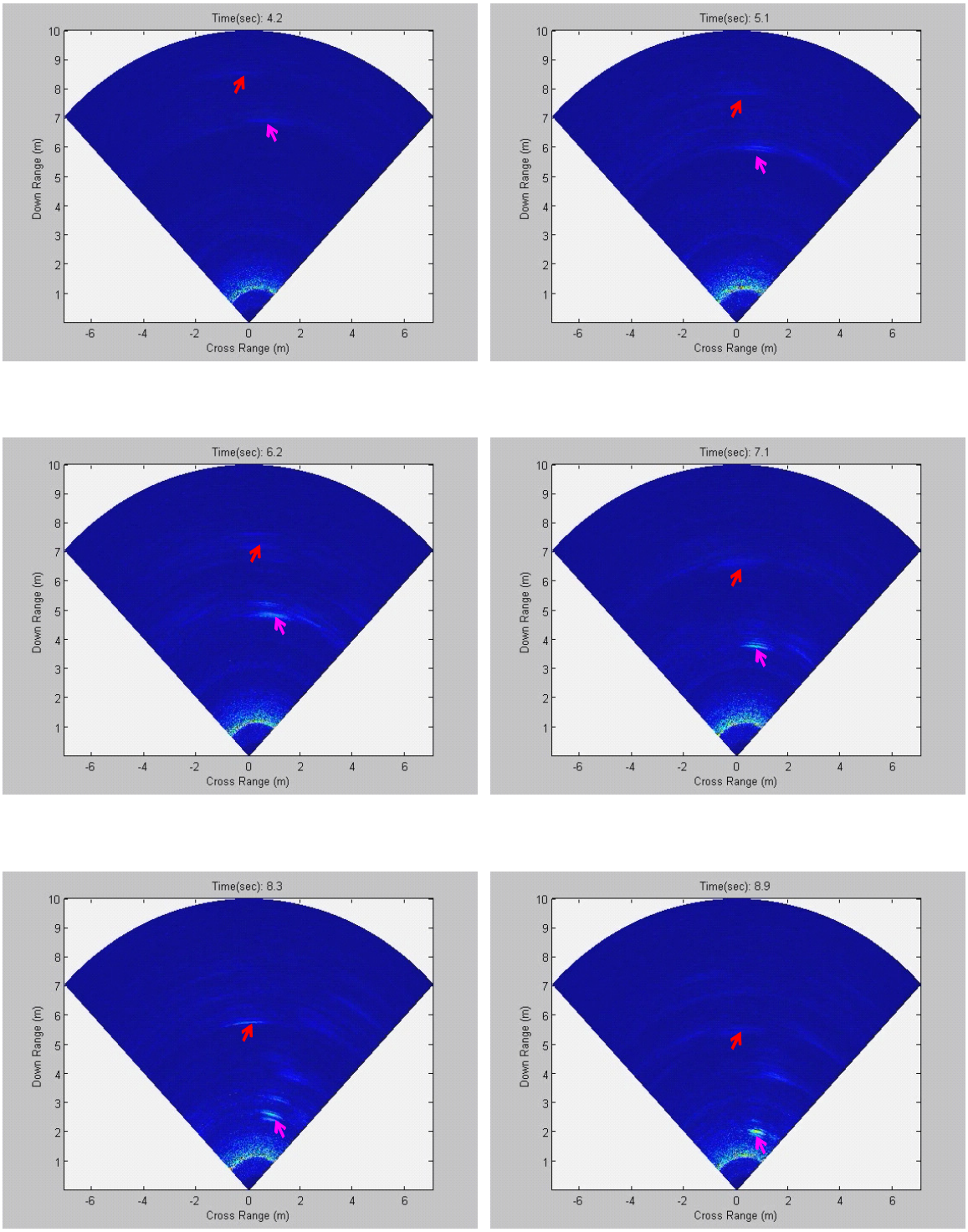


Figure 4.13 Real-time tracking of two walking persons through a cement block, two objects walking toward the same direction.

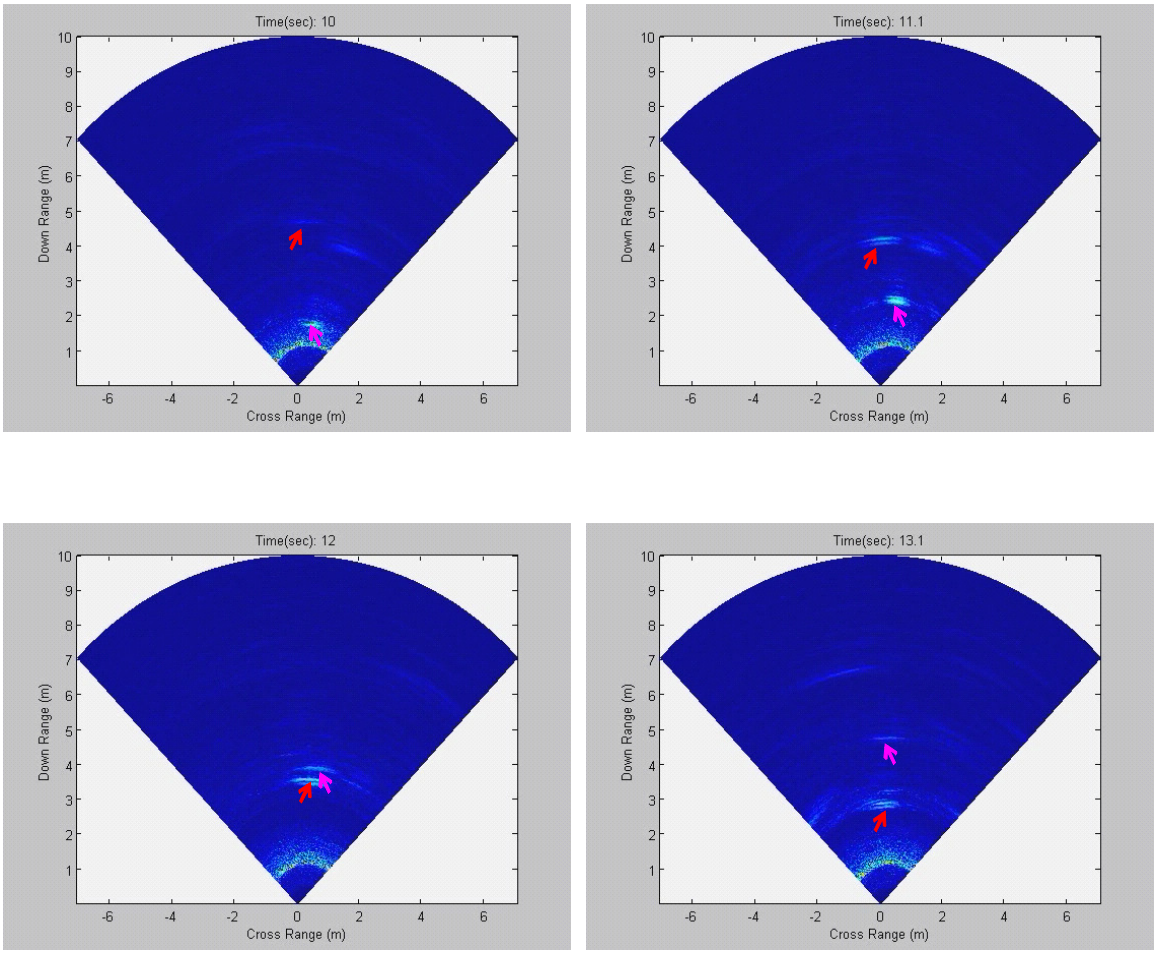


Figure 4.13 Continued.

4.2 3-D Human Imaging

As we discussed before, 2-D radar image is a powerful tool to predict the location, and even track the real-time location of the radar targets through the wall. However, 2-D radar images do not render any shape or outline information of the radar objects, which are quite important in some applications, such as target recognition. In this Section, we will extend 2-D radar imaging into 3-D radar imaging, which goes beyond targets' localization to their shape recognition.

4.2.1 3-D Microwave Beamformer

The three-dimensional radar imaging model is investigated, as shown in Figure 4.14. A two-dimensional planar array is required to obtain 3D images. The flow chart of the 3-D beamforming algorithm is shown in Figure 4.15. Consider a P-element planar transmitting array, located at $\{x_{tp}, y_{tp}, z_{tp}\}_{p=1}^{P}$, and a Q-element planar receiving array, located at $\{x_{rq}, y_{rq}, z_{rq}\}_{q=1}^{Q}$. Let $s_{p,q}(t)$ be the complex received baseband pulse signal. Since s is sampled in time, the sampled version of s is

$$s_{p,q}(n) = a_{p,q}(n) + jb_{p,q}(n) \tag{4-14}$$

where a and b are the in-phase and quadrature components of the received signal; p and q indicate that the signal is sent out by the pth transmitting antenna and acquired by the qth receiving antenna. A matched filter $h(n)$ is applied firstly to eliminate the out-of-band noise of the received baseband pulse, and the new signal is given by

$$z_{p,q}(n) = s_{p,q}(n) \otimes h(n) \tag{4-15}$$

where " $\otimes$ " denotes convolution operator; and $h(n)$ is the impulse response of the matched filter and its frequency response is given by

$$H(f) = \begin{cases} 1, & f \le f_{BW} \\ 0, & f > f_{BW} \end{cases} \tag{4-16}$$

where f_{BW} is the bandwidth of the received baseband pulse.

To recover the 3-D image, the surveillance space is divided into cubic voxels in x, y and z axis. $V_m = \{x_m, y_m, z_m\}$, the confocal microwave imaging algorithm is applied to calculate its absolute image value $I(V_m)$ via

$$I(V_m) = \left| \sum_{p=1}^{P} \sum_{q=1}^{Q} w_{p,q}(V_m) z_{p,q}(n_{p,q}) e^{j\varphi_{p,q}(V_m)} \right| \tag{4-17}$$

where the index $n_{p,q}$ of $z_{p,q}$ locates the signal at correct time delay; $\varphi_{p,q}(V_m)$ shows the phase compensation for different traveling paths; and $w_{p,q}(V_m)$ introduces the amplitude compensation for different scattering loss, through wall attenuation, and propagation loss, respectively. The value of index $n_{p,q}$ is given by

$$n_{p,q} = \frac{l_{pm} + l_{mq}}{c \cdot \Delta t} \tag{4-18}$$

where l_{pm} indicates the equivalent traveling path from the pth transmitting antenna to the voxel V_m; l_{mq} indicates the equivalent traveling path from the voxel V_m to the qth receiving antenna; c is the speed of light in the air; and Δt is the pulse sampling interval. Next, the DAS (delay and sum) is applied to the next voxel to obtain the related imaging information until all the voxels are finished. Lastly, a complete 3-D imaging is displayed.

In Chapter 3.1.6, we have introduced the theory on how to calculate the magnitude compensation coefficient $w_{m,n}(x,y,z)$ and phase compensation $\varphi_{m,n}(x,y,z)$ for a 3-D microwave beamformer. However, it is tedious and time-consuming to obtain the $w_{m,n}(x,y,z)$ and $\varphi_{m,n}(x,y,z)$ values for a 3-D structure, especially the calculation is repeated for M×N×K times, where M×N is the element number of Rx array and K is the total number of cubic voxels. In implementing the 3-D Bakcprojection beamforming algorithm, we have utilized an equivalent method and divided the problem into two: firstly, translate the 3-D geometry into 2-D geometry; and second, acquire the required values using the 2-D geometry.

In order to translate the 3-D geometry into a 2-D problem, the coordinate "translator" in [68] was employed to achieve the same height for the selected antenna and point target in the new coordinate and shown below. The yz plane rotates an angle β along the x axis to achieve a new coordinate system using x', y' and z'. The selected antenna and the selected voxel have the same z' value in the new coordinate. Hence, the calculation of this 3-D model becomes a 2-D calculation only in $x'y'$ plane. The rotation angle β can be calculated using [68]

$$\beta = \arctan \frac{z_v - z_a}{y_v - y_a} \tag{4-19}$$

Figure 4.16(a) depicts how the coordinate translator works. For a selected antenna at (x_a, y_a, z_a), it becomes (x_a', y_a', z_a') at the new coordinate after the rotation of angle β, where

$$\begin{aligned} x_a' &= x_a \cdot \cos\beta + y_a \cdot \sin\beta \\ y_a' &= -x_a \cdot \sin\beta + y_a \cdot \cos\beta \\ z_a' &= z_a \end{aligned} \tag{4-20}$$

Similarly, for the point target in the new coordinate

$$\begin{aligned} x_t' &= x_t \cdot \cos\beta + y_t \cdot \sin\beta \\ y_t' &= -x_t \cdot \sin\beta + y_t \cdot \cos\beta \\ z_t' &= z_t \end{aligned} \tag{4-21}$$

To obtain $y_a' = y_t'$, we get

$$\beta = \arctan\frac{y_t - y_a}{x_t - x_a} \tag{4-22}$$

The new coordinate, after the transformation, is shown in Figure 4.16(b). The selected antenna and point target in the new coordinate are at (x_a', z_a') and (x_t', z_t'), respectively. They also have the same height, i.e., $y_a' = y_t'$. Last, all available 2D electromagnetic methods can be applied to analyze this model. The wall effect, i.e., through wall attenuation and slower traveling speed inside wall, is also accounted for when solving the 2D problems.

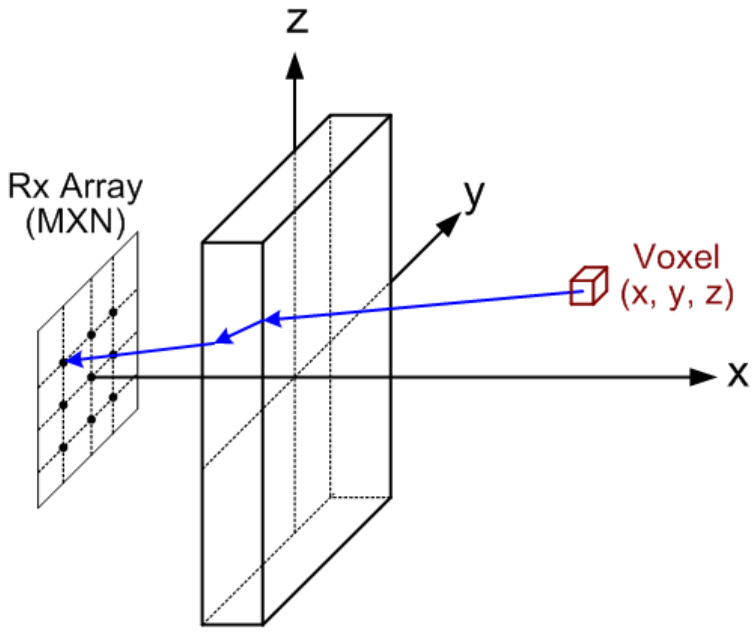


Figure 4.14 3-D microwave beamformer model.

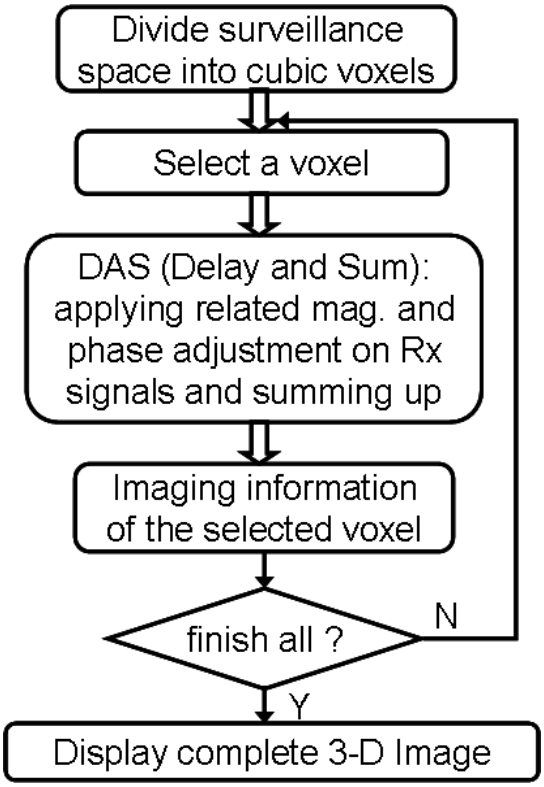
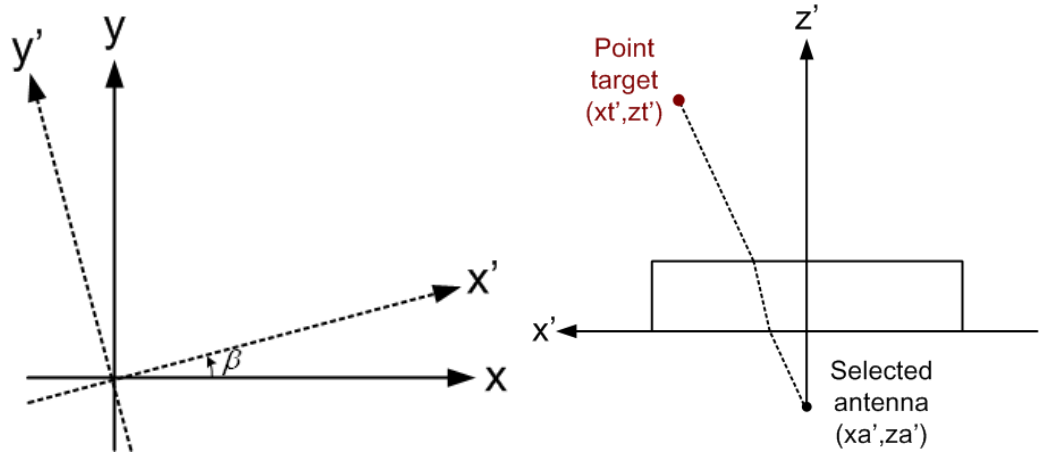


Figure 4.15 3-D beamformer flow chart.



(a) Coordinate transformer (b) The new coordinate (x', y', z')

Figure 4.16 Old coordinate (x, y, z) translates to a new one (x', y', z').

4.2.2 3-D Imaging of a Human Mock-up

A 3-D imaging experiment was performed to detect a human mock-up using the UWB radar system operating at 6-10 GHz in order to achieve a good azimuth resolution. A 300ps pulse generator was utilized in the system. Figure 4.17 indicates the locations of Tx array marked in red and Rx array marked in green. The grid has a spacing of λ_0 at its highest operating frequency in order to achieve the maximum aperture size and avoid the grating lobes. A low-loss drywall was utilized in the experiment. As approximately a 60% of the human body is comprised of water that has a very high dielectric constant of 81, therefore, a strong reflection is expected from the human body and it makes feasible to use a human mock-up model in the right top corner of Figure 4.17 to emulate a real human body. The target has a height of 1.4 m, a width of 0.6 m, and locates at a down range of 2.2 m.

In experimental setup, we have collected the signals at two scenarios: the first from background only before putting any target, and the second after placing the target. By subtracting the two signals (i.e. with and without the target), the newly acquired signals are used in the image recovery process to remove the clutters. We also used the comprehensive simulation platform described in Chapter 3 to simulate the experimental

scenario and acquired the simulated 3-D image of the human mock-up target. Similar clutters removal process was also applied in the simulation by subtracting the simulated signals with and without the target.

The simulation result in Figure 4.18(a) accurately predicts the outline of the human mock-up object, as well as the location. The recovered image from experiment agrees well with that from simulation, as shown in Figure 4.18(b). The obtained 3-D experimental image has a down range resolution of 5cm by using a 300ps pulse and a cross range resolution of approximately 15cm. Using a narrower pulse signal can further improve the down range resolution while increasing the number of detection points and the aperture size can further improve the cross range resolution. The 3-D imaging capability is indispensable for through-wall human beings detection, by distinguishing the human person from other objects successfully.

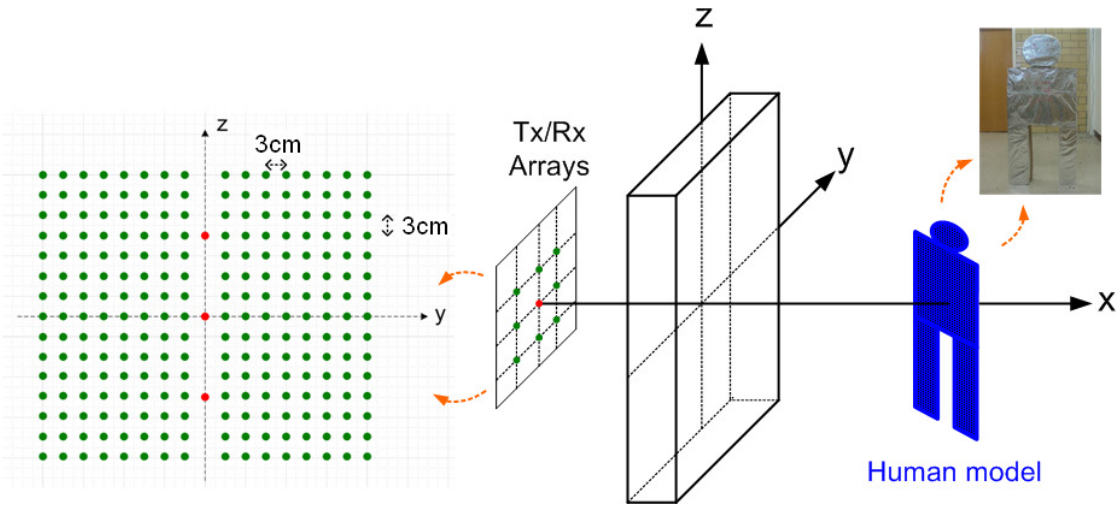
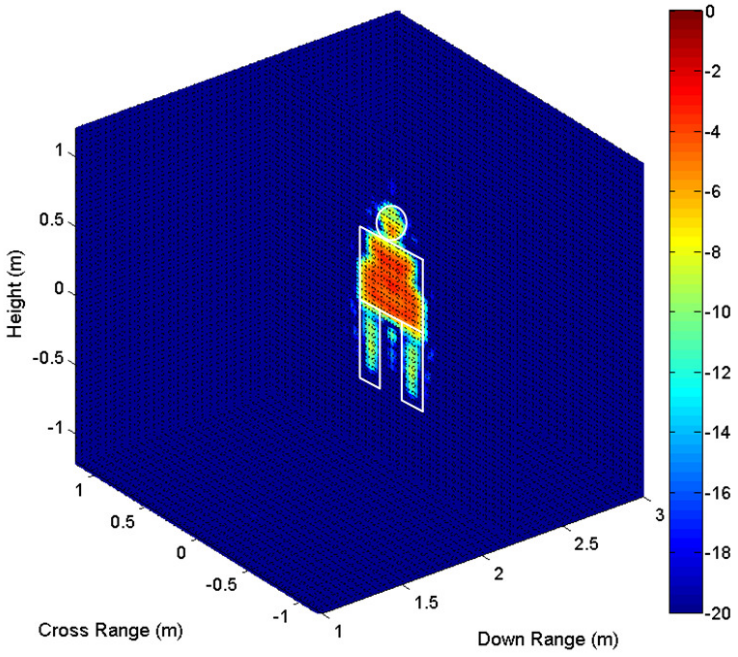
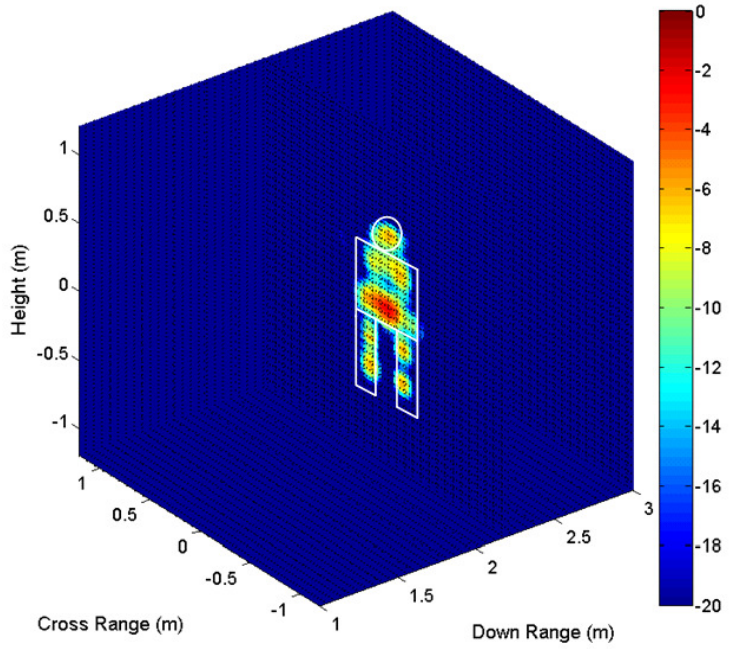


Figure 4.17 A human mock-up object used in 3-D imaging experiment.



(a) Simulation result of human mock-up model



(b) Experimental result

Figure 4.18 Recovered image results of a human mock-up object: (a) Simulation result of human mock-up model, and (b) Experimental result.

4.3 Early Breast Cancer Detection

In US, almost 1/8 of the women develop breast cancer. For example, 192,370 invasive and 62,280 noninvasive cases were diagnosed in US for 2009 alone. Currently, X-ray mammography remains the primary imaging method for detecting nonpalpable early-stage breast tumors but it looks like it is not that effective as people used to think. As, approximately 4%-34% of all breast cancers are missed by conventional mammography [81], while nearly 70% of all breast lesions identified by mammography turn out to be benign [82]. Furthermore, mammography leads to patient discomfort due to breast compression during the scans. These drawbacks of mammography motivate the search of other technologies for early breast cancer detection, one of which is microwave imaging. The principle of microwave imaging is to send out a signal at microwave frequency and then collect the signal scattering due to the significant dielectric constant difference between malignant tumors and normal breast tissue [83]. Compared to all other microwave imaging techniques [84], [85], UWB microwave radar is more competitive and has several inherent advantages for breast cancer detection, including very precise detection accuracy, deep penetration capability, and excellent performance in inhomogeneous and multi-layer structures.

In recent years, UWB microwave imaging systems have attracted a lot of attention for breast cancer detection [86]-[88]. Hagness [86] firstly presented the methodology and results of 3-D FDTD simulations of a pulsed microwave confocal system for breast cancer detection. Li [87] presented an experimental investigation of tumor detection in multilayer breast phantoms using space-time microwave beamforming algorithm. Recently, Klemm [88] introduced an experimental UWB microwave system for breast cancer detection based on VNA. However, all these systems mentioned above still work in the frequency domain and are based on the expensive, bulky VNA/PNA to acquire the experimental data.

Here, we will introduce how we can use our developed UWB pulse radar for early breast cancer detection based on time domain technique. A newly breast imaging system hardware has been developed to operate at 2 to 8 GHz to balance the competing

requirements for imaging resolution and penetration depth into the breast tissue. A compact, wideband microstrip slot antenna has been designed to achieve good performance when attached on the breast tissue. Numerical simulation and phantom experiment results will be discussed in details.

4.3.1 Breast Imaging System

The detailed block diagram of a newly developed breast cancer detection system is outlined in Figure 4.19. A driving clock generated by FPGA circuitry is used to drive a 300ps Gaussian pulse generator. The pulse signal is then modulated by a local oscillator (LO) signal through a Miteq DM0208 mixer. The modulated signal passes through a high gain amplifier and is then transmitted via a wideband microstrip slot antenna. At the Rx link, the wideband Rx antenna is used to acquire the signal, which is then amplified by a wideband LNA Hittite HMC753. Next, the signal is down-converted into both I and Q channels by mixing the same LO with the received signal. Then, the recovered I and Q data are low-pass filtered before being sent to the MAX104 ADCs for sampling using an equivalent-time sampling scheme. Next, all the sampling data are sent to a FPGA circuitry for storage. Lastly, the collected data is transferred to the computer through a USB2.0 cable and a DAS microwave imaging algorithm is applied to recover the image. The radar transceiver operates at 2-8 GHz to make a comprise between imaging resolution and penetration depth into the breast tissue.

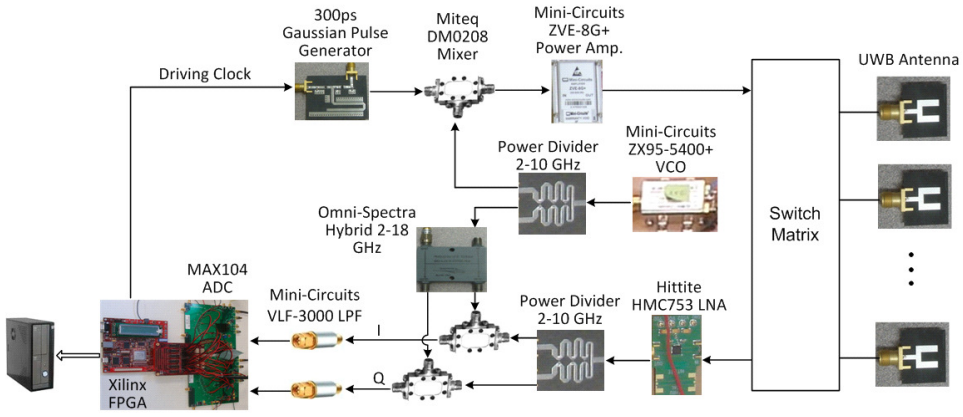


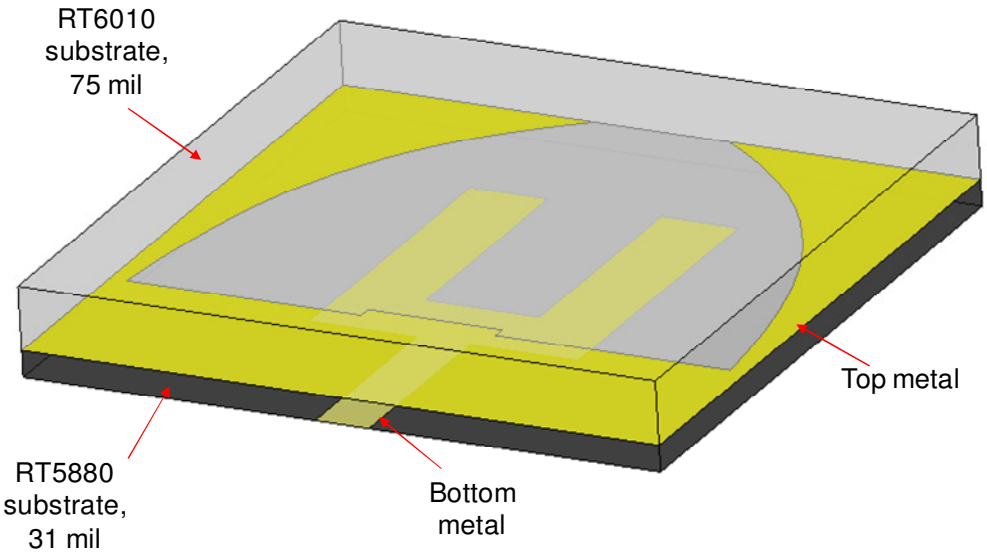
Figure 4.19 Detailed block diagram of the developed UWB microwave imaging system prototype at UT.

4.3.2 Breast Imaging Antenna Design

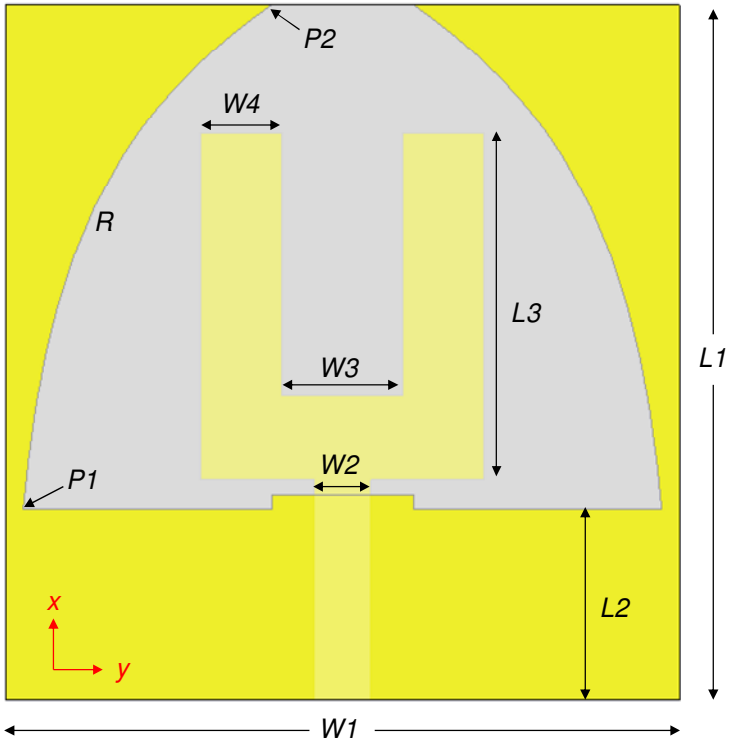
To design a good-performance antenna for microwave breast imaging applications, several requirements need to be satisfied, including wideband radiation, small size, directional radiation patterns, and good penetrating characteristics. In addition, the interaction between the antenna and breast tissue needs to be taken into account during the design stage.

Many efforts have been addressed to design compact wideband antennas for microwave breast imaging. For example, Yun et al. [89] presented a compact bowtie antenna operating at 2-4 GHz for radar-based breast cancer detection. Jafari et al. [90] designed a wideband monopole antenna fed by a 50-Ω coplanar waveguide working at 3.4-9.6 GHz for microwave near-field imaging. Huang et al. [91] introduced a compact dielectric resonator antenna for microwave breast imaging, achieving more than 40% bandwidth centered at 6.5 GHz. Gibbins et al. [92] designed and compared a wide rectangular slot antenna and a stacked patch antenna for the purpose of breast cancer detection, both operating at 4-10 GHz.

The geometry of the proposed wideband tapered microstrip slot antenna is shown in Figure 4.20. The antenna has two substrate layers, 75-mil thick Rogers RT/duroid 6010 on the top with a permittivity of 10.2 and loss tangent of 0.0023, and 31-mil thick Roger RT/duroid 5880 on the bottom with a permittivity of 2.2 and loss tangent of 0.0009, as indicated in Figure 4.20(a). The Rogers RT/duroid 6010 material has a similar permittivity as breast fatty tissue (i.e., ε_r = 9.0) [93] and functions as a buffer layer between the slot antenna and the breast to enhance the matching performance. The parameters of fork-shaped feeding structure and tapered microstrip slot have been optimized for compact size and wide bandwidth and are indicated in Figure 4.20(b).



(a) 3-D view



(b) Top view

Figure 4.20 Geometry of the proposed wideband tapered slot antenna after optimization. *W1* = 19mm, *W2* = 1.6mm, *W3* = 3.4mm, *W4* = 2.3mm, *L1* = 19mm, *L2* = 5.2mm, *L3* = 9.5mm, *R* = 2.0.

Figure 4.21 shows the simulation model of the proposed tapered slot antenna using commercial software Ansoft HFSS. It should be noted that the slot antenna is always attached on a large breast tissue model in the simulation to emulate the real operation environment and account for the interaction between the antenna and the breast tissue. The breast tissue model used in the simulation is assumed to be homogeneous, with a constant permittivity of 9.0 and conductivity of 0.4 S/m.

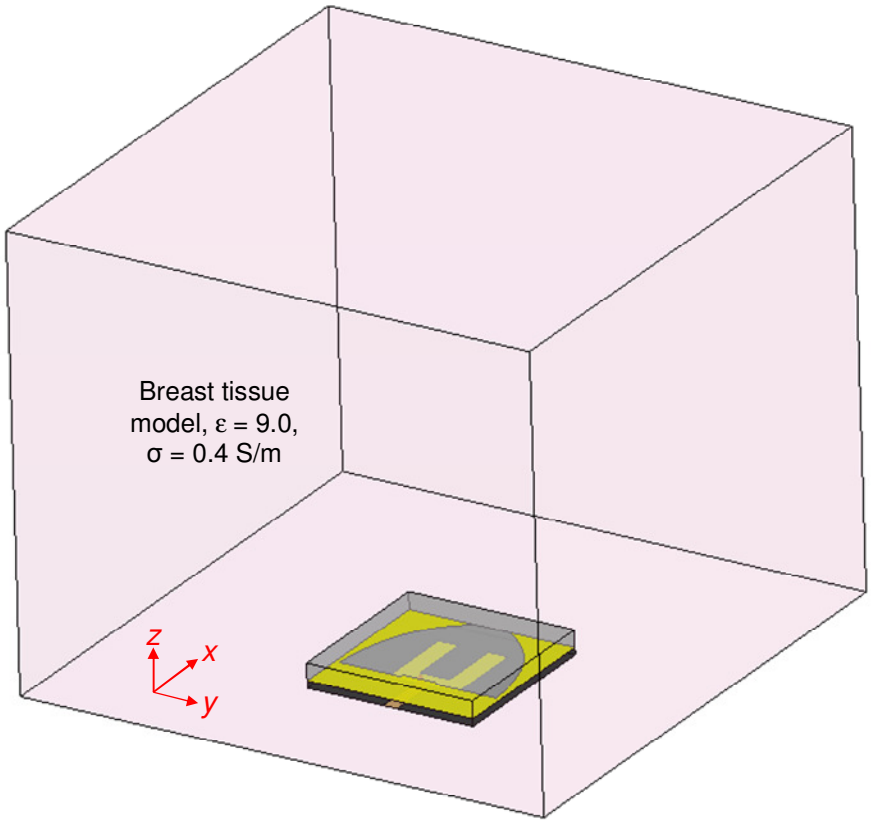
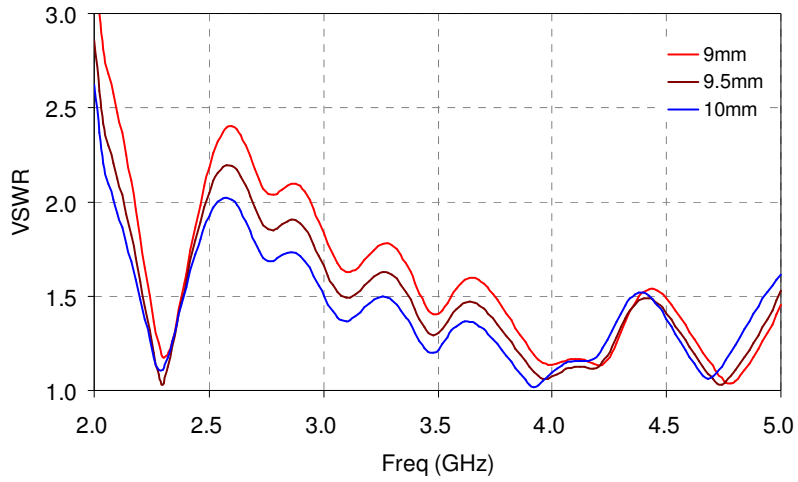


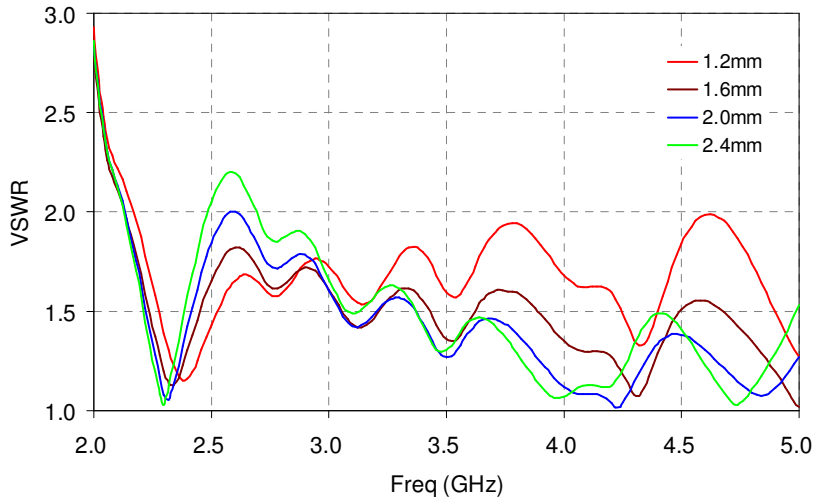
Figure 4.21 Simulation model of the proposed antenna in HFSS. The interaction between antenna and breast tissue is taken into account in the design.

Parametric studies are performed to analyze the effects of varying the antennas geometric parameters. The *VSWR* performance at lower frequency range is mainly determined by the slot structure (top metal) while the higher frequency range is primarily decided by the fork feeding structure (bottom metal). The parametric studies of the three most sensitive parameters are shown here, i.e., *L3, W2* and *R*. Figure 4.22(a) shows the *VSWR* results by varying the length of the fork stub *L3* from 9mm to 10mm with a step of 0.5mm. Increasing *L3* improves the matching performance at the lower frequency range. However, further increment of *L3* may worsen the performance at the higher frequency end. Figure 4.22(b) demonstrates the effects by varying the width of the microstrip feed line *W2*. The *VSWR* performance is greatly improved over the entire operation band, by decreasing *W2* from 2.4mm to 1.6mm. However, further decrease of *W2* will worsen the matching performance around 4.6 GHz and is not recommended. The effects of varying the opening rate *R* is also analyzed, as indicated in Figure 4.22(c). By changing the opening rate, the *VSWR* performance of the antenna can be finely tuned within a small range to pursue better results.

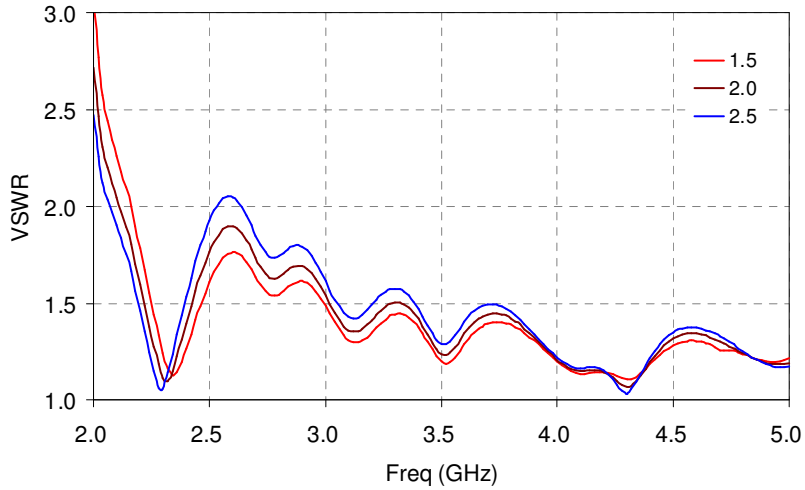
The proposed antenna has been fabricated and assembled, as shown in Figure 4.23. A 50Ω SMA connector is used to feed the fabricated wideband slot antenna. The physical size of the antenna is 19mm x 19mm, which is only 0.13λ x 0.13λ at the antenna lowest operation frequency 2 GHz.



(a) Parametric study of *L3* (*W2* = 2.4mm, *R* = 2.0)

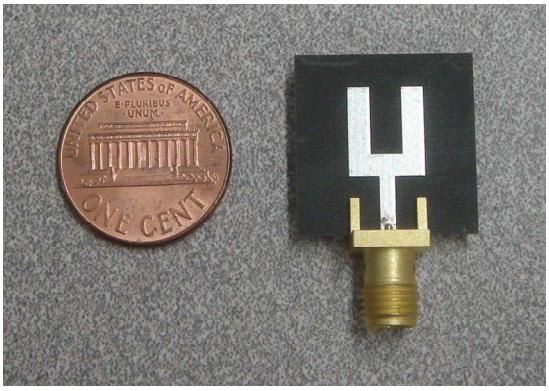


(b) Parametric study of *W2* (*L3* = 9.5mm, *R* = 2.0)

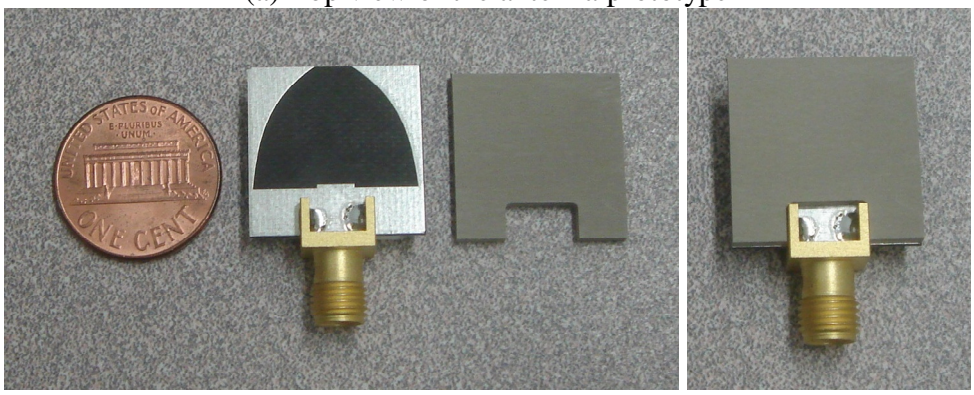


(c) Parametric study of *R* (*W2* = 1.6mm, *L3* = 9.5mm)

Figure 4.22 Parametric studies of the proposed wideband slot antenna.



(a) Top view of the antenna prototype



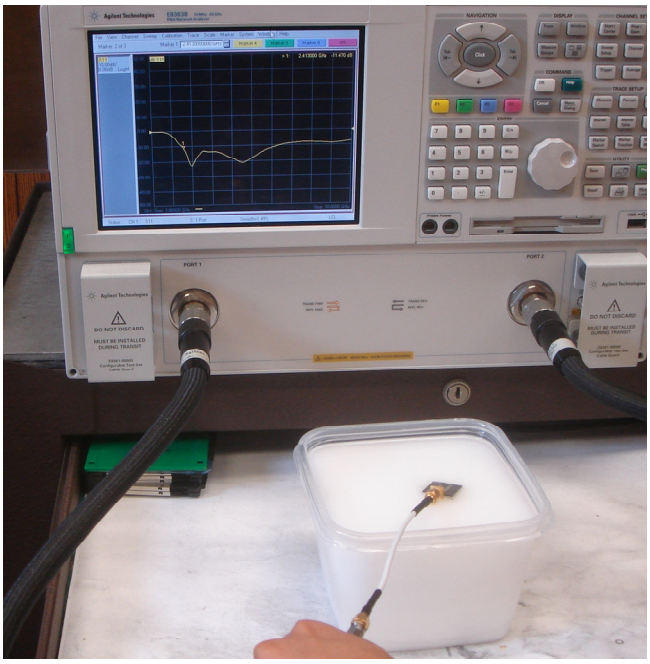
(b) Bottom view of the antenna prototype before and after the assembling

Figure 4.23 Prototype of the proposed wideband slot antenna.

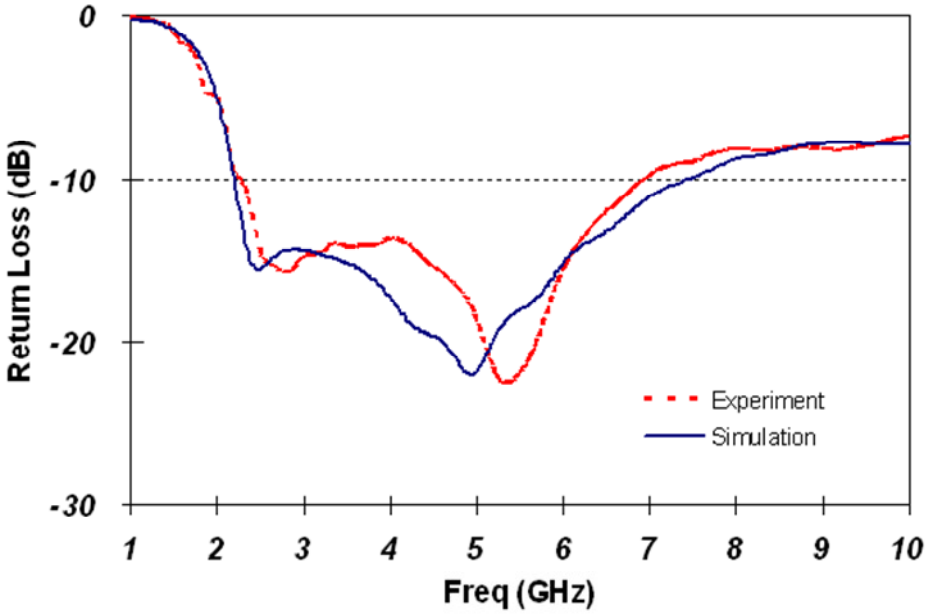
Matching liquid is made to emulate the breast fatty tissue during the return loss measurement. Paraffin oil and distilled water are used as the main components of the emulsion while 5% pharmaceutical quality beeswax is used as the emulsifying agent [94]. An Agilent 85070D coaxial probe connected to an Agilent E8365B PNA is used to measure the permittivity and conductivity of the matching liquid. Almost constant permittivity of 9.0 is achieved from 1 to 10 GHz while the conductivity increases linearly with the frequency from 0 (at 1 GHz) to 1.2 S/m (at 10 GHz).

The experimental setup for return loss measurement is indicated in Figure 4.24(a). The microstrip slot side of the antenna is facing the matching liquid while the fork feed side is exposed to air. Simulation and measurement results agree very well and both results show a good match of the antenna over the 2 to 8 GHz frequency range, as presented in Figure 4.24(b).

The designed antenna can be mounted on a semispherical mold to achieve an antenna array, which can be used in the clinical trial, as shown in Figure 4.25.

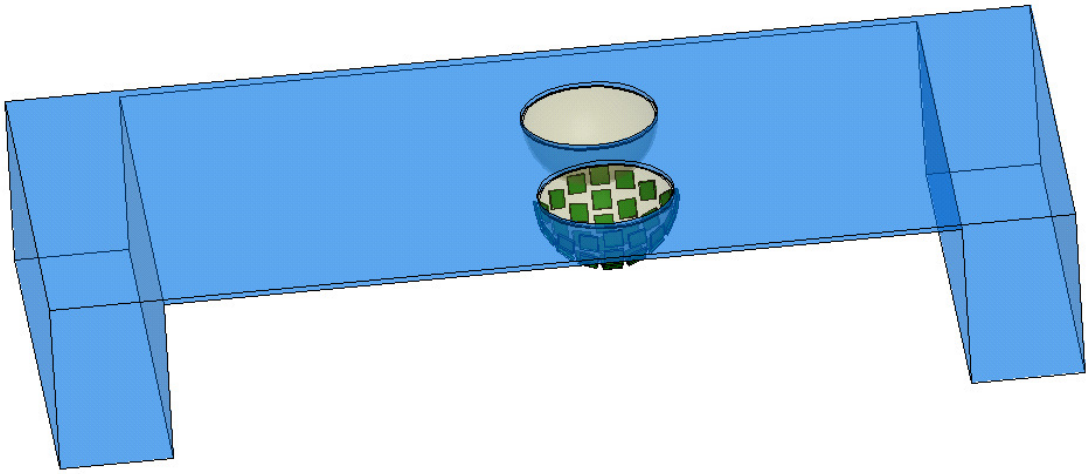


(a) Setup for return loss measurement. The antenna is attached on the matching liquid which has a permittivity of 9.0 and is used to emulate the breast tissue

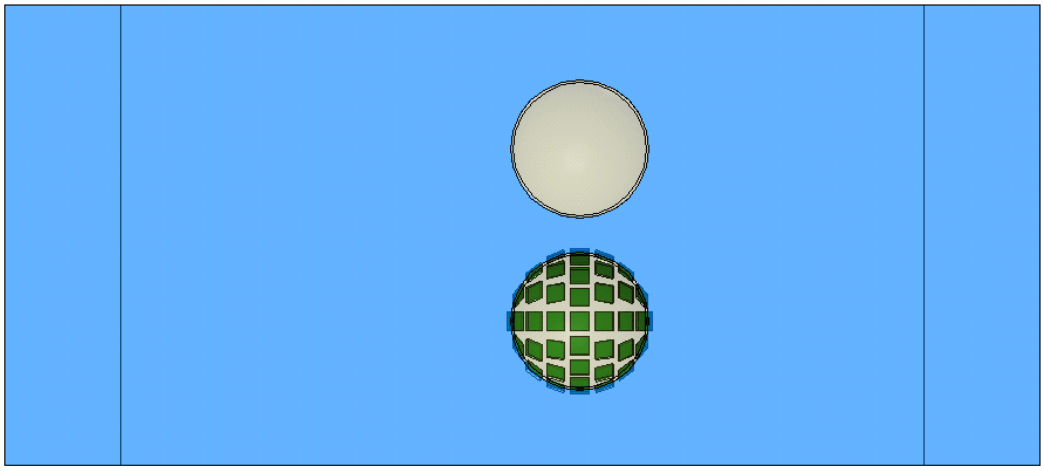


(b) Simulated and measured return loss of the proposed antenna. Good matching performance is achieved at 2 to 8 GHz

Figure 4.24 Return loss measurement of the designed tapered microstrip slot antenna.



(a) Side view



(b) Top view

Figure 4.25 Semispherical antenna array for clinical examination using the designed wideband microstrip slot antenna.

4.3.3 Novel Calibration Approach for Clutter Removal

A main challenge in microwave breast cancer detection is to detect the malignant tumor in a low-contrast condition. Clinical examinations have shown that nearly all breast cancers originate in the glandular tissues [95]. A recently published study suggested that the contrast in dielectric properties between malignant tissues and glandular tissues is not more than 10% [93]. Due to this low-contrast feature, it is expected that the reflected/scattered signal from the malignant tumor is very weak. On

the other hand, the received signals due to skin backscatter and Tx/Rx antennas mutual coupling are much stronger. This makes the desired signal totally immersed in various noise signals.

In order to solve this problem, many possible solutions have been proposed. One common method is to calibrate the system by subtracting the measured signals when no tumor target exists (also called reference signal) from those when tumor targets exist [96]. This method is very efficient to eliminate the noise signals and only highlight the reflections from the objects of interest. However, this method is not practical for real clinical diagnosis since the reference signal is generally not available. Another possible solution is to enhance the contrast of microwave imaging by injecting contrast agents, such as golden nanoparticles or carbon nanotubes [97]. The potential problem of this approach is that some patients may not accept any agent injections. Fear et al. [98] introduced a more practical calibration process to remove the skin reflections. The recommended calibration signal is formed as the average of the signal returns in the relevant given positions, and then the received signals are corrected by subtracting the calibration signal.

Here, we propose a novel, practical calibration approach to eliminate the effects of skin backscatter and Tx/Rx antenna coupling. This approach has improved the robustness of the imaging algorithm when the breast is not perfectly symmetrical. The geometry of a cylindrical microwave imaging system is shown in Figure 4.26, where red lines show Tx/Rx antenna mutual coupling, brown lines indicate skin backscatter, blue lines introduce reflection/scattering from tumor target, and green lines present multi-reflections. The transmitting and receiving antennas are placed very close to each other and their positions are indicated by two filled square icons (position P_i). After finishing the detection at position P_i, the Tx/Rx antenna pair is rotated a small angle (e.g., one degree) to the next position P_{i+1}. At position P_i, the total received signal $S_t^i(t)$ is given by

$$S_t^i(t) = S_{coupling}^i(t) + S_{skin}^i(t) + S_{t\arg et}^i(t) + S_{MR}^i(t) \tag{4-23}$$

where $S^{i}_{coupling}(t)$ is due to the mutual coupling between transmitting and receiving antennas, $S^{i}_{skin}(t)$ is due to the backscatter at air/skin interface, $S^{i}_{t\arg et}(t)$ is the desired reflection/scattering from the object of interest, and $S^{i}_{MR}(t)$ is due to multi-reflections. At the next position P_{i+1}, the total received signal $S^{i+1}_{t}(t)$ is given by a similar equation

$$S^{i+1}_{t}(t) = S^{i+1}_{coupling}(t) + S^{i+1}_{skin}(t) + S^{i+1}_{t\arg et}(t) + S^{i+1}_{MR}(t) \tag{4-24}$$

Figure 4.27 presents the measured signal returns $S^{i}_{t}(t)$ and $S^{i+1}_{t}(t)$ at two adjacent positions P_i and P_{i+1}. The experiment is performed in a low-contrast condition to emulate the true situation that most of the malignant tumors are in glandular tissues. Paraffin oil, with a dielectric constant of 3.5, is used to emulate the breast model while safflower oil, with a dielectric constant of 3.8, is used as the detection target. After an initial guess of the target location, it is found out from Figure 4.27 that the desired signal is totally immersed in the noise signals due to the low-contrast problem. In order to extract the target reflection, the received signals are calibrated using the following procedure. The received signal at any position P_i is corrected by subtracting the signal at the position P_{i+1}. The corrected signal is assumed at a new position, which is the middle point of P_i and P_{i+1}. The corrected signal is given by

$$S_{corrected}(t) = S^{i+1}_{t}(t) - S^{i}_{t}(t) \tag{4-25}$$

Since the transmitting and receiving antennas are rotated simultaneously, the received signal due to Tx/Rx antenna coupling is constant and cancelled in the calibration process. The backscatter from air/skin interface is also eliminated through the calibration step if the breast model is perfectly symmetrical. Even if the breast model has slight asymmetry, it has been found that the signal difference from target reflection still dominates the corrected signal. The signals due to multi-reflections usually have a longer time delay and can be gated in time domain. The corrected signal after the calibration, as shown in Figure 4.28, is based on the experimental signals when a slightly asymmetrical breast model is used. The corrected signal in Figure 4.28 indicates that the calibration has successfully underlined the reflected/scattered signal from the tumor.

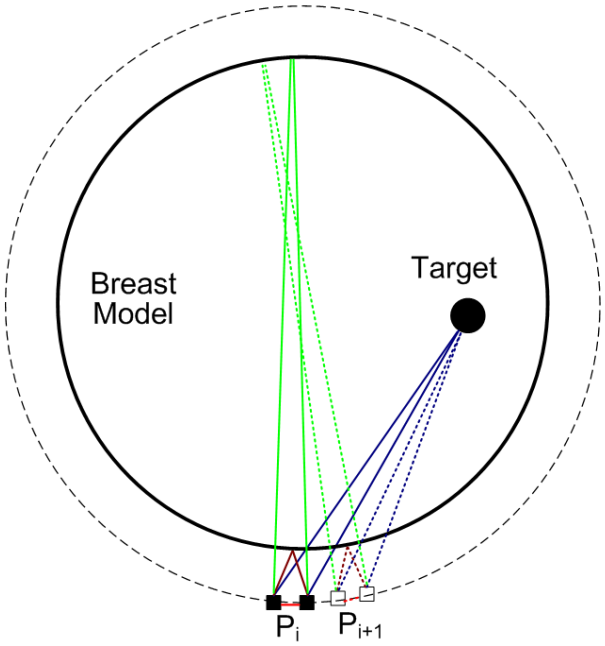


Figure 4.26 Geometry of a cylindrical microwave imaging system. The two filled square icons indicate the Tx/Rx antenna pair at position Pi while the two non-filled square icons show the antenna pair at the next position Pi+1 after the rotation.

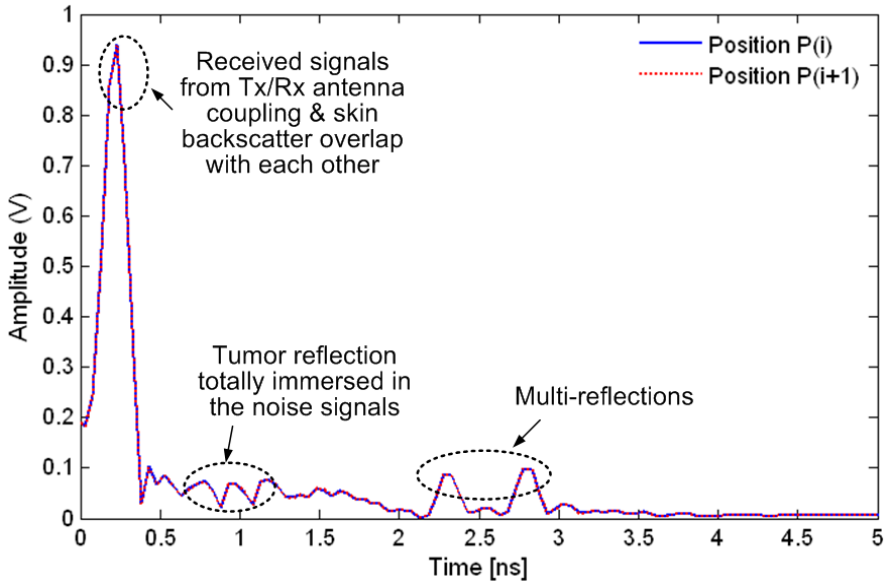


Figure 4.27 Measured signal returns when Tx/Rx antennas are at positions P_i and P_{i+1}.

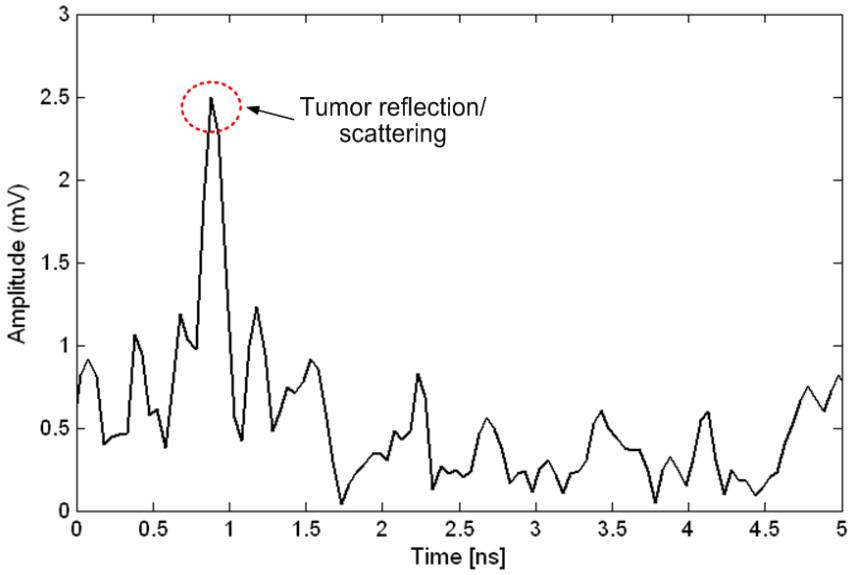


Figure 4.28 Corrected signal after the calibration. The signal due to tumor reflection/scattering is highlighted.

4.3.4 Numerical Simulation and Experimental Results

The geometry of the experimental setup is shown in Figure 4.29. A cylindrical container filled with paraffin oil is used as the breast model. A plastic straw filled with safflower oil is inserted into the container and used as the detection target. The breast model has a diameter of 20cm while the detection target has a diameter of 5mm. The difference in dielectric permittivity between paraffin oil and safflower oil is about 10% to emulate a low-contrast case. Two UWB antennas next to each other are placed at a standoff distance from the breast model and used to transmit and receive signals. A step motor is used to accurately rotate the Tx/Rx antennas from 0 to 359 degrees with a step of 1 degree. All the signals at 360 positions have been collected by the UWB microwave imaging system and then transferred to the computer through a USB2.0 cable.

The recorded raw signals are first used to estimate the boundary of the breast model before applying the calibration. Next, the 360 collected signals are calibrated by subtracting the signals received at the adjacent positions. 359 corrected signals are acquired after the calibration process and used to recover the image of the target. A Backprojection microwave beamforming algorithm has been used to reconstruct the image of the target.

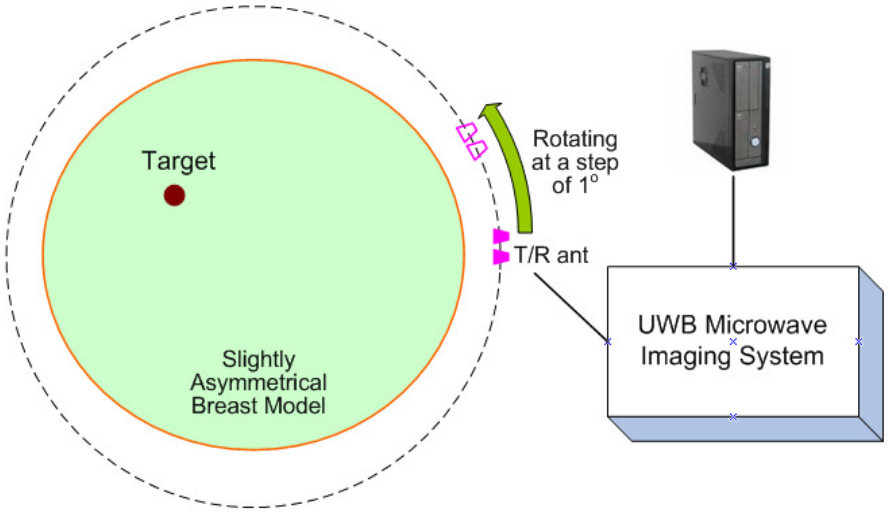
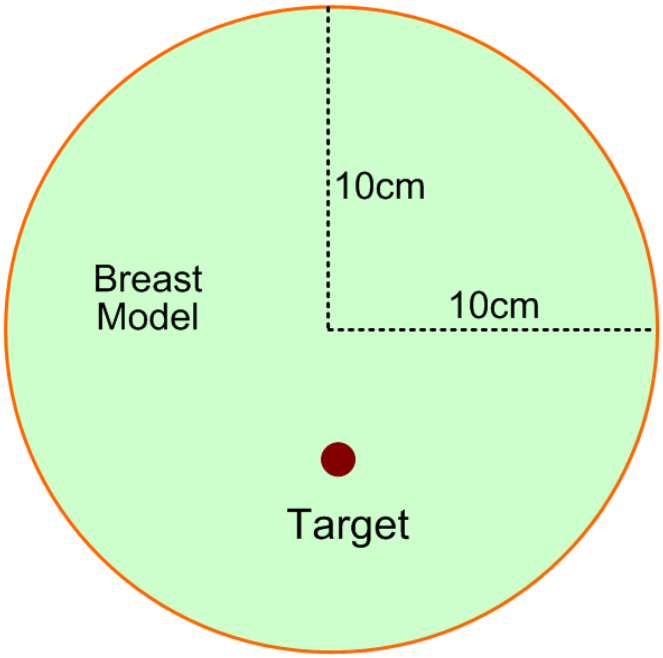


Figure 4.29 Geometry of the experimental setup.

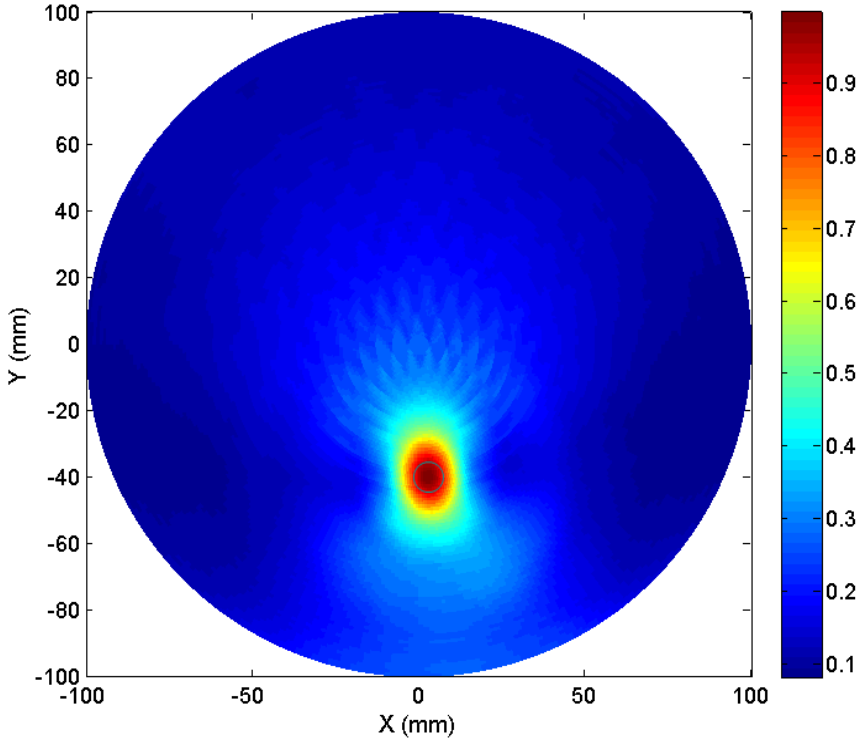
The experimental setup and result of detecting a 5mm diameter breast tumor from a cylindrical breast phantom are shown in Figure 4.30(a) and (b) respectively. It has been found that by using the proposed calibration approach, UWB pulse radar has accurately detected and localized the breast tumor target.

To further demonstrate the capability, UWB pulse radar has been applied to detect more than one tumor target from a cylindrical breast phantom, as the experimental setup introduced in Figure 4.31(a). The two targets have the same diameter of 5mm. The recovered image shown in Figure 4.31(b) has accurately indicated the locations of the two breast tumors.

To validate the performance of the novel calibration method for asymmetrical breast phantom, we have performed a numerical simulation using CST software. The breast phantom was modeled to have a longer radius of 11cm and a shorter radius of 10cm, as shown in Figure 4.32(a). The tumor target was defined with a diameter of 5mm. The boundary of the phantom was firstly reconstructed, as shown in Figure 4.32(b), which has accurately indicated the outline and size of the elliptic cylinder. Next, the novel calibration method was performed to remove the clutter from the received signals, which are then applied for image recovery. The recovered image in Figure 4.32(b) has clearly predicted the location of the human tumor target.

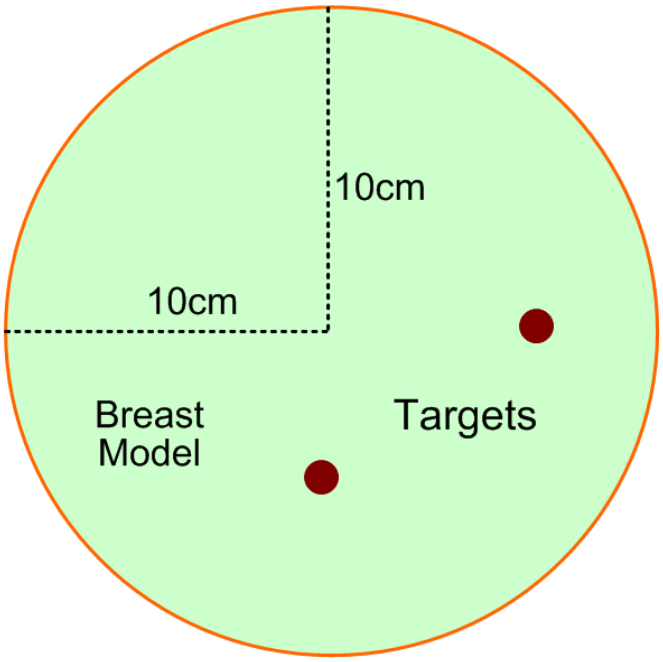


(a) Experimental setup

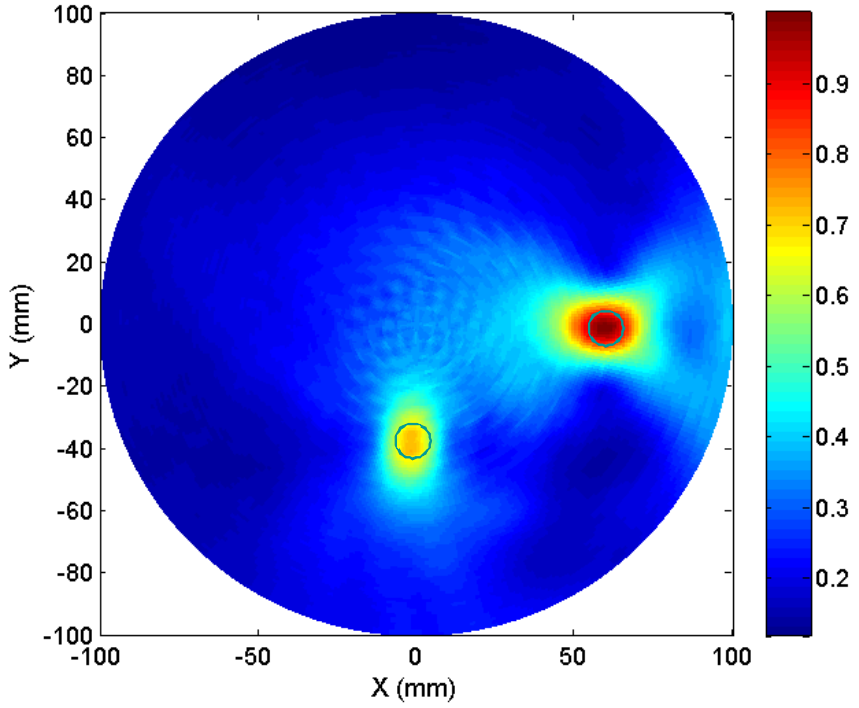


(b) Recovered image

Figure 4.30 Detection of a 5mm diameter tumor from a cylindrical breast phantom based on experimental data.

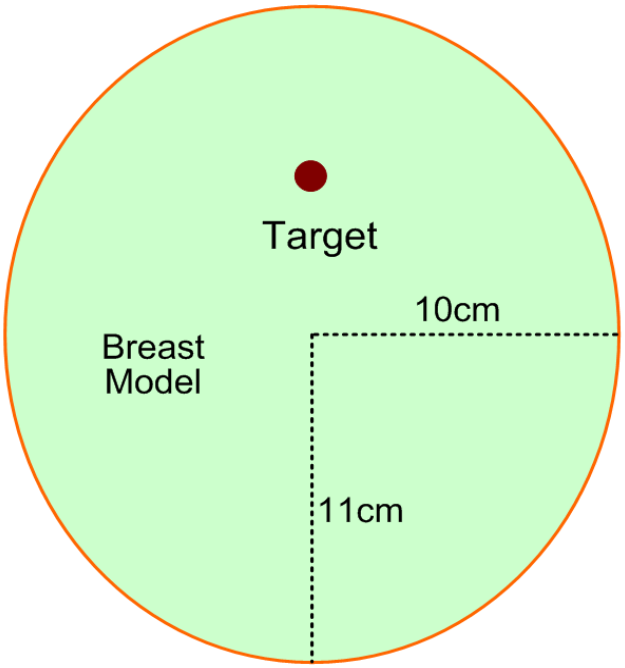


(a) Experimental setup

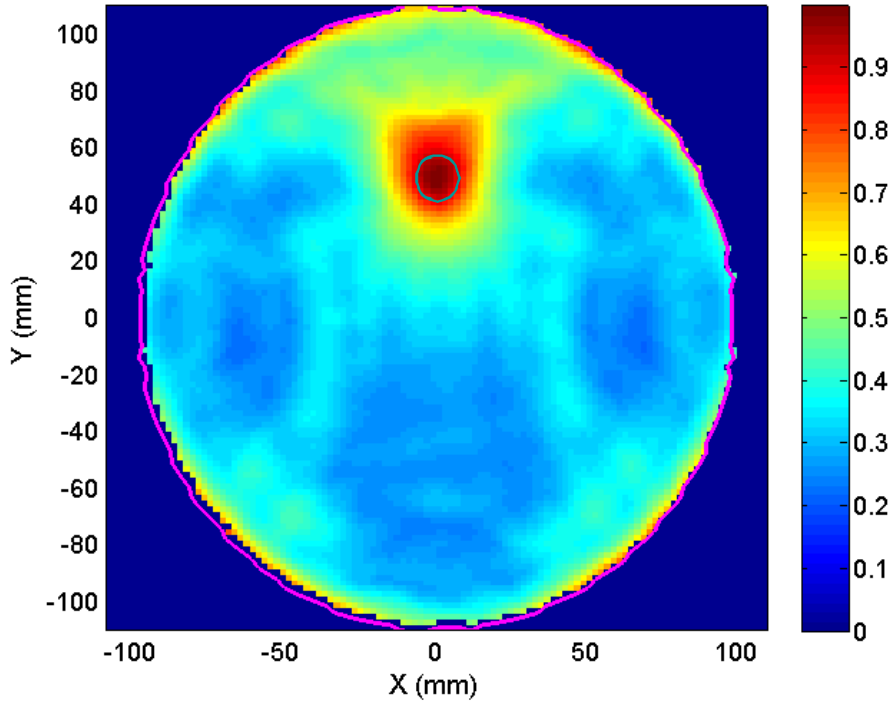


(b) Recovered image

Figure 4.31 Detection of two breast tumors from a cylindrical breast phantom based on experimental data.



(a) FDTD Numerical simulation setup using CST



(b) Recovered image

Figure 4.32 Detection of a 5mm diameter tumor from an ellipse cylindrical breast phantom based on FDTD simulation data using CST.

4.4 Conclusion

In this chapter, we have utilized three examples to demonstrate the capability and performance of UWB pulse radar in imaging applications. UWB technology has several most wanted technical features compared to other imaging techniques, such as low power, high imaging resolution, non-contact remote sensing, non-invasiveness, environment friendly, and so on.

Real-time human tracking example demonstrates that UWB pulse radar is a very attractive technology for security surveillance, human rescuing, and sensitive material tracking. However, the detection range of UWB pulse radar is still limited to about 20m because of the FCC requirement on transmitter emission. When acquiring real-time image, the developed UWB pulse radar captures 75 photo shots per second, which is adequate to track any human activities. However, a higher system refresh rate is still needed if used to track any fast moving targets, such as cars, airplanes, and etc.

The 3-D imaging example shows the capability of UWB pulse radar for target recognition. In the experiment, we moved a linear antenna array mechanically in order to achieve a 2-D array operation. In order to achieve a real-time 3-D imaging feature, a 2-D antenna array is needed, together with a more complicated switch matrix to control the ON/OFF of each array element.

Early breast cancer detection example shows the great potential of UWB pulse radar in medical imaging applications. But the imaging resolution of UWB pulse radar achieved by now is several mm and has limited its potential applications. More research is still needed to improve the imaging resolution to 1 mm or even sub-mm and extend UWB technology for other medical imaging applications, such as cardiology imaging, pneumology imaging, and obstetrics imaging. One direction to go is to integrate microwave imaging technology with ultrasonic imaging technology, to achieve the benefit of good contract from microwave and the good imaging resolution from ultrasound simultaneously.

Chapter 5

UWB Pulse Radar for Doppler Detection Applications

Mechanical vibrations or rotations of structures on a target may introduce frequency modulation on the radar return signal. The modulation due to this vibration or rotation is referred as micro-Doppler (m-D) phenomenon. For example, human physical activity is a complex motion that is comprised of movements of individual body parts, including head, torso, leg, arm and foot. When human is walking, the movements of different components of human body generate a number of different frequency shifts in the radar returned signal, also called Doppler frequency shifts. It should be noted that only the velocity in the radial direction contributes to Doppler frequency shift. Positive Doppler frequency is generated if radar target moves toward the radar while negative one is rendered if radar object moves backward from the radar sensor.

Several radar technologies are usually used to detect the Doppler frequency shift of any human motions, including CW, FMCW, pulse compression, and pulse radar. CW radar is limited to certain applications which do not require target range information. Wideband FMCW and pulse compression radars are quite complicated and expensive to implement. UWB pulse radar technology is used because of its relatively low prototyping cost and capability of providing high resolution range profile.

In this chapter, we will discuss how UWB pulse radar can be used for Doppler detections. After presenting the basic theory and equations on m-D signature extraction, we will introduce three examples using UWB pulse radar for Doppler detections: 1) human gait analysis, 2) Doppler tracking of two persons, and 3) Respiration detection of stationary people.

For certain applications where target range information is not needed, an alternative solution based on CW Doppler radar is a good option. A CW radar prototype will also be introduced and discussed here. The two radar technologies, i.e., UWB pulse radar and CW radar, will be compared and summarized in details.

5.1 Micro-Doppler Signature Extraction

5.1.1 Basic Theory

Consider a UWB pulse radar that sends out a periodic pulse signal at a PRT of T, assuming the n^{th} transmitted pulse is modeled as

$$x_n(t) = A(t - nT)\exp[j(2\pi f_c t + \Phi_0)] \tag{5-1}$$

where $A(t)$ is the pulse envelope, f_c indicates the carrier frequency, and Φ_0 is the initial phase. The pulse signal is sent out by stationary radar and reflected by a target that is moving towards the radar at a constant velocity v. The received pulse signal can be written as [99]

$$y_n(t) = k \cdot x_n\left(\alpha\left(t - \frac{2R_0}{(1+\beta)c}\right)\right) \tag{5-2}$$

where k accounts for all amplitude losses, c is the speed of light, R_0 is the distance between the target and the radar, $\beta = v/c$, and

$$\alpha = \frac{1+\beta}{1-\beta} = \frac{1+v/c}{1-v/c} \tag{5-3}$$

Bring (5-1) into (5-2), we can achieve

$$y_n(t) = k \cdot A\left(\alpha\left(t - \frac{2R_0}{(1+\beta)c}\right) - nT\right)\exp\left[j\left(2\pi\alpha f_c t - \frac{4\pi R_0}{(1-\beta)\lambda} + \Phi_0\right)\right] \tag{5-4}$$

where λ presents the wavelength at carrier frequency.

The received signal has a carrier frequency of αf_c, and the Doppler frequency shift, F_D, is the carrier frequency difference between transmitted and received signal, given by

$$F_D = \alpha f_c - f_c = \frac{2v}{(1-\beta)\lambda} Hz \tag{5-5}$$

The Doppler shift is positive for approaching target ($v > 0$) and negative for receding target ($v < 0$).

Next, the received pulse is demodulated to baseband. The baseband signal after the demodulation can be expressed as

$$z_n(t) = y_n(t)\exp(-j2\pi f_c t) \tag{5-6}$$

Bring (5-4) into (5-6), we have

$$z_n(t) = k \cdot A\left(\alpha t - \frac{2R_0}{(1-\beta)c} - nT\right)\exp\left[j\left(2\pi F_D t - \frac{4\pi R_0}{(1-\beta)\lambda} + \Phi_0\right)\right] \tag{5-7}$$

Assuming the range migration of $A(t)$ is negligible, the baseband signal can be represented as

$$z_n(t) = k\exp\left[j\left(2\pi F_D t - \frac{4\pi R_0}{(1-\beta)\lambda} + \Phi_0\right)\right] \tag{5-8}$$

The baseband pulse is still periodic with a PRT of T, and is sampled at a fast-time sampling interval of T_s. The sampled data at the n^{th} PRT is saved at the n^{th} column of a two-dimensional matrix $s[l,n]$, where l is the row number (i.e., range bin) while n is the column number (i.e., slow-time index). Assuming the target movement/motion happens at range bin l, the sample time for the l^{th} range bin and n^{th} pulse is calculated as $t_{l,n} = nT + T_0 + lT_s$, where T_0 is the initial time. Since $s[l,n] = z_n(t_{l,n})$, the recorded signal sample will be

$$s[l,n] = k\exp\left[j\left(2\pi F_D nT + 2\pi F_D T_0 + 2\pi F_D lT_s - \frac{4\pi R_0}{(1-\beta)\lambda} + \Phi_0\right)\right] \tag{5-9}$$

For a given range bin l, the phase of the signal only depends on the slow-time index n. All others can be grouped into a new phase constant Φ_0' as

$$s[l,n] = k\exp\left[j\left(2\pi F_D nT + \Phi_0'\right)\right] \tag{5-10}$$

Thus, for a constant-velocity target, the slow-time signal in the approximate range bin is a sinusoid at the Doppler frequency. The target Doppler shift can be measured by using the frequency analysis of the slow-time signal.

5.1.2 Radar Signal Processing

As we described before, a received baseband pulse signal is digitized and saved in a two-dimensional data set denoted by $s[l,n]$, where $l = 1,2,\cdots,L$ introduces the range bin while $n = 1,2,\cdots,N$ represents the slow-time index. For M receiving antennas, the data set will be extended to three-dimension shown as $s[l,n,m]$, where m indicates that the data is captured by the m^{th} receiving antenna.

Next, a straightforward algorithm is used to acquire the location and extract the Doppler characteristics of the radar targets, as described below. The Matlab program used to implement the following equations is shown in Appendix A.5.

(1) A matched filter $h(l)$ is applied firstly to eliminate the out-of-band noise and improve the signal to noise ratio of the fast-time sampled signals, given by

$$u_{n,m}(l) = s_{n,m}(l) \otimes h(l) \tag{5-11}$$

where "$\otimes$" denotes convolution operator, $s_{n,m}(l)$ represents the fast-time samples of the n^{th} pulse that is captured by the m^{th} receiving antenna, and $h(l)$ is the impulse response of the matched filter and its frequency response is given by

$$H(f) = \begin{cases} 1, & f \le f_p \\ 0, & f > f_p \end{cases} \tag{5-12}$$

where f_p is the bandwidth of the received baseband pulse.

(2) A Backprojection microwave imaging algorithm is used to reconstruct the image of radar targets. At a given time frame, M receiving antennas collect M complete pulse signals, which are used to recover one image scene. To reconstruct the image, the surveillance space is divided into many pixels by the distance and angle. At time frame n, the imaging intensity of the pixel at distance R and angle θ can be calculated by applying the related amplitude and phase compensations on the received baseband signals and then summing them up [68], given by

$$I_n(R,\theta) = \left| \sum_{m=1}^{M} w_{n,m}(R,\theta) u_{n,m}\left(l_{R,\theta}\right) e^{j\varphi_{n,m}(R,\theta)} \right| \tag{5-13}$$

where m indicates the m^{th} receiving antenna; the index $l_{R,\theta}$ of $u_{n,m}$ locates the data at the correct range bin (i.e., time delay); $\varphi_{n,m}(R,\theta)$ shows the phase compensation for different traveling distances; and $w_{n,m}(R,\theta)$ introduces the amplitude compensation for different losses and attenuations. Equations have been shown in Chapter 4.1.1 on how to calculate these compensation coefficients. A complete image screen is acquired by calculating the imaging intensity of all the pixels. The real-time location tracking of the target can be achieved by investigating the image screen continuously at every time frame.

(3) At every PRT, radar returned signal due to static reflector/scatterer always comes back at the same time delay while that due to target motion/movement has a changing delay profile. For receiving channel m, a reference signal is acquired by averaging the 2-D data set along the row, i.e., slow-time samples.

$$\bar{u}_m(l) = \frac{1}{N}\sum_{n=1}^{N} u_m(l,n) \quad l = 1,2,...,L \tag{5-14}$$

The fast-time sampled pulse signal is calibrated by subtracting the reference signal to remove the reflections from static background and highlight any target motion/movement. The new signal after the calibration is given by

$$v_{n,m}(l) = u_{n,m}(l) - \bar{u}_m(l) \tag{5-15}$$

(4) Plot the range profile (i.e., range vs. time) of the calibrated fast-time sampled pulse $v_{n,m}(l)$ and observe the entire distance that the target has passed by. Those range bins that have been crossed by the target will be used for Doppler frequency extraction later on. Range profile is also widely used to indicate the respiratory rate when detecting human breathing.

(5) Fast Fourier transform (FFT) is applied to the slow-time sampled signal, i.e., the row of $v_m(l,n)$, to extract the Doppler frequency shift. The column (i.e., range bin) l is selected based on if it includes any target motion or not, which is acquired at step 4. FFT is a very useful tool for constant velocity motion detection and has been widely used to extract the Doppler frequency shift of human breathing and heart beats [100].

(6) There are many other motions in practical life that include time-varying frequency contents. A joint time-frequency analysis based on the short time Fourier transform (STFT) of the slow-time signal is usually performed. The spectrogram S(n, f), which shows how the signal power varies with time n and frequency f, is used to analyze the m-D signature of complex human motions and given by [101]

$$S(n, f) = \left| \sum_{p=-\infty}^{\infty} s(p) g(p-n) e^{-jpf} \right|^2 \tag{5-16}$$

where $s(n)$ is the slow-time signal for a selected range bin, and $g(n)$ is a window function. Several window functions are available, including Hamming, Hanning, Kaiser-Bessel, and Gaussian windows. Particularly, Hamming window is an optimized function and utilized in our system to minimize the nearest side lobe [102], as the Matlab code shown in Appendix A.5.

5.2 Doppler Ambiguity

Doppler ambiguity of UWB pulse radar is mainly determined by the radar system update rate. The higher radar system update rate, the more capable the UWB radar can detect faster objects. According to the specifications of the developed UWB PD radar introduced in Chapter 2, the system refresh rate can be calculated as follows when processing 8 channel data sequentially and utilizing a fine sampling interval of 10ps. The time needed to finish the sampling of 1 channel signal is given by

$$t_{sample} = \frac{10ns}{10ps} \times 100ns = 0.1ms \tag{5-17}$$

The time needed in order to upload the sampled data into PC using USB2.0 communication link is given by

$$t_{upload} = \frac{100ns}{10ps} \times 2 \times 2/25M = 1.6ms \tag{5-18}$$

Therefore, the system refresh rate can be acquired as

$$f_r = \frac{1}{8\left(t_{sample} + t_{upload}\right)} = 75Hz \tag{5-19}$$

That determines the maximum detectable Doppler frequency to be ±37.5 Hz for both moving forward and backward targets. Next, the maximum detectable radial velocity of the targets is calculated to be 1.875 m/s using the following Equation [99].

$$v_{\max} = \frac{f_D c}{2 f_c} = \frac{f_D \lambda}{2} = \frac{f_r \lambda}{4} \tag{5-20}$$

where f_r, f_D, and f_c represent system refresh rate, Doppler frequency shift, and carrier frequency respectively, while v_{max} and c introduce maximum detectable velocity and speed of light respectively. A carrier frequency of 3 GHz is utilized in the developed PD radar prototype.

The system can be easily adapted for detecting high speed objects, e.g., running people, running fan, flying wheel of a bicycle, vehicle, and etc. using the following two steps. Firstly, a longer sampling interval can be used to digitize the pulse, for example, using 50ps instead of 10ps is still adequate to reconstruct a fairly good pulse shape. That will generate a 5 times faster system refresh rate, i.e., 375 Hz, and a maximum detectable radial speed of 9.4 m/s. Furthermore, if we just use single receiving channel mode when performing Doppler experiments to detect high speed targets, the system refresh rate will be increased 8 times to 3 kHz. Subsequently, the ambiguous velocity will be increased dramatically to 75 m/s, which is sufficient to detect most of the high speed objects in daily life.

5.3 Human Gait Analysis

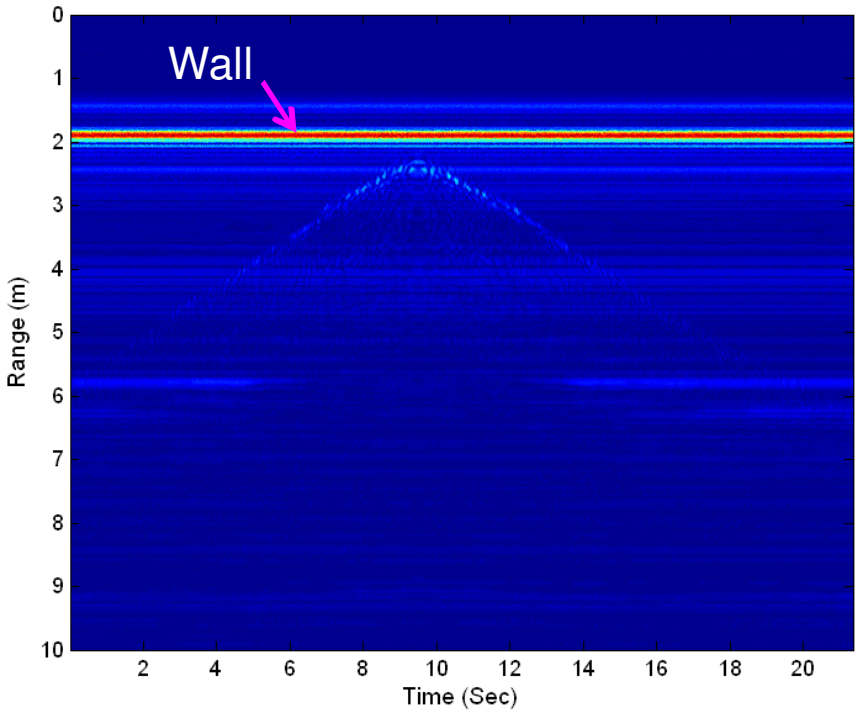
Human gait is the way locomotion is achieved using human limbs. Different gaits are characterized by difference in limb movement patterns, overall velocity, forces, kinetic, and potential energy cycles, and changes in the contact with the ground or floor, etc.

In this section, we will focus on human gait analysis of walking persons using the developed UWB pulse radar. When a person is walking, the movements of torso, head,

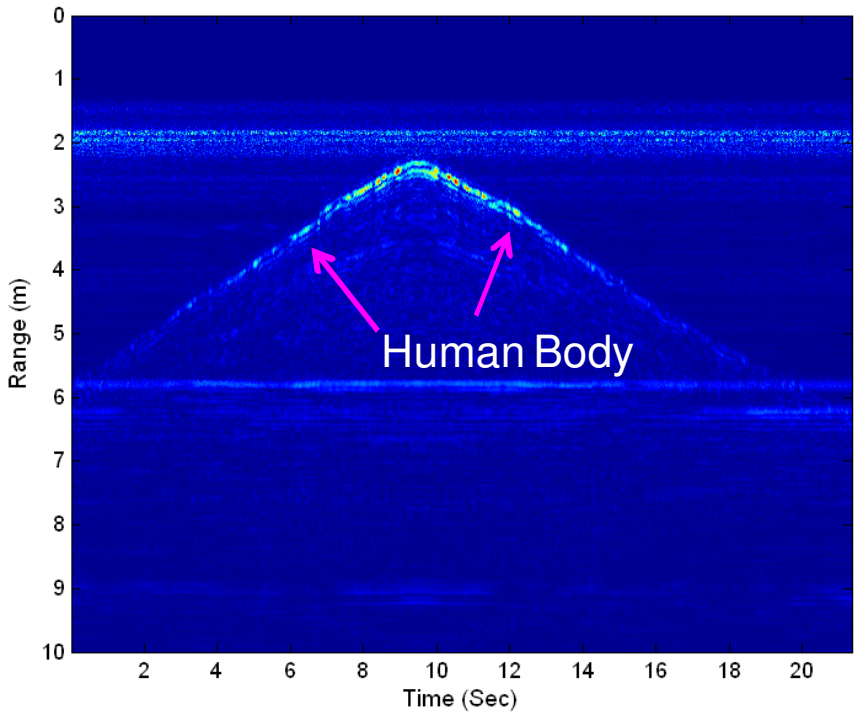
foot, arm, and leg generate different Doppler frequency shifts. Particularly, the swing of arms moves forward and backward periodically and generates positive and negative Doppler frequency shifts sequentially. In addition to m-D signature, UWB pulse radar also gives high resolution range profile. Therefore, the motions of arms can be observed from both range-time plot and the spectrogram of radar returned signal. Experiments were performed to investigate the human gait of three different motions: walking without arm swing, walking with one-arm swing, and walking with two-arm swing. Very promising results have been acquired and will be presented here.

5.3.1 Human Walking Without Arm Swing

In the 1st experiment, the human is walking toward/away from the UWB Doppler radar, without arm swing. The high resolution range profile shown in Figure 5.1(a) has indicated the wall locations at 1.9m, as well as the walking trace of the person. In order to highlight the human movement, static reflections have been removed using equations (5-14) and (5-15) while only the signal changes due to human movement are left. The high resolution range profile after removing the static reflections is shown in Figure 5.1(b), which has clearly shown that the person walked toward the radar from 0 to 9.5s and then walked backward. The walking velocity is estimated to be 0.4 m/s using the range-time characteristics, which also agrees well with the calculation using the Doppler frequency shift in the spectrogram. Positive Doppler frequencies are generated by the torso and legs at 0 to 9.5s and negative ones from 9.5s to 20s, as marked in Figure 5.1(c).

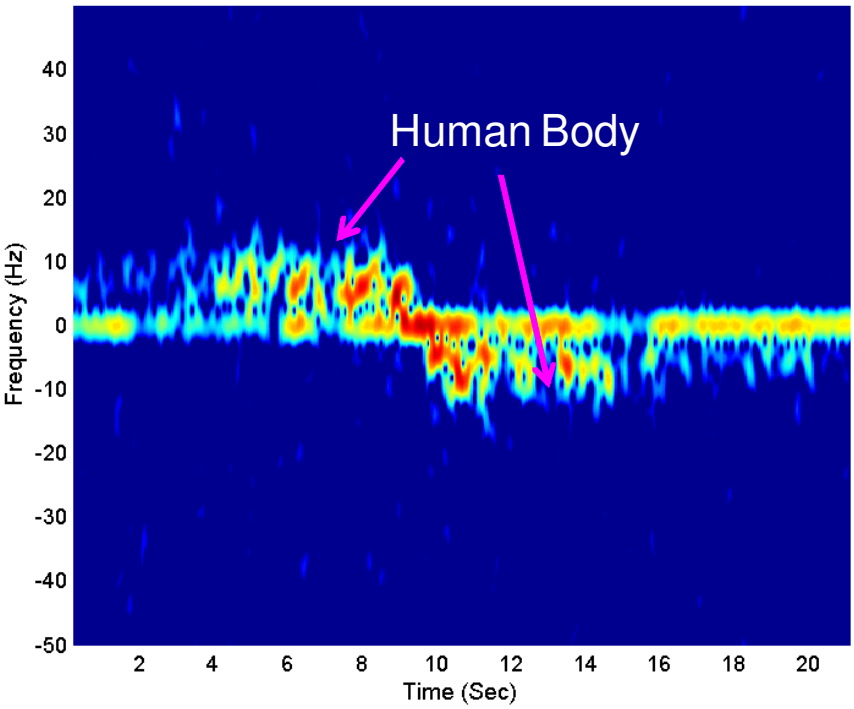


(a) High resolution range profile before removing static reflections



(b) High resolution range profile after removing static reflections

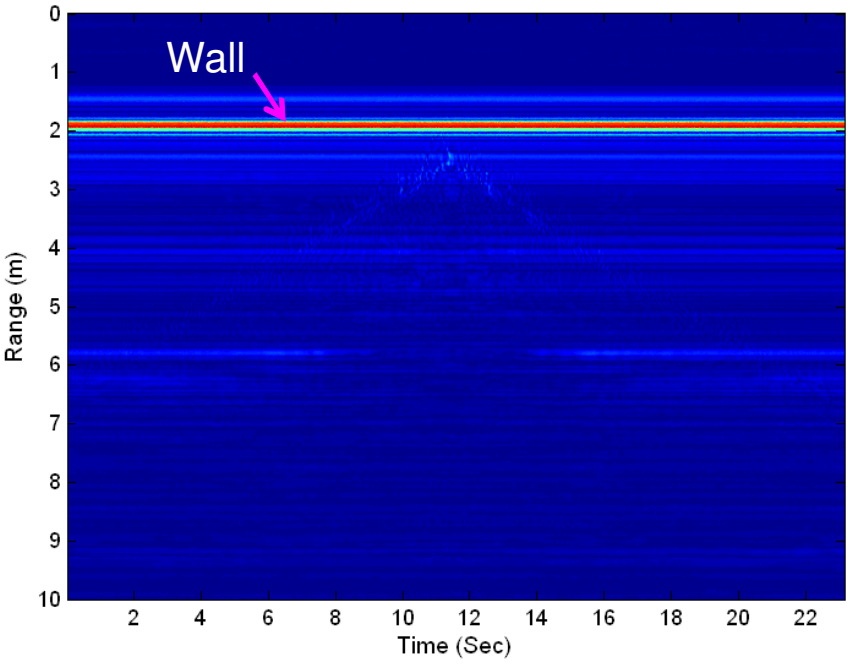
Figure 5.1 Acquired results when the person walking without arm swing.



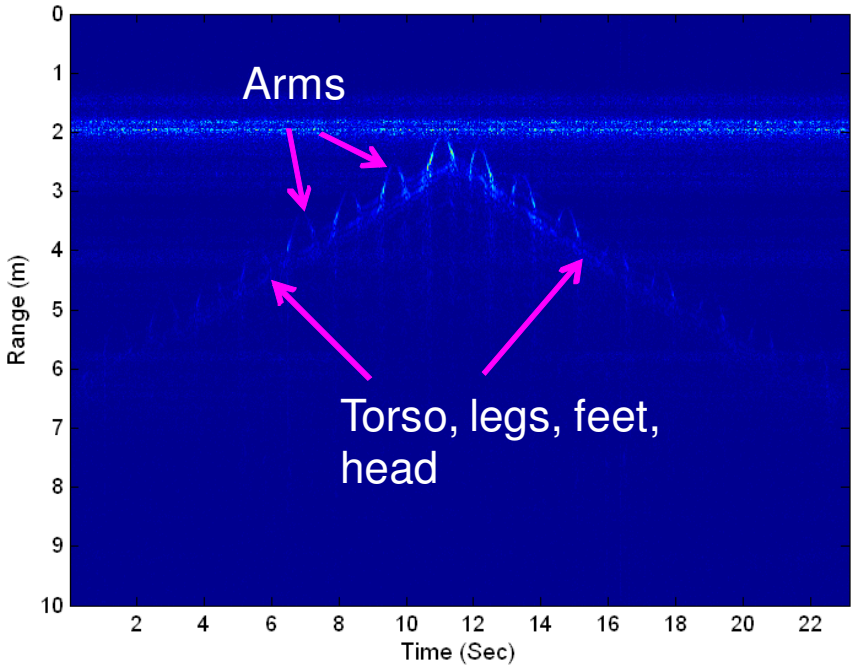
(c) Acquired spectrogram from human body (e.g., torso, legs, head, feet)
Figure 5.1 Continued.

5.3.2 Human Walking With One-Arm Swing

In the 2nd experiment, the human is walking toward/away from the UWB Doppler radar, with one-arm swing. The range-time plot in Figure 5.2(a) has clearly indicated the location of the wall, however, the walking trace of the person is vague because of the weak signal reflection. Additionally, we have removed the reflections from all static background, and the new range profile is shown in Figure 5.2(b). The walking trace of the human object is shown clearly, with many spikes on it that are due to the arm swing. The Doppler spectrogram in Figure 5.2(c) presents the Doppler frequencies due to both walking and swinging. Comparing the two plots, the movements of torso and legs generate a positive Doppler frequency at time range 0 to 11.5s when human target is walking toward the radar and a negative Doppler at 11.5s to 20s when walking backward. The periodic positive/negative Doppler frequencies in the spectrogram are generated by the arm movement, as marked in Figure 5.2(c).

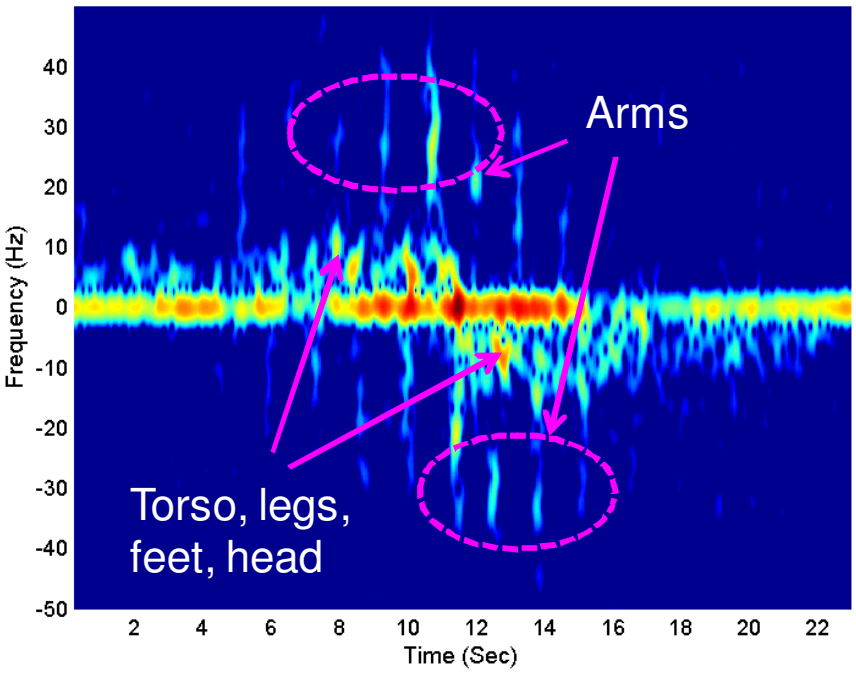


(a) High resolution range profile before removing static reflections



(b) High resolution range profile after removing static reflections

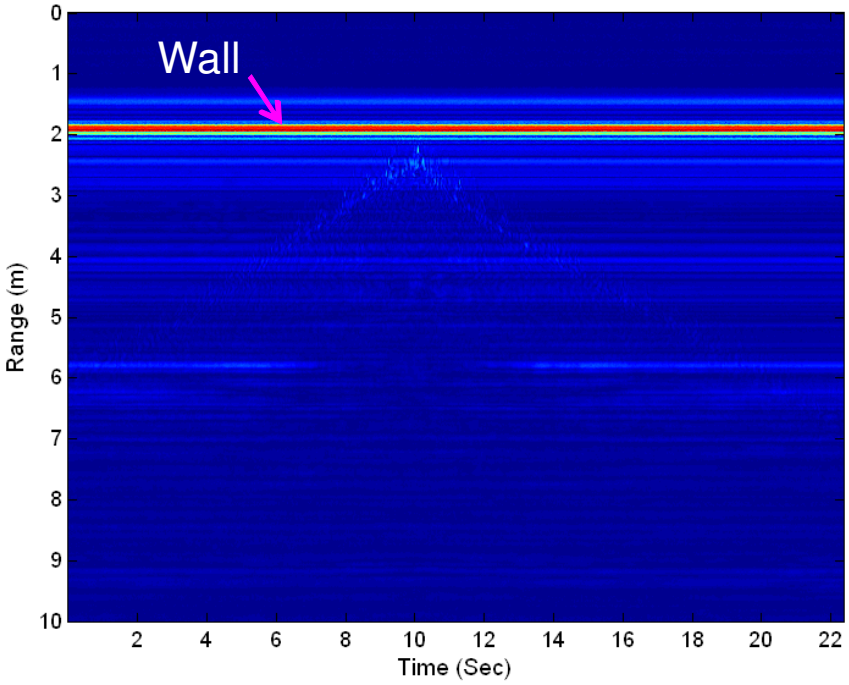
Figure 5.2 Acquired results when the person walking with one-arm swing.



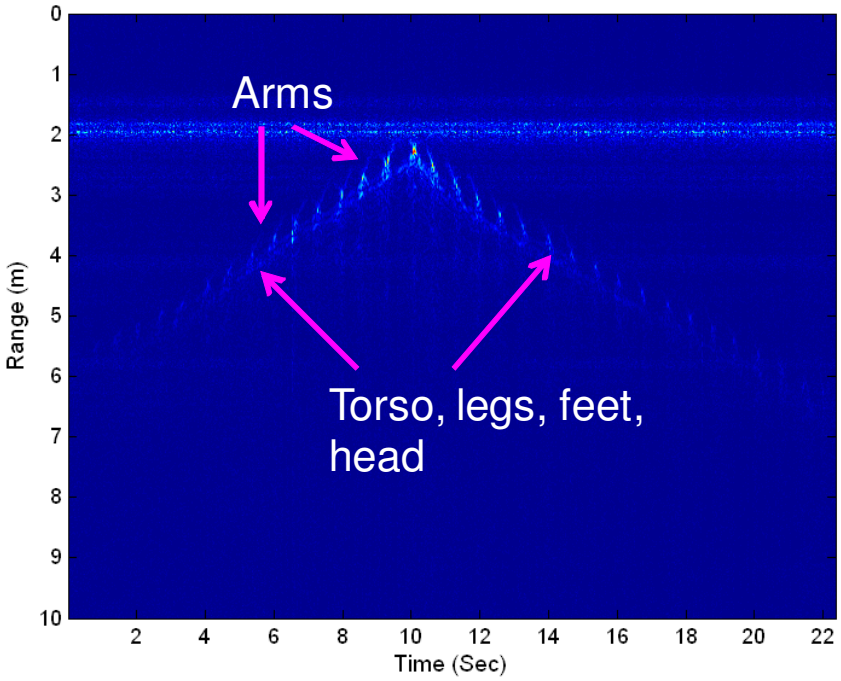
(c) Acquired spectrogram
Figure 5.2 Continued.

5.3.3 Human Walking With Two-Arm Swing

In the 3rd experiment, the human is walking toward/away from the UWB Doppler radar, with two-arm swing. Figure 5.3(a) and (b) shows range-time plot before and after removing the static reflections. After highlighting the signal change, Figure 5.3(b) has clearly shown the walking trace of the person, as well as the vibrations of arms swings. Compared to Figure 5.2(b), the number of vibrations from two-arm swing is almost doubled than that from one-arm swing. If we compare Figures 5.3(b) and (c), a positive Doppler is induced from the approaching of torso and legs at time range 0 to 10s while negative from the ascending at 10s to 20s. As we expect, the two-arm swing generates both positive and negative Doppler frequencies at the same time, as shown in Figure 5.3(c).

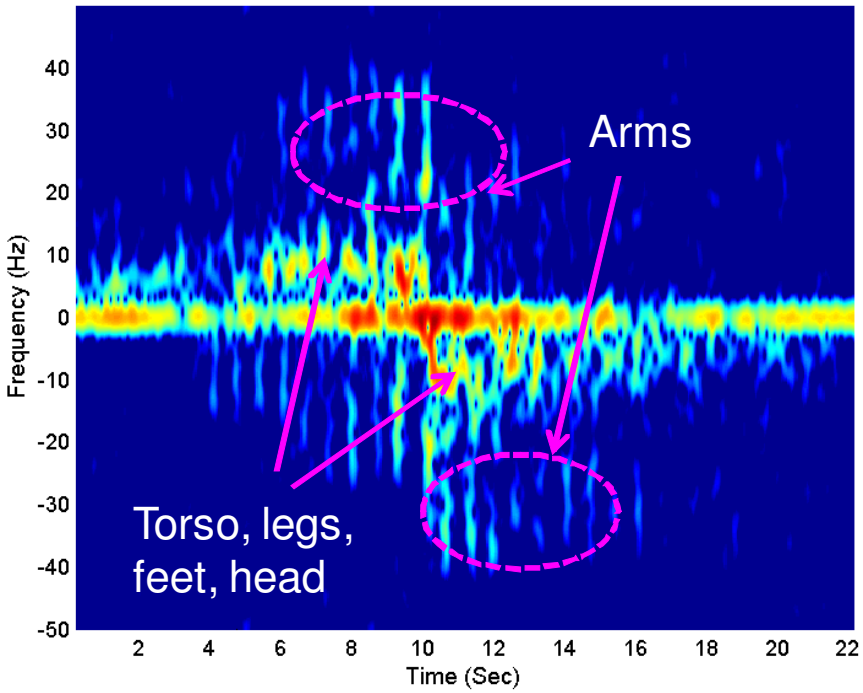


(a) High resolution range profile before removing static reflections



(b) High resolution range profile after removing static reflections

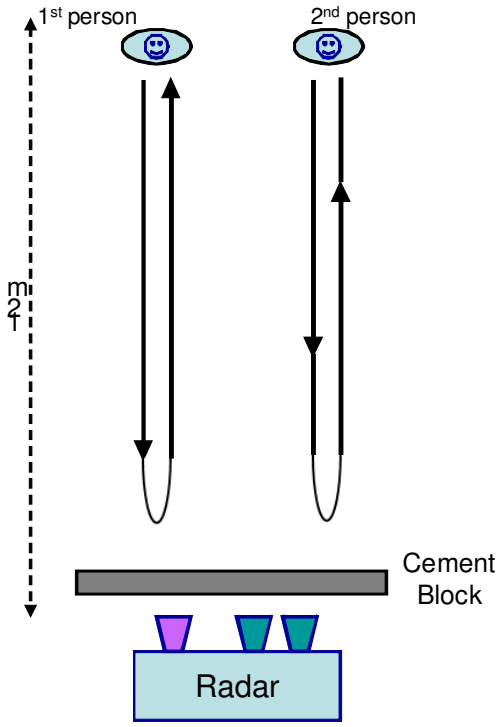
Figure 5.3 Acquired results when the person walking with two-arm swing.



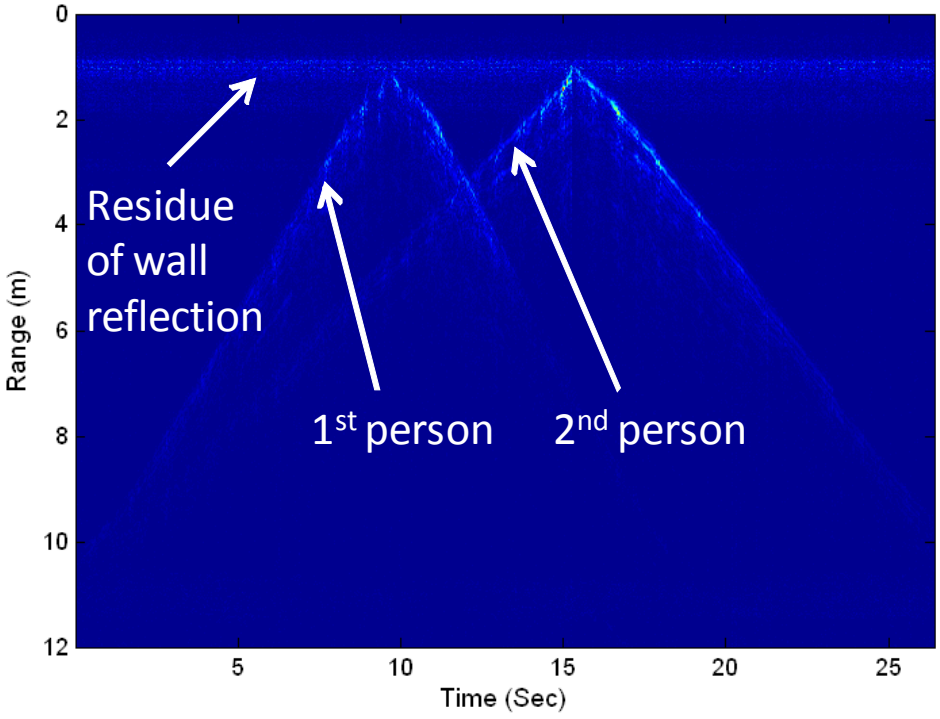
(c) Acquired spectrogram
Figure 5.3 Continued.

5.4 Doppler Tracking of Two Persons

Experiments were also performed to track the activity of more than one human object in a through wall scenario. The radar sensor was installed in front of the wall with a standoff distance of 1m. A cement block was used in the experiment with a thickness of 1cm. In the 1st experiment, two persons walked toward the same direction behind the wall, one walking faster while the other slower, as shown in Figure 5.4(a). The range profile of the radar returned signal after removing the static reflections is plotted in Figure 5.4(b), which has accurately indicated that two objects walked toward the radar sensor first and then walked backward at different speeds. By using a wideband pulse signal in the radar sensor, a high range resolution is achieved and it makes feasible to accurately separate multiple targets at different down ranges from the acquired range profile, which cannot be achieved from narrow band radars. The spectrogram presented in Figure 5.4(c) shows that the 1st person generates an absolute Doppler frequency shift of 20 Hz while the 2nd one renders 15 Hz, which relate to a radial velocity of 1m/s and 0.7m/s, respectively.

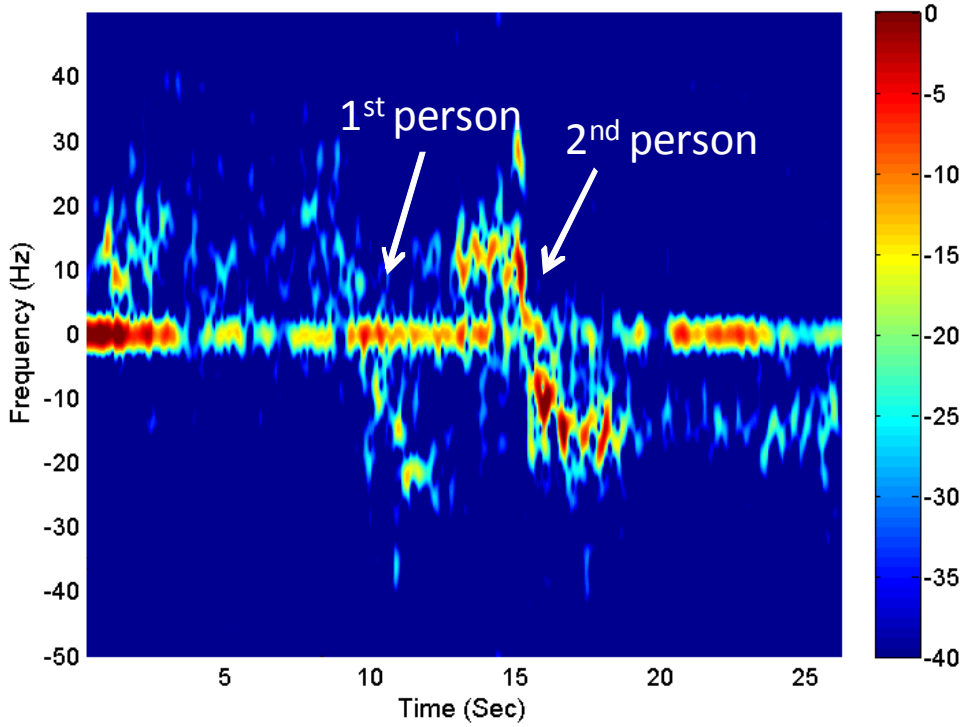


(a) Experimental setup



(b) High resolution range profile after removing static reflections

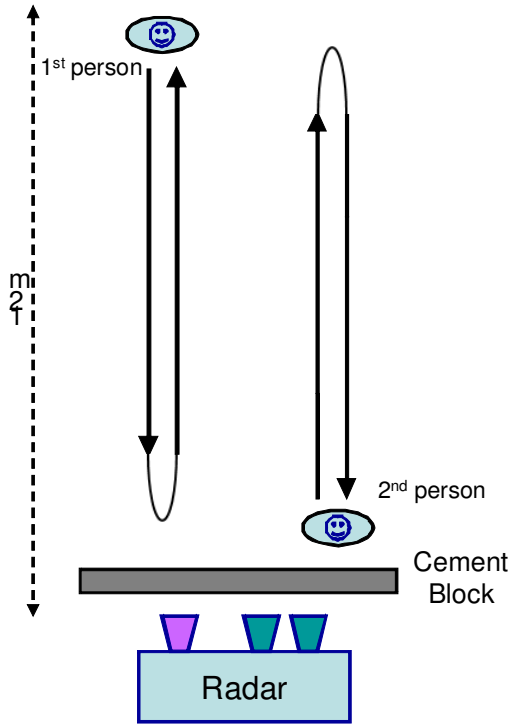
Figure 5.4 Experiment of tracking two persons walking toward same direction, one walking faster while the other slower.



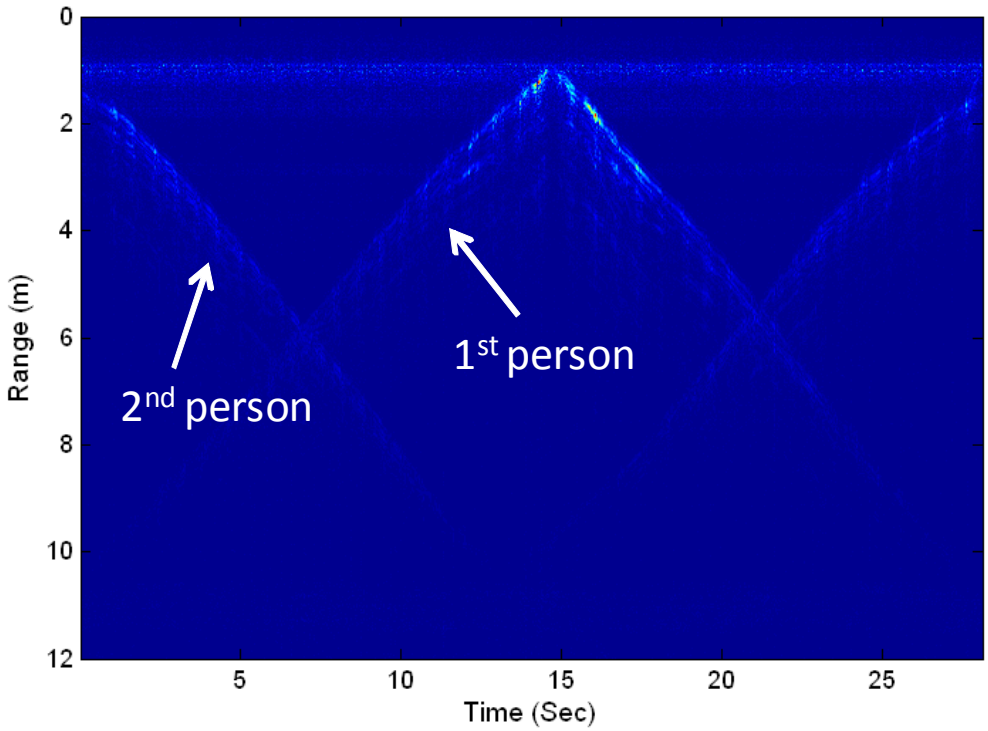
(c) Acquired spectrogram

Figure 5.4 Continued.

The 2nd experiment was carried out to track two persons walking toward opposite directions behind the wall, as the experimental setup shown in Figure 5.5(a). The change detection method based on equations (5-14) and (5-15) was utilized to remove the static reflections and to highlight any movement. The high resolution range profile of the two persons is presented in Figure 5.5(b). It is clearly observed that the 1st person started at a distance of 10m and approached radar sensor from 0 to 15s and then went backward while the 2nd person was around the wall at the beginning and departed radar sensor from 0 to 14s and then walked back to radar. The acquired spectrogram in Figure 5.5(c) matches well with the range profile result, show a positive Doppler frequency due to the target approaching while a negative Doppler frequency due to target receding. The two persons generate a similar absolute Doppler frequency shift of 12 Hz, which relate to an absolute radial velocity of 0.6m/s.

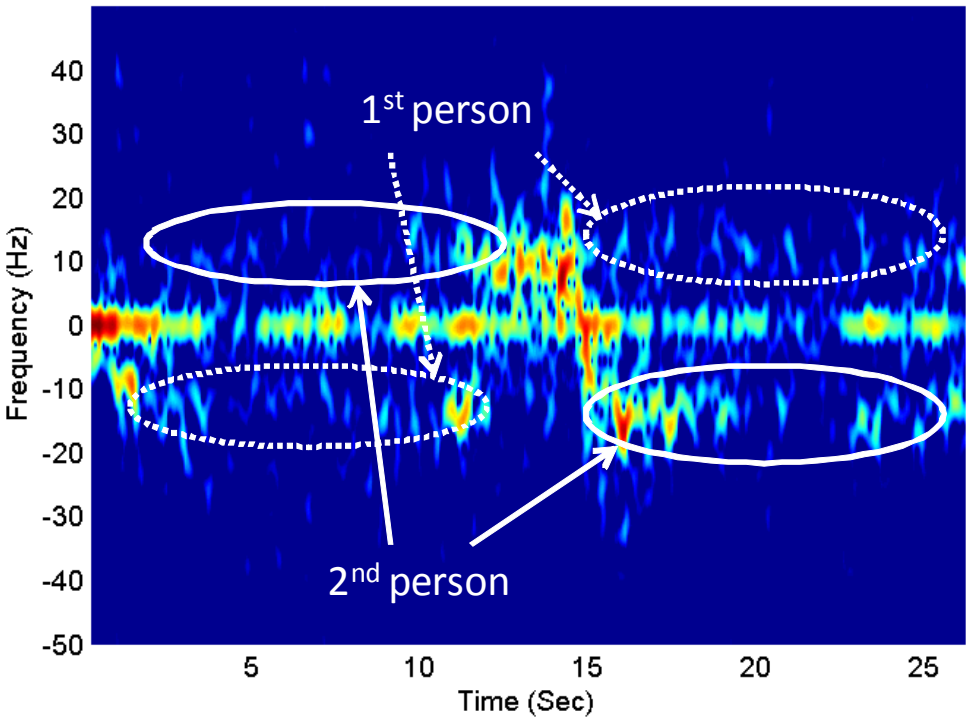


(a) Experimental setup



(b) High resolution range profile after removing static reflections

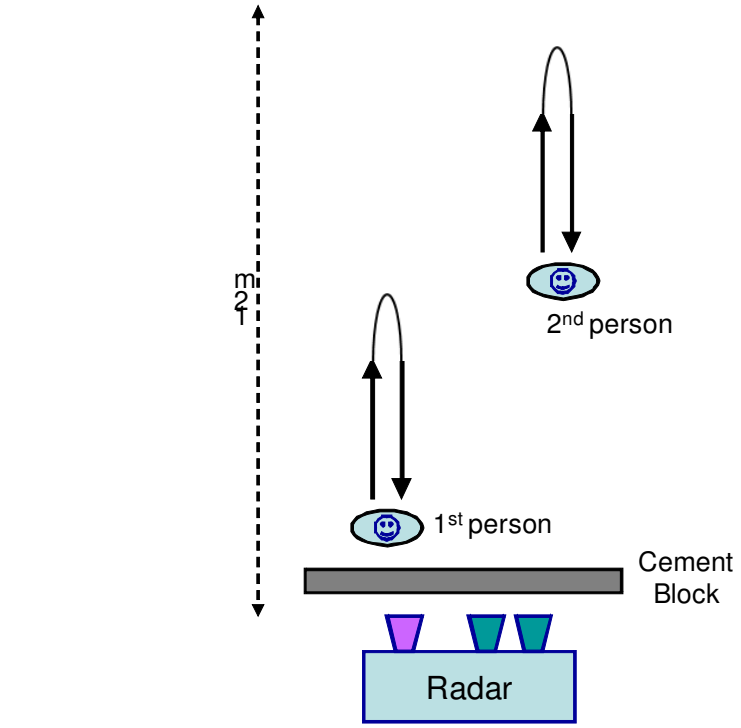
Figure 5.5 Experiment of tracking two persons walking toward opposite directions.



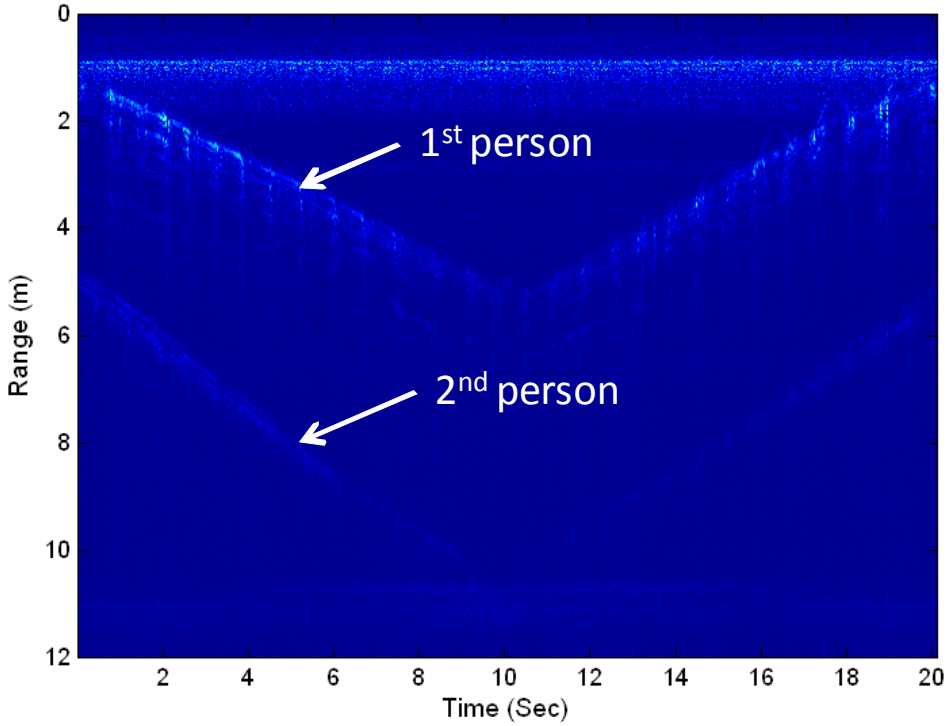
(c) Acquired spectrogram

Figure 5.5 Continued.

The 3rd experiment was carried out to track two persons walking toward the same direction, but at different distances to the radar, as the experimental setup shown in Figure 5.6(a). The high resolution range profile presented in Figure 5.6(b) has clearly shown the walking traces of the two persons. Both persons walked away from radar at 0 to 10s and then walked toward radar sensor at 10s to 20s. However, the 1st person started at a distance of 1m while the 2nd person started at a distance of 5m to the radar. Since the two walking persons cover different range bins, it is feasible to separate them from the collected radar return signal. When acquiring the spectrogram, the signal covering range bin from 1m to 5m was utilized for the 1st person while that covering 5m to 10m was applied for the 2nd person. Figure 5.6(c) and (d) presents the acquired spectrogram of the 1st person and 2nd person, respectively. For both persons, a negative Doppler frequency of -10 Hz was generated from 0 to 10s and a positive Doppler frequency of 10 Hz was rendered after that. The absolute Doppler frequency shift of 10 Hz relates to a radial velocity of 0.5m/s.

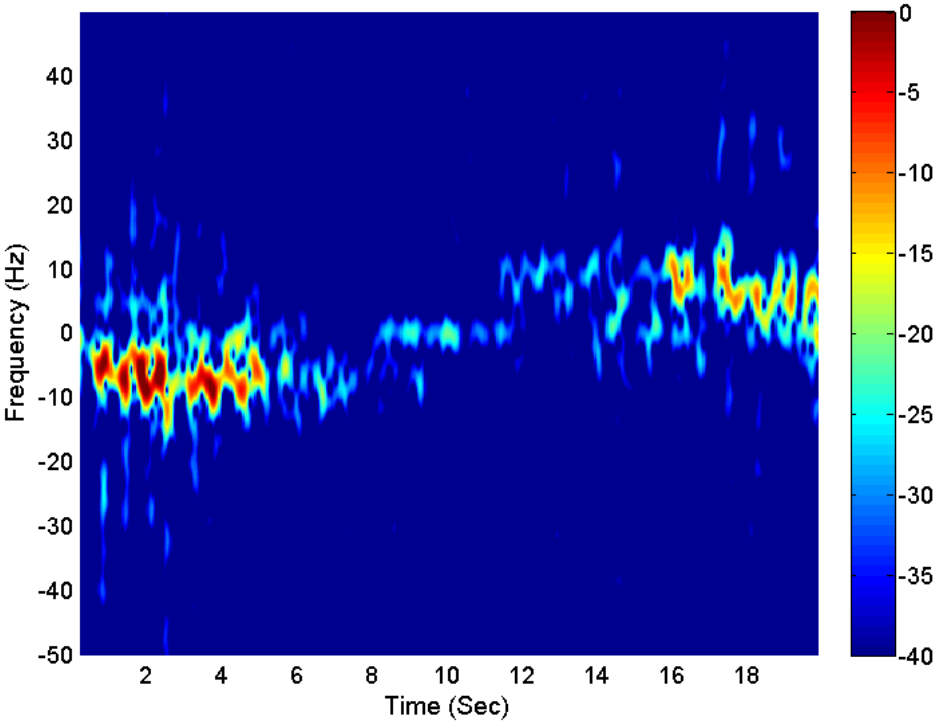


(a) Experimental setup

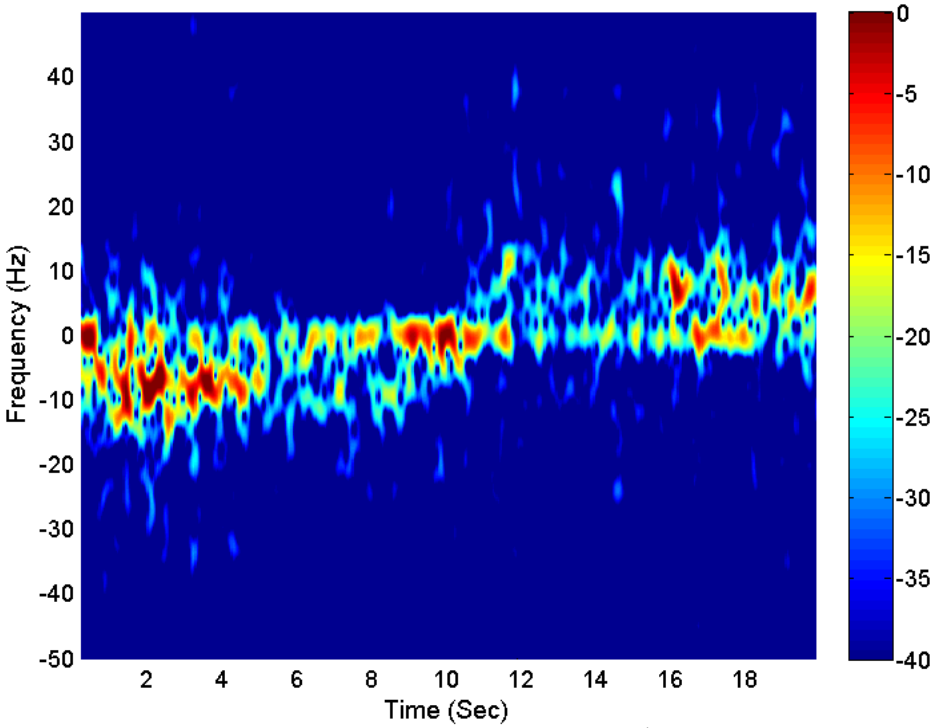


(b) High resolution range profile after removing static reflections

Figure 5.6 Experiment of tracking two persons walking toward the same direction but at different distances, one is closer to the radar while the other further from the radar.



(c) Acquired spectrogram of the 1st person



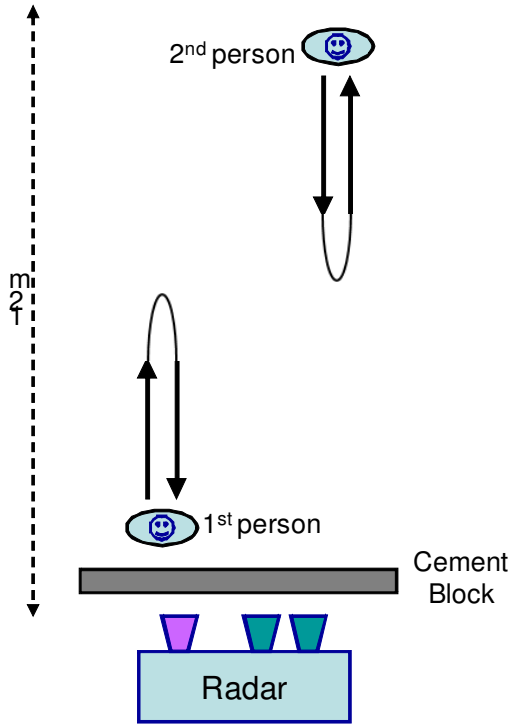
(d) Acquired spectrogram of the 2nd person

Figure 5.6 Continued.

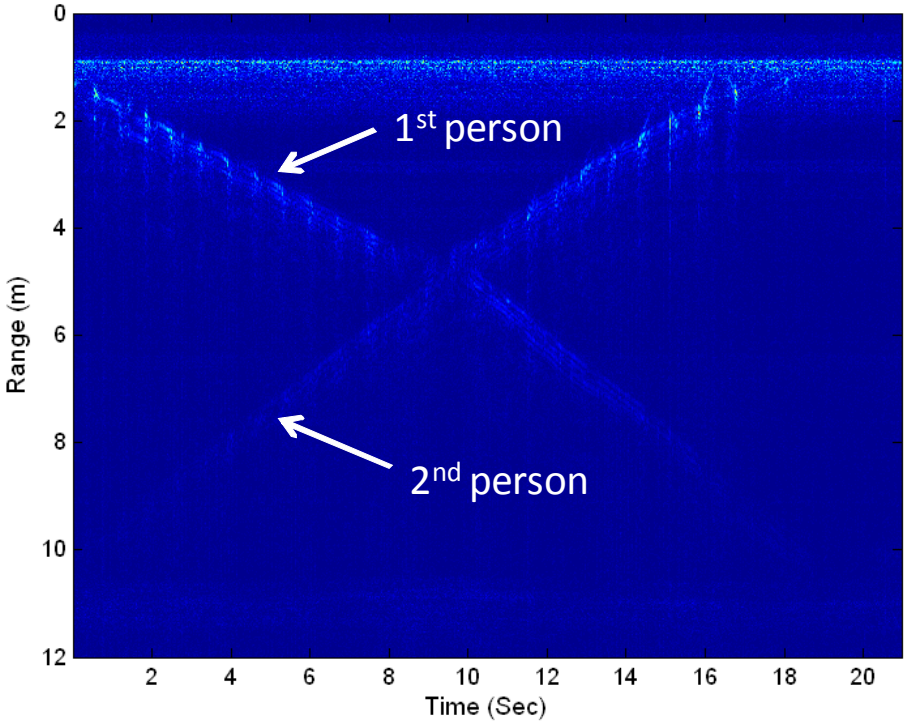
The 4th experiment was performed to track two persons walking toward opposite directions while at different distances too, as the experimental setup shown in Figure 5.7(a). The high resolution range profile of the two persons presented in Figure 5.7(b) while the static reflections have been removed in order to highlight any signal change due to the human motions. The 1st person started from the wall, walking away from the radar first at 0 to 10s and then walked back to radar from 10s to 20s. The 2nd person started at a distance of 10m, approaching radar first from 0 to 10s and then walked backward. The 1st person covers the range from 1m to 5m while the 2nd person walked through the range from 5m to 10m. By successfully separating the range bins, spectrograms generated by the two persons have been recovered separately according to their range bins, as shown in Figure 5.7(c) and (d) respectively. The 1st person generated an absolute Doppler frequency of 8 Hz while the 2nd person gave an absolute Doppler frequency of 10 Hz, which related to an absolute radial velocity of 0.4m/s and 0.5m/s, respectively.

5.5 Through Wall Respiration Detection of Stationary People

It is a very challenging job to detect and monitor stationary targets through a wall or barrier, especially when the target is very close to the wall. In such a scenario, respiration m-D detection is of great help to increase the detection chance by acquiring the chest wall motion during the breathing. It is reported that the average respiratory rate of a healthy adult is usually 12-20 breaths/min at rest and 35-45 breaths/min during strenuous exercise [103]. In addition, respiration detection can also be extended for monitoring patients, searching trapped people under rubble or building collapse, and supervising elderly when they are sleeping.

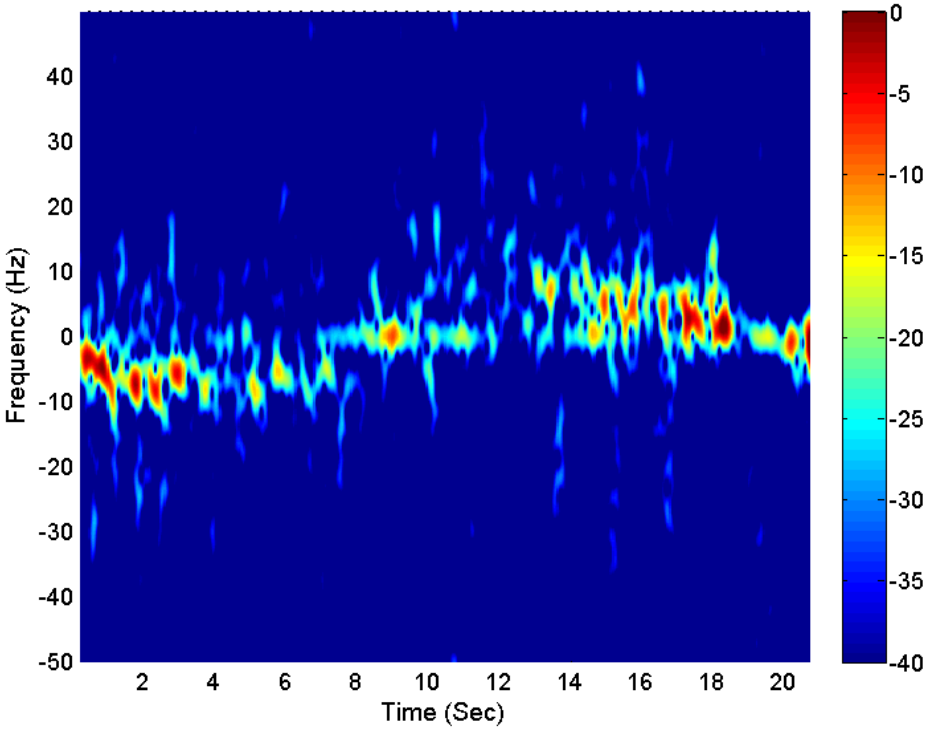


(a) Experimental setup

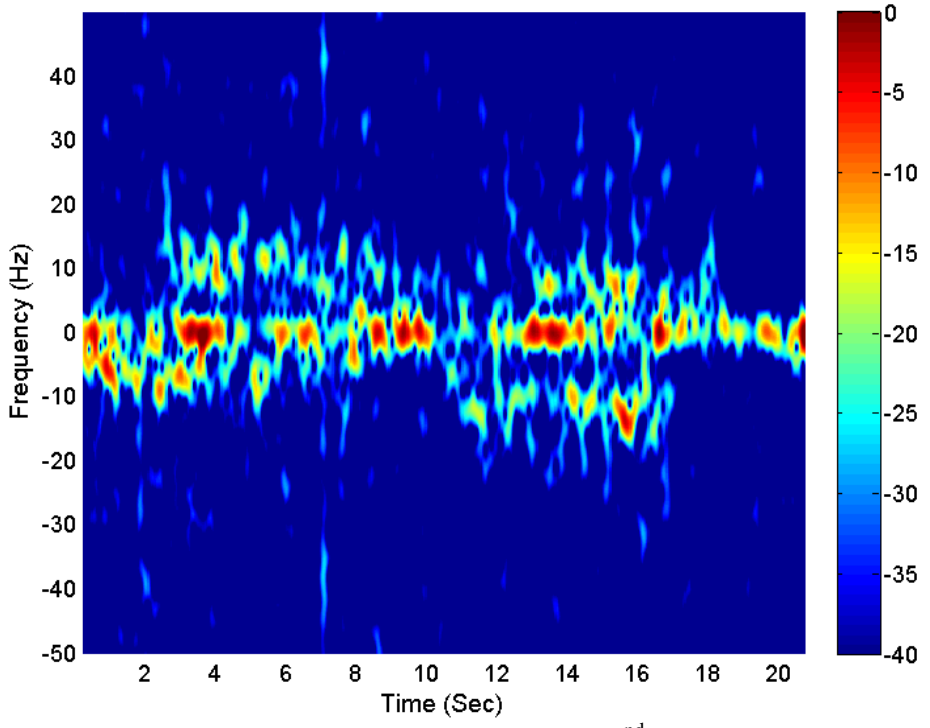


(b) High resolution range profile after removing static reflections

Figure 5.7 Experiment of tracking two persons walking toward different directions and at different distances too.



(c) Acquired spectrogram of the 1st person



(d) Acquired spectrogram of the 2nd person

Figure 5.7 Continued.

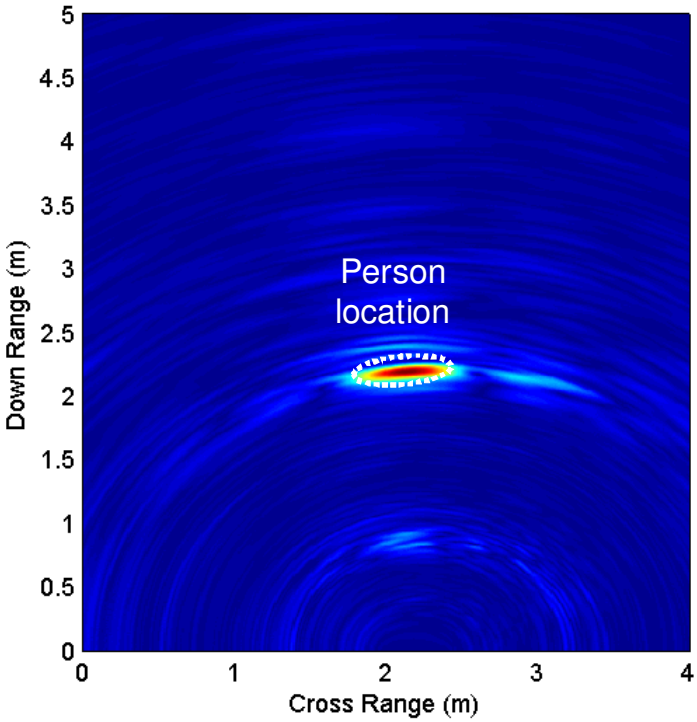
We have successfully detected the breathing signatures of stationary human objects utilizing the developed UWB Doppler radar. Experiments were performed to supervise single and two human targets in a through concrete wall scenario. Distinctly different Doppler frequency spectrums are observed when the person breathes normally and holds the breath. By using UWB technology, the radar sensor shows its capability to separate multiple human objects at different down ranges and to acquire the respiratory characteristics for each individual person. Even for multiple persons at the same down range but at different cross ranges, the developed radar sensor can still accurately separate them by performing the SAR operation. The developed radar prototype shows its advantage for searching/monitoring multiple stationary people through their respiration, when compared to narrow band Doppler radar systems, where a high localization resolution is achieved and is utilized to accurately separate multiple radar targets.

5.5.1 Single Person Experiment

The 1st experiment was performed to localize and detect the respiratory characteristics of a stationary person standing behind a 1-cm thick cement wall, as the experimental setup shown in Figure 5.8(a). The radar was placed to face the wall with a standoff distance of 1m. Equations (5-14) and (5-15) have been used to remove the static reflections, including wall, surrounding scatterer, and even motionless parts of the human body. The signal after removing the static reflections is mainly due to the movement of chest wall when breathing. The position of the target is presented in Figure 5.8(b), showing that the person stands 1.2m behind the wall with a cross range of 2.1m. The range profile in Figure 5.8(c) indicates a respiratory rate of approximately 27 breaths/min, consisting of both shallow breathing and deep breathing. We have also investigated the Doppler frequency spectrum of radar return signal by calculating the FFT of the slow-time sampled pulse. Figure 5.8(d) shows the Doppler frequency spectrum when the person breaths normally while Figure 5.8(e) introduces the case when the person holds his breath. It is observed that the normal breathing generates a fundamental Doppler frequency of 0.48 Hz and high order harmonics while holding the breath do not render any Doppler frequency shift.

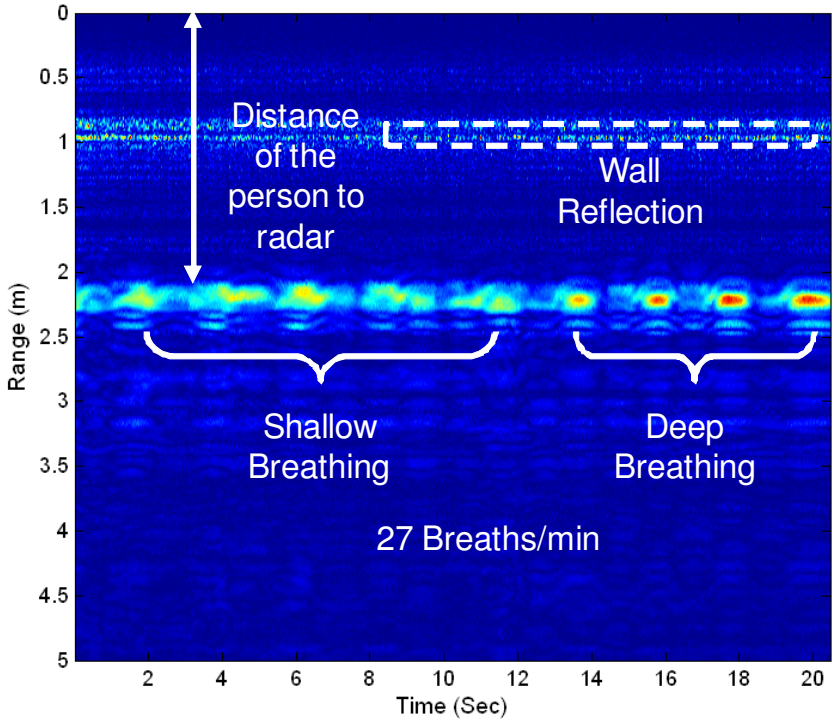


(a) Experimental setup

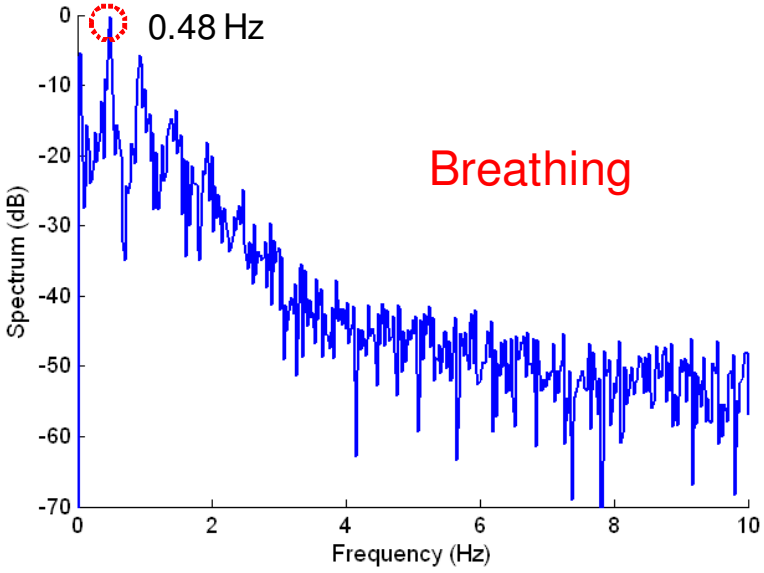


(b) Localization of the human target

Figure 5.8 Localization and respiration detection of single person through a cement wall, showing a respiratory rate of 27 breaths per minute and a Doppler frequency of 0.48 Hz.

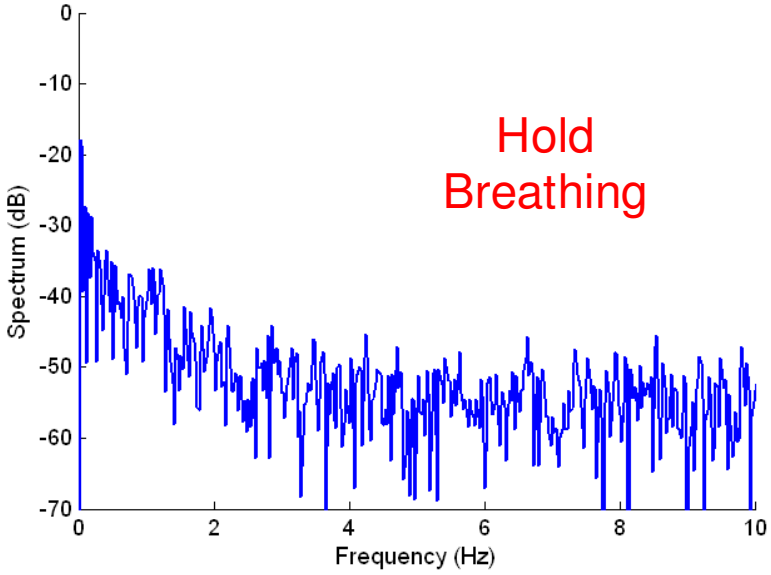


(c) Range profile versus time when the person breathe normally



(d) Doppler frequency spectrum when the person breathes normally

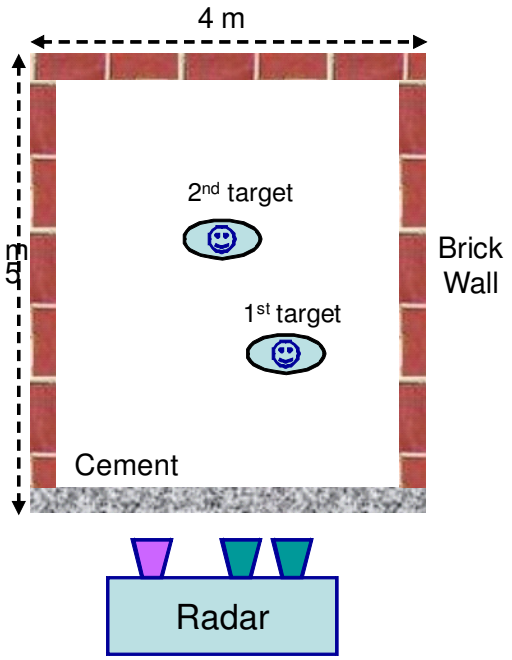
Figure 5.8 Continued.



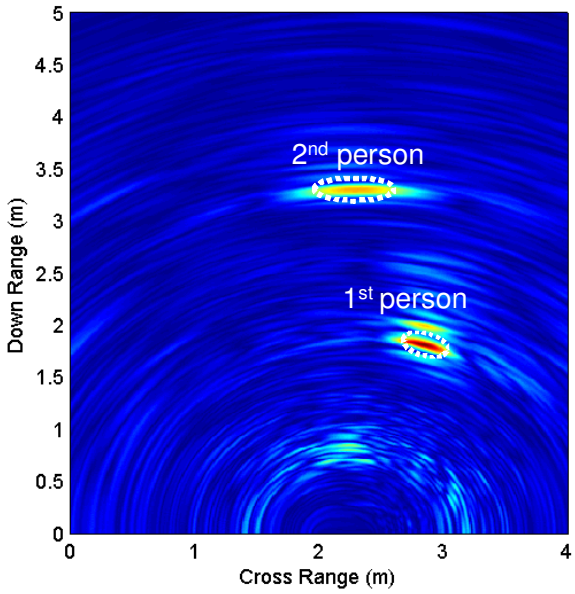
(e) Doppler frequency spectrum when the person holds the breath
Figure 5.8 Continued.

5.5.2 Two Persons at Different Distances

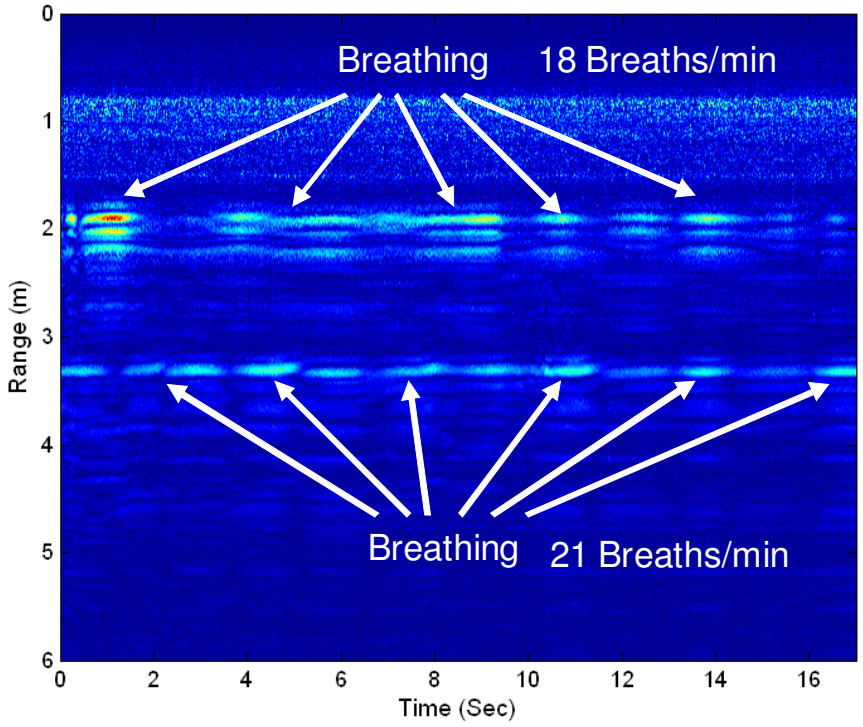
The 2nd experiment was carried out to identify the respiration of two stationary persons, who stand at different distances to the radar sensor behind the wall, as shown in Figure 5.9(a). The similar method based on equations (5-14) and (5-15) has been used to remove the static reflections in the signal processing. By using a 700 ps narrow pulse and a 10 ps fine sampling resolution, the radar sensor has accurately separated two targets by the down range (i.e., distance to radar sensor), as shown in Figure 5.9(b), which shows that the 1st person is at a down range of 3.2m and a cross range of 2.1m while the 2nd person at a down range of 2m and a cross range of 2.9m. The range profile is demonstrated in Figure 5.9(c), which introduces a respiratory rate of 18 breaths/min from the 1st person and 21 breaths/min from the 2nd person. Since radar return signals from the two persons are at distinct range bins, FFT was applied on the slow-time sampled pulse at related range bins to acquire the Doppler frequency spectrum, as shown in Figure 5.9(d) and (e), which shows a Doppler frequency of 0.29 Hz from the 1st person and 0.34 Hz from the 2nd person.



(a) Experimental setup

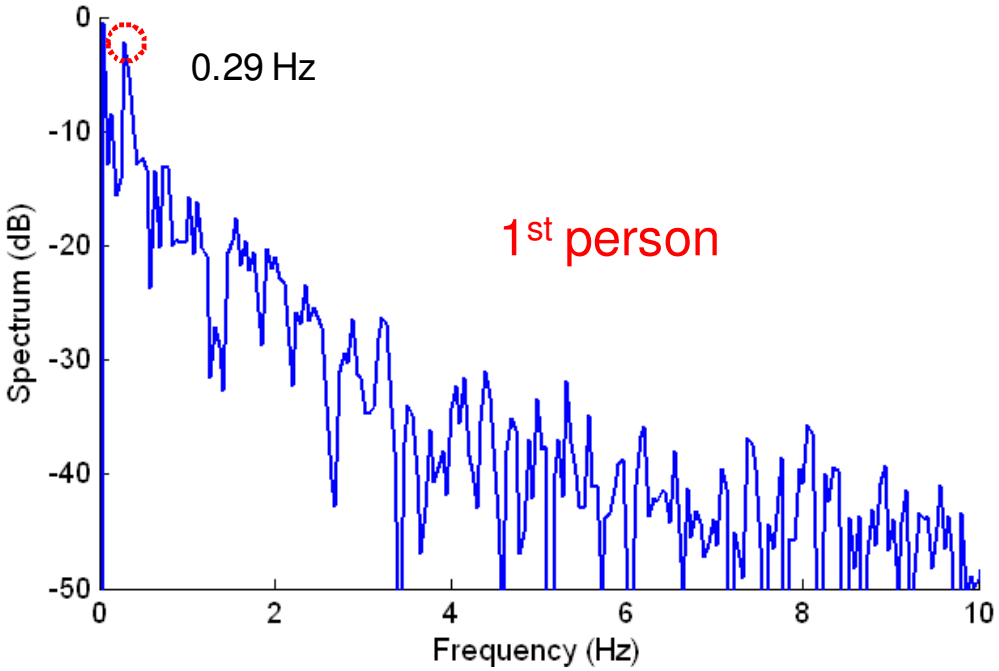


(b) Two human targets localization

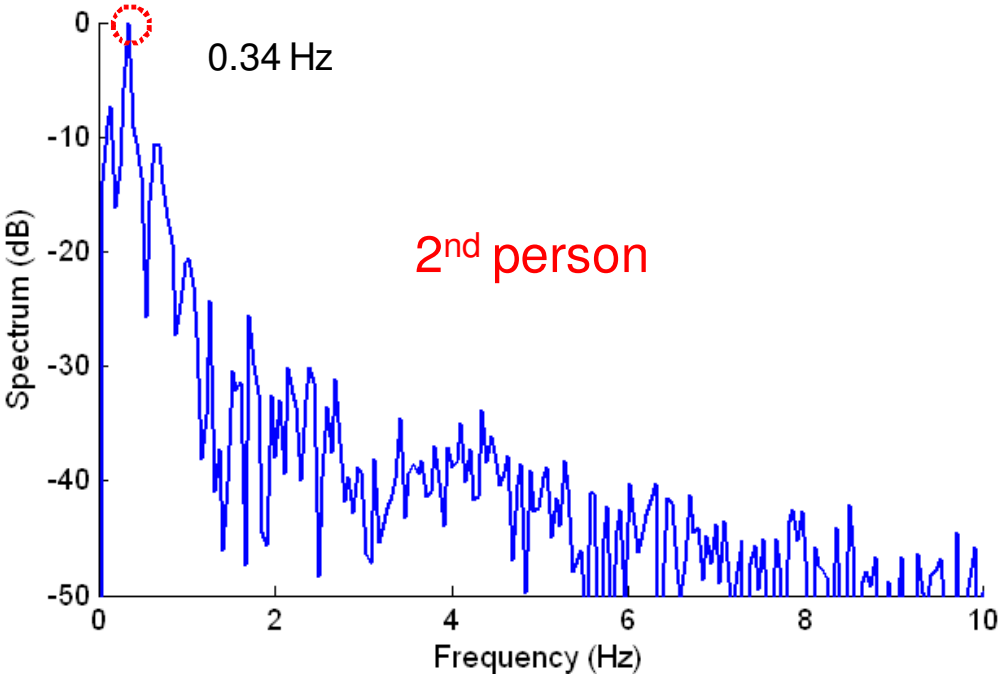


(c) Range profile versus time

Figure 5.9 Localization and respiration detection of two persons through a cement wall. The two persons stand at different distances to the radar, one is closer while the other is further.



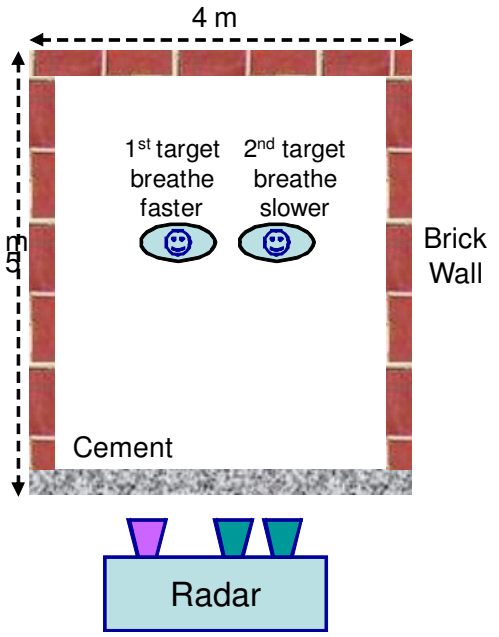
(d) Doppler frequency spectrum due to the breathing of 1st person



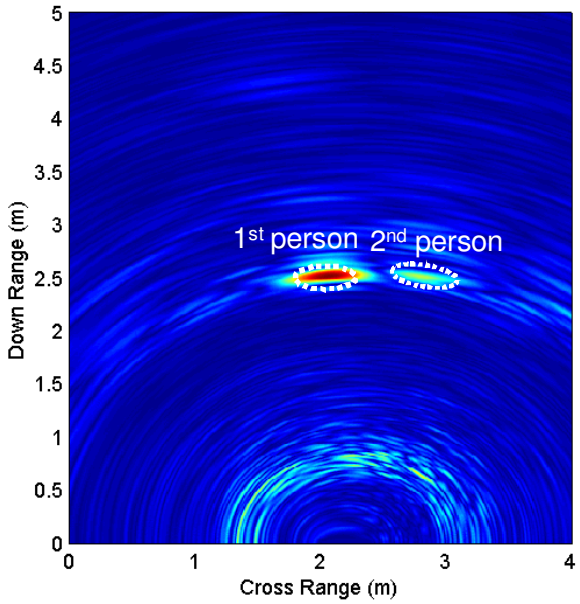
(e) Doppler frequency spectrum due to the breathing of 2nd person
Figure 5.9 Continued.

5.5.3 Two Persons at Same Distance, But Different Angles

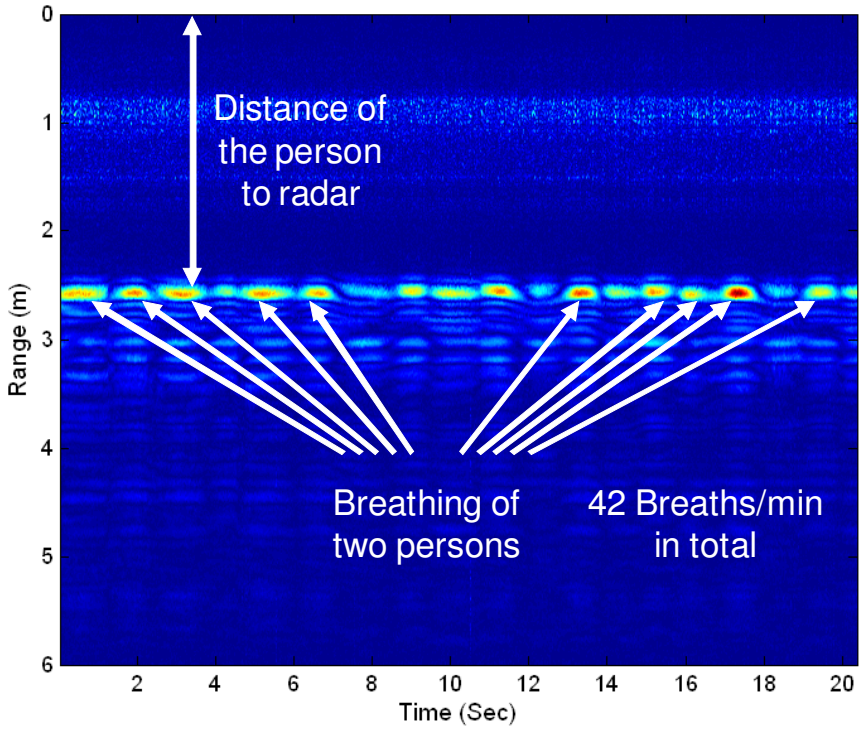
The 3rd experiment was accomplished to recognize the respiration of two stationary persons standing at the same distance but at different cross ranges, as the experimental setup shown in Figure 5.10(a). Two persons breathe at different speeds, the 1st one faster while the 2nd one slower. Similarly, Equations (5-14) and (5-15) have been used to remove the static reflections in post signal processing. By synthetically combining the fast-time signals from the 8 receiving antennas to achieve a very narrow beam, the radar sensor was able to separate the two human objects, as shown in Figure 5.10(b), which introduces that two persons are at the same down range of 2.5m but the 1st person is at a cross range of 2m while the 2nd person at a cross range of 2.9m. The range profile in Figure 5.10(c) only shows a total respiratory rate of 42 breaths/min from two persons but cannot distinguish the individual respiratory rate. In order to separate the respiratory rate, smoothed pseudo Wigner-Ville distribution (WVD) [104] was performed for each individual on the combined signal, which was achieved by synthetically combing the slow-time signals from the 8 receiving antennas according to the true position of the human object. A Matlab program was implemented to acquire the Wigner-Ville spectrum, as shown in Appendix A.6. WVD does not suffer from the window effects as the spectrogram and is very attractive for analysis of non-stationary signals [104]. The Wigner-Ville spectrum in Figure 5.10(d) shows a respiratory rate of 27 breaths/min from the 1st person while that in Figure 5.10(e) presents a respiratory rate of 15 breaths/min from the 2nd person.



(a) Experimental setup

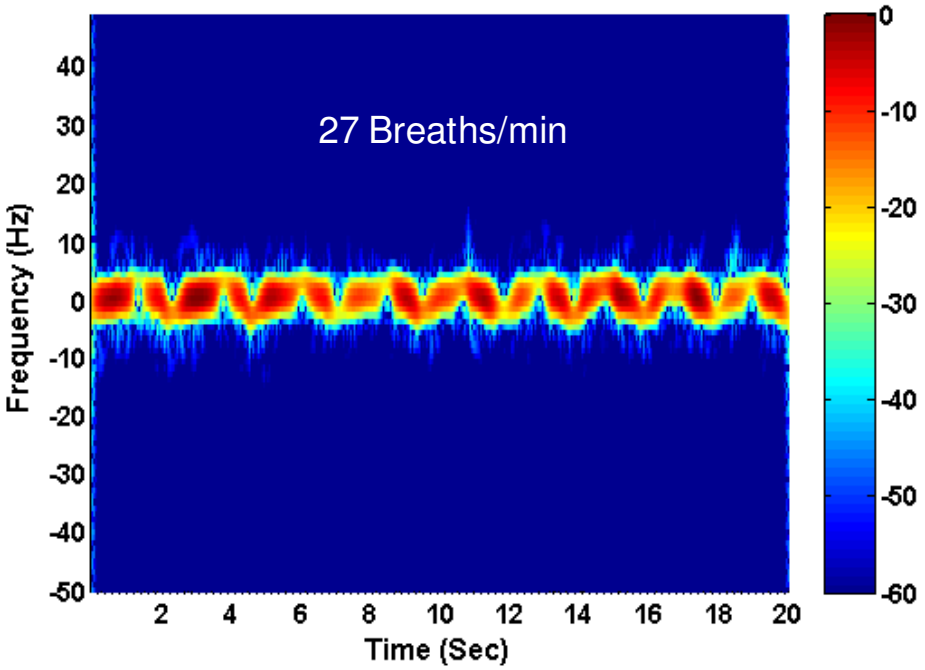


(b) Two human targets localization

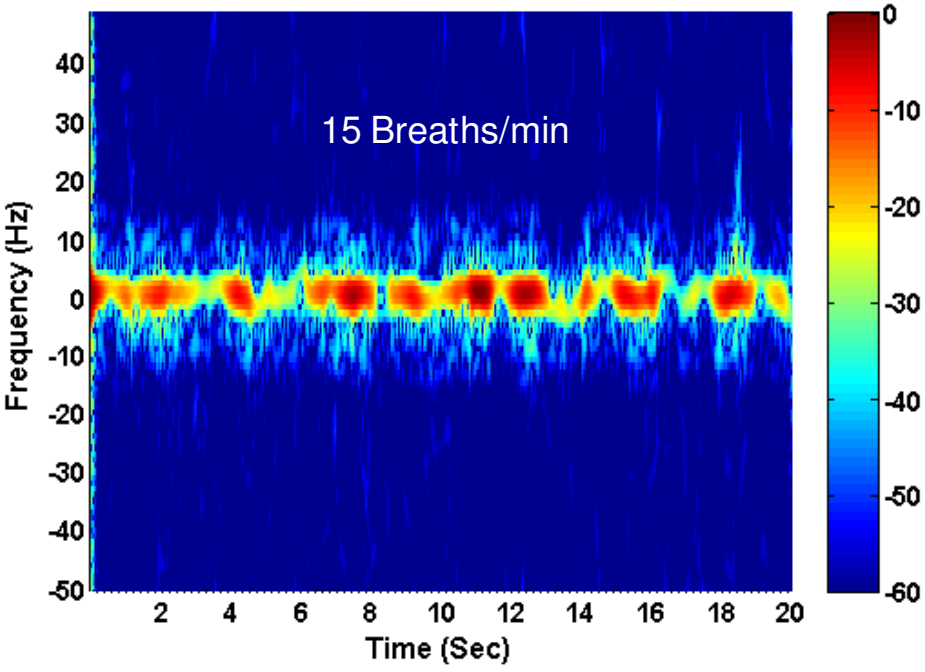


(c) Range profile versus time

Figure 5.10 Localization and respiration detection of two persons through a cement wall. The two persons stand at the same distance to the radar, but at different cross ranges. The 1st person breathes faster while the 2nd one breathes slower.



(d) Wigner-Ville spectrum due to the breathing of 1st person



(e) Wigner-Ville spectrum due to the breathing of 2nd person

Figure 5.10 Continued.

5.6 Alternative Technology: CW Doppler Radar

CW radar has generally simple structure and is well known for its wide range of applications like speed limit enforcement, human gait analysis and vital sign monitoring. This type of radars is useful for determining a target's velocity by comparing the frequency differences in the transmitted and received signals. Typically, CW Doppler radar sends out a signal from a LO, and then collects the reflected signal using a homodyne receiver, where the returned signal is directly down converted to baseband by mixing with the same LO. Although the homodyne receiver is simple in circuit complexity, it suffers from several problems such as DC offset and low frequency noise from power supply and other system components (e.g., amplifier, mixer) [105].

To overcome these associated homodyne receiver's drawbacks, a novel superheterodyne receiver based on FPGA is proposed here and has been developed to process the signal in the frequency domain. The incoming signal is initially converted to an intermediate frequency (IF) to filter out the unwanted low frequency components. Next, the filtered IF signal is shifted to baseband using a digital down converter (DDC) module implemented in FPGA. A large array of configurable logic blocks within the FPGA gives great flexibility to implement the DDC, compared to the conventional dedicated hardware components solution. As an example, a detailed design of a 3 GHz CW Doppler radar prototype, including RF front-end module, signal digitization and DDC have been implemented and will be presented in this paper. Experiment using the developed CW Doppler radar for human activity sensing will be discussed as well.

5.6.1 CW Doppler Radar Prototype

In our implementation, CW Doppler radar shares a lot of common blocks with the developed UWB pulse radar, including the transmitting and receiving antennas, power amplifier, LNA, and mixer to save prototyping cost. All selected components demonstrate wideband performance in order to adapt for UWB pulse radar, however, they can be easily replaced with narrow band components in the CW radar prototype.

A detailed block diagram of our developed CW Doppler radar prototype is shown in Figure 5.11. In the transmitter side, a 3 GHz CW signal generated by an Agilent signal generator, 83622B, is amplified through a Mini-Circuits ZHL-42 power amplifier before being sent for transmission through a Vivaldi antenna. In the receiver side, the radar returned signal collected by the receiving Vivaldi antenna is firstly amplified by a Hittite HMC753 LNA. Next, the amplified signal is down converted to 20 MHz IF band by being mixed with a 2.98 GHz LO, which is generated by another Agilent signal generator, E8257D. The two Agilent signal sources are synchronized by wiring their 10 MHz reference clock. It is worthy noted that the two Agilent signal sources can be replaced with commercially available phase-locked loop that features an integrated VCO, such as HMC830LP6GE from Hittite [106]. Next, the 20 MHz IF signal is band pass filtered to remove the low frequency noise/interference and then sent to the ADC, ADC16DV160 from National Semiconductor, for signal digitization. The IF signal is digitized using a 60 MHz sampling clock, which is provided by an external clock and is synchronized with the FPGA reference clock. Next, the sampled data is sent to the FPGA for digital down conversion. The DDC implemented in Xilinx Virtex-5 FPGA, XC5VSX35T, as shown in Figure 5.11, consists of three subcomponents: direct digital synthesizer (DDS), multiplier, and decimation filter. The VHDL code that was used to implement the DDC is shown in Appendix C.

A detailed block of the quadrature DDS implemented in FPGA is shown in Figure 5.12. The simplest configuration of the DDS core, i.e., phase truncation DDS [107] is used, which includes three subcomponents: phase accumulator, quantizer, and lookup table. The phase accumulator has a width of B = 28 bits and computes a phase slope that is mapped into a complex sinusoid by a lookup table (LUT). The quantizer, working simply as a slicer, accepts the high-precision phase angle $\theta(n)$ and generates a lower-precision representation of the angle denoted as $\Theta(n)$. This value is presented to the address port of a LUT that performs the mapping from phase-space to time. The output frequency, f_{out}, of the DDS waveform is a function of the system input clock frequency f_{clk}, the phase width B, and the phase increment value $\Delta\theta$. For example, the phase increment value $\Delta\theta$ required to generate an output frequency of 20 MHz is:

$$\Delta\theta = \frac{f_{out}\,2^{B}}{f_{clk}} = \frac{20M \cdot 2^{28}}{60M} = 89{,}478{,}485.333 \tag{5-21}$$

This value must be truncated to an integer giving the following actual output frequency:

$$f_{out} = \frac{\Delta\theta f_{clk}}{2^{B}} = \frac{89{,}478{,}485 \cdot 60M}{2^{28}} = 19{,}999{,}999.925\,Hz \tag{5-22}$$

The actual output frequency has a small constant deviation of 0.075 Hz, which will generate a constant frequency offset at the Doppler frequency shift and has been compensated for in our post data processing.

Next, the down conversion is performed through two multipliers, as presented in Figure 5.11, where the digitized input signal is multiplied with amplitude values of the sine and cosine functions stored in the LUT respectively. Both data I and Q are acquired in order to avoid the overlap of positive and negative Doppler frequency shifts. The utilized Xilinx FPGA can generate two different multiplier architectures, i.e., parallel and constant-coefficient multipliers, for two complement signed or unsigned data. In our design, a parallel multiplier is utilized, which accepts two signed input buses with a width of 16-bit and generates the product of these two values as the output with a width of 32-bit.

After that, a decimation filter, i.e., cascaded integrator-comb (CIC) filter combined with a decimator, is utilized to low pass filter and down sample the I/Q data, as indicated in Figure 5.11. CIC filters are typically employed in applications that have a large excess sample rate, i.e., the system sample rate is much larger than the bandwidth occupied by the processed signal as in digital DDCs. The general system response of a CIC is

$$H(z) = \frac{\left(1 - z^{-RM}\right)^{N}}{\left(1 - z^{-1}\right)^{N}} \tag{5-23}$$

where N is the number CIC stages, R is the rate change (decimation), and M is the differential delay in the comb section stages of the filter. In our design, the data digitized by the 60 MHz sampling clock is decimated to achieve a sampling rate of 2 MS/S by using the CIC filter, with $N = 3$, $R = 1$, and $M = 20$, to remove the out-of-band spectrum.

Next, the I/Q data after undersampling is transferred to a computer in *real-time* through a USB2.0 communication link, which allows a maximum data uploading rate of 25 MB/S.

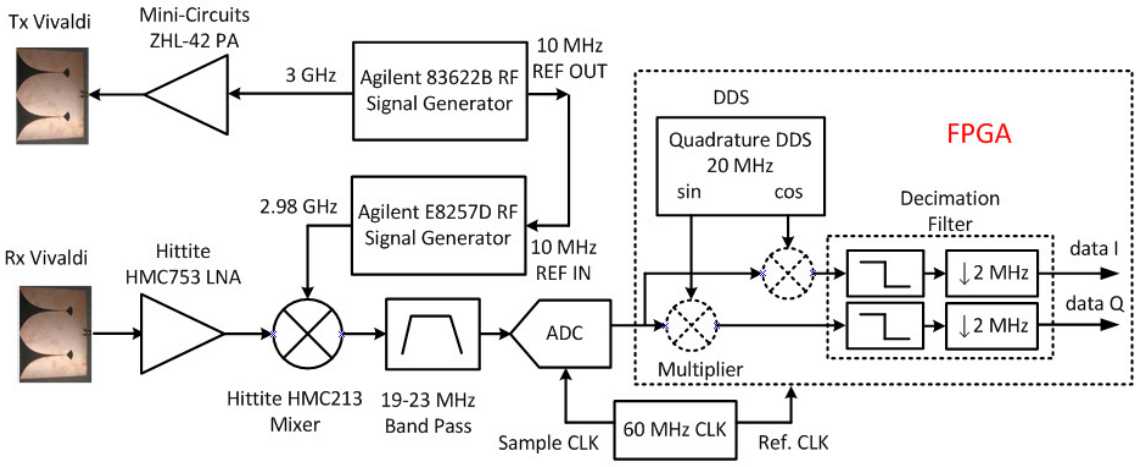


Figure 5.11 Detailed block diagram of the CW Doppler radar prototype.

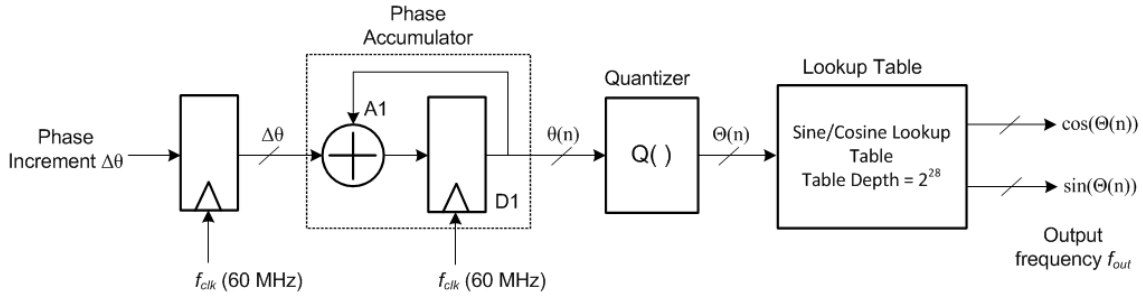


Figure 5.12 Detailed block of the quadrature DDS implemented in FPGA.

5.6.2 Doppler Detection Experiment

To demonstrate the performance of the developed CW Doppler radar based on FPGA technique, two experiments have been carried out to investigate the m-D signatures of human physical activities. The 1st experiment performed is to extract the Doppler information when a person was riding an exercise bike, as shown in Figure 5.13. This activity is comprised of many motions from both human body and the bike, including the movement of arms, the cycling of legs, the swinging of arm handles, the speedy rotation of flywheel, and etc. STFT tool based on equation (5-16) has been

utilized in the post data processing to extract the Doppler frequency shift of the radar object. Figure 5.14(a) introduces the acquired spectrogram when the person was riding the bike slowly, with the colormap scale from 0 to -100dB. The Doppler frequency shifts due to the arm handles and the human body are within the range of ± 10 Hz and have a higher intensity, as shown in Figure 5.14(a). The running flywheel has generated a series of positive and negative Doppler frequency shifts in the range of 20 Hz to 60 Hz. Next, the person has speeded up pedaling the bike, with the newly acquired spectrogram presented in Figure 5.14(b). The Doppler frequency shifts generated by the arm handles and the human body have significantly increased, and so do those from the flywheel. The repetition rate of the motion has increased from 32 rounds/min to 68 rounds/min, according to Figure 5.14(a) and (b). After the workout, the person has left while the radar was still monitoring the exercise bike, with the acquired spectrogram indicated in Figure 5.14(c). The m-D signatures of the flywheel, arm handles and pedals have indicated that the bike slowed down gradually and stopped completely after 16 seconds.

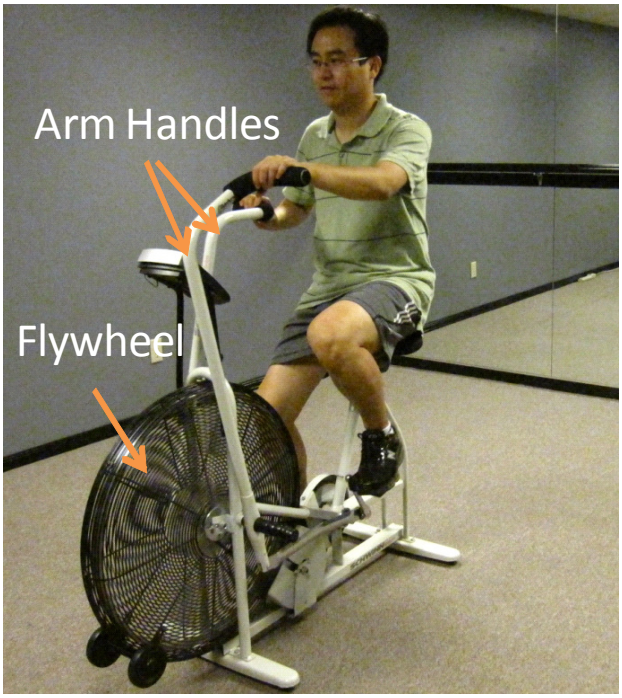
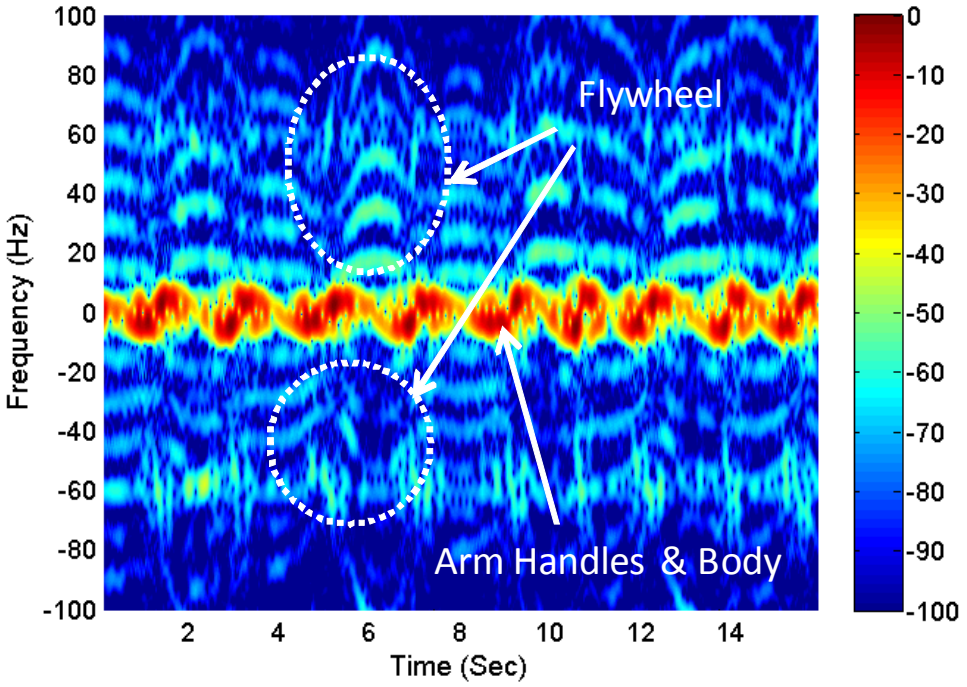
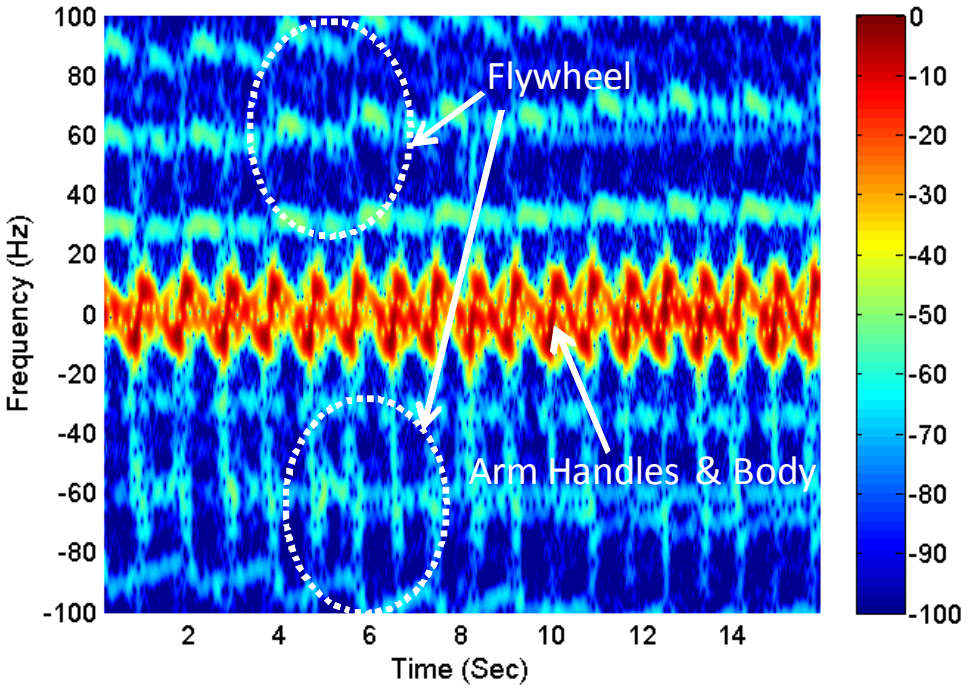


Figure 5.13 Experimental setup of sensing a person riding exercise bike.

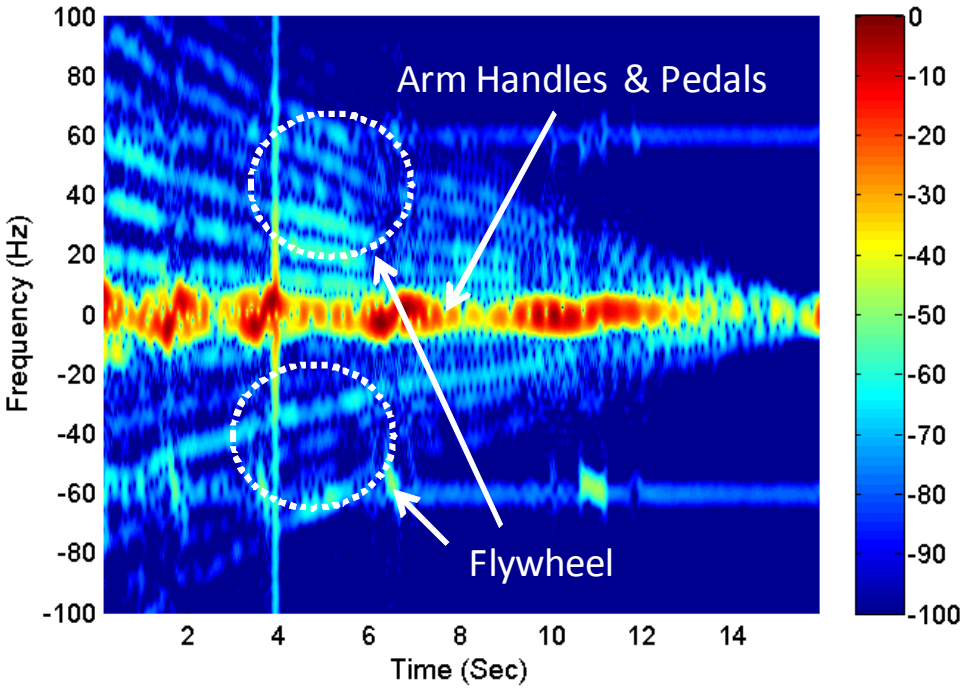


(a) Acquired spectrogram when person riding the bike at a slower speed



(b) Acquired spectrogram when person riding the bike at a faster speed

Figure 5.14 Acquired spectrogram when sensing a person riding exercise bike using the developed CW Doppler radar.



(c) Acquired spectrogram when person left the bike after the exercise

Figure 5.14 Continued.

The 2nd experiment was carried out to investigate the m-D signature of a person walking/jogging on the treadmill, as shown in Figure 5.15. Time-frequency analysis tool based on STFT has been utilized to acquire the Doppler information of the human motions. The acquired spectrogram results shown in Figure 5.16(a) and (b) indicate the motions of the person when he is walking and jogging on the treadmill, respectively. Figure 5.16(a) has presented the Doppler frequency pattern within ± 20Hz due to the movement of legs, feet and torso, as well as frequency shift humps at 20-60 Hz from the arms motion. Positive and negative Doppler frequency humps have been generated simultaneously because of the two-arm swinging; one arm swings forward while the other swings backward. The maximum radial velocity of the arm (i.e., due to the hand) can be calculated as 3 m/s, using equation (5-20), where f_D (60 Hz) is the measured maximum Doppler frequency shift and indicated in Figure 5.16(a), and λ (10 cm) is the wavelength of the 3 GHz CW signal. The jogging activity on the treadmill shows distinct spectrogram pattern from the walking motion and a much faster repetition frequency, as

indicated in Figure 5.16(b). When jogging, the person typically swings the arms in a smaller range, compared to walking activity. The Doppler frequency shifts due to the arms movement overlap with those generated by the torso and legs, as shown in Figure 5.16(b). We did not see obvious frequency shift humps from the arms movement in the jogging activity.

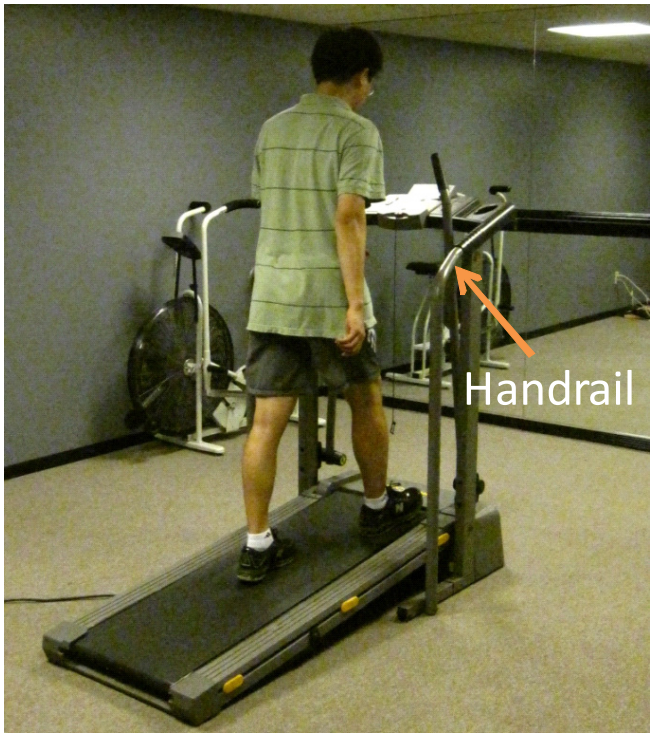
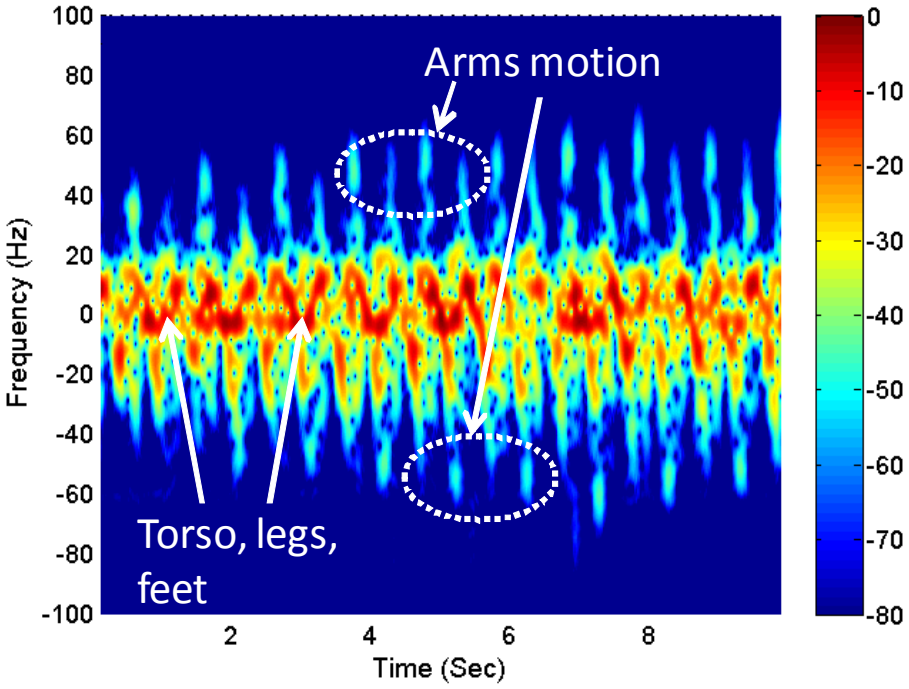
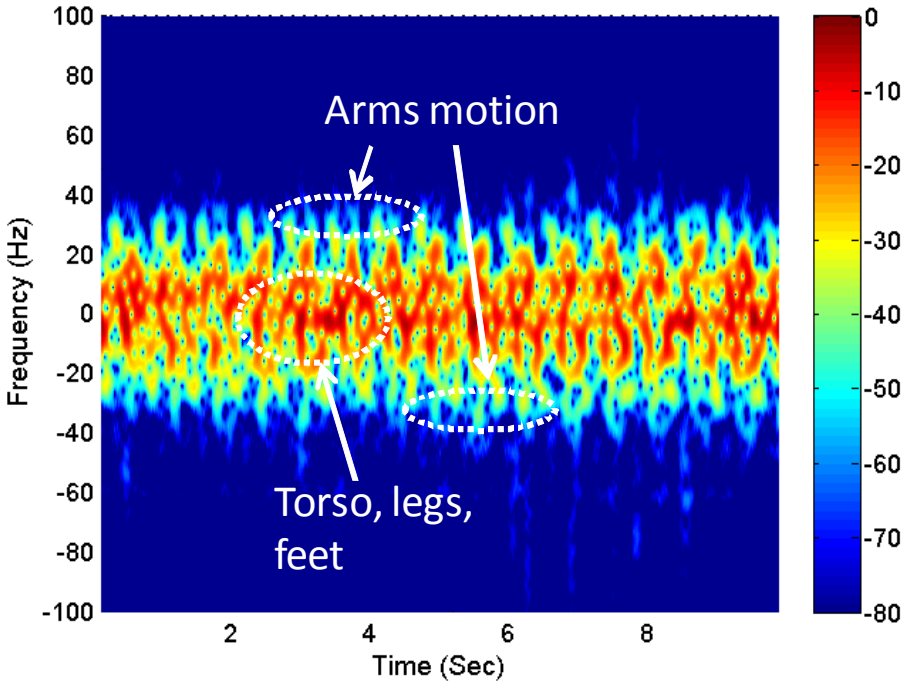


Figure 5.15 Experimental setup of sensing a person walking/jogging on the treadmill.



(a) Acquired spectrogram when person walking on the treadmill



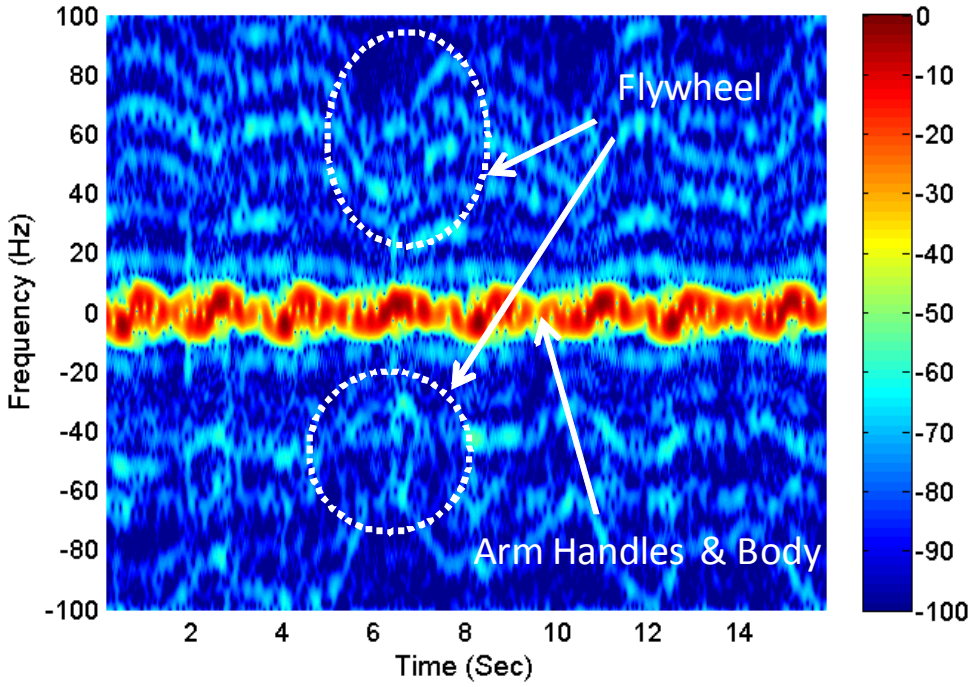
(b) Acquired spectrogram when person jogging on the treadmill

Figure 5.16 Acquired spectrogram of sensing a person walking/jogging on the treadmill using the developed CW Doppler radar.

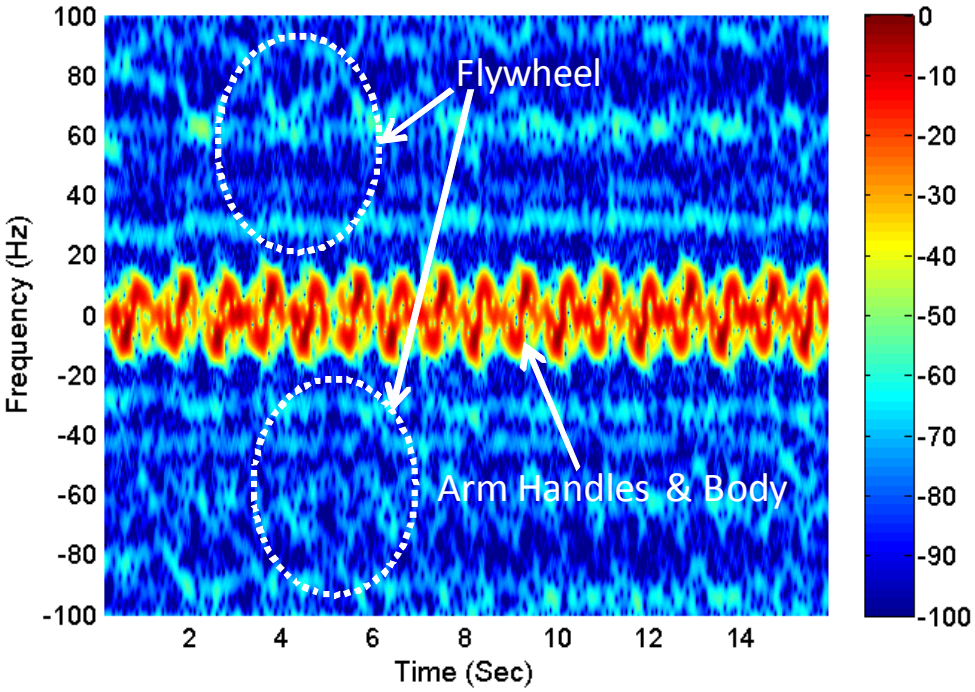
5.6.3 Comparison with UWB Pulse Radar

To compare the two developed radar prototypes, i.e., CW Doppler radar and UWB PD radar, we have performed the same experiments using the developed UWB pulse radar as we did in Section 5.6.2: the 1st experiment was to sense a person riding the exercise bike while the 2nd to sense a person walking/jogging on the treadmill. Figure 5.17 presents the acquired spectrogram when a person was riding the exercise bike in three different scenarios: ride slower, rider faster, and leave the bike after the exercise. Comparing Figure 5.17 with Figure 5.15, UWB PD radar has acquired very similar Doppler spectrogram as the developed CW radar did. Figure 5.18 shown the acquired spectrogram when the person was walking/jogging on the treadmill using UWB PD radar. Similar results were achieved when using UWB PD radar, compared with Figure 5.16 acquired by CW Doppler radar.

It is found that UWB PD radar can achieve similar Doppler results as CW Doppler radar when sensing a single target. However, beyond single target, UWB PD radar can be used to separate and sense multiple targets at different range or cross-range locations, by achieving a high resolution range profile, which cannot be provided by CW Doppler radar.

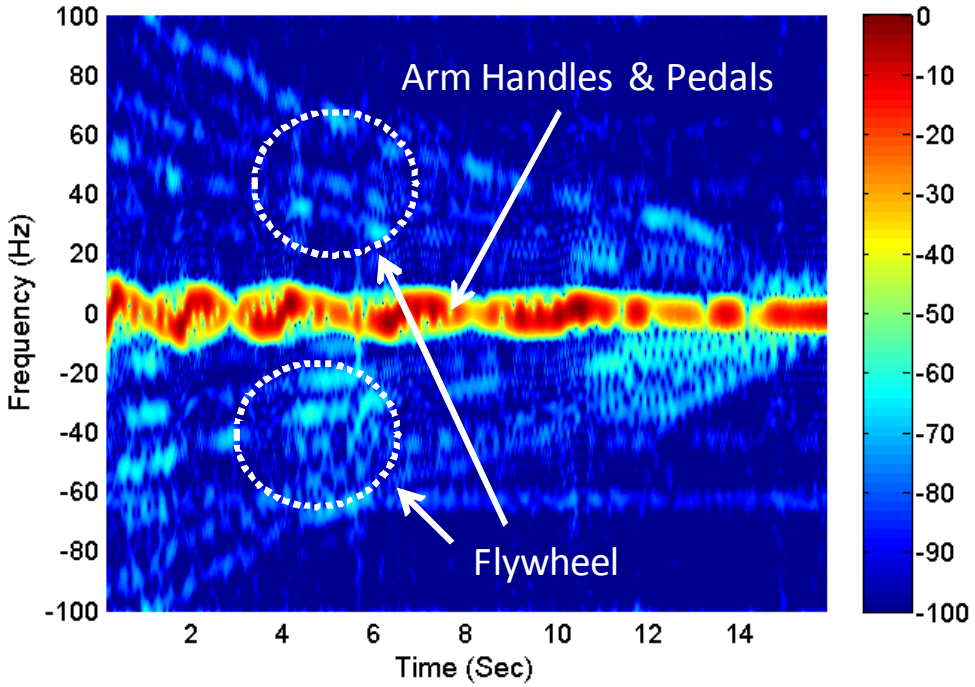


(a) Acquired spectrogram when person riding the bike at a slower speed



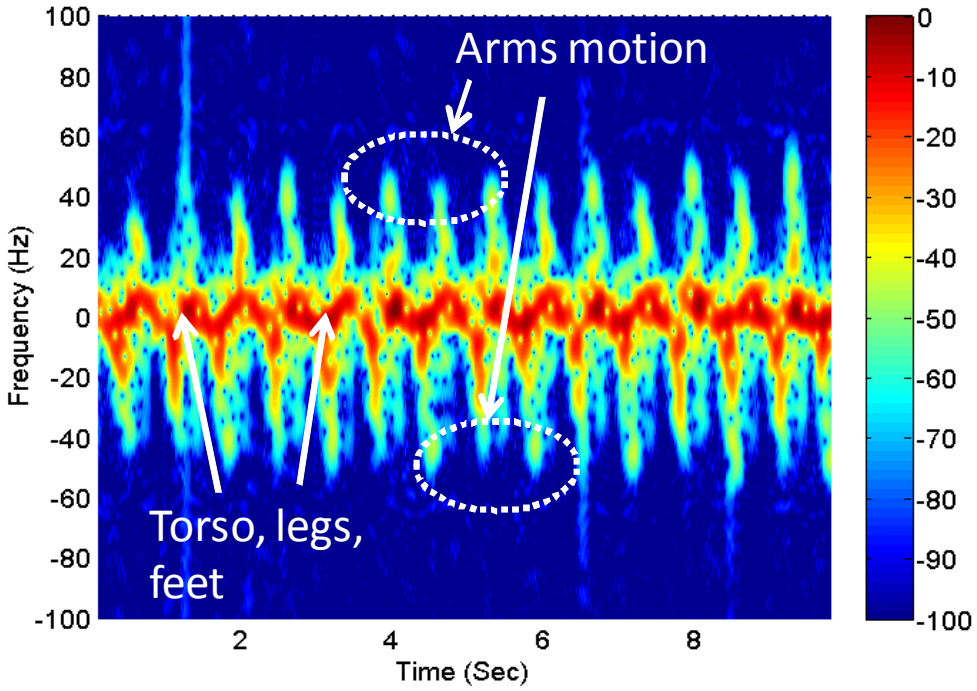
(b) Acquired spectrogram when person riding the bike at a faster speed

Figure 5.17 Acquired spectrogram of sensing a person riding exercise bike using the developed UWB PD radar.

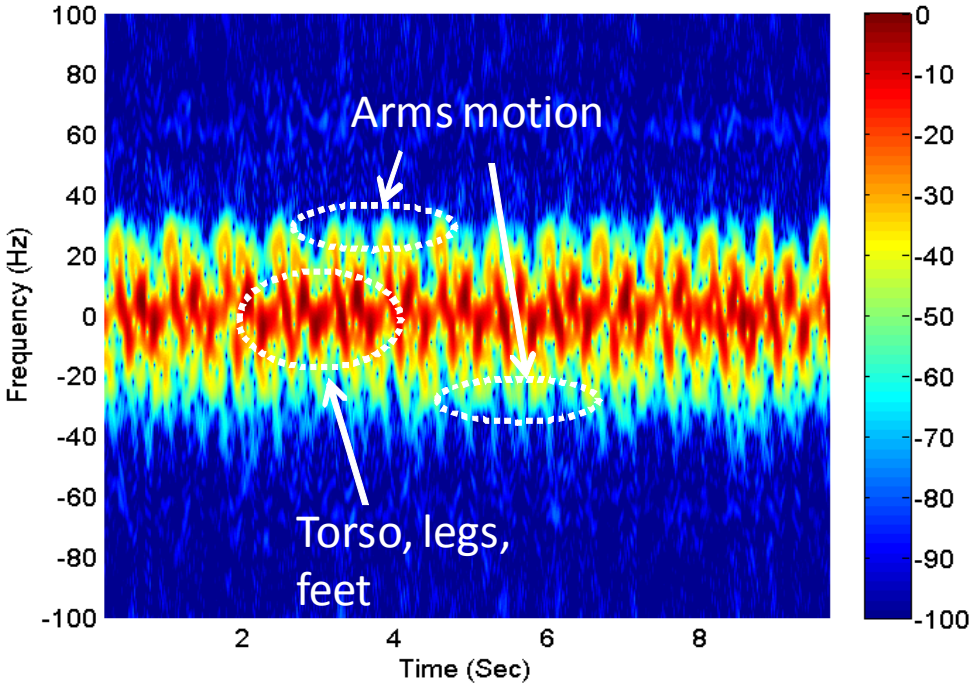


(c) Acquired spectrogram when person left the bike after the exercise

Figure 5.17 Continued.



(a) Acquired spectrogram when person walking on the treadmill



(b) Acquired spectrogram when person jogging on the treadmill

Figure 5.18 Acquired spectrogram of sensing a person walking/jogging on the treadmill using the developed UWB PD radar.

5.6.4 Summary of Two Radar Technologies

The CW Doppler radar and UWB PD prototypes utilized here are compared and summarized, as shown in Table 5.1. The CW Doppler radar transmits a 3 GHz signal while the UWB PD radar utilizes a 3 GHz carrier with a single side bandwidth of 1.5 GHz. Both radar prototypes use a peak power of 25 dBm to satisfy the FCC requirements.

CW Doppler radar usually does not have Doppler ambiguity but is limited to detect the Doppler frequency within ± 1MHz in the developed prototype because of the down-sampling in the post data processing to reduce the data size. However, this limitation can be easily resolved by re-programming the FPGA code of DDC to modify the decimation factor. The developed pulse radar presents a Doppler ambiguity of 300 Hz and an ambiguous velocity of 15 m/s, which is adequate for human sensing applications. As far as the cost and functionality, CW Doppler radar is simpler in system complexity and cheaper to implement, and is an attractive technology for single person activity monitoring and vital sign detection. In addition, CW Doppler radar is superior in fast speed object detection.

On the other hand, UWB pulse radar has an inherent advantage to separate multipath propagations, which makes it a great candidate for through wall applications and operation in heavily cluttered environment. By achieving a high resolution range profile as well as m-D signatures, UWB pulse radar also shows its superiority for detecting and sensing multiple radar objects.

Table 5.1 Comparison of Developed CW and UWB PD Radar Prototypes

	CW Doppler Radar	UWB PD Radar
Frequency	3 GHz	1.5 - 4.5 GHz, 3 GHz carrier
Power	25 dBm	25 dBm, peak
Range Resolution	Not Available	10 cm
Doppler Resolution	TOT	PRT × total pulse number
Doppler Ambiguity	± 1 MHz	± 300 Hz (single Rx channel)
Ambiguous Velocity	50 km/s	15 m/s (single Rx channel)
Detection Range	Much Longer	15 m
Separate Multipath Propagations	Poor	Good
Doppler Processing Method	STFT on sampled data	STFT on slow-time samples
System Complexity	Simpler	Marginal
Cost	Low	Marginal
Applications	Single person activity monitoring; Vital sign detection	Through wall sensing; Multiple Objects detection; Target Localization

5.7 Conclusion

In this Chapter, we have introduced how UWB pulse radar can be used for Doppler applications. A developed UWB pulse radar sensor has been utilized for human gait analysis, moving people monitoring and breathing detection of stationary persons, adapted for both LOS and through wall environment. UWB pulse radar shows its advantages in Doppler detection of more than one target, by achieving a high resolution range profile. In addition, UWB pulse radar utilizes narrow pulse signal in time domain

and is capable of separating strong wall reflections with the weak target scattering when working in through wall environment, by applying time gaiting. The developed UWB pulse radar prototype has an ambiguous velocity of 15 m/s, when using a sampling interval of 10ps and single receiving antenna. The Doppler ambiguity can be further improved if using a longer sampling interval.

An alternative solution using CW Doppler radar for Doppler detections has also been introduced. The developed CW radar prototype utilizes a superheterodyne receiver and a DDC module implemented in FPGA to process the signal in frequency domain. Both UWB pulse and CW radar prototypes were used to acquire the m-D signature of single target and very similar results were acquired. However, UWB pulse radar has shown its capability of detecting and monitoring more than one human targets even in a through wall environment, which is beyond the capability of a CW radar. The pros and cons of the two radar alternatives have been compared and summarized. Each radar technology has its inherent advantages in certain applications. But, it is believed that UWB PD radar can provide more accuracy, more functionality, especially for tracking more than one target and even in a harsh environment with many scatterers like walls or debris.

Chapter 6

Conclusions and Future Work

We have investigated UWB pulse radar technology extensively in this dissertation, including 1) implementation of UWB system hardware, 2) system level comprehensive simulation, 3) its application in human imaging, and 4) pursuing UWB radar for Doppler detection. In UWB radar hardware implementation, we have presented the guidelines of designing a high dynamic range radar transceiver, developing wideband antenna arrays, and implementing a high speed data acquisition module. The developed system level simulator includes both linear and nonlinear analysis of the radar system to be an efficient tool for UWB radar performance prediction and optimization, as well as a fast prototyping setup of any designing the next generation of UWB systems. Three examples have been utilized to demonstrate the capability of the UWB pulse radar for imaging applications. Systematic analyses have been given for both 2-D and 3-D Backprojection microwave beamforming algorithms for radar image recovery. Examples have been given to show the features of UWB pulse radar for Doppler detections. By acquiring the m-D signatures, UWB pulse radar is capable of monitoring moving persons as well as detecting stationary people through respiration. Several contributions have been presented through this dissertation and will be summarized here in this chapter.

6.1 Accomplishments and Contributions

First and foremost, a robust UWB pulse radar prototype operating at 1.5-4.5 GHz was developed and implemented, achieving real-time imaging, 3-D radar imaging, and Doppler detection features in one platform. The developed radar prototype consists of a 1×8 wideband Vivaldi antenna array, a robust high dynamic range radar transceiver, and a high speed data acquisition and transfer module based on equivalent-time sampling strategy and USB2.0 data link.

Second, a reconfigurable UWB pulse radar architecture was developed to operate at either at a lower UWB band (i.e., 1.5-4.5 GHz) or a higher UWB band (i.e., 8-10 GHz), in order to achieve a good compromise between imaging resolution and through barrier attenuation. A wideband Vivaldi antenna array was developed for the reconfigurable UWB radar, covering the entire UWB imaging band from 1.5 to 10.6 GHz.

Third, an advanced system level simulation platform has been developed to optimize and predict the performance of UWB pulse radar systems, by integrating linear and nonlinear analysis, circuit and electromagnetic simulation in one model. The comprehensive simulator includes 6 blocks and has been utilized to accurately emulate the operation of our UWB pulse radar system.

Fourth, the operation of the UWB pulse radar has been extended for real-time imaging at a high system refresh rate of 75 Hz, imaging of multiple objects in through wall environment, and 3-D image reconstruction of radar targets. Meanwhile, the UWB imaging technology was also extended for early breast cancer detection, demonstrating the capability of detecting 5mm diameter tumor in phantom experiment.

Fifth, UWB pulse radar has also been extended for monitoring/detecting both moving persons and stationary human, through the m-D signatures. Spectrogram patterns were used to investigate and monitor the physical activities of moving persons and to acquire the breathing information of stationary human.

Last, but not the least, a CW Doppler radar prototype was developed and implemented, as an alternative to UWB pulse radar for Doppler detection applications. The pros and cons of the two technologies have been compared and summarized.

6.2 Publications

Journal Papers

[1] **Y. Wang**, and A.E. Fathy, "Advanced system level simulation platform for three-dimensional UWB through wall imaging SAR using time-domain approach," *IEEE Trans. Geosci. Remote Sens.*, vol. 50, no. 5, May 2012.

[2] Q. Liu, **Y. Wang**, and A.E. Fathy, "Towards 100 GSPS, low cost data acquisition module for multifunctional UWB radar," *IEEE Trans. Aerosp. Electron. Syst.*, accepted with revision.

[3] **Y. Wang**, Q. Liu, and A.E. Fathy, "Real-time human activity monitoring and respiration detection using UWB pulse Doppler radar sensor," *IEEE Trans. Inf. Technol. Biomed.*, under review.

[4] **Y. Wang**, Q. Liu, and A.E. Fathy, "CW and PD radar processing based on FPGA for human sensing applications," *IEEE Trans. Geosci. Remote Sens.*, under review.

[5] Y. Yang, **Y. Wang**, A.E. Fathy, "Design of compact Vivaldi antenna arrays for UWB see through wall applications," *Progress In Electromagnetics Research*, PIER 82, pp. 401-418, 2008.

Conference Papers

IEEE MTT-S International Microwave Symposium (IMS)

[1] **Y. Wang**, Q. Liu, and A.E. Fathy, "Simultaneous localization and respiration detection of multiple people using low cost UWB biometric pulse Doppler radar sensor," *2012 IEEE MTT-S Int. Microwave Symp.*, Montreal, Canada, Jun. 2012.

[2] **Y. Wang**, M. Kuhn, and A.E. Fathy, "Advanced system level simulation of UWB three-dimensional through-wall imaging radar for performance limitation prediction," *2010 IEEE MTT-S Int. Microwave Symp.*, Anaheim, CA, May 2010.

[3] A.E. Fathy, M.R. Mahfouz, **Y. Wang**, M. Kuhn, J. Turnmire, "UWB technology for precise indoor positioning & see through wall imaging applications," *2010 IEEE MTT-S Int. Microwave Symp. Workshop*, Anaheim, CA, May 2010.

[4] **Y. Wang**, Y. Yang, and A.E. Fathy, "Experimental assessment of the cross coupling and polarization effects on ultra-wide band see-through-wall imaging reconstruction," *2009 IEEE MTT-S Int. Microwave Symp.*, Boston, MA, Jun. 2009.

IEEE Radio and Wireless Symposium (RWS)

[5] Q. Liu, **Y. Wang**, and A.E. Fathy, "A compact integrated 100GS/s sampling module for UWB see through wall radar with fast refresh rate for dynamic real time imaging," *2012 IEEE Radio and Wireless Symposium*, Santa Clara, CA, Jan. 2012.

[6] **Y. Wang**, A.E. Fathy, and M.R. Mahfouz, "UWB microwave imaging system with a novel calibration approach for breast cancer detection," *2011 IEEE Radio and Wireless Symposium*, Phoenix, AZ, Jan. 2011.

[7] **Y. Wang**, Y. Yang, A. E. Fathy, "A reconfigurable UWB system for real-time through wall imaging applications," *2010 IEEE Radio and Wireless Symposium*, New Orleans, LA, Jan. 2010. (Best Paper Award)

[8] M.R. Mahfouz, M.J. Kuhn, **Y. Wang**, J. Turnmire, and A.E. Fathy, "Towards sub-millimeter accuracy in UWB positioning for indoor medical environments," *2011 IEEE Radio and Wireless Symposium*, Phoenix, AZ, Jan. 2011.

[9] M.J. Kuhn, M.R. Mahfouz, J. Turnmire, **Y. Wang**, and A.E. Fathy, "A multi-tag access scheme for indoor UWB localization systems used in Medical Environments," *2011 IEEE Radio and Wireless Symposium*, Phoenix, AZ, Jan. 2011.

IEEE International Symposium on Antennas and Propagation (APS)

[10] **Y. Wang**, and A.E. Fathy, "Micro-Doppler signatures for intelligent human gait recognition using a UWB impulse radar," *2011 IEEE AP-S Int. Symp. on Antennas and Propagat.*, Spokane, WA, Jul. 2011.

[11] **Y. Wang**, M. Mahfouz, and A.E. Fathy, "Novel compact tapered microstrip slot antenna for microwave breast imaging," *2011 IEEE AP-S Int. Symp. on Antennas and Propagat.*, Spokane, WA, Jul. 2011.

[12] **Y. Wang**, and A.E. Fathy, "Three-dimensional through wall imaging using an UWB SAR," *2010 IEEE AP-S Int. Symp. on Antennas and Propagat.*, Toronto, Canada, Jul. 2010.

[13] **Y. Wang**, M. Kuhn, M. Mahfouz, and A.E. Fathy, "A comprehensive system-level simulation paradigm for UWB systems," *2010 IEEE AP-S Int. Symp. on Antennas and Propagat.*, Toronto, Canada, Jul. 2010.

[14] **Y. Wang**, Y. Yang, and A.E. Fathy, "Ultra-wideband Vivaldi arrays for see-through-wall imaging radar applications," *2009 IEEE AP-S Int. Symp. on Antennas and Propagat.*, Charleston, SC, Jun. 2009.

[15] **Y. Wang**, Y. Yang, and A.E. Fathy, "Reconfigurable ultra-wide band see-through-wall imaging radar system," *2009 IEEE AP-S Int. Symp. on Antennas and Propagat.*, Charleston, SC, Jun. 2009.

USNC-URSI National Radio Science Meeting (URSI)

[16] **Y. Wang**, D. Yang, A.E. Fathy, and M.G. Amin, "Through wall imaging and gate recognition of human objects using an IR-UWB radar," *2011 National Radio Science Meeting (USNC-URSI)*, Boulder, CO, Jan. 2011.

[17] **Y. Wang**, and A.E. Fathy, "UWB radar through-wall detection based on three-dimensional imaging – experimental results," *2010 National Radio Science Meeting (USNC-URSI)*, Boulder, CO, Jan. 2010.

Other Conferences

[18] **Y. Wang**, and A.E. Fathy, "Development of a through wall UWB system for three-dimensional imaging using time domain tools," *14th Int. Symp. on Antenna Tech. and Applied EM and American EM Confer.*, Ottawa, Canada, Jul. 2010.

[19] M.R. Mahfouz, A.E. Fathy, M.J. Kuhn, and **Y. Wang**, "Recent trends and advances in UWB positioning," *Wireless Sensing, Local Positioning, and RFID, 2009 IEEE MTT-S Int. Microwave Workshop on*, Sep. 2009.

[20] **Y. Wang**, and A.E. Fathy, "Development of a reconfigurable UWB three-dimensional see-through-wall radar imaging system," *2009 Antenna Applications Symposium*, Champaign, IL, Sep. 2009.

[21] M. Kuhn, C. Zhang, B. Merkl, D. Yang, **Y. Wang**, M. Mahfouz, and A.E. Fathy, "High accuracy UWB localization in dense indoor environments," *2008 IEEE Int. Conference on UWB*, Vol. 2, pp. 129-132, Sep. 2008.

[22] **Y. Wang**, and A.E. Fathy, "Design of a compact tapered slot Vivaldi antenna array for see through concrete wall UWB applications," *XXIX General Assembly of the Int. Union of Radio Science* (*URSI*), Chicago, IL, Aug. 2008.

6.3 Conclusion

This dissertation investigates the UWB pulse radar technology extensively, from radar system hardware implementation and simulation, to imaging and Doppler detection applications. Several points are given here to conclude the dissertation.

1) UWB technology has several most desirable technical features compared to other imaging techniques, such as low power, high imaging resolution, non-contact remote sensing, non-invasiveness, environment friendly, and most importantly, to see through walls.
2) UWB radars are excellent candidate to address both imaging and human motion tracking. UWB Doppler radars are able to discriminate the motion Doppler effects of more than one object in the scene that are discriminated by their different locations in the scene.
3) The first step in designing TWI radar is selecting the operation frequency. High frequency leads to high azimuth resolution, while using a relatively low

frequency allows penetrating through walls with acceptable attenuation. 1-4 GHz is regarded as the optimal frequency band for seeing through high-loss materials, such as brick-wall and concrete-wall.

4) Using a wideband antenna and a reconfigurable platform gives the flexibility of radar transceiver to operate at either 9 GHz or 3 GHz, combining these two features in one platform.
5) Vivaldi antennas/arrays are good candidate for UWB radar system because of their wideband performance and directional radiation characteristic. But the phase center variation with frequency may bring few mm errors in target localization. This is acceptable for imaging applications but not for precise localization.
6) FPGA can be used to carry out the array switch control, the data storage and handling, and real-time image recovery.
7) UWB pulse radar simulation requires a time domain solver to account for pulse dispersion, delay, and attenuation. The time domain solver includes combined Ptolemy and transient simulation for active/passive devices and frequency domain analysis combined with Fourier transform.
8) In UWB radar system simulation, walls are assumed to be infinite to simplify transmission and reflection calculations using a stratified media. TE or TM modes are assumed and no coupling between the modes was assumed. Additionally, the walls are homogeneous with known parameters and physical dimensions. In real scenarios, most likely the wall characteristics are not known. Future work should include the development of algorithms to estimate wall parameters.
9) Accurate statistic channel models are still not available for UWB through wall applications and are eagerly desired to include indoor/outdoor mixed environment and wall interference in the system level simulation platform.
10) Detection range of UWB pulse radar is still limited to about 20m because of the FCC requirement on transmitter emission. When acquiring real-time image, the developed UWB pulse radar captures 75 photo shots per second,

which is adequate to track any human activities. However, a higher system refresh rate is still needed if used to track any fast moving targets, such as cars, airplanes, and etc.

11) The 3-D imaging example shows the capability of UWB pulse radar for target recognition. A linear antenna array was moved mechanically in order to achieve a 2-D array operation. In order to achieve a real-time 3-D imaging feature, a 2-D antenna array is needed, together with a more complicated switch matrix to control the ON/OFF of each array element.
12) Early breast cancer detection example shows the great potential of UWB pulse radar in medical imaging applications. But the imaging resolution of UWB pulse radar achieved by now is several mm and has limited its potential applications. More research is still needed to improve the imaging resolution to 1 mm or even sub-mm.
13) Doppler detection examples demonstrate the capability of the UWB pulse radar for human gait analysis and moving people monitoring, as well as breathing detection of stationary people, adapted for both LOS and through wall environment.
14) An alternative solution using CW Doppler radar for Doppler detections has also been introduced. Each radar technology has its inherent advantages in certain applications. But, it is believed that UWB PD radar can provide more accuracy, more functionality, especially for tracking more than one target and even in a harsh environment with many scatters like walls or debris.

6.4 Direction of Future Work

In this dissertation, a UWB pulse Doppler radar prototype was developed and presented for imaging and Doppler detection applications. The radar prototype includes a robust radar transceiver, a 1×8 linear Vivaldi antenna array, and a high speed data

acquisition module. Both radar transceiver and linear antenna array may be re-designed for size reduction, to achieve a portable or even handheld radar system.

The UWB pulse radar prototype achieves a system refresh rate of 75 Hz (i.e., 75 photo screens per second), when using a sampling interval of 10ps and processing the data from 8 receiving channels sequentially. To speed up the system refresh rate for detecting/imaging fast moving targets, the receiving channels can be processed in parallel and a system refresh rate of 600 Hz will be achieved.

A comprehensive system level simulation platform was presented for UWB radar system performance prediction and optimization. Linear and nonlinear components, wall effect, radar scattering were accounted for in the simulator to accurately emulate a practical radar operation. However, an accurate statistical channel model for UWB through wall applications is still not available and eagerly desired, in order to compensate for wall interference and indoor/outdoor mixed environments.

UWB pulse radar has demonstrated the capability of detecting 5mm diameter tumor in early breast cancer detection example. More research is still needed to improve the imaging resolution to 1 mm or even sub-mm. Integration of microwave imaging with ultrasound imaging is one direction to pursue, to achieve both advantages of good contrast from microwave and good resolution from ultrasound.

UWB pulse radar has been applied for human gait analysis, physical activity monitoring and respiration detection by acquiring the m-D signatures. Distinctly different m-D signatures are achieved for different human motions. It provides the prerequisites to solve the inverse problem for human activity classification and recognition by using certain classifier, such as support vector machine.

List of References

[1] S. L. Coetzee, C. J. Baker, and H. D. Griffiths, "Narrow band high resolution radar imaging," 2006 IEEE Conf. on Radar, Verona, NY, Apr. 2006.

[2] D. Wang, X. Ma, and Y. Su, "Two-dimensional imaging via a narrowband MIMO radar system with two perpendicular linear arrays," *IEEE Trans. Image Process.*, vol. 19, no. 5, pp. 1269-1279, May 2010.

[3] C. Lai, and R. M. Narayanan, "Ultrawideband random noise radar design for through-wall surveillance," *IEEE Trans. Aerosp. Electron. Syst.*, vol. 46, no. 4, pp. 1716-1730, Oct. 2010.

[4] S. Hantscher, A. Reisenzahn, and C. G. Diskus "Through-wall imaging with a 3-D UWB SAR algorithm," *IEEE Signal Process. Lett.*, vol. 15, pp. 269-272, 2008.

[5] S. Kidera, T. Sakamoto, and T. Sato, "Accurate UWB radar three-dimensional imaging algorithm for a complex boundary without range point connections," *IEEE Trans. Geosci. Remote Sens.*, vol. 48, no. 4, pp. 1993-2004, Apr. 2010.

[6] A. Nezirovic, A.G. Yarovoy, L.P. Ligthart, "Experimental study on human being detection using UWB radar," in *IRS 2006 Int. Radar Symp*., pp. 1-4, 2006.

[7] A.G. Yarovoy, X. Zhuge, T.G. Savelyev, and L.P. Ligthart, "Comparison of UWB technologies for human being detection with radar," *2007 European Radar Conf.*, pp. 295-298, 2007.

[8] S. Foo, and S. Kashyap, "Cross-correlated back projection for UWB radar imaging," in *IEEE AP-S Int. Symp. Antennas and Propag.*, Jun. 2004.

[9] J. H. Williams, C. D. Johnson, "Acoustic and optical borehole-wall imaging for fractured-rock aquifer studies," *Journal of Applied Geophysics*, 55 (2004) pp. 151-159.

[10] N. T. Thanh, H. Sahli, and D. N. Hao, "Infrared thermography for buried landmine detection: inverse problem setting," *IEEE Trans. Geosci. Remote Sens.*, vol. 46, no. 12, pp. 3987-4004, Dec. 2008.

[11] M. Dehmollaian, and K. Sarabandi, "Refocusing through building walls using synthetic aperture radar," *IEEE Trans. Geosci. Remote Sens.*, vol. 46, no. 6, pp. 1589-1599, Jun. 2008.

[12] B. Panzner, A. Jostingmeier, and A. Omar, "Radar signatures of complex buried objects in ground penetrating radar," in *2010 11th Int. Radar Symp.*, Vilnius, Lithuania, Jun. 2010.

[13] M. Klemm, J. A. Leendertz, D. Gibbins, I. J. Craddock, A. Preece, and R. Benjamin, "Microwave radar-based breast cancer detection: imaging in inhomogeneous breast phantoms," *IEEE Antennas Wireless Propag. Lett.*, vol. 8, pp. 1349-1352, 2009.

[14] C. Le, Traian Dogaru, L. Nguyen, and M. A. Ressler, "Ultrawideband (UWB) radar imaging of building interior: measurements and predictions," *IEEE Trans. Geosci. Remote Sens.*, vol. 47, no. 5, pp. 1409-1420, May 2009.

[15] A. R. Hunt, "A wideband imaging radar for through-the-wall surveillance," *Proc. of SPIE*, vol. 5403, pp. 590-596, 2004.

[16] Y. Yang, and A. E. Fathy, "Development and implementation of a real-time see-through-wall radar system based on FPGA," *IEEE Trans. Geosci. Remote Sens.*, vol. 47, no. 5, pp. 1270-1280, May 2009.

[17] Yang, Yunqiang, "Development of a Real-time Ultra-wideband See Through Wall Imaging Radar System." PhD diss., University of Tennessee, 2008.

[18] Time Domain Corp., PulsON 400 radar sensor datasheet, Huntsville, AL. [Online]. Available: http://www.timedomain.com/p400.php.

[19] Cambridge Consultants Inc., Prism 200, Cambridge, MA. [Online]. Available: http://www.cambridgeconsultants.com/prism_200.html.

[20] Camero USA Corp., Xaver™ 800 Vision System, Vienna, VA. [Online]. Available: http://www.camero-tech.com/xaver800.shtml.

[21] A. Lin, and H. Ling, "Doppler and direction-of-arrival (DDOA) radar for multiple-mover sensing," *IEEE Trans. Aerosp. Electron. Syst.*, vol. 43, no. 4, pp. 1496-1509, Jan. 2007.

[22] C. Li, J. Ling, J. Li, and J. Lin, "Accurate Doppler radar noncontact vital sign detection using the RELAX algorithm," *IEEE Trans. Instrum. Meas.*, vol. 59, no. 3, pp. 687-695, Mar. 2010.

[23] Q. Zhou, A. Host-Madsen, O. Boric-Lubecke, and V. Lubecke, "Detection of multiple heartbeats using Doppler radar," *IEEE Int. Conf. Acoustics, Speech and Signal Processing*, Toulouse, France, May 2006.

[24] K. Chen, D. Misra, H. Wang, H. Chuang, and E. Postow, "An X-band microwave life-detection system," *IEEE Trans. Biomed. Eng.*, vol. BME-33, no. 7, pp. 697-701, Jul. 1986.

[25] K. Chen, Y. Huang, J. Zhang, and A. Norman, "Microwave life-detection system for searching human subjects under earthquake rubble or behind barrier," *IEEE Trans. Biomed. Eng.*, vol. 27, no. 1, pp. 105-114, Jan. 2000.

[26] J. Silvious, J. Clark, T. Pizzillo, and D. Tahmoush, "Micro-Doppler phenomenology of humans at UHF and Ku-band for biometric characterization," *Proc. of SPIE*, vol. 7308, 2009.

[27] V. C. Chen, "Detection and analysis of human motion by radar," *2008 IEEE Radar Conference*, May 2008.

[28] J. Li, X. Zhu, P. Stoica, and M. Rangaswamy, "High resolution angle-Doppler imaging for MTI radar," *IEEE Trans. Aerosp. Electron. Syst.*, vol. 46, no. 3, pp. 1544-1556, Jul. 2010.

[29] B. Armstrong, and B. S. Holeman, "Target tracking with a network of Doppler radars," *IEEE Trans. Aerosp. Electron. Syst.*, vol. 34, no. 1, pp. 33-48, Jan. 1998.

[30] T. Thayaparan, L. Stankovic, and I. Djurovic, "Micro-Doppler-based target detection and feature extraction in indoor and outdoor environments," *Journal of The Franklin Institute*, 345, pp. 700-722, Sep. 2008.

[31] J. L. Geisheimer, W. S. Marshall, and E. Greneker, "A continuous-wave (CW) radar for gait analysis," *35th Asilomar Conf. on Signals, Systems and Computers*, pp. 834-838, Nov. 2011.

[32] M. Otero, "Application of a continuous wave radar for human gait recognition," *Proc. of SPIE*, vol. 5809, 2005.

[33] B. G. Mobasseri, and M. G. Amin, "A time-frequency classifier for human gait recognition," *Proc. of SPIE*, vol. 7306, 2009.

[34] A. R. Hunt, "Use of a frequency-hopping radar for imaging and motion detection through walls," *IEEE Trans. Geosci. Remote Sens.*, vol. 47, no. 5, pp. 1402-1408, May 2009.

[35] Boris Lembrikov, *Ultra Wideband*, Sciyo, 2010, pp. 323-346.

[36] J. Sachs, M. Aftanas, S. Crabbe, M. Drutarovsky, R. Klukas, D. Kocur, T. Nguyen, P. Peyerl, J. Rovnakova, E. Zaikov, "Detection and tracking of moving or trapped people hidden by obstacles using ultra-wideband pseudo-noise radar," *European Radar Conference*, pp. 408-411, Oct. 2008.

[37] A. Lazaro, D. Girbau, and R. Villarino, "Analysis of vital signs monitoring using an IR-UWB radar," *Progress in Electromagnetics Research*, PIER 100, pp. 265-284, 2010.

[38] V. Jain, S. Sundararaman, and P. Heydari, "A 22-29GHz UWB pulse-radar receiver front-end in 0.18-μm CMOS," *IEEE Trans. Microw. Theory Tech.*, vol. 57, no. 8, pp. 1903-1914, Aug. 2009.

[39] I. Gresham et al., "Ultra-wideband radar sensors for short-range vehicle applications," *IEEE Trans. Microw. Theory Tech.*, vol. 52, no. 9, pp. 2105-2122, Sep. 2004.

[40] Brian Yamauchi, "Daredevil: ultra-wideband radar sensing for small UGVs," *Proc. of SPIE*, vol. 6561, May 2007.

[41] Comlab Inc. Final Report, Ultra-wideband radar through-wall measurements, Jun. 2003.

[42] Y. Wang, and A. E. Fathy, "Micro-Doppler signatures for intelligent human gait recognition using a UWB impulse radar," *in IEEE AP-S Int. Symp. Antennas and Propag*., Spokane, WA, Jul. 2011.

[43] Y. Wang, Y. Yang, and A. E. Fathy, "A reconfigurable UWB system for teal-time through wall imaging applications," *in IEEE Radio and Wireless Symp. (RWS)*, New Orleans, LA, Jan. 2010, pp. 633-636.

[44] Y. Wang, Y. Yang, and A. E. Fathy, "Ultra-wideband Vivaldi arrays for see-through-wall imaging radar applications," *in IEEE AP-S Int. Symp. Antennas and Propag*., Charleston, SC, Jun. 2009.

[45] Q. Liu, Y. Wang, A.E. Fathy, "A compact integrated 100 GS/s sampling module for UWB see through wall radar with fast refresh rate for dynamic real time imaging," *2012 IEEE Radio and Wireless Symposium*, Santa Clara, CA, Jan. 2012.

[46] S. Guo, S. Sun, and Z. Zhang, "A novel equivalent sampling method using in the digital storage oscilloscopes," *IEEE Instrumentation and Measurement Technology Conf.*, pp. 530-532, May 1994.

[47] M. Farwell, J. Ross, R. Luttrell, D. Cohen, W. Chin, and T. Dogaru, "Sense through the wall system development and design considerations," *Journal of The Franklin Institute*, 345, pp. 570-591, Sep. 2008.

[48] Inigo Cuinas et al., "Permittivity and conductivity measurements of building materials at 5.8 GHz and 41.5 GHz," *Wireless Personal Communications*, pp. 93-100, 2002.

[49] C. A. Balanis, *Advance Engineering Electromagnetics*, New York: Van Nostrand Reinhold, 1990.

[50] Y. Yang, C. Zhang and A. Fathy, "Development of an ultra-wideband Vivaldi antenna array," in *IEEE AP-S Int. Symp. Antennas and Propag*, pp.606-609, Washington, D.C., 2005.

[51] B. R. Crowgey, E. J. Rothwell, and L. C. Kempel, "Comparison of UWB short-pulse and stepped-frequency radar systems for imaging through barriers," *Progress In Electromagnetics Research*, vol. 110, pp. 403-419, 2010.

[52] D. Gibbins, M. Klemm, I. Craddock, J. Leendertz, A. Preece, and R. Benjamin, "A comparison of a wide-slot and a stacked patch antenna for the purpose of breast cancer detection," *IEEE Trans. Antennas Propag.*, vol. 58, no. 3, pp. 665-674, Mar. 2010.

[53] Y. Yang, Y. Wang, A.E. Fathy, "Design of Compact Vivaldi Antenna Arrays for UWB See Through Wall Applications," *Progress In Electromagnetics Research*, PIER 82, pp. 401-418, 2008.

[54] A. Elsherbini, and K. Sarabandi, "UWB high-isolation directive coupled-sectorial-loops antenna pair," *IEEE Antennas Wireless Propag. Lett.*, vol. 10, pp. 215-218, 2011.

[55] K. Browne, R. Burkholder, and J. Volakis, "Through-wall radar imaging system utilizing a light-weight low-profile printed array," in *2010 4th European Antennas and Propag*, pp.606-609, Barcelona, Spain, Apr. 2010.

[56] M. M. Zinieris et al., "A broadband microstrip-to-slot-line transition," *Microwave and Optical Technology Letters*, Vol. 18, No. 5, Aug. 1998

[57] S.B. Cohn, "A Class of Broadband Three-Port TEM-Mode Hybrids", *IEEE Trans. Microwave Theory and Tech.*, vol. MTT-16, No. 2, pp. 110-116, Feb. 1968.

[58] G. Wang, M. G. Amin, and Y. Zhang, "New approach for target locations in the presence of wall ambiguities," *IEEE Trans. Aerosp. Electron. Syst.*, vol. 42, issue 1, pp. 301-315, Jan 2006.

[59] Fujitsu Semiconductor America Inc., 56GS/s 8-bit Analog-to-Digital Converter Fact Sheet, Sunnyvale, CA [Online]. Available:http://www.fujitsu.com/downloads/MICRO/fma/pdf/56G_ADC_FactSheet.pdf.

[60] D. Yang, A. E. Fathy, H. Li, M. R. Mahfouz, G. D. Peterson, "Millimeter accuracy UWB positioning system using sequential sub-sampler and time difference estimation algorithm," *IEEE Radio and Wireless Symposium*, pp. 539-542, Jan. 2010.

[61] Y. Guo, Y. Zhang, A. Rasmita, and M. Leong, "Equivalent circuit modeling of UWB antennas for system co-design," in *IEEE AP-S Int. Symp. Antennas and Propag.*, Toronto, Canada, Jul. 2010.

[62] A. D. Angelis, M. Dionigi, A. Moschitta, R. Giglietti, and P. Carbone, "Characterization and modeling of an experimental UWB pulse-based distance measurement system," *IEEE Trans. Instrum. Meas.*, vol. 58, no. 5, pp. 1479-1486, Mar. 2009.

[63] M. D. Renzo, F. Graziosi, and F. Santucci, "An exact framework for performance analysis of IR-UWB systems: the need for approximations," *IEEE Commun. Lett.*, vol. 11, no. 10, pp. 769-771, Oct. 2007.

[64] M. Kuhn, C. Zhang, S. Lin, M. R. Mahfouz, and A. E. Fathy, "A system level design approach to UWB localization," in *IEEE MTT-S Int. Microw. Symp. Dig.*, Boston, MA, Jun. 2009, pp. 1409-1412.

[65] M. Kuhn, M. R. Mahfouz, C. Zhang, B. C. Merkl, and A. E. Fathy, "A system-level simulation framework for UWB localization," *IEEE Trans. Microw. Theory Tech.*, vol. 58, no. 12, pp. 3527-3537, Dec. 2010.

[66] M. R. Mahfouz, C. Zhang, B. C. Merkl, M. Kuhn, and A. E. Fathy, "Investigation of high accuracy indoor 3-D positioning using UWB technology," *IEEE Trans. Microw. Theory Tech.*, vol. 56, no. 6, pp. 1316-1330, Jun. 2008.

[67] C. Zhang, M. Kuhn, B. C. Merkl, A. E. Fathy and M. R. Mahfouz, "Real-time noncoherent UWB positioning radar with millimeter range accuracy: theory and experiment," *IEEE Trans. Microw. Theory Tech.*, vol. 58, no. 1, pp. 9-20, Jan. 2010.

[68] F. Ahmad, Y. Zhang, and M. G. Amin, "Three-dimensional wideband beamforming for imaging through a single wall", *IEEE Geosci. Remote Sens. Lett.*, vol. 5, no. 2, Apr. 2008, pp. 176-179.

[69] C. Su and T. K. Sarkar, "Adaptive multiscale moment method (AMMM) for analysis of scattering from three-dimensional perfectly conducting structures," *IEEE Trans. Antennas Propag.*, vol. 50, no. 4, pp. 444-450, Apr. 2002.

[70] J. Li, and L. Li, "Electromagnetic scattering by a mixture of conducting and dielectric objects: analysis using method of moments," *IEEE Trans. Veh. Vechnol*., vol. 53, no. 2, pp. 514-520, Mar. 2004.

[71] A. Glisson, "An integral equation for electromagnetic scattering from homogeneous dielectric bodies," *IEEE Trans. Antennas Propag*., vol. AP-32, no. 2, pp. 173-175, Feb. 1984.

[72] D. E. Livesay, and K. M. Chen, "Electromagnetic fields induced inside arbitrarily shaped biological bodies," *IEEE Trans. Microw. Theory Tech*., vol. MTT-22, no. 12, pp. 1273-1280, Dec. 1974.

[73] G. Gouesbet, B. Maheu, and G. Grehan, "Light scattering from a sphere arbitrarily located in a Gaussian beam, using a Bromwich formulation," *J. Opt. Soc. Am. A*, vol. 5, pp. 1427-1443, 1988.

[74] MiePlot Program, [Online]. Available: http://philiplaven.com/mieplot.htm.

[75] H. Estephan, M. Amin, K. Yemelyanov, and A. Hoorfar, "Waveform design for through-the-wall radar imaging applications," *Proc. of SPIE*, vol. 6934, 69430S, pp. 1-11, 2008.

[76] M. R. Bell, "Information theory and radar waveform design," *IEEE Trans. Inf. Theory*, vol. 39, no. 5, pp. 1578-1597, Sep. 1993.

[77] S. Gabriel, R. W. Lau, and C. Gabriel, "The dielectric properties of biological tissues: II. measurements in the frequency range 10 Hz to 20 GHz," *Phys. Med. Biol*, 41, pp. 2251-2269, 1996.

[78] Moeness G. Amin, *Through-the-wall Radar Imaging*, CRC Press, 2011, pp. 107-118.

[79] Fauzia Ahmad, G. Frazer, S. Kassam and M. G. Amin, "Design and implementation of near-field, wideband synthetic aperture beamformers", *IEEE Trans. Aerosp. Electron. Syst.*, vol. 40, no. 1, Jan 2004.

[80] M. I. Skolnik, *Radar Handbook* (*2nd Edition*), McGraw-Hill, 1990, pp. 2.1-2.10.

[81] P.T. Huynh, A.M. Jarolimek, and S. Daye, "The false-negative mammogram," *Radiograph*, vol. 18, no. 5, pp. 1137-1154, 1998.

[82] J.G. Elmore, M.B. Barton, V.M. Moceri, S. Polk, P.J. Arena, and S.W. Fletcher, "Ten-year risk of false positive screening mammograms and clinical breast examinations," *New Eng. J. Med.*, vol. 338, no. 16, pp. 1089-1096, 1998.

[83] S.S. Chaudhary, R.K. Mishra, A. Swarup, and J.M. Thomas, "Dielectric properties of normal and malignant human breast tissues at radiowave and microwave frequencies," *Indian J. Biochem. Biophy.*, vol. 21, pp. 76-79, 1984.

[84] P.M. Meaney, M.W. Fanning, D. Li, S.P. Poplack, and K.D. Paulsen, "A clinical prototype for active microwave imaging of the breast," *IEEE Trans. Microwave Theory Tech.*, vol. 48, pp. 1841-1853, Nov. 2000.

[85] A.E. Bulyshev, S.Y. Semenov, A.E. Souvorov, R.H. Svenson, A.G. Nazarov, Y.E. Sizov, and G.P. Tatsis, "Computational modeling of three-dimensional microwave tomography of breast cancer," *IEEE Trans. Biomed. Eng.*, vol. 48, pp. 1053-1056, 2001.

[86] S.C. Hagness, A. Taflove, and J.E. Bridges, "Three-dimensional FDTD analysis of a pulsed microwave confocal system for breast cancer detection: Design of an antenna-array element," *IEEE Trans. Antenna and Propagat.*, vol. 47, no. 5, pp. 783-791, May 1999.

[87] X. Li, S.K. Davis, S.C. Hagness, D.W. Weide, B.D. Van Veen, "Microwave imaging via space-time beamforming: experimental investigation of tumor detection in multilayer breast phantoms," *IEEE Trans. Microwave Theory Tech.*, vol. 52, no. 8, pp. 1856-1865, Aug 2004.

[88] M. Klemm, I.J. Craddock, J.A. Leendertz, A. Preece, and R. Benjamin, "Radar-based breast cancer detection using a hemispherical antenna array – experimental results," *IEEE Trans. Antenna Propagat.*, vol. 57, no. 6, pp. 1692-1704, Jun. 2009.

[89] X. Yun, E. C. Fear, R. H. Johnston, "Compact antenna for radar-based breast cancer detection," *IEEE Trans. on Antennas and Propagation*, vol. 53, no. 8, Aug. 2005, pp. 2374-2380.

[90] H. M. Jafari, M. J. Deen, S. Hranilovic, N. K. Nikolova, "A study of ultrawideband antennas for near-field imaging," *IEEE Trans. on Antennas and Propagation*, vol. 55, no. 4, Apr. 2007, pp. 1184-1188.

[91] W. Huang, A. A. Kishk, "Compact dielectric resonator antenna for microwave breast cancer detection," *IET Microwaves, Antennas & Propagation*, Vol. 3, Iss. 4, pp. 638-644, 2009.

[92] D. Gibbins, M. Klemm, I. J. Craddock, J. A. Leendertz, A. Preece, R. Benjamin, "A comparison of a wide-slot and a stacked patch antenna for the purpose of breast cancer detection," *IEEE Trans. on Antennas and Propagation*, vol. 58, no. 3, Mar. 2010, pp. 665-674.

[93] M. Lazebnik, L. McCartney. D. Popovic, C. Watkins, M. Lindstrom, J. Harter, S. Sewall, A. Magliocco, J. Booske, M. Okoniewski, S. Hagness, "A large-scale study of the ultrawideband mcirowave dielectric properties of normal breast tissue obtained from reduction surgeries," *Phys. Med. Biol.*, 52 (2007), pp. 2637-2656.

[94] J. Leendertz, A. Preece, R. Nilavalan, I. J. Craddock, R. Benjamin, "A liquid phantom medium for microwave breast imaging," *6th Int. Congress Eur. Bioelectromagn. Assoc.*, Budapest, Hungary, Nov. 2003.

[95] American Cancer Society, Breast Cancer Overview Guide, [Online]. Available: http://www.cancer.org/Cancer/BreastCancer/OverviewGuide/index.

[96] R. Amineh, M. Ravan, A. Trehan, N. K. Nikolova "Near-field microwave imaging based on planar aperture scanning," in *Proc. 2010 IEEE MTT-S Int. Microwave Symp*., Anaheim, CA, pp. 760-763.

[97] M. Klemm, J. Leendertz, D. Gibbins, I. J. Craddock, A. Preece, R. Benjamin "Towards contrast enhanced breast imaging using UWB microwave radar system," *in Proc. 2010 IEEE Radio and Wireless Symp*., New Orleans, LA.

[98] E. C. Fear, X. Li, S. C. Hagness, M. A. Stuchly, "Confocal microwave imaging for breast cancer detection: localization of tumors in three dimensions," *IEEE Trans. Biomed. Eng,* VOL. 49, NO. 8, Aug. 2002.

[99] Mark A. Richards, *Fundamentals of Radar Signal Processing*, McGraw-Hill, New York, 2005.

[100] M. Y. W. Chia, S.W. Leong, C.K. Sim, and K.M. Chan, "Through-wall UWB radar operating within FCC's mask for sensing heart beat and breathing rate," *European Radar Conference*, pp. 267-270, Oct. 2005.

[101] Victor C. Chen, and Hao Ling, *Time-Frequency Transforms for Radar Imaging and Signal Analysis*, Artech House, Boston, 2002, pp. 25-31.

[102] A.V. Oppenheim and R.W. Schafer, *Discrete-Time Signal Processing*, Prentice-Hall, 1989, pp. 447-448.

[103] Lauralee Sherwood, *Fundamentals of Physiology: A Human Perspective*, Thomson Brooks/Cole, 2006, pp. 364-403.

[104] G. Andria, M. Savino, and A. Trotta, "Application of Wigner-Ville distribution to measurements on transient signals," *IEEE Trans. Instrum. Meas*., vol. 43, no. 2, pp. 187-193, Apr. 1994.

[105] B. Park, O. Boric-Lubecke, and V. Lubecke, "Arctangent demodulation with DC offset compensation in quadrature Doppler radar receiver systems," *IEEE Trans. Microw. Theory Tech.*, vol. 55, no. 5, pp. 1073-1079, May 2007.

[106] Hittite Microwave Corp., HMC830LP6GE Data Sheet: Fractional-N PLL with Integrated VCO SMT, Chelmsford, MA [Online]. Available: http://www.hittite.com/content/documents/data_sheet/hmc830lp6g.pdf.

[107] A. Torosyan, and A. N. Willson, "Exact analysis of DDS spurs and SNR due to phase truncation and arbitrary phase-to-amplitude errors," i*n IEEE Int. Conf. Frequency Control Symp. and Exposition*, Vancouver, BC, Canada, Aug. 2005.

Appendix

Appendix A Matlab Code

This appendix presents all the Matlab code we have used in this dissertation.

A.1 Reflection and Transmission Through a Multiple Layer Wall

The reflection and transmission through a multiple layer wall is calculated by using the plane wave theory [49], as mentioned in Chapter 2.1 and Chapter 3.1.3. An iterative step was used to acquire the multiple reflections inside the wall. Each layer was assumed to be homogeneous and infinite large. The loss of the wall can be defined using loss tangent or conductivity values.

```
%****** perpendicular polarization case **********

% clean up
clc
clear all

%% time/frequency resolution

Fs = 50e9; % sampling frequency >= 2*fm
Tm = 50e-9; % maximum time for the signal
Ts = 1/Fs;
t = Ts:Ts:Tm;
f = linspace(Fs/length(t),Fs,length(t));

% define input pulse signal
w0 = 0.5e-9; % pulse width
f0 = 3e9; % center frequency
x = exp(-((t-5e-9)/w0).^2) .* exp(i*2*pi*f0*t);

%% Wall Parameters

% total # of wall layers
N=3;

% d
d(1)=0*1e-2; % distance from radar to the 1st wall
d(2)=20*1e-2; % thickness of 1st wall
d(3)=30*1e-2; % thickness of 2nd wall
d(4)=20*1e-2; % thickness of 3rd wall
```

```
% episilon
e0=1/36/pi*10^(-9);
e(1)=e0;
e(2)=4*e0; % er1=4
e(3)=1*e0; % er2=1
e(4)=4*e0; % er3=4
e(5)=e0;

% mu
u0=4*pi*10^(-7);
u(1)=u0; % air
u(2)=1*u0; % ur1=1
u(3)=1*u0; % ur2=1
u(4)=1*u0; % ur3=1
u(5)=u0; % air

% loss tangent delta
delta(1)=0; % loss tangent of air
delta(2)=0.1; % loss tangent of 1st wall
delta(3)=0; % loss tangent of 2nd wall
delta(4)=0; % loss tangent of 3rd wall
delta(5)=0; % loss tangent of air

% Incidence angle
theta(1)=0*pi/180;

%% Calculation

RC=[];
TC=[];

% frequency
for f1=Fs/length(t):Fs/length(t):Fs;
    w=2*pi*f1;

    % Transmitted angle
    theta(N+2)=theta(1);
    % useful parameters
    A(N+2)=1;
    B(N+2)=0;

r(N+2)=sqrt(j*w*u(N+2)*(w*e(N+2)*delta(N+2)+j*w*e(N+2)));

    for i=N+1:-1:1
```

```
        r(i)=sqrt(j*w*u(i)*(w*e(i)*delta(i)+j*w*e(i)));
        theta(i)=asin(r(i+1)*sin(theta(i+1))/r(i));

Y(i+1)=cos(theta(i+1))/cos(theta(i))*sqrt(e(i+1)/e(i)*(1-
j*delta(i+1))/(1-j*delta(i)));
        phi(i)=d(i)*r(i)*cos(theta(i));
        A(i)=1/2*exp(phi(i))*(A(i+1)*(1+Y(i+1))+B(i+1)*(1-
Y(i+1)));
        B(i)=1/2*exp(-phi(i))*(A(i+1)*(1-
Y(i+1))+B(i+1)*(1+Y(i+1)));
    end

    % Reflection and Transmission
    R=B(1)/A(1); % Reflection Coefficient
    T=1/A(1); % Transmission Coefficient

    RC=[RC R]; % Reflection Coefficient with freq.
    TC=[TC T]; % Transmission Coefficient with freq.
end

% transmitted signal
y_F=fft(x).*TC;
y_T=ifft((fft(x).*TC));

%% Plot
figure

subplot(3,3,1)
plot(f/1e9, abs(RC),'b','linewidth',2)
xlabel('Freq [GHz]')
ylabel('Magnitude')
title('Reflection')
% axis([0.5 1.5 0 0.8])

subplot(3,3,2)
plot(f/1e9, angle(RC),'r','linewidth',2)
xlabel('Freq [GHz]')
ylabel('Phase [Deg]')
title('Reflection')
% axis([0.5 1.5 -4 4])

subplot(3,3,3)
plot(f/1e9, abs(TC),'b','linewidth',2)
xlabel('Freq [GHz]')
ylabel('Magnitude')
```

```
title('Transmission')
% axis([0 5 0 1])

subplot(3,3,4)
plot(f/1e9, angle(TC)*180/pi,'r','linewidth',2)
xlabel('Freq [GHz]')
ylabel('Phase [Deg]')
title('Transmission')
% axis([0 5 -180 180])

subplot(3,3,5)
plot(t/1e-9-5,abs(x),'g','linewidth',2);
xlabel('Time [ns]')
title('Input Signal (V)')
axis([-5 15 0 1])
grid on

subplot(3,3,6)
plot(f/1e9,abs(fft(x)),'b','linewidth',2);
xlabel('Freq [GHz]')
title('Input Signal Spectrum')
axis([0 5 0 50])
grid on

subplot(3,3,7)
plot(f/1e9,abs(y_F),'b','linewidth',2);
xlabel('Freq [GHz]')
title('Output Signal Spectrum')
axis([0 5 0 50])
grid on

subplot(3,3,8)
plot(t/1e-9-5, abs(y_T),'g','linewidth',2);
xlabel('Time [ns]')
title('Output Signal (V)')
axis([-5 15 0 1])
grid on
```

A.2 2-D Backprojection Beamformer for Microwave Imaging

The 2-D Backprojection microwave beamforming algorithm was used to recover the 2-D image of the radar objects in Chapter 4.1.

```
clc
clear all
close all

%% Define parameters

% calibrate the time delay of the system hardware in ns
time_delay = 20;
% total # of sample points in a 100ns period
num = 7680;

% distance between transmitting antenna and 1st receiving
antenna in cm
s = 40;

%% Raw data

prt_num = 100;
raw_data = zeros(num, 8);
filename = '20110226_163042_CH0.dat'; % read saved data
acquired by the receiving antenna array
filename_len = length(filename);

% there are 8 receiving antennas in totoal, numbered from 0
to 7
for i1 = 0:7
    filename(filename_len-4) = num2str(i1); % CH0
    fp=fopen(filename,'rb');
    fseek(fp,prt_num*num*2*2,-1); % begin of file, I Q,
16bit
    data=fread(fp,num*2,'uint16');% I0 Q0 I1 Q1 ...
    fclose(fp);
    data_I = data(1:2:end)-2048;
    data_Q = data(2:2:end)-2048;
    raw_data(:, i1+1) = data_I + j*data_Q;
end

% filter out the out-of-band noise in the freqeuency domain
```

```
raw_data_fft = fft(raw_data);
raw_data_fft(301:7380,:) = 0;
raw_data = ifft(raw_data_fft);


%% put raw data in the matrix zz

zz = raw_data;

%% Part 2
% Open the I&Q data from the file
%----------------------------------------
% use one tx antenna and N receiving antennas
N = 8;
% distance between adjacent receiving antennas in cm
t = 6;
% assume digital oscilloscope resolution in ns
p = 0.01302;
% center frequency in GHz
f0 = 3;
% wavelength in cm
lamda = 30 / f0;

%% scan angle from -30 to 30 degrees
stangle = -45:1:45;
r = 2 : 2 : 1000;

mag = zeros(length(r),length(stangle));

for i3 = 1:1:length(stangle);  % i represents steering
angle from -30 to 30
    for i2 = 1:1:length(r); % r represents distance from 1
to 1000, r=1 means 0.3cm
        % transmitting path in cm, a value dependent of
distance and angle
        Lt = r(i2)*1;
        % receiving path in cm, an array depedent of
distance, angle and #n
        n = 1:1:N; % n represents # of receiving antenna
from 1 to N
        Lr = sqrt((s+(n-1)*t).^2+r(i2)^2-2*(s+(n-
1)*t)*r(i2)*cos(pi/2-stangle(i3)*pi/180)); % Lr is a 1*N
array
        % phase delay of N receiving antennas
        phi_steer = 2*pi/lamda*Lr;
```

```
        % phase difference regarding to the central one
        dphi_steer = phi_steer-phi_steer(round((N+1)/2));
        % distance difference was corrected in this program,
it's necessary especially when s>>t
        % mth row data in matrix zz
        m = round((Lt+Lr)/(p*30)+time_delay/p);
        for i4 = 1 : 1 : N
            mag(i2,i3) = mag(i2,i3) +
zz(m(i4),i4)*exp(j*dphi_steer(i4)');
        end
        x(i2,i3) = r(i2)*1*sin(stangle(i3)*pi/180);
        y(i2,i3) = r(i2)*1*cos(stangle(i3)*pi/180);
        z(i2,i3) = abs(mag(i2,i3));
    end
end

%% Time-gating the coupling and wall reflection

% mag(1:190,:) = 0;

figure
h = pcolor(x/100,y/100,z);
set(h, 'LineStyle', 'none')
colormap('default')
% colorbar
%caxis([-20 0])
xlabel('Cross Range (m)')
ylabel('Down Range (m)')
% title('BP Image')
%axis ([-150 150 50 250])
```

A.3 3-D Backprojection Beamformer for Microwave Imaging

The 3-D Backprojection microwave beamforming algorithm was used to recover the 3-D image of the radar objects in Chapter 4.2.

```
clc;
clear all;
close all;

%% Define target parameters

er1 = 1;


%% Calculate Scattered field at any pisitions

% # of Rx antennas in y,z axis
MY = 31;
MZ = 31;
%
% array spacing in cm
sy = 6;
sz = 6;

%% Define input signal

% Import received complex I/Q data into matrix zz

% ***** matrix zz **********

% assume digital oscilloscope resolution in ps
p = 10;


%% beamforming ********************

% transmitter location before rotation transfer (0,0,0)
yt0 = 0;
zt0 = 0;
xt0 = 0;

% wavelength in cm
lamda0 = 3e8 / f0 * 100;
```

```
rangex = 100 : 3 : 301;%[100 150 200 221 250 300];
rangey = -120 : 3 : 120;
rangez = -120 : 3 : 120;


%% Beamforming
% array position
for a = 1 : 1 : MZ
    for b = 1 : 1 : MY
        %ytn((a-1)*MY+b) = ( b - MY ) * sy;
        %ztn((a-1)*MY+b) = ( a - MZ ) * sz;
        ytn((a-1)*MY+b) = ( b - (MY+1)/2 ) * sy;
        ztn((a-1)*MY+b) = ( a - (MZ+1)/2 ) * sz;
        xtn((a-1)*MY+b) = xt0;
    end
end

for k1 = 1:1:length(rangex)
    for i1 = 1:1:length(rangey)
        for j1 = 1:1:length(rangez)
            %********************calculate Tx path in
cm*****************
            Lt = sqrt(er1) * abs( rangex(k1) - xt0 );
            %********************calculate Rx path in
cm*****************
            Lr = sqrt(er1) * sqrt( (ytn - rangey(i1)).^2 +
(ztn - rangez(j1)).^2 + (xtn - rangex(k1)).^2 );  % Lr is a
1*N array
            % phase delay of N receiving antennas
            phi_steer = - 2 * pi / lamda0 * Lr;
            % phase difference regarding to the central one
            dphi_steer = phi_steer -
phi_steer(round((MY*MZ+1)/2));
            % location of data
            m  =  round((Lt+Lr(round((MY*MZ+1)/2)))/(p*0.03));
            %if m>760
            %    m=760;
            %end
            v(i1,k1,j1)=abs( zz(m,:) *
(exp(j*dphi_steer)') );
        end
    end
end
```

```
v_nom = v/max(max(max(v)));


%% Plot

figure

[range_x,range_y,range_z]=meshgrid(rangex/100,rangey/100,ra
ngez/100);
yslice=[0 1.2];
zslice=-1.2;
xslice=[2.2 3];
slice(range_x,range_y,range_z,20*log10(v_nom),xslice,yslice
,zslice)
xlabel('Down Range (m)','fontsize',12)
ylabel('Cross Range (m)','fontsize',12)
zlabel('Height (m)','fontsize',12)
axis([1.0 3.0 -1.2 1.2 -1.2 1.2])
colormap('default')
colorbar
caxis([-20 -0])
```

A.4 3-D Electromagnetic Scattering Using MoM

The electromagnetic scattering of a 3-D radar object was analyzed using MoM numerical method. Here is the Matlab code to implement the MoM mentioned in Chapter 3.1.4.

```
%% clear
clc;
clear all;
close all;

%% Define target parameters
% length of the cube
R = 32e-2;
% cubic step
H = R / 8;
% cubic equivalent to a sphere (radius an)
an = H * (0.75 / pi)^(1/3);
% define cells #
N = 206 * 2 * 2;

% define target properties
e0 = 1 / 36 / pi * 1e-9;
mu0 = 4 * pi * 1e-7;

er1 = 1;
%sig1 = 0;
er2 = 50;
sig2 = 4;

%% Define all the cells of 3-D radar object

xd = [ 0.5*H*ones(1,22)+0e-2 1.5*H*ones(1,20)+0e-2
2.5*H*ones(1,18)+0e-2 3.5*H*ones(1,16)+0e-2
4.5*H*ones(1,28)+0e-2 5.5*H*ones(1,28)+0e-2
6.5*H*ones(1,28)+0e-2 7.5*H*ones(1,28)+0e-2 ...
       8.5*H*ones(1,2)+0e-2 9.5*H*ones(1,2)+0e-2
10.5*H*ones(1,2)+0e-2 11.5*H*ones(1,2)+0e-2
12.5*H*ones(1,2)+0e-2 13.5*H*ones(1,2)+0e-2
14.5*H*ones(1,2)+0e-2 15.5*H*ones(1,2)+0e-2
16.5*H*ones(1,2)+0e-2 ...
       0.5*H*ones(1,22)+0e-2 1.5*H*ones(1,20)+0e-2
2.5*H*ones(1,18)+0e-2 3.5*H*ones(1,16)+0e-2
```

```
4.5*H*ones(1,28)+0e-2 5.5*H*ones(1,28)+0e-2
6.5*H*ones(1,28)+0e-2 7.5*H*ones(1,28)+0e-2 ...
       8.5*H*ones(1,2)+0e-2 9.5*H*ones(1,2)+0e-2
10.5*H*ones(1,2)+0e-2 11.5*H*ones(1,2)+0e-2
12.5*H*ones(1,2)+0e-2 13.5*H*ones(1,2)+0e-2
14.5*H*ones(1,2)+0e-2 15.5*H*ones(1,2)+0e-2
16.5*H*ones(1,2)+0e-2 ];
yd = [ 17.5*H:-H:-3.5*H  16.5*H:-H:11.5*H 9.5*H:-H:-3.5*H
15.5*H:-H:12.5*H 9.5*H:-H:-3.5*H 14.5*H:-H:13.5*H 9.5*H:-
H:-3.5*H  9.5*H:-H:-17.5*H 9.5*H:-H:-17.5*H 9.5*H:-H:-
17.5*H 9.5*H:-H:-17.5*H ...
       9.5*H:-H:8.5*H  8.5*H:-H:7.5*H  7.5*H:-H:6.5*H
6.5*H:-H:5.5*H  5.5*H:-H:4.5*H  4.5*H:-H:3.5*H  3.5*H:-
H:2.5*H  2.5*H:-H:1.5*H  1.5*H:-H:0.5*H ...
       17.5*H:-H:-3.5*H  16.5*H:-H:11.5*H 9.5*H:-H:-3.5*H
15.5*H:-H:12.5*H 9.5*H:-H:-3.5*H 14.5*H:-H:13.5*H 9.5*H:-
H:-3.5*H  9.5*H:-H:-17.5*H 9.5*H:-H:-17.5*H 9.5*H:-H:-
17.5*H 9.5*H:-H:-17.5*H ...
       9.5*H:-H:8.5*H  8.5*H:-H:7.5*H  7.5*H:-H:6.5*H
6.5*H:-H:5.5*H  5.5*H:-H:4.5*H  4.5*H:-H:3.5*H  3.5*H:-
H:2.5*H  2.5*H:-H:1.5*H  1.5*H:-H:0.5*H ];
zd = [ -0.5 * H * ones(1,206) 0.5 * H * ones(1,206)];

xdn = [xd -xd];
ydn = [yd yd];
zdn = [zd zd];

r = [xdn(:) ydn(:) zdn(:)];

%% define frequency
Esf = [];

for f1 = 1e9 : 0.02e9 : 11e9;

w = 2 * pi * f1;

k0 = w * sqrt(mu0 * e0) * sqrt(er1); % free space
%r1 = sqrt( j * w * mu0 * ( sig1 + j * w * er1 * e0) );


% Calculate G matrix
% define tow
tow = (sig2 + j * w * e0 * (er2 - 1)) * ones(N, 1);

% define constant values
```

```
A = - j * w * mu0 * k0 * H^3 / 4 / pi;
C = - 2 * j * w * mu0 / 3 / k0^2 * ( exp(-j * k0 * an) * (1
+ j * k0 * an) - 1 ) - 1 / 3 / j / w / e0;

% Gxx
for m = 1 : N
    for n = 1 : N
        if m == n
            Gxx(m, n) = C * tow(n) - 1;
        else
            Rmn = norm(r(m,:) - r(n,:));
            almn = k0 * Rmn;
            cxpmn = (r(m,1) - r(n,1)) / Rmn;
            cxqmn = (r(m,1) - r(n,1)) / Rmn;
            B = (almn^2 - 1 - j * almn) + cxpmn * cxqmn *
(3 - almn^2 + 3 * j * almn);
            Gxx(m,n) = A * tow(n) * exp(- j * almn) /
almn^3 * B;
        end
    end
end

% Gyy
for m = 1 : N
    for n = 1 : N
        if m == n
            Gyy(m, n) = C * tow(n) - 1;
        else
            Rmn = norm(r(m,:) - r(n,:));
            almn = k0 * Rmn;
            cxpmn = (r(m,2) - r(n,2)) / Rmn;
            cxqmn = (r(m,2) - r(n,2)) / Rmn;
            B = (almn^2 - 1 - j * almn) + cxpmn * cxqmn *
(3 - almn^2 + 3 * j * almn);
            Gyy(m,n) = A * tow(n) * exp(- j * almn) /
almn^3 * B;
        end
    end
end

% Gzz
for m = 1 : N
    for n = 1 : N
        if m == n
            Gzz(m, n) = C * tow(n) - 1;
```

```
        else
            Rmn = norm(r(m,:) - r(n,:));
            almn = k0 * Rmn;
            cxpmn = (r(m,3) - r(n,3)) / Rmn;
            cxqmn = (r(m,3) - r(n,3)) / Rmn;
            B = (almn^2 - 1 - j * almn) + cxpmn * cxqmn *
(3 - almn^2 + 3 * j * almn);
            Gzz(m,n) = A * tow(n) * exp(- j * almn) /
almn^3 * B;
        end
    end
end

% Gxy
for m = 1 : N
    for n = 1 : N
        if m ~= n
            Rmn = norm(r(m,:) - r(n,:));
            almn = k0 * Rmn;
            cxpmn = (r(m,1) - r(n,1)) / Rmn;
            cxqmn = (r(m,2) - r(n,2)) / Rmn;
            B = cxpmn * cxqmn * (3 - almn^2 + 3 * j * almn);
            Gxy(m,n) = A * tow(n) * exp(- j * almn) /
almn^3 * B;
        end
    end
end

% Gxz
for m = 1 : N
    for n = 1 : N
        if m ~= n
            Rmn = norm(r(m,:) - r(n,:));
            almn = k0 * Rmn;
            cxpmn = (r(m,1) - r(n,1)) / Rmn;
            cxqmn = (r(m,3) - r(n,3)) / Rmn;
            B = cxpmn * cxqmn * (3 - almn^2 + 3 * j * almn);
            Gxz(m,n) = A * tow(n) * exp(- j * almn) /
almn^3 * B;
        end
end
    end

% Gyx
for m = 1 : N
```

```
    for n = 1 : N
        if m ~= n
            Rmn = norm(r(m,:) - r(n,:));
            almn = k0 * Rmn;
            cxpmn = (r(m,2) - r(n,2)) / Rmn;
            cxqmn = (r(m,1) - r(n,1)) / Rmn;
            B = cxpmn * cxqmn * (3 - almn^2 + 3 * j * almn);
            Gyx(m,n) = A * tow(n) * exp(- j * almn) /
almn^3 * B;
        end
    end
end

% Gyz
for m = 1 : N
    for n = 1 : N
        if m ~= n
            Rmn = norm(r(m,:) - r(n,:));
            almn = k0 * Rmn;
            cxpmn = (r(m,2) - r(n,2)) / Rmn;
            cxqmn = (r(m,3) - r(n,3)) / Rmn;
            B = cxpmn * cxqmn * (3 - almn^2 + 3 * j * almn);
            Gyz(m,n) = A * tow(n) * exp(- j * almn) /
almn^3 * B;
        end
    end
end

% Gzx
for m = 1 : N
    for n = 1 : N
        if m ~= n
            Rmn = norm(r(m,:) - r(n,:));
            almn = k0 * Rmn;
            cxpmn = (r(m,3) - r(n,3)) / Rmn;
            cxqmn = (r(m,1) - r(n,1)) / Rmn;
            B = cxpmn * cxqmn * (3 - almn^2 + 3 * j * almn);
            Gzx(m,n) = A * tow(n) * exp(- j * almn) /
almn^3 * B;
        end
    end
end

% Gzy
for m = 1 : N
```

```
    for n = 1 : N
        if m ~= n
            Rmn = norm(r(m,:) - r(n,:));
            almn = k0 * Rmn;
            cxpmn = (r(m,3) - r(n,3)) / Rmn;
            cxqmn = (r(m,2) - r(n,2)) / Rmn;
            B = cxpmn * cxqmn * (3 - almn^2 + 3 * j * almn);
            Gzy(m,n) = A * tow(n) * exp(- j * almn) /
almn^3 * B;
        end
    end
end

G = [Gxx Gxy Gxz; Gyx Gyy Gyz; Gzx Gzy Gzz];


%% calculate E matrix (field inside the body)
% calculate incidence field E0 = 1

Ei = [1 * exp(- j * k0 * (220e-2 + zdn(:))); 0 * exp(- j *
k0 * (220e-2 + zdn(:))); 0 * exp(- j * k0 * (220e-2 +
zdn(:)))];

E = - G \ Ei;

%% Calculate scattered field at any positions

% ---------------------------------
% # of Tx antennas in y,z axis
MY = 31;
MZ = 31;

% array spacing in cm
sy = 6;
sz = 6;

% Define observation points

OP_X = [ -90e-2 : 6e-2 : 90e-2 -90e-2 : 6e-2 : 90e-2 -90e-
2 : 6e-2 : 90e-2 -90e-2 : 6e-2 : 90e-2 -90e-2 : 6e-2 : 90e-
2 -90e-2 : 6e-2 : 90e-2 -90e-2 : 6e-2 : 90e-2 -90e-2 : 6e-
2 : 90e-2 -90e-2 : 6e-2 : 90e-2 -90e-2 : 6e-2 : 90e-2 ...
         -90e-2 : 6e-2 : 90e-2 -90e-2 : 6e-2 : 90e-2 -90e-
2 : 6e-2 : 90e-2 -90e-2 : 6e-2 : 90e-2 -90e-2 : 6e-2 : 90e-
```

```
2 -90e-2 : 6e-2 : 90e-2 -90e-2 : 6e-2 : 90e-2 -90e-2 : 6e-
2 : 90e-2 -90e-2 : 6e-2 : 90e-2 -90e-2 : 6e-2 : 90e-2 ...
         -90e-2 : 6e-2 : 90e-2 -90e-2 : 6e-2 : 90e-2 -90e-
2 : 6e-2 : 90e-2 -90e-2 : 6e-2 : 90e-2 -90e-2 : 6e-2 : 90e-
2 -90e-2 : 6e-2 : 90e-2 -90e-2 : 6e-2 : 90e-2 -90e-2 : 6e-
2 : 90e-2 -90e-2 : 6e-2 : 90e-2 -90e-2 : 6e-2 : 90e-2 -90e-
2 : 6e-2 : 90e-2 ];
OP_Y = [ -90e-2 * ones(1,31) -84e-2 * ones(1,31) -78e-2 *
ones(1,31) -72e-2 * ones(1,31) -66e-2 * ones(1,31) -60e-2 *
ones(1,31) -54e-2 * ones(1,31) -48e-2 * ones(1,31) -42e-2 *
ones(1,31) -36e-2 * ones(1,31) -30e-2 * ones(1,31) -24e-2 *
ones(1,31) -18e-2 * ones(1,31) -12e-2 * ones(1,31) -6e-2 *
ones(1,31) ...
         0e-2 * ones(1,31) 6e-2 * ones(1,31) 12e-2 *
ones(1,31) 18e-2 * ones(1,31) 24e-2 * ones(1,31) 30e-2 *
ones(1,31) 36e-2 * ones(1,31) 42e-2 * ones(1,31) 48e-2 *
ones(1,31) 54e-2 * ones(1,31) 60e-2 * ones(1,31) 66e-2 *
ones(1,31) 72e-2 * ones(1,31) 78e-2 * ones(1,31) 84e-2 *
ones(1,31) 90e-2 * ones(1,31) ];
OP_Z = -220e-2 * ones(1,961);

OP = [OP_X(:) OP_Y(:) OP_Z(:)];

% ---------------------------------

% find new G - GN

% GNxx
for m1 = 1 : length(OP_X)
    for n1 = 1 : N
        Rmn = norm(OP(m1,:) - r(n1,:));
        almn = k0 * Rmn;
        cxpmn = (OP(m1,1) - r(n1,1)) / Rmn;
        cxqmn = (OP(m1,1) - r(n1,1)) / Rmn;
        B = (almn^2 - 1 - j * almn) + cxpmn * cxqmn * (3 -
almn^2 + 3 * j * almn);
        GNxx(m1,n1) = A * tow(n1) * exp(- j * almn) /
almn^3 * B;
    end
end

% GNyy
for m1 = 1 : length(OP_X)
    for n1 = 1 : N
        Rmn = norm(OP(m1,:) - r(n1,:));
```

```
        almn = k0 * Rmn;
        cxpmn = (OP(m1,2) - r(n1,2)) / Rmn;
        cxqmn = (OP(m1,2) - r(n1,2)) / Rmn;
        B = (almn^2 - 1 - j * almn) + cxpmn * cxqmn * (3 -
almn^2 + 3 * j * almn);
        GNyy(m1,n1) = A * tow(n1) * exp(- j * almn) /
almn^3 * B;
    end
end

% GNzz
for m1 = 1 : length(OP_X)
    for n1 = 1 : N
        Rmn = norm(OP(m1,:) - r(n1,:));
        almn = k0 * Rmn;
        cxpmn = (OP(m1,3) - r(n1,3)) / Rmn;
        cxqmn = (OP(m1,3) - r(n1,3)) / Rmn;
        B = (almn^2 - 1 - j * almn) + cxpmn * cxqmn * (3 -
almn^2 + 3 * j * almn);
        GNzz(m1,n1) = A * tow(n1) * exp(- j * almn) /
almn^3 * B;
    end
end

% GNxy
for m1 = 1 : length(OP_X)
    for n1 = 1 : N
        Rmn = norm(OP(m1,:) - r(n1,:));
        almn = k0 * Rmn;
        cxpmn = (OP(m1,1) - r(n1,1)) / Rmn;
        cxqmn = (OP(m1,2) - r(n1,2)) / Rmn;
        B = cxpmn * cxqmn * (3 - almn^2 + 3 * j * almn);
        GNxy(m1,n1) = A * tow(n1) * exp(- j * almn) /
almn^3 * B;
    end
end

% GNxz
for m1 = 1 : length(OP_X)
    for n1 = 1 : N
        Rmn = norm(OP(m1,:) - r(n1,:));
        almn = k0 * Rmn;
        cxpmn = (OP(m1,1) - r(n1,1)) / Rmn;
        cxqmn = (OP(m1,3) - r(n1,3)) / Rmn;
        B = cxpmn * cxqmn * (3 - almn^2 + 3 * j * almn);
```

```
        GNxz(m1,n1) = A * tow(n1) * exp(- j * almn) /
almn^3 * B;
    end
end

% GNyx
for m1 = 1 : length(OP_X)
    for n1 = 1 : N
        Rmn = norm(OP(m1,:) - r(n1,:));
        almn = k0 * Rmn;
        cxpmn = (OP(m1,2) - r(n1,2)) / Rmn;
        cxqmn = (OP(m1,1) - r(n1,1)) / Rmn;
        B = cxpmn * cxqmn * (3 - almn^2 + 3 * j * almn);
        GNyx(m1,n1) = A * tow(n1) * exp(- j * almn) /
almn^3 * B;
    end
end

% GNyz
for m1 = 1 : length(OP_X)
    for n1 = 1 : N
        Rmn = norm(OP(m1,:) - r(n1,:));
        almn = k0 * Rmn;
        cxpmn = (OP(m1,2) - r(n1,2)) / Rmn;
        cxqmn = (OP(m1,3) - r(n1,3)) / Rmn;
        B = cxpmn * cxqmn * (3 - almn^2 + 3 * j * almn);
        GNyz(m1,n1) = A * tow(n1) * exp(- j * almn) /
almn^3 * B;
    end
end

% GNzx
for m1 = 1 : length(OP_X)
    for n1 = 1 : N
        Rmn = norm(OP(m1,:) - r(n1,:));
        almn = k0 * Rmn;
        cxpmn = (OP(m1,3) - r(n1,3)) / Rmn;
        cxqmn = (OP(m1,1) - r(n1,1)) / Rmn;
        B = cxpmn * cxqmn * (3 - almn^2 + 3 * j * almn);
        GNzx(m1,n1) = A * tow(n1) * exp(- j * almn) /
almn^3 * B;
    end
end

% GNzy
```

```
for m1 = 1 : length(OP_X)
    for n1 = 1 : N
        Rmn = norm(OP(m1,:) - r(n1,:));
        almn = k0 * Rmn;
        cxpmn = (OP(m1,3) - r(n1,3)) / Rmn;
        cxqmn = (OP(m1,2) - r(n1,2)) / Rmn;
        B = cxpmn * cxqmn * (3 - almn^2 + 3 * j * almn);
        GNzy(m1,n1) = A * tow(n1) * exp(- j * almn) /
almn^3 * B;
    end
end

GN = [GNxx GNxy GNxz; GNyx GNyy GNyz; GNzx GNzy GNzz];

Es = GN * E;

Esf = [Esf Es]; % Scattered field at all O.P.s

end
```

A.5 UWB Pulse Radar Micro-Doppler Spectrogram Extraction

The following Matlab code was used to implement the equations in Chapter 5.1 and to extract the micro-Doppler spectrogram signatures from UWB pulse radar.

```
close all
clear all
clc

%% Read signal from saved data

filename = '20110226_163042_CH5.dat';

num = 7680;
% Starting from the 10th pulse to make sure the system
works stable
prt_num = 10;

fp=fopen(filename,'rb');
fseek(fp,prt_num*num*2*2,-1); % begin of file, I Q, 16bit
data=fread(fp,'uint16');% I0 Q0 I1 Q1 ...
fclose(fp);

% total # of pulses, make it an even number
N_pulse = 2*round(length(data)/num/2/2-1);
sigwave = zeros(num, N_pulse);

for i1 = 1 : 1 : N_pulse
    data_I = data((i1-1)*num*2+1:2:i1*num*2)-2048;
    data_Q = data((i1-1)*num*2+2:2:i1*num*2)-2048;
    sigwave(:,i1) = data_I + j*data_Q;
end

%% X-correlation step
% In this case, a rectangular filter is used to filter out
the noise

sigwave_fft = fft(sigwave);
sigwave_fft(301:7380,:) = 0;
sigwave_denoise = ifft(sigwave_fft);

% sigwave_denoise = sigwave;
```

```
%% Static targets cancellation (method 1) - Subtract
averaged signal

sigwave_denoise_avg = mean(sigwave_denoise,2);
sigwave_denoise_cal1 = zeros(num, N_pulse);

for i2 = 1 : 1 : N_pulse
    sigwave_denoise_cal1(:,i2) = sigwave_denoise(:,i2) -
sigwave_denoise_avg;
end

%% Static targets cancellation (method 2) - One delay
canceler

% sigwave_denoise_cal2 = zeros(num, N_pulse);
% sigwave_denoise(:,N_pulse+1) = sigwave_denoise(:,1);
%
% for i3 = 1 : 1 : N_pulse
%     sigwave_denoise_cal2(:,i3) = sigwave_denoise(:,i3+1)
- sigwave_denoise(:,i3);
% end

%% Spectrogram Plot

sigwave_slow = sum(sigwave_denoise_cal1(2200:6600, :));

[S,F,T,P] =
spectrogram(sigwave_slow,44,40,N_pulse,100,'yaxis'); %
default Hamming window if not defined

PC = [P(N_pulse/2+1:N_pulse,:); P(1:N_pulse/2,:)];
PC_nom = PC/max(max(PC));

figure
surf(T,F-50,20*log10(abs(PC_nom)),'EdgeColor','none');
axis xy; axis tight; colormap(jet); view(0,90);
colorbar
caxis([-60 0])
xlabel('Time (Sec)');
ylabel('Frequency (Hz)');
```

A.6 UWB Pulse Radar Micro-Doppler Wigner-Ville spectrum Extraction

The following Matlab code was used in Chapter 5.5.3 to extract the micro-Doppler Wigner-Ville spectrum signatures from UWB pulse radar.

```
close all
clear all
clc

%% Read signal from saved data

filename = '20110226_163042_CH5.dat';

num = 7680;
% Starting from the 10th pulse to make sure the system
works stable
prt_num = 10;
fr = 100;

fp=fopen(filename,'rb');
fseek(fp,prt_num*num*2*2,-1); % begin of file, I Q, 16bit
data=fread(fp,'uint16');% I0 Q0 I1 Q1 ...
fclose(fp);

% total # of pulses, make it an even number
N_pulse = 2*round(length(data)/num/2/2-1);
sigwave = zeros(num, N_pulse);

for i1 = 1 : 1 : N_pulse
    data_I = data((i1-1)*num*2+1:2:i1*num*2)-2048;
    data_Q = data((i1-1)*num*2+2:2:i1*num*2)-2048;
    sigwave(:,i1) = data_I + j*data_Q;
end

%% X-correlation step
% In this case, a rectangular filter is used to filter out
the noise

sigwave_fft = fft(sigwave);
sigwave_fft(301:7380,:) = 0;
sigwave_denoise = ifft(sigwave_fft);

% sigwave_denoise = sigwave;
```

```
%% Static targets cancellation (method 1) - Subtract
averaged signal

sigwave_denoise_avg = mean(sigwave_denoise,2);
sigwave_denoise_cal1 = zeros(num, N_pulse);

for i2 = 1 : 1 : N_pulse
    sigwave_denoise_cal1(:,i2) = sigwave_denoise(:,i2) -
sigwave_denoise_avg;
end

%% Wigner-Ville spectrum Plot

sigwave_slow = sum(sigwave_denoise_cal1(2200:6600, :));

g = tftb_window(15,'Kaiser');
h = tftb_window(63,'Kaiser');

[TFR, T, F] = tfrspwv(conj(sigwave_slow'), 1:N_pulse, fr, g,
h, 1);
TFRA = [TFR(fr/2+1:fr,:); TFR(1:fr/2,:)];
TFRA_max = max(max(abs(TFRA)));
figure
surf((1:N_pulse)/100,-fr/2:fr/2-
1,20*log10(abs(TFRA)/TFRA_max),'EdgeColor','none');
axis xy; axis tight; colormap(jet); view(0,90);
colorbar
xlabel('Time (Sec)');
ylabel('Frequency (Hz)');
caxis([-60 0])
```

Appendix B MoM Method for Solving Electromagnetic Scattering Problem

This appendix introduces the details of MoM to solve the 3-D radar scattering briefly described in Chapter 3.1.4.

To calculate the radar scattering from a homogeneous lossy dielectric target with complex permittivity ε^* and permeability μ_0 illuminated by an incident plane wave. The induced current inside the target can be replaced with an equivalent free-space current density J_{eq} given by [72]

$$J_{eq}(\vec{r}) = jw(\varepsilon^* - \varepsilon_0)E(\vec{r}) = \tau E(\vec{r}) \tag{B-1}$$

where $E(\vec{r})$ is the total electric field inside the object given by the sum of incident field E^i and scattered field E^s

$$E(\vec{r}) = E^i(\vec{r}) + E^s(\vec{r}) \tag{B-2}$$

The dyadic Green's function relates the scattered electric field E^s to the equivalent internal current density via

$$E^s(\vec{r}) = \int_v \overline{G}(\vec{r},\vec{r}') \cdot J_{eq}(\vec{r}')dr' \tag{B-3}$$

where

$$\overline{G}(\vec{r},\vec{r}') = jw\mu_0\left[\bar{I} + \frac{\nabla\nabla}{k_0^2}\right]g(\vec{r},\vec{r}') \tag{B-4}$$

$$g(\vec{r},\vec{r}') = \frac{e^{-jk_0(\vec{r}-\vec{r}')}}{4\pi|\vec{r}-\vec{r}'|} \tag{B-5}$$

The dielectric target has been divided into N cubic cells. As long as each cell is very small, we can assume that $E(\vec{r})$ is constant within each cell. Then (B-2) to(B-5) can be represented using matrix equation in the form as

$$\begin{bmatrix} A_{xx} & A_{xy} & A_{xz} \\ A_{yx} & A_{yy} & A_{yz} \\ A_{zx} & A_{zy} & A_{zz} \end{bmatrix} \begin{bmatrix} E_x \\ E_y \\ E_z \end{bmatrix} = \begin{bmatrix} -E_x^i \\ -E_y^i \\ -E_z^i \end{bmatrix} \tag{B-6}$$

where $E_u = [E_{u1}, E_{u2}, \cdots, E_{uN}]^T$ (u = x, y, z) are the internal total electric field, which are unknown; $E_u^i = [E_{u1}^i, E_{u2}^i, \cdots, E_{uN}^i]^T$ (u = x, y, z) are the incident electric field, which are given; and $A_{uv} = [A_{uv}^{mn}]_{N\times N}$ (u, v = x, y, z) are constant matrices, whose elements are defined by [72]

$$A_{uu}^{mm} = \frac{2}{3}(\varepsilon_r^* - 1)e^{-jk_0 a_m}(1 + jk_0 a_m) - \varepsilon_r^* \tag{B-7}$$

$$A_{uu}^{mn} = \frac{(\varepsilon_r^* - 1)V_n e^{-j\phi_{mn}}}{4\pi|r_m - r_n|^3}[(\phi_{mn}^2 - j\phi_{mn} - 1) - (u_m - u_n)^2(\phi_{mn}^2 - 3j\phi_{mn} - 3)], \quad m \neq n \tag{B-8}$$

$$A_{uv}^{mn} = \frac{(1 - \varepsilon_r^*)V_n e^{-j\phi_{mn}}}{4\pi|r_m - r_n|^3}(u_m - u_n)^2(\phi_{mn}^2 - 3j\phi_{mn} - 3), \quad m \neq n, u \neq v \tag{B-9}$$

$$A_{uv}^{mm} = 0, \quad u \neq v \tag{B-10}$$

where V_n is the volume of cell n and

$$\phi_{mn} = k_0|r_m - r_n|, \; a_n = \left(\frac{3V_n}{4\pi}\right)^{1/3} \tag{B-11}$$

$$r_m = (x_m, y_m, z_m), \; r_n = (x_n, y_n, z_n) \tag{B-12}$$

After addressing the internal total electric field using (B-6), the scattered filed can be calculated based on (B-1) and (B-3). We have implemented the theoretical formulas using Matlab code.

Appendix C FPGA Source Code Used to Implement the DDC in CW Radar

This appendix introduces the FPGA VHDL source code used to implement the DDC function in the developed CW radar, shown in Chapter 5.6.1.

```
-- Create Date:    11:52:32 09/07/2011
-- Design Name:
-- Module Name:    ddc - Behavioral
-- Project Name:
-- Target Devices:
-- Tool versions:
-- Description:
--
-- Dependencies:
--
-- Revision:
-- Revision 0.01 - File Created
-- Additional Comments:
--
----------------------------------------------------------------------------
library IEEE;
use IEEE.STD_LOGIC_1164.ALL;
use IEEE.STD_LOGIC_ARITH.ALL;
use IEEE.STD_LOGIC_UNSIGNED.ALL;

-- Uncomment the following library declaration if using
-- arithmetic functions with Signed or Unsigned values
--use IEEE.NUMERIC_STD.ALL;

-- Uncomment the following library declaration if instantiating
-- any Xilinx primitives in this code.
--library UNISIM;
--use UNISIM.VComponents.all;

entity ddc is
   Port ( clk : in  STD_LOGIC;
          adc_data_in : in  STD_LOGIC_VECTOR (15 downto 0);
          reset : in  STD_LOGIC;
                        ddc_rdy : out std_logic;
          dataI : out  STD_LOGIC_VECTOR (15 downto 0);
          dataQ : out  STD_LOGIC_VECTOR (15 downto 0));
end ddc;
```

```
architecture Behavioral of ddc is

component NCO20MHz
        port (
        clk: IN std_logic;
        cosine: OUT std_logic_VECTOR(15 downto 0);
        sine: OUT std_logic_VECTOR(15 downto 0);
        phase_out: OUT std_logic_VECTOR(27 downto 0));
end component;

component multiplier
        port (
        clk: IN std_logic;
        a: IN std_logic_VECTOR(15 downto 0);
        b: IN std_logic_VECTOR(15 downto 0);
        p: OUT std_logic_VECTOR(31 downto 0));
end component;

component cic_filter
        port (
        din: IN std_logic_VECTOR(15 downto 0);
        clk: IN std_logic;
        dout: OUT std_logic_VECTOR(15 downto 0);
        rdy: OUT std_logic;
        rfd: OUT std_logic);
end component;

signal cosine : std_logic_vector(15 downto 0);
signal sine : std_logic_vector(15 downto 0);
signal data_signed : std_logic_vector(15 downto 0);
signal data32bit_mix_out_i : std_logic_vector(31 downto 0);
signal data32bit_mix_out_q : std_logic_vector(31 downto 0);
signal d_inphase_cic : std_logic_vector(15 downto 0);
signal d_quart_cic  : std_logic_vector(15 downto 0);

begin

LO_inst : NCO20MHz
                port map (
                        clk => clk,
                        cosine => cosine, --20MHz
                        sine => sine,
                        phase_out => open);
```

```
-- raw data -> abs_data
process(clk)
begin
  if reset='1' then
                    data_signed <= (others=>'0');
  elsif rising_edge(clk) then
      data_signed <= adc_data_in - 32768;
  end if;
end process;

-- multiply sin/cos
u_mul_cos : multiplier
port map(
    clk  =>  clk,  --60M
                    a    =>  data_signed,
                    b    =>  cosine,
                    p    =>  data32bit_mix_out_i
);

u_mul_sin : multiplier
port map(
    clk  =>  clk,  --60M
                    a    =>  data_signed,
                    b    =>  sine,
                    p    =>  data32bit_mix_out_q
);

--fir truncate bits:32->16
process(reset,clk)
begin
   if reset='1' then
      d_inphase_cic<=(others=>'0');
      d_quart_cic  <=(others=>'0');
   elsif clk'event and clk='1' then
      d_inphase_cic <=data32bit_mix_out_i(31 downto 16);
      d_quart_cic  <=data32bit_mix_out_q(31 downto 16);
   end if;
end process;

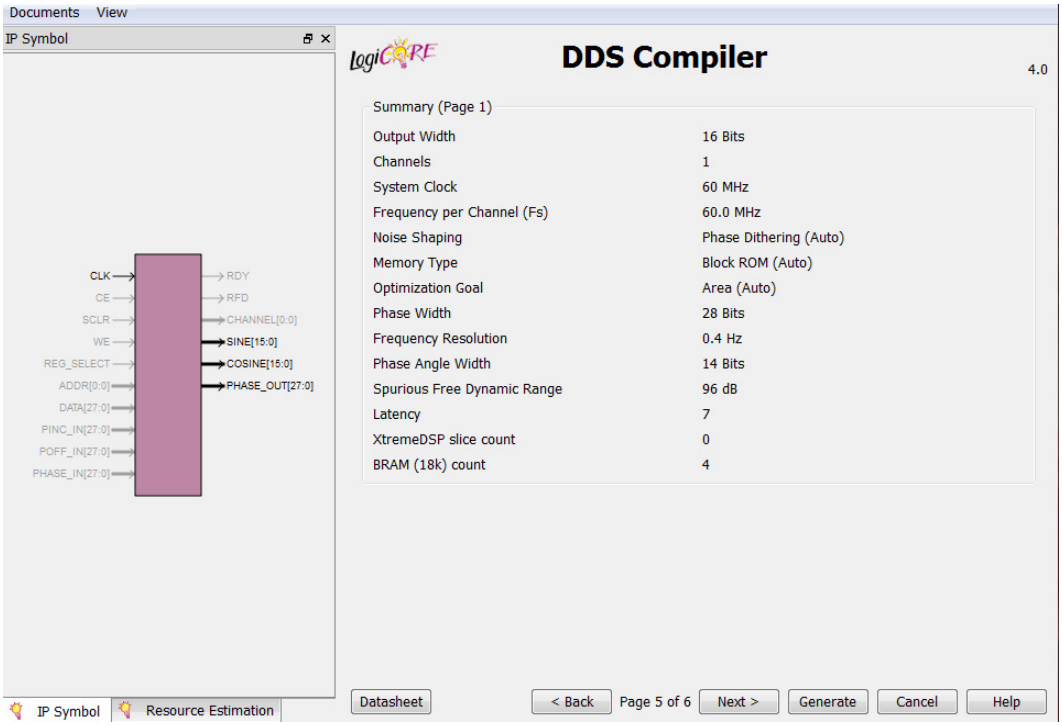
cic_i  : cic_filter
                    port map (
                              din => d_inphase_cic,
                              clk => clk,
                              dout => dataI,
```

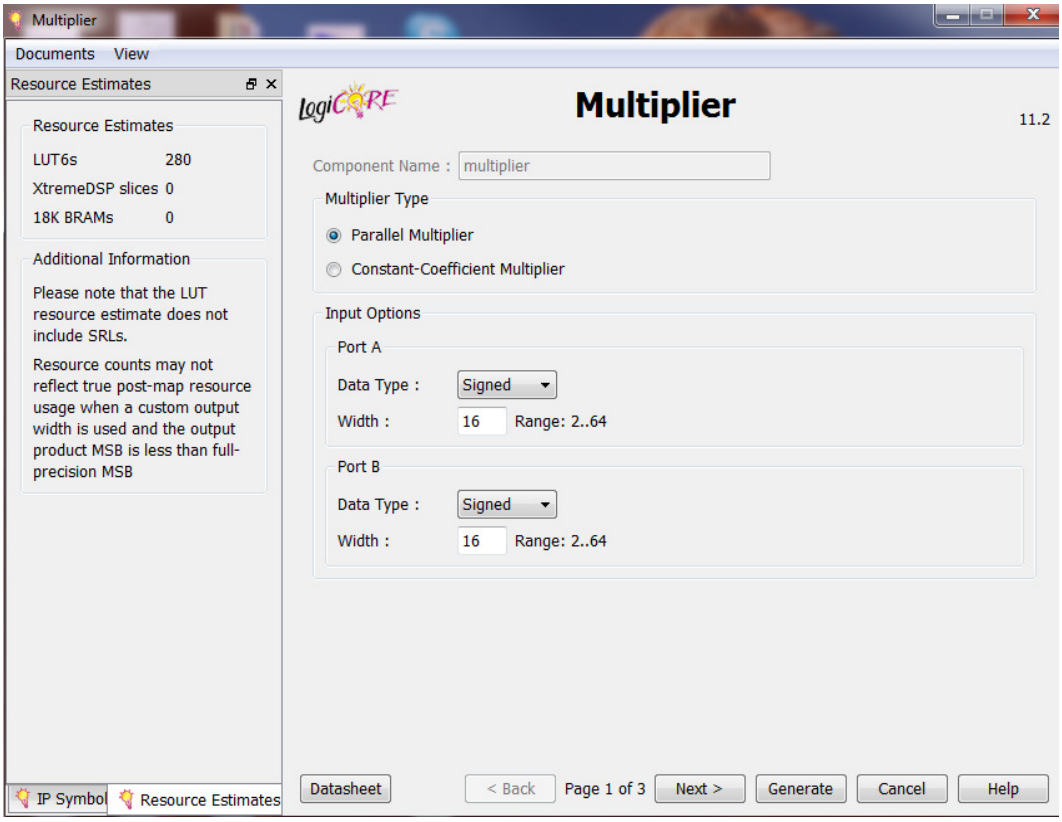
```
                    rdy => ddc_rdy,
                    rfd => open);

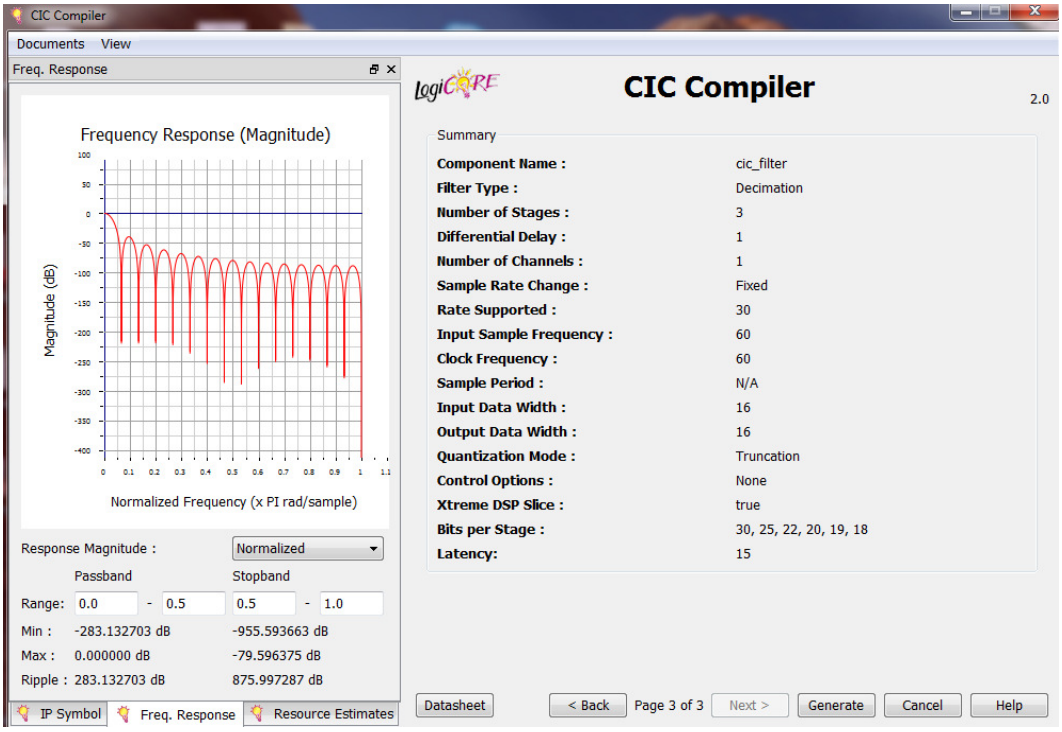
cic_q  : cic_filter
                port map (
                    din => d_quart_cic,
                    clk => clk,
                    dout => dataQ,
                    rdy => open,
                    rfd => open);


end Behavioral;
```

The parameters setup to implement the three IP cores, i.e., DDS, Multiplier, and CIC, are shown as follows.




Multiplier
Documents View
Resource Estimates
Resource Estimates
LUT6s 280
XtremeDSP slices 0
18K BRAMs 0
Additional Information
Please note that the LUT resource estimate does not include SRLs.
Resource counts may not reflect true post-map resource usage when a custom output width is used and the output product MSB is less than full-precision MSB
LogiCORE
Multiplier
11.2
Component Name : multiplier
Multiplier Type
Parallel Multiplier
Constant-Coefficient Multiplier
Input Options
Port A
Data Type : Signed
Width : 16 Range: 2..64
Port B
Data Type : Signed
Width : 16 Range: 2..64
IP Symbol
Resource Estimates
Datasheet
< Back
Page 1 of 3
Next >
Generate
Cancel
Help


CIC Compiler
Documents View
Freq. Response
Frequency Response (Magnitude)
Magnitude (dB)
Normalized Frequency (x PI rad/sample)
Response Magnitude : Normalized
Passband
Stopband
Range: 0.0 - 0.5 0.5 - 1.0
Min : -283.132703 dB -955.593663 dB
Max : 0.000000 dB -79.596375 dB
Ripple : 283.132703 dB 875.997287 dB
LogiCORE
CIC Compiler
2.0
Summary
Component Name : cic_filter
Filter Type : Decimation
Number of Stages : 3
Differential Delay : 1
Number of Channels : 1
Sample Rate Change : Fixed
Rate Supported : 30
Input Sample Frequency : 60
Clock Frequency : 60
Sample Period : N/A
Input Data Width : 16
Output Data Width : 16
Quantization Mode : Truncation
Control Options : None
Xtreme DSP Slice : true
Bits per Stage : 30, 25, 22, 20, 19, 18
Latency: 15
IP Symbol
Freq. Response
Resource Estimates
Datasheet
< Back
Page 3 of 3
Next >
Generate
Cancel
Help

Vitae

Yazhou Wang was born in Chifeng, China, in 1983. He received the B.S. degree in electronic and information engineering from Beihang University, Beijing, China, in 2004. He joined The University of Tennessee, Knoxville in August 2007 and received the M.S. degree in electrical engineering in 2009. He is studying toward his Ph.D. degree in electrical engineering at The University of Tennessee, Knoxville,

From 2005 to 2006, he was an intern RF engineer with the Intel Corporation, Beijing, China, where he was engaged in the coexistence simulation and analysis of an integrated multi-service platform. In summer 2011, he was an intern design engineer with the RF Micro Devices, Inc., Boston, MA, where he was engaged in the development of RFIC amplifiers for 5 GHz 802.11a/n and 800 MHz LTE, respectively. He has authored or coauthored over 25 journal/conference papers and presented at numerous international conferences. His current research interests include UWB systems for security/rescuing/biomedical applications, RFIC/MMIC design, and UWB antennas.

Mr. Wang was the recipient of Best Paper Award of 2010 IEEE Radio and Wireless Symposium student paper competition and 2010 IEEE Microwave Theory and Techniques Society (MTT-S) Graduate Fellowship Award (for Medical Applications). He was also the recipient of Min Kao Graduate Fellowship from EECS department, in 2007 and 2008, and Chancellor's Citation for Extraordinary Professional Promise, in 2011, both from The University of Tennessee.